Space Sweeper Final Report

Creating Space in Space

DSE Group 13

TU Delft

DELFT UNIVERSITY OF TECHNOLOGY

FACULTY OF AEROSPACE ENGINEERING

AE3200

DESIGN SYNTHESIS EXERCISE

Space Sweeper Final Report

Creating Space in Space

Mission: Space Sweeper
Tutor: Dr. ir. Erwin Mooij
Coaches: Dr. Nathan Eskue and Dr. Iklim Akay

June 21, 2022

DSE Group 13

Gabriel Alves Teixeira	4820592	Juan Bas Fernández	5020239
Elias Bögel	5080894	Hugo Buurmeijer	5060354
Frank Meijering	5040175	Daniel Rehling	5056985
Jan Struziński	5052750	Per van Wolfswinkel	5040728
Lorenz Veithen	5075211	Niek Zandvliet	4796403

TU Delft Delft University of Technology

Executive Summary

In 1978, Donald J. Kessler, a former NASA scientist, was the first to estimate the potential impact of the world's indifference towards the threat of space debris. He hypothesised that the exponential nature of the increase of the number of space debris pieces in low Earth orbit (LEO) would lead to a cascade of events that could render this orbital region close to useless, and called this hypothesis the Kessler Syndrome. After decades of knowing how serious the possibility of this disaster is, a debris detecting and cleaning mission has yet to be flight tested, a sad and frankly embarrassing fact. Only one good thing comes from this, a brand new market to explore. Of course, this market will only generate revenue once our planet's governments turn existing space debris mitigation procedures into law. As things stand, the only thing to gain by cleaning space debris is a sense of sustainability, which is sadly not enough for almost any private businessman or woman. This report therefore aims to provide a detailed design of what could be the world's first space-based laser cleaning system, which can hopefully leap over the existing socioeconomic barriers and tackle the Kessler syndrome head on, as it is of utmost interest to this project team to convince the world that the space environment should be just as safeguarded as our own planet.

The mission need statement and the project objective statement, as derived from the user requirements and the current world needs, are the following:

Mission Need Statement

The continuous use of the orbital region up to 1,000 km altitude must be protected from the threat of space debris.

Project Objective Statement

DSE group 13 will design a modular system to sustainably clean up one to ten centimetre sized space-debris objects, arising from a break-up event, from orbital altitudes below 1,000 km, by 10 engineers in 10 weeks.

A fairly simple structure is followed in this report. As is the case with typical mission design reports, the mission's objectives and main requirements are first introduced. A thorough functional analysis is made, and the preliminary mass, power, and cost budgets are then derived. The S/Cs subsystems are then designed in detail, leading to the creation of preliminary CAD models of the system. This is followed by an analysis of the system as a whole, checking wether the subsystems that have been designed in detail can work correctly with each other. Consequently, a compliance matrix is generated, checking if all of the requirements have been met. The final design characteristics are then summarised, and the launcher to be used is chosen following a trade-off procedure. The sustainability strategy and the technological development plans required for the system are also explained, and the report is completed by doing an economic valuation of the mission as a whole, as well as providing some recommendations for future studies.

Payload

An ablation laser and lidar detection laser are selected as the payload. The combination of these two systems allows for removal operations up to 250 km, and detection up to 300 km. The ablation laser is an Nd:YAG laser, operating at 532 nm. The average power while ablating and mass requirements are 27.7 kW and 1282 kg respectively. The payload is equipped to de-orbit debris with an area-to-mass ratio of 0.0795 kg/m^2, which is found to be the limiting factor for debris removal capabilities rather than characteristic length, as suggested in literature. The lidar system operates at an average power of 243 W and has a mass of 286 kg.

GNC

The GNC allows the spacecraft to determine its position required for all orbital manoeuvres by using PODRIX GNSS GPS with precision of 11 cm. Furthermore, its sensors allow the spacecraft to determines its attitude, which has direct impact on the determined accuracy of debris cataloguing. This sensor package consists of two ASTROXP star sensors and 6 gyroscopes inside ASTROgyro, which complement each others performance and allow to achieve accuracy of 0.5 arcsec. Additional PODRIX GNSS GPS sensors are provided to course attitude determination for redundancy during anomalies. The actuators of the spacecraft, 75-75S Control Moment Gyros, are able to provide large torque of 62 Nm to stabilise the spacecraft when laser gimbal is rotated. Finally, large magnetic torquers MT-800B-28V with dipole moment of 800 Am^2 need to be used to dump momentum from external disturbances.

EPS

By means of a solar array, a set of Li-Ion batteries, an appropriate PCDU, and a set of LI-Ion capacitors, the required power at all times can be ensured for each of the components. Even when the system has to ablate 243 particles per day, the capacitors are charged and discharged fast enough for an effective mission. In addition, the subsystem is modular, being able to change the solar array area and the number of capacitors for three different altitudes: 500 km, 750 km, and 1000 km. The maximum total mass of the subsystem was found to be 166 kg, with a solar array area of 35 m^2.

Propulsion

Following a top-level trade-off between cold gas, liquid monopropellant, liquid bi-propellant, and electric propulsion, and using required propellant mass, volume, power, and complexity as criteria, the liquid monopropellant concept is chosen to be designed in more detail by means of three separate trade-offs. The winners of these three trade-offs for thruster, propellant tank, and pressurant tank are: one MONARC-90HT thruster, four PTD-96 propellant tanks, and one 80586-1 pressurant tank. This configuration results in a total dry mass of 49.6 kg, and a total wet mass of 401 kg. The propellant mass is 344 kg, and the pressurant mass is 7.07 kg.

CDHS

The requirements imposed by the detection system are vast, requiring a data rate of 10 Gbps to allow for the images taken by lidar (at 10 kHz) to be input to the processing algorithm. Therefore, the Airbus NEMO-2 was selected, given its excellent data rate and storage performance. Regarding processing requirements, the algorithm, which may have been infeasible to implement in the past, requires the state-of-the-art Airbus HPDP, which can run the remaining subsystem operations at the same time as the detection algorithm. 5 Gbit of RAM on the Airbus HPDP allow for sufficient storage space for all subsystem code. The final configuration of the system involves one Airbus NEMO-2, and two Airbus HPDPs, at a power of 25.64 W, and mass of 9.32 kg.

Thermal Management System

With extreme power draw during ablation operations at only 25.2% efficiency, the thermal management system (TMS) must be able to transport away and reject approximately 26 kW of waste power during active periods of the ablation laser. This requires a strong thermal connection from the primary payload, as well as connected subsystems like the battery and capacitor units, as well as the power conditioning and distribution unit (PCDU). This calls for heavy use of heat pipes and efficient radiators with optical solar reflector (OSR) surfaces. 35 heat pipes of 8 mm diameter connect the laser system to 16 m^2 of radiators, with four further heat pipes connecting both the PCDU, as well as the Li-ion batteries to another 2.4 m^2 set of OSR radiators. As the average power consumption throughout the mission decreases drastically, variable conductance heat pipes are employed to control the amount of heat rejected. The TMS design chosen has a mass of 65 kg and requires 74 W.

Telecommunication

The telecommunication architecture uses the ESTRACK core and augmented network for longer communication windows, with an minimum time of communication of 11% of the time for 350 km orbital altitude. The subsystem on the spacecraft makes use of a fully redundant architecture with two low-gain patch antennas to be positioned on the lower side of the spacecraft and two transceivers. Diplexers are used to use the same antenna for both receiving and sending activities. The lowest link budget estimation, using the lowest G/T figure of merit ground station is 16.36 dB using a BPSK modulation along a Convolutional-RS coding method.

Final Structure

The final configuration of the spacecraft consists of a cylindrical, load-carrying internal structure, fully aluminium. The thickness of this cylinder varies along the length of the spacecraft, as the load, that the structure is subjected to during the launch, is higher at the bottom of the spacecraft. The gimbal for the laser antenna dish is assumed to be load carrying, as well.

System Analysis

An important aspect of the design is how well the different subsystems are integrated, and the system performs as a whole. Varying different key parameters, shows that the chosen final design is indeed optimal, by means of a sensitivity analysis. Also, the final design is within the initially determined mass and power budgets, and almost all mission requirements are satisfied. The most important requirement that is not met, is minimal launch cost, which is deemed infeasible with the current design. The system also encounters many risks during its mission, with the most critical risk being system collision with debris, which is mitigated using shielding.

Risk Analysis

The risk analysis is grouped into risks from all subsystems. Any risks, that have a high likelihood and a high consequence, need to be mitigated. This is the case for a total of 16 risks, of which the most critical risk is SS-TL-MI-RISK-ENV-005: **System collision with debris**. This is because the spacecraft is sent to an orbit, which is highly populated with debris. This risk is mitigated by having a slightly higher orbital altitude than the debris.

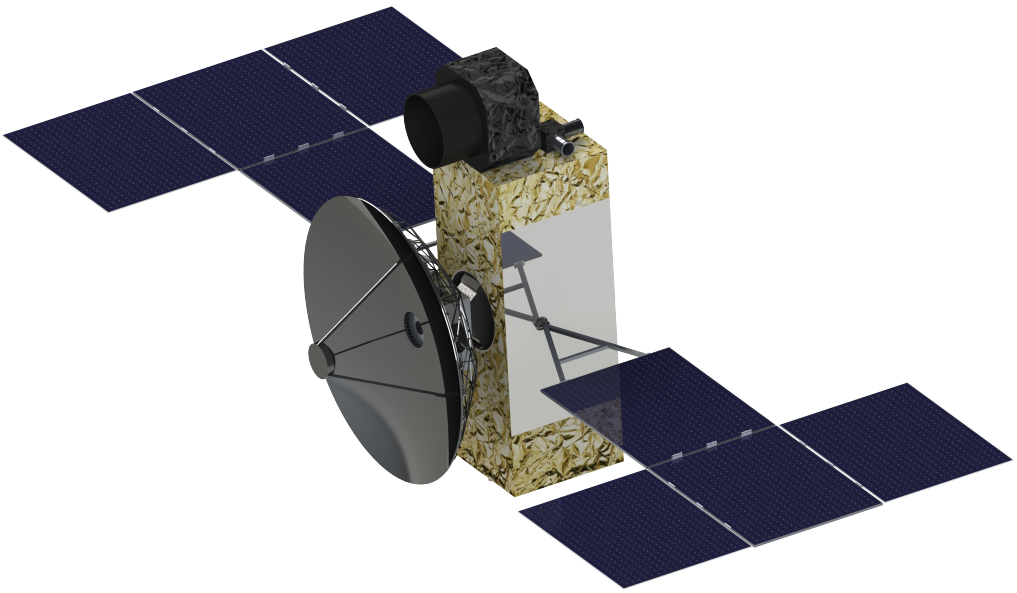

Figure 1: Isometric view of the external layout of the Space Sweeper. It mainly shows the bus, covered in Multi-Layer Insulation, solar arrays, radiator panels, ablation laser, lidar.

Final Design Characteristics

The launcher is also chosen in this stage. A trade-off between the Falcon 9, Ariane 62, and H-IIA202 was carried out using orbital insertion, allowable loads, reliability and cost as criteria, with the Ariane 62 coming out as the winner. In terms of operations and logistics, the Space Sweeper is to be used as an emergency mission, to be launched within 20 days of the collision or explosion event. This requires final assembly near the Kourou launch site and a launcher to be quickly available. The latter is ensured using a fast lane contract with ArianeSpace. Additionally, special End of Life procedures are automatically started in case a hacking is detected. The reliability and the availability of the spacecraft are to be maximised to ensure a successful mission and, as a result, not becoming part of the space debris itself. The reliability and the availability of the Space Sweeper are 0.915 and 0.993 respectively.

Development Strategy & Planning

Dedicated research into the debris properties that influence the ablation process (size, shape, material, and rotational rates) is discussed, as well as further development of the novel laser payload. Two facilities in the US are selected, and one in the EU, which will provide adequate facilities to perform laser development and debris research. A brief summary of interested third parties is given, to allow for faster development of current technologies, and shared costs if applicable.

The aim of the project team is to create a system that deserves a platinum certified rating in the newly created Space Sustainability Rating (SSR)[1]. To accomplish this, the team will take into account all debris mitigation guidelines published by the IADC, and perform a thorough Environmental Life Cycle Assessment (E-LCA), following the ESA's "*Space System Life Cycle Assessment Guidelines*" handbook.

Economic Valuation

A rigorous cost estimation process was adopted, estimating the labour, component, and facility costs for all phases of the project. The total cost of the project was estimated at €652 million, with a contingency margin of 20%. This estimate includes the launch costs with launch insurance considered. A large portion of this cost was allocated to research and technology development, at 47% of the total mission cost. This is expected, as prototyping and testing facilities are highly expensive and the novelty of the mission demands extensive research and testing.

The market value of LEO is considerable, and the debris removal market is an ever-growing field that is bound to gain a lot of attention in the years to come. However, due to the issue of accountability and liability for debris producing fragmentations, the marketability of the debris removal system depends largely on global political action in the future. However, the socio-economic benefit of space debris removal is expected to vastly outweigh the associated costs.

[1] URL: https://spacewatch.global/2022/04/space-sustainability-rating-to-launch-in-june/ [Accessed on 13-06-2022]

Contents

List of Symbols

Latin Letters	Quantity	Symbol Unit
A_{cone}	Area of the end of a cone; projection onto a sphere's surface	[m^2]
A_{debris}	Frontal area of the debris	[m^2]
A_{hemi}	Area of the curved side of a hemisphere	[m^2]
A_p	Cross-sectional area of piping	[m^2]
$A_{pattern}$	Same as A_{cone}, but for a complete scanning pattern	[m^2]
A_{SA}	Solar array area	[m^2]
a	Semi-major axis	[m]
a_l	Constant regulated by diffraction	[-]
a_{J_2}	Acceleration due to J_2 effect	[m/s^2]
a_{Earth}	Acceleration due Earth's gravitation	[m/s^2]
a_{drag}	Acceleration due to drag	[m/s^2]
B	Parameter relating fluence to pulse duration	[$W/m^2 s^{1/2}$]
B_{sensor}	Bandwidth of the lidar receiver sensor	[m]
C	Capacitance	[F]
CF	Compression Factor	[-]
C_m	Coupling coefficient	[N/W]
C_{m0}	Variable used to determine C_m	[N/W]
D	Mirror (aperture) diameter	[m]
d_d	Diameter of debris	[m]
D	Diameter	[m]
D_{debris}	Debris diameter	[m]
D_{eff}	Effective mirror (aperture) diameter	[m]
D_{sp}	Yearly solar panel degradation	[-]
DR_{image}	Data rate for images	[bps]
d_h	Diameter of piping	[m]
d_s	Spot diameter at target range	[m]
E	Total Energy	[J]
E	Material Young's modulus	[N/m^2]
E_{cap}	Capacitor energy	[J]
E_{bat}	Battery energy	[J]
E_p	Pulse Energy	[J]
$E_{pulse_{lidar}}$	Lidar pulse energy	[J]
E_ρ	Energy density	[J/kg]
f	Pulse frequency	[Hz]
f_e	Eclipse fraction	[-]
f_{lat}	Lateral natural frequency	[Hz]
f_{lon}	Longitudinal natural frequency	[Hz]
$f_{rep_{lidar}}$	Pulse repetition rate (frequency)	[Hz]
g	Sea level gravitational acceleration	[m/s^2]
g_0	Earth's Gravity	[m/s^2]
h	Altitude over surface of the Earth	[m]
I	Area moment of inertia	[m^4]
I_{back}	Background radiation intensity	[W/m^2]
I_d	Inherent degradation factor	[-]
I_{debris}	Power flux received at the debris	[W/m^2]
I/LOC	Instructions carried out per LOC	[-]
I_{sp}	Specific Impulse	[s]
I_{xx}	Mass moment of inertia about the X-axis	[kgm^2]
I_{yy}	Mass moment of inertia about the Y-axis	[kgm^2]
I_{zz}	Mass moment of inertia about the Z-axis	[kgm^2]
$I_{xy} = I_{yx}$	Product moment of inertia of the X- and Y-axis	[kgm^2]
$I_{xz} = I_{zx}$	Product moment of inertia of the X- and Z-axis	[kgm^2]
$I_{yz} = I_{zy}$	Product moment of inertia of the Y- and Z-axis	[kgm^2]
J_2	J_2 constant	[-]
I_λ	Radiation intensity per wavelength	[$Wm^{-3}sr^{-1}$]
k	Absolute roughness	[m]
k_{lat}	Beam lateral spring constant	[N/m]
k_{lon}	Beam longitudinal spring constant	[N/m]
$\hat{k}$	Z-axis in the ECEF coordinate system	[-]
L	Target range	[m]
LOC	Lines of Code	[-]
M^2	Corrected beam quality	[-]
M_{dry}	Dry mass	[kg]
M_{feed}	Mass of feed system	[kg]
M_{fin}	Final mass	[kg]
$M_{tank_{tot}}$	Total mass of propellant tanks	[kg]
$M_{tank_{pre}}$	Pressurant tank mass	[kg]
$M_{tank_{prop}}$	Propellant tank mass	[kg]
M_{th}	Mass of thruster	[kg]

$M_{tot_{prop}}$	Total mass of propellant tank, incl. mass of pressurant	[kg]
M_{lidar}	Lidar mass	[kg]
M_p	Propellant mass	[kg]
$M_{p_{man}}$	Propellant mass per manoeuvre	[kg]
$M_{p_{loaded}}$	Loaded propellant mass	[kg]
$M_{pr_{pro}}$	Total mass of pressurant inside propellant tank	[kg]
M_{pre}	Pressurant mass	[kg]
M_{wet}	Wet mass	[kg]
m	Spacecraft mass	[kg]
$\dot{m}$	Mass flow	[kg/s]
$margin_{feed}$	Margin of feed system	[-]
$N2O4$	Dinitrogen Tetroxide	[-]
N_{images}	Number of images digitised per second	[Hz]
N_{LOC}	Number of lines of code processed per unit time	[-]
N_{pixels}	Sensor resolution	[-]
n_{bits}	Number of bits per sample/pixel	[-]
n_e	Number of ablated particles per eclipse	[-]
n_{orb}	Number of ablated particles per orbit	[-]
n_{tot}	Number of ablated particles per day	[-]
P_{avg}	Average power	[W]
P_{bus}	Spacecraft's bus required power	[W]
P_{debris}	Total power reflected by the debris	[W]
P_{out}	Output power of the laser	[W]
P_{pulse}	Pulse power	[W]
P_{SA}	Solar array required power	[W]
P_{sc}	Spacecraft required power	[W]
P_{search}	Lidar required power	[W]
P_{shoot}	Laser required power	[W]
$Pulse_{min}$	Minimum pulse duration	[s]
$p_{max_{allow}}$	Maximum allowable pressure	[Pa]
$p_{min_{req}}$	Minimum required pressure	[Pa]
$p_{pre_{BOL}}$	Pressurant pressure at BOL	[Pa]
P_ρ	Power density	[W/kg]
R	Distance (range) to debris	[m]
R	Universal gas constant	[J/K/mol]
R_b	Lateral stress ratio	[-]
R_c	Longitudinal stress ratio	[-]
R_E	Radius of Earth = 6,378,137 ([1])	[m]
r	radius	[m]
$\boldsymbol{r}$	Position vector of the ground station	[-]
T_{eff}	Product of all system losses	[-]
T_{ion}	Thrust provided by ion propulsion system	[N]
T_{Hall}	Thrust provided by Hall-effect propulsion system	[N]
t	Thickness	[-]
$t_{dumpfraction}$	Time between data downlinks	[s]
t_d	Daylight duration per orbit	[s]
t_e	Eclipse duration per orbit	[s]
t_{min}	Minimum thickness	[m]
$t_{b_{min}}$	Minimum burn time	[s]
$t_{mission}$	Mission time	[s]
$t_{transmit}$	Time to transmit data to ground	[s]
t_{shoot}	Time the laser is shooting	[s]
V	Velocity	[m/s]
V	Voltage	[V]
V_{p_l}	Loaded propellant volume	[m^3]
V_{p_u}	Usuable propellant volume	[m^3]
V_{tank}	Total propellant tank volume	[m^3]
$V_{tank_{pre}}$	Pressurant tank volume	[m^3]
$V_{tank_{pro}}$	Propellant tank volume	[m^3]
V_{lidar}	Lidar volume	[m^3]
$V_{p_{pro}}$	Pressurant volume in propellant tank	[m^3]
$V_{produced}$	Volume/size of data produced	[b]
$V_{t_{req}}$	Required tank volume	[m^3]
$V_{tot_{prop}}$	Rectangular volume occupied by propellant tank	[m^3]
$V_{transmit}$	Volume of data to be transmitted	[b]
V_{us}	Usable tank volume	[m^3]
V_1	Volume of pressurant tank	[m^3]
V_2	Volume of propellant and pressurant tank	[m^3]
v_{SC}^{GS}	Satellite position in the ground station coordinate frame	[-]
x	X coordinate in Cartesian coordinate system	[m]
y	Y coordinate in Cartesian coordinate system	[m]
z	Z coordinate in Cartesian coordinate system	[m]

[1] URL https://codata.org/ [Accessed 16-05-2022]

Greek Letters	Quantity	Symbol Unit
α	Absorptivity	[-]
β	Angle between the Sun and the spacecraft's orbital plane	[rad]
Δ	Change	[-]
δ_{target}	Divergence between beam and target	[m]
θ	An angle	[rad]
η_{bat}	Battery efficiency	[-]
η_d	Power distribution efficiency during daylight	[-]
η_e	Power distribution efficiency during eclipse	[-]
η_q	Quantum efficiency of the lidar receiver sensor	[-]
η_{plas}	Plasticity coefficient	[-]
η_r	Efficiency of the lidar receiver optics	[-]
η_{sp}	Solar cell efficiency	[-]
η_t	Efficiency of the lidar transmitter optics	[-]
μ	Dynamic viscosity	[Pa· s]
μ_E	Gravitational parameter of the Earth	[m^{3/s^2}]
μ_{pos}	Poisson's ratio	[-]
λ	Friction coefficient	[-]
λ	Wavelength	[m]
ρ	Density	[kg/m^3]
ρ	Reflectivity	[-]
σ	Stress	[Pa]
σ_{cr}	Critical stress	[Pa]
σ_{yield}	Yield stress	[Pa]
τ	Pulse duration	[s]
Φ_{sun}	Solar constant	[W/m^2]
Ω	Solid angle	[sr]

List of Abbreviations

1Φ-MPFL	*Single-Phase Mechanically Pumped Fluid Loop*
2Φ-MPFL	*Two-Phase Mechanically Pumped Fluid Loop*
3D	*3-Dimensional*
ADCS	*Attitude Determination and Control*
AMR	*Area-to-Mass Ratio*
BCR	*Battery Charge Regulator*
BDR	*Battery Discharge Regulator*
BER	*Bit Error Rate*
BEC	*Backward Error Coding*
BoL	*Begin-of-Life*
BPSK	*Binary Phase Shift Keying*
CAD	*Computer Aided Design*
CAGR	*Compound Annual Growth Rate*
CBS	*Cost Breakdown Structure*
CCSFS	*Cape Canaveral Space Fore Station*
CDHS	*Command and Data Handling System*
CDM	*Conjunction Data Messages*
CG	*Centre of Gravity*
CM	*Centre of Mass*
COTS	*Commercial Off-The-Shelf*
CPU	*Central Processor Unit*
DET	*Direct Energy Transfer*
DOT	*Design Options Tree*
DOD	*Depth Of Discharge*
ECEF	*Earth-centered, Earth-fixed*
ECI	*Earth-centered, Inertial*
EIRP	Equivalent Isotropic Radiated Power
EKF	*Extended Kalman Filter*
E-LCA	*Environmental Life Cycle Assessment*
EM	*Electromagnetic*
EMC	*Electromagnetic Cleanliness*
EOP	*Early Operational Phase*
EOM	*Earth Observation Mission*
EoL	*End-of-Life*
EPS	*Electrical Power Subsystem*
ESA	*European Space Agency*
FEC	*Forward Error Coding*
FEM	*Forward Error Method*
FoV	*Field of View*
GHG	*Green House Gases*
GNC	*Guidance, Navigation and Control*
GS	*Ground Station*
HAS	*High Accuracy Service*
HK	*Housekeeping*
HP	*High Pressure*
HPBW	*Half Power Beam Width*
ICBM	*Inter-Continental Ballistic Missile*
ILCD	*International Reference Life-Cycle Data System*
IR	*Infrared*
IPS	*Instruction per Second*
IR	*Infrared*
ISS	*International Space Station*
ITU	*International Telecommunication Union*
LAP	*Laser Ablation Propulsion*
LCI	*Life Cycle Inventory*
LCIA	*Life Cycle Impact Assessment*
LEO	*Low Earth Orbit*
LEOP	*Launch and Early Operations Phase*
LOC	*Lines of Code*
LP	*Low Pressure*
LHC	*Left Handed Circular*
lidar	*Light Detection and Ranging*
MIB	*Minimum Impulse Bit*
MLI	*Multi-Layer Insulation*
MMH	*Monomethylhydrazine*
MNS	*Mission Need Statement*
MPFL	*Mechanically Pumped Fluid Loop*
Nd:YAG	*Neodymium-doped Yttrium Aluminum Garnet*
NOC	*Network Operations Centre*
OBC	*On Board Computer*
ODE	*Ordinary Differential Equation*
OSR	*Optical Solar Reflector*
PCDU	*Power Conditioning and Distribution Unit*
PF	*Particle Filter*
PID	*Proportional-Integral-Derivative*
POS	*Project Objective Statement*
PPT	*Peak Power Tracker*
radar	*Radio Detection and Ranging*
RAM	*Random-Access Memory*
RAAN	*Right Ascension of the Ascending Node*
R&D	*Research and Development*
RF	*Radio Frequency*
RFQ	*Request for Quote*
RHC	*Right Handed Circular*
RTG	*Radioisotope Thermoelectric Generator*
RTO	*Radial, Tangential, Out-of-plane*
S3R	*Sequential Switching Shunt Regulators*
SADA	*Solar Array Drive Actuator*
SAR	*Solar Array Regulator*
SC	*Spacecraft*
SDRAM	*Synchronous Dynamic Random-Access Memory*
SF	*Safety Factor*
SLOC	*Source Lines of Code*
SNR	*Signal-to-Noise Ratio*
SSN	*Space Surveillance Network*
SST	*Space Surveillance and Tracking*
TC	*Telecommand*
TM	*Telemetry*
TMS	*Thermal Management System*
TRL	*Technology Readiness Level*
TSC	*Tanegashima Space Center*
TT&C	*Telemetry, Tracking, and Command*
UKF	*Unscented Kalman Filter*
URES	*Resultant Displacement*
VSFS	*Vandenberg Space Force Station*

Introduction 1

The Kessler syndrome describes the scenario in which space debris collide with each other in an exponentially increasing rate, as derived by Kessler et al. (2010). This snowball effect can result in space not being accessible anymore for future missions, and even for current widely-used services such as GPS. Ever since Sputnik 1 was brought into orbit, debris has been accumulated in space. The amount and spread of this debris has been accelerated by the rapidly growing space industry and missions, like the Russian anti-satellite missile test in 2021 [1]; having now more than 900,000 debris particles larger than 1 cm orbiting the Earth[2], with 75% of them concentrated in LEO (IADC, 2013). The industry has come to the realisation that actions need to be taken to prevent, slow down, and possibly reverse the tendency of the space debris population to increase. Proof of concepts missions, like RemoveDEBRIS[3] and Clearspace-1, have been developed to test the feasibility of performing this task (n.a., 2020).

The aim of this report is to present the final stage of the design process followed by the team in the past four weeks. This is following a concept selection done by Teixeira et al. (2022b), in which the space-based laser concept emerged as the winner. This stage involves designing the different subsystems of the space-based laser in detail, and integrating them to create a full working spacecraft.

With maximal readability and a logical flow of events in mind, this report is structured as follows. As typical with these type of reports, the mission's objectives and requirements are first presented in Chapter 2. Chapter 3 then starts by summarising the procedure followed to selected the concept being designed in this report, as an aid for the potential reader. A functional analysis, including both a flow diagram and a breakdown structure, and the preliminary mission budgets are also seen in this chapter, as well as the orbital simulations done by the team. This is followed by the detailed design stage of every subsystem, as seen in Chapters 4 through 10. Next, using the results from the subsystem designs, Chapter 11 presents the preliminary general layout of the final design, by means of detailed engineering drawings. The system as a whole is then analysed in terms of sensitivity, compliance, and subsystem integration, in Chapter 12. Chapter 13 includes the launch vehicle selection, the operations and logistics plan and the RAMS characteristics of the mission as a whole. Technical development plans for instruments that require them at this stage are included in Chapter 14, which also shows the sustainability strategy and planning to be followed in future development. Finalising the content of the report, Chapter 15 presents the mission's economic valuation, including a cost breakdown and a thorough market analysis. Note that this cost breakdown include subsystem costs, these are not determined in the dedicated subsystem chapters. The results are finally concluded on, and a few recommendations for further work are given in Chapter 16.

[1] URL:https://www.timesofisrael.com/russian-missile-test-causes-debris-cloud-threatening-international-space-station/ [Accessed on 29-04-2022]
[2] URL: https://www.esa.int/Safety_Security/Space_Debris/About_space_debris [Accessed on 28-04-2022]
[3] URL: https://www.surrey.ac.uk/surrey-space-centre/missions/removedebris [Accessed on 29-04-2022]

Mission Overview 2

In this chapter, the overall mission considered in this report is presented and explained. First, the mission objectives are detailed in Section 2.1. Second, the mission requirements are presented in Section 2.2.

2.1 Mission Objectives

A mission need statement (MNS) aims to define what market opportunities or needs the mission is based on, and allows determining whether a mission was successful or not. The MNS of this project is as follows:

> **Mission Need Statement**
>
> *The continuous use of the orbital region up to 1,000 km altitude must be protected from the threat of space debris.*

The project objective statement (POS) specifies what the project will focus on to satisfy the mission need, including constraints. It is given by the following statement:

> **Project Objective Statement**
>
> *DSE group 13 will design a modular system to sustainably clean up small sized space-debris, arising from a break-up event, from orbital altitudes below 1,000 km, by 10 people in 10 weeks.*

To elaborate on the MNS and the POS, the mission targets break-up events, either explosions or collisions, which generate a large amount of space debris fragments, with the potential of catastrophically damaging spacecraft (usually fragments larger than 1 cm (Wright, 2009, p.2)), polluting the entire orbit in less than 20 orbital periods, and making, in less than a year, an altitude range highly dangerous or even inoperative for numerous decades (Klinkrad, 2006, p.73). The idea is to send a system capable of de-orbiting a percentage of this large-sized space debris to immediately clean the affected orbits, or at least accelerate the process. In addition, the system shall not create any extra space debris, and it should be as sustainable as possible, since the amount of space collisions is expected to increase in the future[1]. The focus on altitudes up to 1,000 km comes from the fact that the highest debris concentrations are at an altitude between 800-1,000 km, and that the probability of collision, if a fragmentation event takes place, increases with lower altitude.

Challenges the team will need to face include among others: the debris spread in altitude, the rapidly increasing spread in the cross-track direction, the high relative velocities (beyond 1 km/s (Klinkrad, 2006, p.71)), and the different debris materials, shapes, and sizes.

The primary and secondary missions are derived directly from the client's requirements. The primary mission is to clean at least 50% of the orbit in which the break-up event has occurred. The secondary mission is to detect space debris objects that cannot be detected from ground, therefore the Space Sweeper must detect debris object smaller than 1 cm (Flohrer et al., 2005). This leads to the following mission objectives:

1. The primary mission consists of the ablation of the detected debris above 1 cm, and starts right after the end of the early operational phase.
2. The secondary mission consists of detecting 1 mm or higher particles, and to catalogue them. Additionally, another payload will be taken on-board to extend the market size of the mission, as will be investigated in Chapter 15.

2.2 Mission Requirements

The top level requirements of the Space Sweeper mission were analysed during the previous phases. This resulted in the derivation of both mission and system level requirements, as well as a negotiation with the client to determine a set of relaxed user requirements. The table below presents a list with the most important user, top-level, and system-level requirements to perform the trade-off.

Table 2.1: Driving and key requirements.

Requirement ID	Description	Rationale
		General

[1] URL: https://www.esa.int/Safety_Security/Space_Debris/About_space_debris [Accessed on 28-04-2022]

SS-TL-STK-US-REQ-G-002	The system shall be operable at orbital heights between 350 and 1,000 km	The system will target the lowest altitude at which there is significant amount of satellites[2]. Lower altitudes are also not considered due to the fast aerodynamic decay. Up to 1000 km to consider the altitudes with higher object flux (IADC, 2013, p.11)
SS-TL-STK-US-REQ-G-003	The system shall be able to remove at least 50% of the space debris fragments of size larger than 1 cm and smaller than 10 cm, when focusing on the ones with larger orbits.	Roughly 50% of the particles decrease their semi-major axis after a collision. These particles usually re-enter within a few years, even at high altitudes (Wang, 2010, p.99). Particles over 1 cm are the ones usually critical for spacecraft (Wright, 2009, p.2). Only a small percentage of fragments exceed 10 cm, even for big collisions (Wang, 2010, p.90).
SS-TL-STK-US-REQ-G-007	The cost of a single system including operation, and launch, shall not exceed M€ 400.	Derived from client and cost breakdown.
SS-TL-STK-US-REQ-G-012	The minimum mass of a single space object to be considered is 350 kg.	Minimum mass such that the mission is worth it. Average mass of LEO satellites[3]
		Mission
SS-TL-STK-US-MI-001	The system shall be operational before the end of 2028.	Negociated with client in Teixeira et al. (2022b)
SS-TL-STK-US-REQ-MI-002	Minimum operation time for the primary mission shall be six months.	After six months, the debris spread in the cross-track direction is too large for the mission to be effective (Wang, 2010, p.100).
SS-TL-STK-US-REQ-MI-003	Debris detection and removal during nominal system operation shall be autonomous, but some modes for which ground human support is desirable shall be automatic.	Due to short response time and for safety reasons.
SS-TL-STK-US-REQ-MI-013	Minimum operation time for the secondary missions shall be six months.	Derived from client and from primary mission analysis.
SS-TL-MI-REQ-001	The system shall detect debris smaller than 1 cm.	It shall be better than ground debris tracking available capabilities (Flohrer et al., 2005).
		Sustainability
SS-TL-STK-US-REQ-STB-001	The maximum NASA Toxicity Hazard Level allowed for the system shall be zero.	Effectively harmless to humans (NASA, 2014).
SS-TL-STK-US-REQ-STB-006	Operation of the space-debris removal satellite shall not increase the space-debris population.	It would be very detrimental to leave more debris in an orbit already highly polluted.
SS-TL-STK-US-REQ-STB-007	The space-debris removal satellite shall have a clear End of Life (EoL) strategy.	To avoid generating more debris at EoL.

[2]URL: https://www.ucsusa.org/resources/satellite-database [Accessed on 04-05-2022]
[3]URL: https://www.ucsusa.org/resources/satellite-database [Accessed on 04-05-2022]

Space-Based Laser System 3

This chapter aims to introduce the system in more detail, and defines some of the general tools that will be used throughout the design activities that follow. First, the concept selection procedure, as performed in Teixeira et al. (2022b), is briefly reiterated. Then, the potential of the inclusion of a ground segment for detection and/or ablation is discussed in Subsection 3.1.1. Subsequently, a detailed functional analysis on the system is performed in Section 3.2. Following, the system is broken up into subsystems and their interfaces are detailed in Section 3.3. Preliminary budgets are presented in Section 3.4. Finally, two simulation tools that are used throughout the design are presented, namely the orbital decay simulation in Section 3.5, and the debris removal simulation in Section 3.6.

3.1 Concept Selection Procedure

Succeeding the generation of a Design Option Tree (DOT) by the entire project team, all but the following four concepts were discarded:

- **Space-based Laser:** uses the principle of ablative laser propulsion to decelerate debris objects and making them re-enter Earth's atmosphere.
- **Net:** using two or more S/C to passively capture debris objects, by traversing the debris orbit with a large area, high strength to weight ratio fabric.
- **Foam:** sprays a type of expanding foam at the debris objects, increasing drag and making them eventually re-enter Earth's atmosphere.
- **Thruster plume:** orienting the plume of a thruster at individual debris objects at close range, decelerating said objects to make them re-enter the atmosphere.

A trade-off was then done to select the concept to be designed in more detail. The criteria were chosen as a first step, allowing the team to analyse the four concepts on each of the chosen criteria. These were complexity, risk, debris removal speed, power, dry mass, wet mass, and volume. During this concept analysis stage, the net was immediately removed from the trade-off procedure due to various reasons, such as the fact that no material exists capable of surviving the very high relative velocities expected, as well as the tonnage of propellant required to maintain a lower speed at a certain orbit. For the sake of completeness, and to have at least four concepts to trade off, a new concept was added, consisting of a constellation of space-based lasers. The trade-off resulted in the single S/C laser concept as the winner, by outscoring the second place concept by almost 20%, as seen below.

Table 3.1: Trade-off results at an orbital altitude of 1,000 km (part 1).

Criteria	**Complexity, 8.37%**	**Risk, 35.0%**	**Debris removal speed, 32.4%**
Design Concept	(61, 122) Low Best, $\sigma = 0.4$	(38, 67) Low Best, $\sigma = 0$	(1, 5) High Best, $\sigma = 0.894$
Laser	red 122 → 0	green 38 → 1	yellow 3 → 0.5
Laser constellation	red 122 → 0	red 67 → 0	green 5 → 1
Foam	green 74 → 0.787	yellow 47 → 0.69	red 1 → 0
Thruster	green 61 → 1	orange 55 → 0.414	red 1 → 0

Table 3.2: Trade-off results at an orbital altitude of 1,000 km (part 2).

Criteria	**Power [W], 2.0%**	**Dry mass [kg], 8.1%**	**Wet mass [kg], 9.75%**	**Volume [m^3], 4.39%**	**Total**
Design Concept	(8.75e+03, 9.99e+04) Low Best, $\sigma = 0.447$	(868.56, 1.46e+04) Low Best, $\sigma = 0.825$	(1.48e+03, 3.48e+04) Low Best, $\sigma = 0.933$	(8.25, 64.2) Low Best, $\sigma = 0.64$	
Laser	yellow 5.00e+04 → 0.548	green 3.68e+03 → 0.795	green 4.02e+03 → 0.924	yellow 32.1 → 0.574	0.703
Laser constellation	red 9.99e+04 → 0	yellow 7.37e+03 → 0.526	green 8.05e+03 → 0.803	red 64.2 → 0	0.445
Foam	green 1.09e+04 → 0.977	green 868.56 → 1	green 1.48e+03 → 1	green 8.25 → 1	0.549
Thruster	green 8.75e+03 → 1	red 1.46e+04 → 0	red 3.48e+04 → 0	yellow 27.48 → 0.656	0.277

3.1.1 Potential for Hybrid System

As discussed in Teixeira et al. (2022b), ground-based systems could allow for the optimal solution to the space debris problem, and should be considered. This was left to be determined and will be decided on first. Given that SS-TL-MI-REQ-001 (Teixeira et al., 2022b, p.5) dictates that the space-based system must be able to detect debris smaller than what is possible from ground, to comply with the requirements would imply that the ground-based system would include the laser, and the space-based system the detection system. Communication with Phipps [1] also confirmed that the atmospheric effects (especially scattering) are very difficult to accurately compensate, given the need for non-linear optics, and would result in a system that relies on approximations. On the other hand, should technology improve (especially in a directed fashion, i.e., specific research on how to compensate for atmospheric effects), it is believed that the inclusion of a ground-based system could be fundamental to a robust solution. Considering that power, mass, and volume are limiting to the spacecraft, relaxing these requirements, distributing some functionality to a ground system could relax the constraints on the system, and provide a more (cost) effective solution.

3.2 Functional Analysis

Now that it has been decided to go for a space-based only system, a functional analysis is performed. This is done by first creating a functional flow diagram, followed by a functional breakdown structure. Figure 3.4 introduces functional flow diagram, while Figure 3.5 details some of its more complex functions. Both figures can be found at the end of this chapter.

Firstly, the spacecraft needs to be developed and the design approved. In case it is not, it needs to be reiterated. The sub-assemblies of the spacecraft needs to be then manufactured and assembled, after which they are transported to the launch site for the last integration. The spacecraft is then validated, loaded with propellants and mounted on the launch tower. During launch, the spacecraft is in safe mode and relies on the launch tower for power and telemetry until it disconnects. In the Early Operational Phase that activities are happening in series, with the most essential subsystems being initialised first. This allows to incrementally build up the reliability of the system. Fault Detection, Isolation and Recovery mode is switched on during that period to help resolve any issues with the spacecraft that are likely in that period. During Operational Phase a lot of these functions depend on each other to fulfil their tasks and some of outputs as inputs. When both primary and secondary missions are finished, End of Life phase is entered when spacecraft is deorbited. Figure 3.6 details more sophisticated elements of the functions. Most of these are related to repeating spacecraft modes and functions. Figure 3.6 can be found at the end of this chapter as well.

3.3 System Breakdown and Interfaces

As shown in the previous section, the spacecraft has many functions to perform. These functions can be assigned to different subsystems, that have to interact to perform the overall mission objective. These subsystems will be designed accordingly in the next chapters. Although this will be done largely in parallel, the interactions between the subsystems should be taken into account during the design, by means of interfaces. In the Midterm Report (Teixeira et al., 2022b, p.14), an N^2 chart was provided, which shows all subsystems and their interfaces. With a better knowledge of the system, an updated N^2 chart is created and shown in Figure 3.1.

Furthermore, a design structure matrix is created to provide insight on the design dependencies between the all the subsystems. Although often used interchangeably with N^2 chart, this tool is focused on the system design specifically. For example, the structural stiffness affects the pointing accuracy, which again should be taken into account in the ADCS design. This tool aims to help with the data streams during the design process, which should limit the waiting times and avoid confusion on where parameters should come from. To complement this, a sheet is used to keep track of all these parameters, that will change frequently during the design iterations. The design structure matrix is shown in Figure 3.2. It should be noted that this matrix is not exhaustive, many more data dependencies will be identified during the design process, which will then be added accordingly.

From these two matrices, a number of conclusions can be drawn. First, it is observed that the Guidance, Navigation, and Control (GNC) subsystem has many interfaces with other subsystems, and will have to be designed in close collaboration with the payload subsystem, to ensure sufficient pointing performance. Also, the Thermal Management System (TMS), requires input from almost all subsystems, and will therefore be designed relatively late. The same holds for the Command and Data Handling System (CDHS). Although the same could be said for the Electrical Power System (EPS), the required power mainly depends on the payload, and its design should therefore be started earlier. Furthermore, the launch vehicle has to be selected at an early stage, because it strongly influences the structures subsystem. The CDHS and the tracking, telemetry, and command (TT&C) subsystem are very interrelated, whereby iterations are needed to settle on a certain data budget. These matrices capture more dependencies, which are used to create a coherent final design.

3.4 Preliminary Budgets

Aside from the different design parameters that are to be monitored during the design process, also technical budgets will be defined, and those parameters will be consistently checked to ensure they maintain within budget. Budgets can be exceeded, but should be avoided to end up with a realistic full spacecraft design.

[1] Personal communication Claude Phipps, meeting dd. 23/5/2022, 14:30

Payload - detection	Debris positions	Required pointing	Required power		Debris positions Health info					
	Payload - removal	Required pointing	Required power		Debris removal data Health info	Laser temperature				
Orbital parameters	Pointing info	GNC	Required power	Required ΔV	Orbit Health info Attitude	Eclipse info	Provide pointing info	Attitude control loads		
Power	Power	Power Required pointing	EPS	Power	Power Pointing info Health info	Power	Power			
		Manoeuvre info	Required power	Propulsion	Health info	Thruster thermal info		Thrust loads		
			Required power Power distribution		CDHS	System temperature info	Compressed data			
Controlled temperature	Controlled temperature	Controlled temperature	Required power Controlled temperature	Controlled temperature	Controlled temperature Health info	TMS	Controlled temperature	Controlled temperature		
		Required attitude	Required power		GS data Health info		TT&C		Data	
								Structures		
							Received data		Ground Station	
								Adapter interface Launch loads		Launch Vehicle

Figure 3.1: N2 chart with the subsystem interfaces.

3.4.1 Mass and Power

Preliminary mass and power budgets were calculated in the Midterm Report. However, these lacked resolution and accuracy, since a basic method was used to calculate them, without taking into account the relative importance of different subsystems. A more detailed analysis for each subsystem is required to start the detailed design phase. It is crucial that contingency percentages and margins are included in this analysis. The contingency percentage allows for freedom during the design phase, such that the designer has a more relaxed choice of components when looking at mass and power. The margin is added to compensate for unforeseen circumstances. For this analysis, a percentage of 25% has been chosen for the margin. (Wertz, Everett, et al., 2011)

Methodology

As mentioned before, the method used in the Midterm Report lacked resolution and accuracy. The resolution here is the mass and power budgets per subsystem. The accuracy was lacking, since basic statistical analysis were applied without looking at what missions were used to build this analysis. The new method used will take this into account by creating a range of possible percentages for the mass and power fractions. This range is constructed by using the average values and the sample standard deviations (SSD) for all subsystems in Table 3.5. The range is simply one SSD subtracted from the mean and one SSD added to mean, as can be seen in Table 3.3. Now, engineering judgement can be combined with these ranges of mass and power fractions to arrive at more accurate values for each subsystem, by tweaking the fractions as required. This allows for more detailed budgets, since the defining characteristics of the mission can be taken into account. For this method, it is crucial that both mass and power fractions add up to 100%.

The application of this method for both mass and power budgets is the same. For this method, the payload is taken as a starting point because extensive research into this subsystem has already been done, clearly showing this subsystem is critical. The payload mass, and required power is already determined with quite some accuracy in Chapter 4. Using the mass and power of the payload, combined with the tweaked mass and power fractions, the dry mass and the spacecraft power can be found. The budgets for the other subsystems can also be found by applying the tweaked fractions to the total mass and power budgets.

Budgets require margins and contingencies for unforeseen circumstances and more freedom for design choices. The percentage ranges found for both sets of fractions already include contingency values. These values are shown in Table 3.4. The margins have been set to 25% of the remaining mass and power, which in this case is the target value minus

Payload - detection		Required pointing accuracy Required rotational rate	Required power	ollision avoidanc	Generated data	Material Geometry Operational temperature	Generated data	Size and mass		
Removal range Laser pointing accuracy	Payload - removal	Required pointing accuracy Required rotational rate	Required power Rate of discharge Ablation time		Generated data	Material Geometry Operational temperature	Generated data	Size and mass Laser movement		
		GNC	Required power Eclipse time Requirent current	Required ΔV	Telemetry data	Material Geometry Operational temperature	Orbit	Size and mass Control loads Sensor locations		
		Required solar array pointing Solar panel area	EPS		Telemetry data	Material Geometry Operational temperature		Size and mass Required panel stiffness Solar array movement		
		Thrust	Required power	Propulsion	Telemetry data	Material Geometry Operational temperature		Size and mass Quasi-static loads Tank volume depletion		
			Required power		CDHS	Material Geometry Operational temperature	Necessary data budget	Size and mass		
			Required power		Telemetry data	TMS		Size and mass		
		Required antenna pointing	Required power		Available data budget	Material Geometry Operational temperature	TT&C	Size and mass		
		System interia and stiffness		System mass		Surface area Layout		Structures		Mass and volume
					Ground station dump time		Ground station exposure Ground station characteristics		Ground Station	
			Volume constraint	Orbital insertion				Volume constraint Dynamic/static loads CG constraint		Launch Vehicle

Figure 3.2: Design structure matrix.

Table 3.3: Possible ranges for mass and power fractions for each subsystem (Wertz, Everett, et al., 2011).

	Mass Fraction			**Power Fraction**		
Subsystem	**Mean**	**SSD**	**Range**	**Mean**	**SSD**	**Range**
Payload	0.319	0.175	0.144 - 0.494	0.485	0.106	0.378 - 0.591
Structures & Mechanisms	0.265	0.093	0.172 - 0.357	0.008	0.016	0.008 - 0.024
Thermal	0.025	0.015	0.01 - 0.04	0.091	0.081	0.009 - 0.172
Power	0.205	0.065	0.14 - 0.269	0.090	0.049	0.041 - 0.139
TT&C	0.016	0.020	0.004 - 0.036	0.113	0.166	0.054 - 0.279
On-board Processing	0.046	0.026	0.02 - 0.072	0.144	0.108	0.036 - 0.252
ADCS	0.063	0.038	0.025 - 0.101	0.125	0.099	0.026 - 0.223
Propulsion	0.031	0.025	0.006 - 0.055	0.003	0.007	0.003 - 0.01
Other (Balance + Launch)	0.025	0.043	0.018 - 0.068	-	-	-

the contingency. The outcome of these calculations are the scaling fractions per subsystem, which are split up into three parts: the target value, the contingency, and the margin. However, it must be noted that the contingency percentages for the power budget were taken to be 25% for all subsystems as a first order estimate. Now that the basic method is outlined, attention can be focused towards determining the percentages for each mass fraction by analysing the mission in more detail. Engineering judgement is required to do so. The allocation of percentages will be justified below.

Justification of mass and power percentages

As mentioned before, the average mass and power fractions shown above are based on a set of statistics from other spacecraft. For these to be applied to our system, the fractions for the subsystems of the Space Sweeper that deeply differ from those used to create the statistical relationship must be tweaked, making sure to keep them within the ranges shown in Table 3.3.

Table 3.4: Contingency and margin factors for both mass and power budgets (Wertz, Everett, et al., 2011).

	Mass		Power	
Subsystem	**Contingency**	**Margin**	**Contingency**	**Margin**
Payload	0.3	0.25	0.3	0.25
Structures & Mechanisms	0.1	0.25	0.1	0.25
Thermal	0.15	0.25	0.2	0.25
Power	0.15	0.25	0.1	0.25
TT&C	0.1	0.25	0.05	0.25
On-board Processing	0.1	0.25	0.1	0.25
ADCS	0.15	0.25	0.15	0.25
Propulsion	0.2	0.25	0.1	0.25
Other (Balance + Launch)	0.25	0.25	-	-

Table 3.5: Updated values and reasoning for each mass fraction used for preliminary budgeting.

Subsystem	**Original**	**Updated**	**Reasoning**
Payload	0.31	0.35	Increased, as payload mass is much larger than other S/Cs used as statistics.
Structures & Mechanisms	0.27	0.24	Decreased, as average percentage of S/Cs with similar payload weights is lower
Thermal	0.02	0.03	Low laser efficiency leads to a higher heat disposal requirement.
Power	0.21	0.21	Average power is not critical, no change required.
TT&C	0.02	0.02	TT&C does not differ from other S/C, no change required.
On-board Processing	0.05	0.05	CDHS similar to every other S/C, no change required.
ADCS	0.06	0.04	Decreased, as criticality lies in the laser steering, which will have independent control.
Propulsion	0.03	0.03	Similar to other S/C, no change required.
Other (Balance + Launch)	0.03	0.03	Similar to other S/C, no change required.

Table 3.6: Updated values and reasoning for each power fraction used for preliminary budgeting.

Subsystem	**Original**	**Updated**	**Reasoning**
Payload	0.46	0.47	Increased, as payload is more power intensive than usual, as per Chapter 4.
Structures & Mechanisms	0.01	0.01	Similar to other S/C, no change required.
Thermal	0.1	0.12	Increased, as the heat to be dissipated is higher than normal, requiring more power, as seen in Chapter 9.
Power	0.09	0.09	Power is not critical, no change required.
TT&C	0.12	0.09	High level of autonomy leads to less data exchange.
On-board Processing	0.12	0.12	Similar to other S/C, no change required.
ADCS	0.1	0.09	Decreased, as a smaller ADCS can be used due to the independent laser steering.
Propulsion	0	0.01	Some power, however little, is always needed for this subsystem.

Resulting budgets

Following the methodology described above leads to the generation of the preliminary mass and power budgets presented in Table 3.7.

3.4.2 Volume and Preliminary Launch Vehicle

Taking the preliminary volume budget of 34.1 m^3 calculated in the Midterm report (Teixeira et al., 2022b, p.41) as a starting point, a preparatory analysis was carried out on the launcher to be chosen for the mission. This was done to make sure that there indeed are launchers that can safely ferry our spacecraft into its desired orbit upon a breakup event. Due to political reasons, and relating to the project's main stakeholders as derived in (Teixeira et al., 2022a, p.2), the launcher choices were limited to European, American, and Japanese made launch vehicles. The chosen launchers are the state-of-the-art ones from each of the three chosen producers, noting that not enough information was found for the new japanese H3 launcher, and their main specifications can be seen below. All the options are known to have a payload fairing that can easily fit our system. Note that the larger versions of each launch vehicle, the Falcon Heavy, Ariane 64, and H-IIA204 respectively, are not considered as their payload fairing is typically the same for a much higher cost. They are designed to take payloads to higher altitudes than our mission requires.

Table 3.7: Preliminary mass and power budgets per subsystem, where M stands for mass, and P stands for power.

	Target Value		Contingency		Margin		Total	
Subsystem	**M [kg]**	**P [W]**	**M [kg]**	**P [W]**	**M [kg]**	**P [W]**	**M [kg]**	**P [W]**
Payload	615	3631	231	1362	154	908	1000	5900
Structures & Mechanisms	499	91	62	11	125	23	686	126
Thermal	60	1004	11	251	15	251	86	1506
EPS	417	822	78	103	104	205	600	1130
TT&C	42	861	5	54	10	215	57	1130
CDHS	104	1096	13	137	26	274	143	1506
GNC	80	786	15	147	20	196	114	1130
Propulsion	57	91	15	12	14	23	86	126
Other (Balance + Launch)	55	N/A	17	N/A	14	N/A	86	N/A
Totals	**1928**	**8382**	**447**	**2076**	**482**	**2095**	**2857**	**12553**

Table 3.8: Performance parameters of preliminary launchers. Please note that every parameter refers to a LEO orbit. (*Falcon User's Guide* 2021)(*Ariane 6 User's Manual* 2021)(*H-IIA User's Manual* 2015)

	Launch Vehicle		
Performance	**Falcon 9**	**Ariane 62**	**H-IIA202**
Mass [kg]	22800	10300	8000
Insertion Inclination [deg]	28.5-145	All inclinations	30.4, 51.6
Launch Cost [M€]	62.5 [2]	72 [3]	71.2 [4]
Launch Site	Cape Canaveral, Vandenberg	Kourou	Tanegashima

Besides fitting in the launch vehicle, volume is important for transportability. However, it should be noted that the system will be stored close to the selected launch site, to minimise the required preparation and transportation time. Therefore, the transportation of the system is aimed to be minimal, in accordance with the operations and logistics plan set forth by the team.

3.4.3 Cost

Space systems are well-known for their high costs and their tendency to consistently exceed their allocated costs budgets. Therefore, it is considered key to design with costs in mind, right from the start. Especially for the mission at hand, the removal of space debris, where accountability is one of the biggest concerns, budget overruns are likely to discourage other parties to contribute to space sustainability by means of debris removal. Inversely, if this mission proves to be cost-effective, other entities may decide to invest in this product as well, such that little to no additional development costs are required, and essentially only extra systems have to be manufactured. Provided the pollution of space is caused not by a single entity, but instead by the numerous nations and companies that make use of space, nation-wide participation is a crucial part of its solution, and should therefore be stimulated.

Budget

As per requirement SS-TL-STK-US-REQ-G-003, determined by the customer, the cost of a single system, including operation, but excluding launch, shall not exceed M€400. Obviously, it is the aim to avoid exceeding this budget. This has been identified as a major challenge in the design, given the novelty of the system, particularly of the use of the payload in a space environment. Therefore, a qualitative analysis on the cost of the system is performed, and guidelines to minimise the cost of the system are presented. This is rather high-level, and simply used as an aid in the design process, and not to provide an in-depth analysis of the costs per subsystem, given the many unknowns of the system before subsystem design. A detailed cost breakdown, however, will be done once all subsystems are analysed individually, and more details about the system are known, which can be found in Section 15.1.

Subsystem costs

As mentioned previously, the payload for the chosen design concept is expected to drive the costs of this mission. Both the detection mechanism, and the ablation laser require performance that has not yet been demonstrated in space, which in turn is likely to demand special development. These technologies are very complex, and need advanced facilities for development, testing, and manufacturing. During the design, it is thus essential to constantly monitor the performance of

[2] URL: https://www.spacex.com/media/Capabilities&Services.pdf [Accessed on 06-06-2022]

[3] URL:https://www.inverse.com/innovation/ariane-6-vs-spacex#:~:text=In%20January%202021%2C%20Politico%20reported,9%20launch%20at%20%2462%20million. [Accessed on 06-06-2022]

[4] URL: https://www.tel.com/museum/magazine/spacedev/130422_topics_05/04.html [Accessed on 06-06-2022]

the system, such that performance requirements of the payload subsystem can be kept to the minimum, thereby minimizing the costs involved. The costs of the other subsystems very much depend on the payload. For instance, the power that the EPS shall generate mainly depends on the necessary payload power, which probably requires a large amount of power, given the nature of laser technology. If solar arrays are used, this simply translates into large solar panels, which have high associated costs. Similarly, if more heat is generated by the payload, the TMS will be larger, heavier, and more complex, resulting in higher subsystem costs. Aside from the strong dependency on the payload, other general guidelines for minimising costs can be made. For the GNC, for example, it is beneficial to have autonomous orbit control, to reduce the on ground personnel requirement (Wertz, Everett, et al., 2011).

The use of COTS hardware and software

In general, to maximise reliability and minimise development costs, Commercial Off-The-Shelf (COTS) components are selected. This will probably not apply for the payload, but is expected to be achievable for the other subsystems. With very clear advantages of using COTS components, also a number of downsides are worth mentioning. First, the COTS component is not tailored to your needs, which may lead to substantial inefficiencies, or large modifications. The latter requires extensive testing and collaboration with the manufacturer. To that end, one is highly dependent on the vendor, both for potential technical collaboration, and simply for the availability of their products. Delay in product delivery is a known risk and has jeopardised projects in the past. Besides hardware, this also holds for the software needed to operate the spacecraft. Software is known to be very expensive, which can easily exceed $100 per source line of code (Wertz, Everett, et al., 2011, p.305). The use of standardised, well-documented COTS software is therefore recommended. Particularly for subsystems such as GNC, CDHS, and TT&C, many functionalities are common across different spacecraft and can thus be (partially) re-used. Also, for simulation purposes during the development phase, COTS software is available and can improve its fidelity at a lower cost. It is estimated that, COTS software can be a factor of five to ten cheaper compared to custom software (Fox et al., 2008, p.97). This should be done with caution, however, because if modifications are needed, thorough testing is required, and custom development may actually be more cost-effective. Also, the software is likely suboptimal for this specific use, and its use should thus be carefully traded-off.

Launch costs

Although not taken into account in the overall cost budget mentioned before, the launcher will also contribute to the cost of the mission. In Subsection 3.4.2, three potential launchers were identified, which should be able to fulfil this mission's needs, based on preliminary numbers. Of course, if the mass and volume budgets are exceeded by large amounts (or significantly less), potentially a different launch vehicle shall be selected. This would change the cost of the launch, which is undesirable. Furthermore, it should be noted that the target orbit by definition is not set in stone, because the collision orbit is unknown beforehand. Different orbits require different amounts of delta V, which translates to different fuel costs.

Modularity

Another consideration relating to cost is the modularity of the design. By incorporating modularity on a subsystem level, costs can be reduced. The first mission will be designed such that it can accomplish the mission, even if the collision is the worst case scenario, which corresponds to a heavy collided spacecraft (more debris fragments to be removed), at the highest considered altitude (1000 km). However, when this design proves feasible, and more mission are planned to launch, it would be highly beneficial to have a modular design that, without structural change, can be prepared for a specific type of collision. Already in the previous design phase, it has been decided to use a laser for all targeted altitudes. However, modularity can still be explored for, for example, the EPS subsystem, which can reduce mass, complexity and cost. Individual solar array modules would be designed and manufactured, which can be assembled in the spacecraft beforehand, according to the estimated power needs. This has already been achieved in the past, for instance by the WIRE spacecraft (Wertz, Everett, et al., 2011, p.416). A similar approach would be used for the batteries, where modules of batteries would be developed and installed based on the specific mission needs. Also, modularity in secondary payload could be considered, where the type and/or number of modules taken onboard can be varied depending on the available power, which would be a trade-off with the EPS modules taken onboard, and the available data rates, which is larger for higher orbits. A larger number of secondary payloads would result in more additional revenue, such that higher costs are allowed to have a profitable mission.

3.5 Orbital Decay Simulation

A crucial input for the system design process is the extent to which the altitude, specifically the periapsis altitude, of the space debris shall be lowered. Obviously, the lower one decreases the perigee of the respective debris, the faster it will decay, which is desirable. This, however, comes at the cost of requiring more energy. Thus, a detailed simulation is created to characterise the orbital decay for different perigee altitudes. In addition, this simulation can be used to estimate the required ΔV for orbit maintenance and atmospheric re-entry at EoL, used in the design process of the propulsion subsystem.

3.5.1 Model Assumptions

Table 3.9: List of assumptions used for the orbital decay simulation.

Assumption ID	Description	Validity
DECSIM-AS-01	The atmospheric model NRL-MSISE-00 is used to model atmospheric density.	The NRL-MSISE-00 model is especially appropriate since not only does it account for the exponential approximation of the atmospheric density with altitude, but also for the variation with latitude, longitude, time, magnetic index, and solar activity. The atmosphere is modelled below 1000 km altitude, coinciding with the maximum orbit altitude of the mission.
DECSIM-AS-02	Only disturbances of the so-called J_2 effect are included.	As explained in (Slotten, 2017, p.2), it is the largest perturbation parameter, and it would be acceptable to exclude the rest for a preliminary simulation.
DECSIM-AS-03	The frontal area and drag coefficient of the object do not change over time.	The spacecraft operation requires the same attitude with respect to the orbit at any point during the mission (enforced by ADCS). For small debris objects, the dimensions are small and do not differ significantly (Schuhmacher, 2021).
DECSIM-AS-04	Perturbations due to solar radiation and third body gravity are neglected.	Third-body perturbation due to the moon and solar radiation cause accelerations on the order of 10^{-5} m / s and 10^{-6} m / s, respectively. Further, these perturbations largely cancel each other out across one orbit.

3.5.2 Model Description

The model is based on an object, either a spacecraft or a debris object, being represented by a single point in space, which is then propagated using particle dynamics in 3 dimensions.

Inputs and Outputs

Even though the numerical solving of equation (3.4) for $\vec{p}$ requires only the initial position and initial velocity of the spacecraft in Cartesian coordinates, the inputs to the simulation are supplied in form of initial Kepler orbit elements: periapsis and apoapsis altitudes, inclination, the argument of periapsis and the right ascension of the ascending node, as well as the initial mean anomaly. From these parameters, the initial position and the initial velocity are derived. Furthermore, the initial UTC time is specified to enable the lookup of input parameters for the NRL-MSISE-00 model.

In debris mode, the output of the simulation is the Cartesian position $\vec{p}$ as a function of time. From this, the orbital radius r as a function of time is derived. Furthermore, the simulation keeps track and produces a graph of the lowest altitude with respect to the WGS84 reference ellipsoid as a function of time.

When a spacecraft is analysed, the output of the function changes slightly. While the core of the model is identical, the simulation is run only for a specified number of orbits, and a measure of the ΔV necessary to maintain the orbit with one maintenance burn per number of simulated orbits.

Orbit Propagation

The dynamics of the object simulated can be described by the vector Equation (3.4), with its terms being expressed in Equations (3.1) through (3.3).

$$\vec{a}_{\text{Earth}} = -\frac{\mu_E}{r^3}\vec{p} \tag{3.1}$$

$$\vec{a}_{\text{drag}} = -\frac{1}{m}C_d\frac{1}{2}\rho V^2 A\frac{\vec{V}}{V} \tag{3.2}$$

$$\boldsymbol{a}_{J_2} = \begin{bmatrix} -\frac{\mu_E x}{r^3}J_2\frac{3}{2}\left(\frac{R_E}{r}\right)^2\left(5\frac{z^2}{r^2}-1\right) \\ -\frac{\mu_E y}{r^3}J_2\frac{3}{2}\left(\frac{R_E}{r}\right)^2\left(5\frac{z^2}{r^2}-1\right) \\ -\frac{\mu_E z}{r^3}J_2\frac{3}{2}\left(3-\frac{R_E}{r}\right)^2\left(5\frac{z^2}{r^2}\right) \end{bmatrix} \tag{3.3}$$

$$\vec{a}_{Earth} + \vec{a}_{drag} + \vec{a}_{J_2} = \frac{d^2\vec{p}}{dt^2} \tag{3.4}$$

where $\vec{p}$ is the position vector of the spacecraft, and r is the euclidean norm of $\vec{p}$ and orbital radius. The air density is obtained using the NRL-MSISE-00 model via the Matlab function *atmosnrlmsise00*. The magnetic index, the 10.7 cm 81-day average solar flux index, and the 10.7 cm solar flux index are all inputs to the NRL-MSISE-00 atmosphere model from the previous day can be obtained from the National Centers for Environmental Information [2] (NCEI). The code used to retrieve the indices and compute the averages is taken from (Ju, 2017).

[2] URL: https://www.ngdc.noaa.gov/ [accessed 05-06-2022]

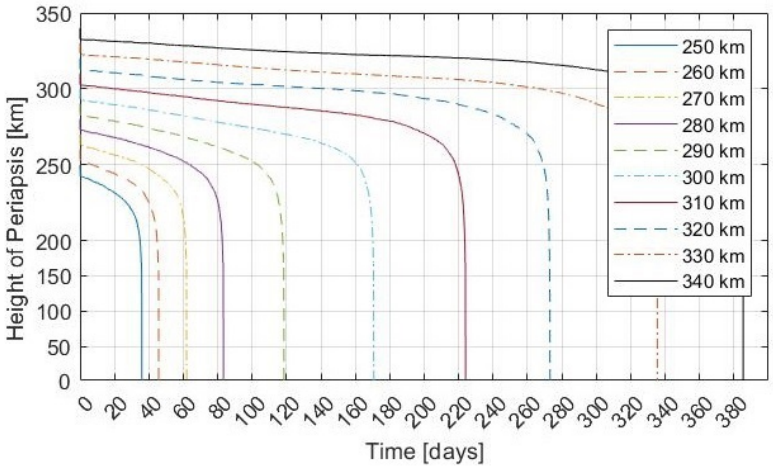

Figure 3.3: Time for atmospheric re-entry of a debris particle for different perigee altitudes.

3.5.3 Results

The simulation was used for two distinct analyses. Firstly, the estimation of the required ΔV for station keeping in a worst-case orbit, and secondly, the determination of debris decay characteristics, including an estimate of the debris periapsis altitude needed for a natural decay within one year.

Spacecraft Orbital Decay

The simulation was used to evaluate the orbital decay due to the two main orbital perturbations experienced by the spacecraft according to (Montenbruck et al., 2000), namely the drag and the J2 effect. The primary purpose is to estimate the ΔV required per orbit to maintain the spacecraft orbit as one of the core inputs to the propulsion system design. The propulsion system must be sized to maintain the orbit even in maximum decay rate scenarios. For this reason, the analysis was performed at the lowest orbit considered (380 km) and during a high sun cycle (initial time set during March 2014). Further, an AMR of 0.022 m^2 / kg was considered. Using these parameters, the simulation estimates a per-orbit maintenance ΔV of 0.0587 m/s if maintenance is performed every orbit. For the entire mission life of 1 year, a ΔV of 117 m/s is required.

Debris Orbital Decay

From the equations, the mission requirements, and the atmospheric model, the worst-case scenario for the longest decay time would be the particle with the lowest mass-to-area ratio, with the apogee of its orbit at 1000 km, and at a point in time with the lowest solar activity (March 2008). These three conditions were used to find the suitable altitude to with the perigee of the particles need to be lowered in order to size the laser.

Since the particles with the lowest area-to-mass ratios (AMRs) predicted by the NASA break-up model are outliers, the system would be greatly over designed if those particles were used to set the requirement. A design decision was made for the requirement, stated as: "At least 95% of the particles de-orbited by the system shall re-enter the atmosphere within a year", finding an AMR of 0.07946 m^2 / kg. The 95% value is acceptable since requirement SS-TL-STK-US-REQ-G-003 can still be fulfilled. In addition, this value is also suitable for the sizing of the ablating laser performed in Chapter 4. The value of one year was deemed appropriate because at those high altitudes the particles would stay in orbit for numerous decades (Wang, 2010), and one year is already a drastic improvement, reducing the probability of collision by more than an order of magnitude (since the probability of collision scales linearly with time in orbit (Klinkrad, 2006)).

It should be noted that most of the particles will re-enter in much less than a year, since the average AMR is much greater than the one used for this simulation. Furthermore, at lower altitudes the perigee will be lowered even farther, since the power of the laser will be the same, and particles will re-enter in much shorter times. Lastly, the atmospheric density has shown to increase by two orders of magnitude during high solar activity with respect to low, meaning that the set requirement is considerably conservative. Figure 3.3 shows the decay time of the considered debris fragment for different perigee altitudes (with the same apogee at 1000 km). It is evident from the figure that at 340 km the particle re-enters in roughly a year, which will then be the target perigee altitude that will be used to size the payload.

3.5.4 Verification and Validation

Verification and validation of the model and implementation was primarily done based on simple test cases for which solutions are known in advance. Different terms of the particle acceleration were tested individually. Firstly, a completely unperturbed orbit was simulated and compared to an analytical Kepler orbit solution. For this, a circular, equatorial orbit of 1000 km altitude was used, with the initial position at [7378137, 0, 0] m and circular velocity. Propagating this orbit for precisely one orbit, the final position is [7378136.99, -0.0023, 0], an absolute error of less than one centimeter in

each axis. To achieve this precision, a high order ODE solver was used, in conjunction with a narrow tolerance band. Furthermore the effect of J_2 perturbations on an equatorial orbit is investigated individually in a similar fashion. The simulated orbit exhibits the oscillations in orbital radius that would be expected from an orbit with non-zero inclination.

3.6 Debris Removal Simulation

One of the key performance indicators of the mission is how quickly a certain percentage of the targeted space debris can be removed. Equivalently, one can investigate how much space debris the system can remove in a certain time frame. To do so, the following debris removal simulation has been developed, which is used throughout the design process to include performance in the decision-making. This simulation also is intended to prove or disprove the feasibility of the mission concept with respect to the mission requirements.

3.6.1 Model Assumptions

Table 3.10: List of assumptions used for debris removal simulation.

Assumption ID	Description	Validity
REMSIM-AS-01	ΔV is only imparted on an object if it meets range, FoV, incidence angle, and visibility time requirements.	Both the laser and lidar systems have restrictions on the field of view, and range. Furthermore, ablation operations require that an object is visible for at least 60 seconds, and the incidence angle is less than 20°.
REMSIM-AS-02	Only disturbances of the so-called J_2 effect are included.	As explained in (Slotten, 2017, p.2), it is the largest perturbation parameter, and it would be acceptable to exclude higher order terms.
REMSIM-AS-03	The system is operational in 5 days.	If this mission is considered as an emergency action, it should be deployable relatively fast.
REMSIM-AS-04	Only objects between 1 cm and 10 cm in diameter, and only objects with elliptical orbits above 340 km are considered.	The user requirements specify that only objects between 1 cm and 10 cm are to be considered for removal. Furthermore, objects that dip below 340 km are of no interest due to natural decay.
REMSIM-AS-05	The altitude at which a debris object is considered removed is set to 340 km.	The results of the debris orbital decay model show that, using a 95% worst-case object, a perigee altitude of 340 km with an apogee altitude of 1000 km is enough for the object to decay within one year during worst-case solar activity.

3.6.2 Model Description

During the time leading up to the Midterm Report (Teixeira et al., 2022b, pp.18-20), a simulation was created to analyse the coverage of the laser system, with the aim to determine whether a single space-based laser system would be able to meet the mission requirements, or multiple spacecraft would be needed. This debris removal simulation is built on top of this, by extending it with additional secondary effects for increased accuracy, migrating it to a compiled programming language (Julia) to accelerate the simulation process, and including the laser-specific required conditions that shall be satisfied for effective debris removal to occur. This simulation also includes the ablation of the debris itself, namely how the (effective) energy is transferred to the debris to slow it down, using the Gaussian perturbation equations (Klinkrad, 2006, p.325).

Inputs and Outputs

Firstly, the simulation requires a data set of the debris population to be removed. This comes as an output of the NASA Breakup model (Schuhmacher, 2021) and provides the Kepler orbit elements, including the initial mean anomaly, as well as the mass, area, and equivalent diameter per object. This dataset is then filtered according to assumption REMSIM-AS-04. Another input is the set of Kepler orbit elements for the initial spacecraft orbit. Furthermore, several performance parameters of the detection and removal payload must be specified, such as the range, detection FoV and scan time, the maximum incidence angle for ablation, as well as the time necessary to impart enough ΔV in a single pass.

Orbit Propagation

The model is based on the propagation using Kepler orbit elements rather than Cartesian positions. Therefore, the Kepler elements must directly be updated directly. The J_2 effect can be taken into account through (Klinkrad, 2006, Eq. A.54 - A.56). After applying perturbations due to J_2, the mean anomaly must be advanced according to Equation (3.5).

$$\frac{dM}{dt} = \sqrt{\frac{a^3}{\mu_e}} \tag{3.5}$$

$$\Delta V = \Phi C_m f \frac{A}{M} \Delta t \tag{3.6}$$

3.6.3 Removal Conditions and Application of Perturbations

To apply ΔV through laser ablation to an object, several conditions must be met:

1. Distance between object and spacecraft must be less than detection/ablation range.
2. Laser angle with respect to the debris velocity vector must be less than the maximum incidence angle.
3. The debris object must be within the detection FoV.
4. The time since the last ablation even must be longer than the cool-down time.
5. The expected time that the object will meet constraints 1 and 2 must be greater than the pulse duration.

Should all conditions be met, the object's orbit will be perturbed by applying a ΔV according to Equation (3.6), in a direction opposite to the object's velocity vector, where Φ is the fluence, C_m is the coupling coefficient, f is the frequency of the laser, and A and M are the area and mass of the individual debris object. The Kepler elements of the debris object are then modified based on (Klinkrad, 2006, Eq. A.33 - A.38) with several integration steps to avoid inaccuracies.

3.6.4 Verification and Validation

Verification of the code was primarily split into two separate parts in terms of functionality, verification of the orbit propagation, and verification of the removal algorithm. Firstly, the orbit propagation functions were verified individually to be correct through comparison with hand calculations. Furthermore, A variety of orbital parameters were tested and their propagation observed. Orbital perturbations based on J2 modify the orbit every time step of the simulation, however, the change in RAAN angle and the argument of periapsis can be compared to existing relations for per-orbit changes in the same parameters. For example, the total change in RAAN angle per orbit (precession of the ascending node over time) can be determined through:

$$\Delta\Omega = -3\pi J_2 \left(\frac{R_E}{a(1-e^2)} \right)^2 \cos(i) \tag{3.7}$$

When applying this to a circular test orbit at 500 km altitude with inclination of 60 °, the expected precession rate of the ascending node is -4.386996·10^{-3} rad/orbit, whereas the same test orbit, the simulation predicts a precession after one orbit of -4.386322·10^{-3}, within 0.015% of the analytical value. Secondly, the algorithms used to model the removal of debris pieces, including the change of orbit, are verified. The method consists of several parts: Checks for several conditions that must be met in order to commit to the use of the ablation laser, as well as the perturbation of the debris object orbit due to the laser. The former can be verified through several test debris orbits with a single debris piece, for which the initial condition it is known that either the FoV, range, or incidence angle condition is met. For instance, the range condition was verified by This way, each condition check are tested accurately and independently from each other. Furthermore, the change in orbital parameters using the Gaussian perturbation equations (Klinkrad, 2006) is verified using hand calculations and checked for consistency in effect of the orbit. For example, should ΔV be applied to a particle in the direction opposite of its movement in a circular orbit, the orbit altitude directly opposite of the point where ΔV is imparted, should decrease and conform to predictions from 2D orbital mechanics equations. Applying a test acceleration of 100 m/s to a circular, equatorial starting orbit at 1000 km altitude (circular velocity 7350.1 m/s), the implementation of the Gaussian perturbation equations produces an elliptical orbit with new periapsis altitude of 611555.8 m, while a hand calculation leads to the same circular orbit, with a periapsis altitude of 611556.53 m, a relative error on the order of 10^{-5}.

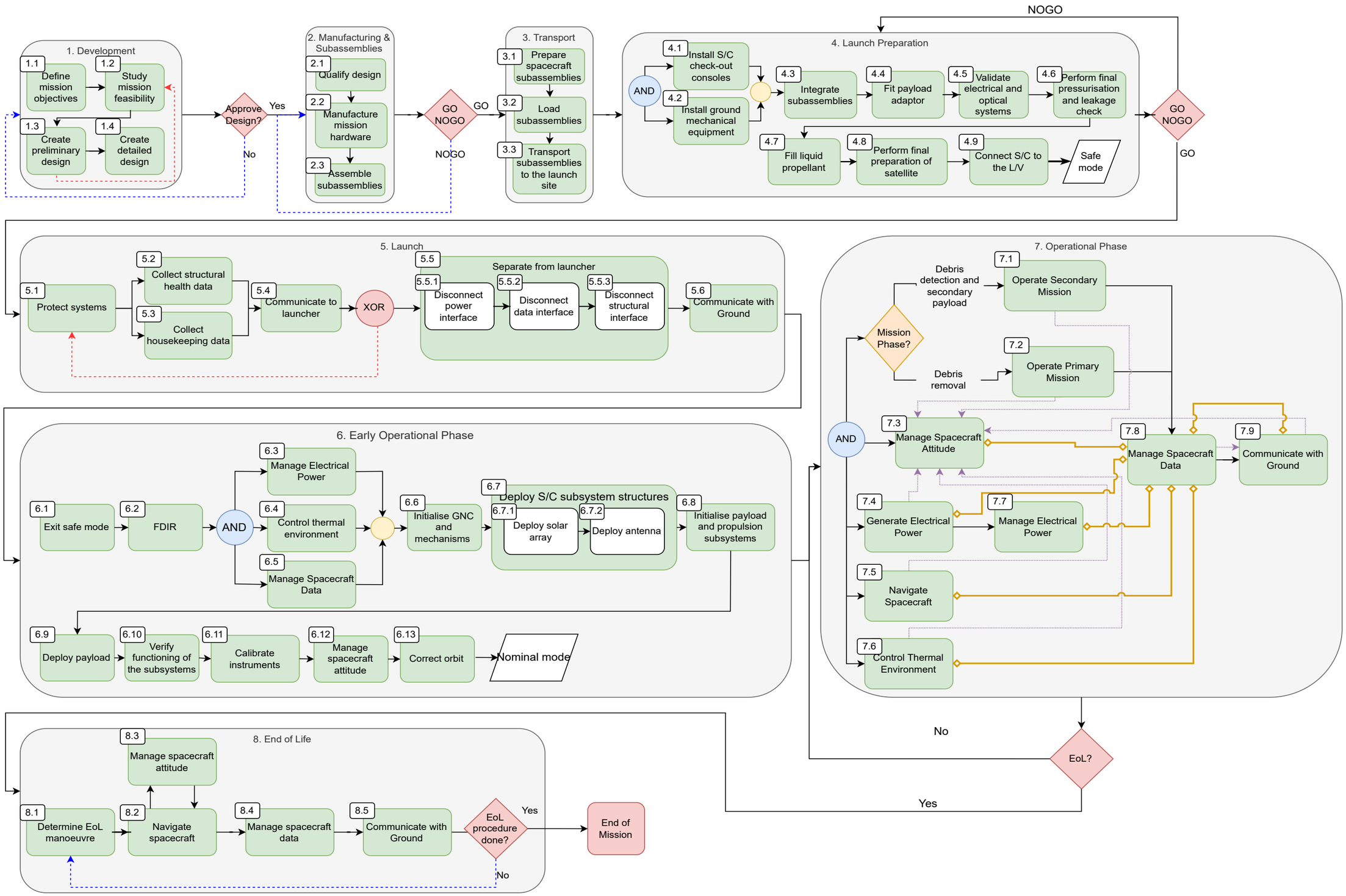

Figure 3.4: Detailed Design FFD.

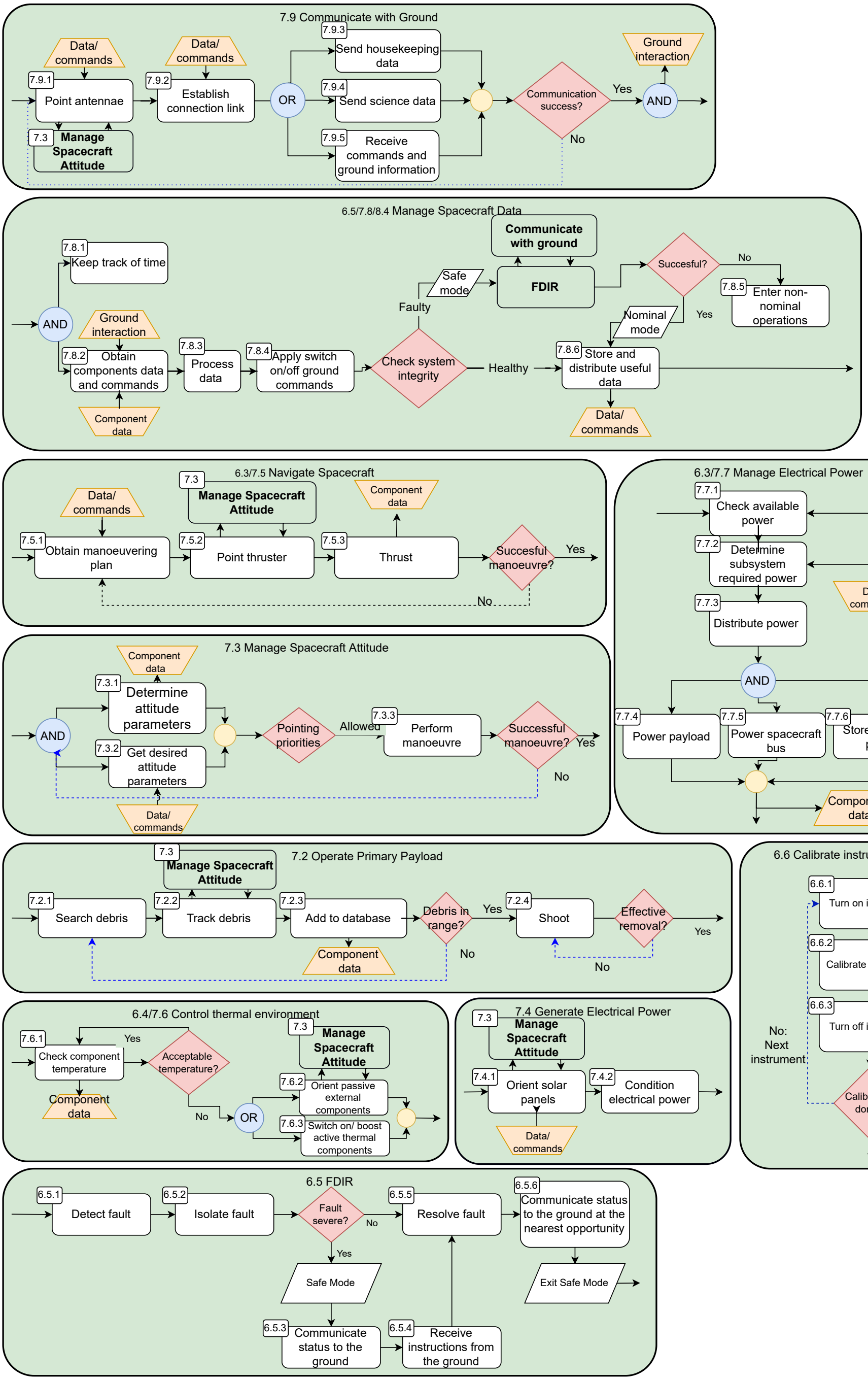

Figure 3.5: Detailed Design FFD.

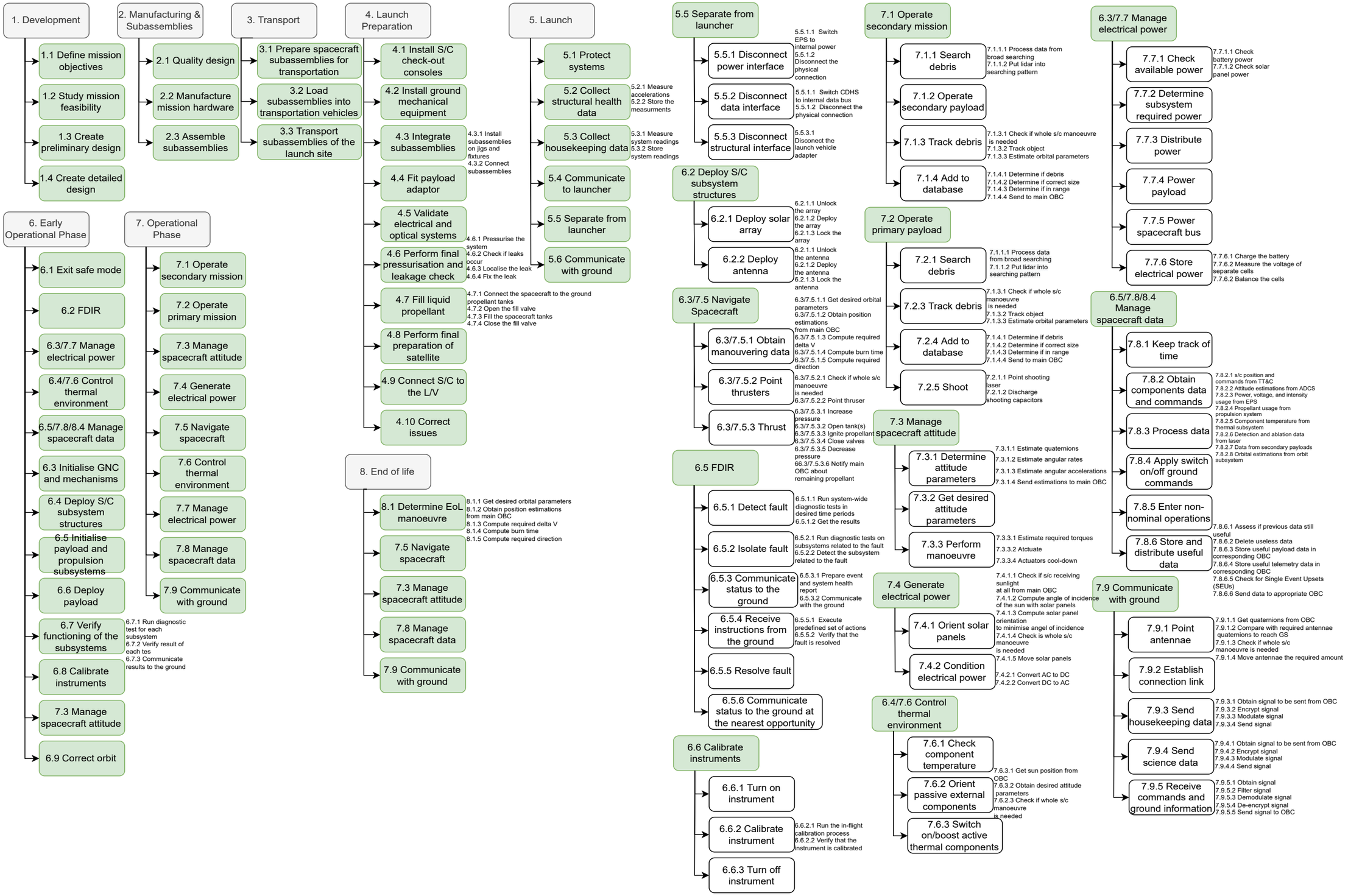

Figure 3.6: Detailed Design FBS.

Payload 4

The payload consists of a system to detect space debris, and a laser to ablate the debris. The payload is the driving factor for spacecraft budget estimations, and accuracy requirements. The following chapter introduces the payload requirements in Section 4.1, followed by an introduction to lasers in Section 4.2. Section 4.3 describes the design of the lidar, while Section 4.4 explains the design of the debris removal payload.

4.1 Subsystem Initial Requirements

The initial subsystem requirements are shown in the table below. The values for the mass and power budget originate from the preliminary budget estimation.

Table 4.1: Payload subsystem requirements.

Requirement ID **Rationale**	**Description**
SS-SYS-PL-REQ-001	The payload shall be able to detect a 1 cm object at a distance of 300 km and a relative velocity of 1.72 km/s.
SS-SYS-PL-REQ-002	The payload detection shall have an angular accuracy of at least 5 mm at a distance of 250 km.
SS-SYS-PL-REQ-003	The payload detection shall have a distance accuracy of at least 1 m.
SS-SYS-PL-REQ-004	The payload shall be able to autonomously track a detected object, during nominal operation.
SS-SYS-PL-REQ-005	The payload shall be able to de-orbit debris of sizes between 1 cm and 10 cm.
SS-SYS-PL-REQ-006	The mass of the payload shall not exceed 1000 kg.
SS-SYS-PL-REQ-007	The power used by the payload shall not exceed 5900 W.

4.2 Laser Theory

The following section gives an introduction to the concepts behind lasers, specifically when applied to provide propulsive effects on a target object. Firstly, the main theory behind ablative propulsion is presented in Subsection 4.2.1, after which the effects of wavelengths on ablation rate are discussed in Subsection 4.2.2. Thirdly, the laser fluence and coupling coefficient are explained, and the required formulae shown, in Subsection 4.2.3. Subsection 4.2.5 introduces the reader to the pulse geometry, which is influenced by various parameters, including the aforementioned fluences, coupling coefficient, and wavelengths.

4.2.1 Ablative Propulsion

The concept of ablation considers using energy to remove material from an object, which will be ejected from the material. In the case of using a laser, this is called "laser ablation propulsion" (LAP), in which "an intense laser beam [pulsed or continuous wave (CW)] strikes a condensed- matter surface (solid or liquid) and produces a jet of vapour or plasma." (Phipps, Birkan, et al., 2010, p.611). This ejected vapour or plasma is always formed "perpendicular to each element, independent of the angle at which the laser strikes the target" (C.Phipps et al., 2012, p.1286). In other words, regardless of the angle of incidence on the object, the debris is always ejected away normal to whichever surface the laser hits. This leads into the assumption that the debris target is always oriented such that the surface that is hit by the beam is perpendicular to the velocity vector of the debris. Hence, the vapour or plasma ejected will, by extension, always be parallel to the velocity vector. In the case that a head-on interaction occurs between the laser and the incoming debris, this means that the ejected mass would always fully contribute to decelerating the debris.

It is important to realise that, although ablation takes place, the entire debris piece is not vaporised. Instead, only material from the surface is removed to apply a thrust force, effectively de-orbiting the debris piece, and, eventually, the re-entering and consequently burning up of the debris piece in Earth's atmosphere.

Table 4.2: Efficiency breakdown of second harmonic pulse laser[1].

Efficiency parameter	**Efficiency [%]**
Electric-to-electric efficiency of power conditioning	95
Electric-to-electric efficiency of pump diodes	65
Optical-to-optical efficiency of Yb fiber lasers	65
Combining efficiency	90
Frequency doubling efficiency	70
Total electric-to-optic efficiency	25.2

The relationship between the so-called "coupling coefficient" C_m, and the energy E that is imparted on an object is related to its momentum by:

$$m\Delta v = C_m E \tag{4.1}$$

where m and ΔV are the mass and velocity change of the debris object respectively. The coupling coefficient can thus be observed to be a parameter that essentially describes with what "efficiency" the total energy given to the debris is transferred into changing the momentum of the debris.

4.2.2 Laser wavelengths

A laser has a fundamental harmonic, which has a characteristic wavelength (and thus frequency) based on the element used in the laser crystal. This primary harmonic may be altered using frequency doubling, tripling, etc., which in turn changes the wavelength and frequency output to create so-called harmonics. As an example, (Hodgson et al., 2019) shows that for an original wavelength of 1035 nm, the second and third harmonic exist with wavelength of 517 nm and 345 nm respectively.

The existence of these harmonics may be utilised for laser ablation, as experimental research performed by (Hodgson et al., 2019) shows that the second harmonic generally provides the highest ablation rate (defined as mm^3/W min). This is, of course, fully dependent on the material that is being ablated, specifically whether it absorbs or reflects the wavelength that is fired at it. Experimental data shows that for steel, a wavelength of 345 nm and repetition time 400 fs achieves a maximum ablation rate of 0.2 mm^3/W min, compared to 0.32 mm^3/W min for a wavelength of 517 nm and repetition time 500 fs (Hodgson et al., 2019, p.7). Furthermore, the higher effectiveness of the second harmonic is not only limited to steel, as more materials, like Molybdenum, BK7 and Silicon also display the same behaviour. Most importantly, between the fundamental (first) harmonic, second, and third harmonic, the rate of ablation of aluminium was highest for the second harmonic. The corresponding values are ablation rate maxima of 0.3 mm^3/W min for the first harmonic, 0.5 mm^3/W min for the second harmonic, and around 0.45 mm^3/W min for the third harmonic (Hodgson et al., 2019, p.7). However, the pulse duration was increased from 0.4 ps to 0.5 ps for the final, third harmonic.

Phipps suggests that using a third harmonic pulsed laser is optimal for the application in question, proposing a 355 nm UV laser for ablation of debris (Phipps, 2014). The process of converting lasers from the fundamental harmonic to higher harmonics leads to significant energy losses. The efficiency (loss) breakdown for a diode-pumped Yb laser with a fundamental wavelength of 1020-1080 mm is provided in Table 4.2. It is assumed that such a laser payload, with a 532 mm wavelength in the second harmonic, is to be adopted for this application.

4.2.3 Optimising Fluence and Coupling Coefficient

Given a cross-section of the laser beam at a range L, the energy that is imparted on debris is clearly dependent on the energy density - also known as fluence. This fluence can be formulated as shown in the left equation below

$$\phi = \frac{4E_p D_{eff}^2 T_{eff}}{\pi (M^2)^2 a_l^2 \lambda^2 L^2} \tag{4.2}$$

$$\Phi_{opt} \approx B\sqrt{\tau} = 8500 \text{J/m}^2 \tag{4.3}$$

where E_p is the pulse energy of the laser (energy delivered per pulse), D_{eff} is the effective diameter of the mirror (and thus aperture) on the spacecraft, T_{eff} "is the product of all system losses, including anodisation, obscuration and atmospheric transmission" (Phipps, 2014, p.251), M^2 is the beam quality factor, a_l is a constant influenced by diffraction, λ is the wavelength and L indicates the range at which this fluence is achieved.

There exists, for each material, an optimum fluence at which the highest coupling coefficient exists, and thus the lowest energy required to de-orbit a debris object. This behaviour can be observed in Figure 4.1. Whereas (Pieters, 2020, p. 38) proposes that the optimal fluence is a threshold fluence, above which the rate of ablation would increase further, increasing the fluence actually decreases the rate of ablation [2]. Significantly above this threshold fluence, the plasma generated absorbs the laser energy, effectively shielding the debris surface. Thus, another challenge of the laser system is to maintain the optimal fluence at the target object throughout the shooting duration. The optimum fluence is most reliable and accurate when determined experimentally, though Phipps proposes the following model (Phipps, 2014, p.250), shown

[1] Personal communication Fabio Di Teodoro (senior engineer, Raytheon), email dd. 08-06-2022.

[2] Personal communication Fabio Di Teodoro (senior engineer, Raytheon), email dd. 03-06-2022

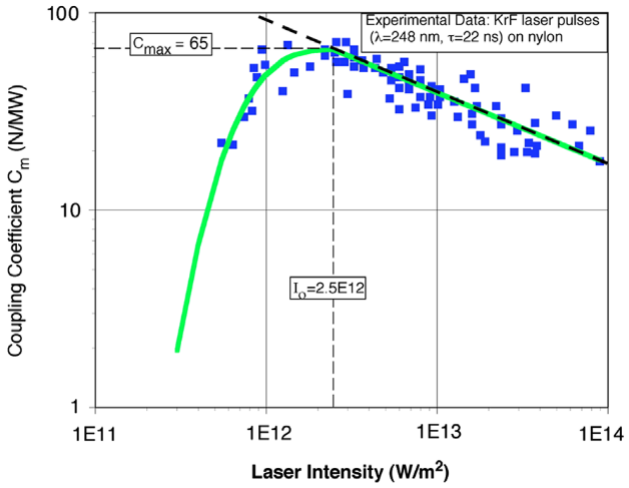

Figure 4.1: Figure showing the relationship between fluence and coupling coefficient.

in Equation (4.3). Where B = 8.5E8 W/m^{2}s$^{1/2}$ "for robust coupling across all materials" (Phipps, 2014, p.250), and τ represents the pulse duration of the laser. Using this optimum fluence, a coupling coefficient can be found by substituting $\Phi_{opt}\sqrt{\tau}$ into (Phipps, 2014, p.249):

$$C_m = \frac{C_{m0}}{(I\lambda\sqrt{\tau})^{\frac{1}{4}}} \tag{4.4}$$

$$C_m = \frac{C_{m0}}{(B\lambda)^{\frac{1}{4}}} \tag{4.5}$$

with a C_{m0} = 420 N/MW. As Equation (4.5) shows, the coupling coefficient can thus be treated as scaling with wavelength for a constant B. However, it can also be seen that this coupling equation implies that the lower the wavelength, the higher the coupling coefficient is, seemingly contradicting the statement that the second harmonic is more efficient at ablation. This effect is negated due to the conversion efficiency to go from the fundamental harmonic to the second or third, where the increased losses in power for the third harmonic result in a worse performing laser - despite the increase in C_m, as discussed in Subsection 4.2.2

4.2.4 Mirror Sizing

Given the laser wavelength, the optimum fluence for ablation, and coupling coefficient are already defined, there are still many ways to constrain the design to move forward. The spot size of the laser is defined as the diameter of the laser beam at the target debris. Spot size has a significant impact on the power requirement of the ablative laser, where a smaller spot size imparts a given energy on the debris for a lower output power. The spot size, d_s is given by the equations below.

$$d_s = \frac{a_l M^2 \lambda L}{D_{eff}} \tag{4.6}$$

$$d_s = d_d + \cdot 2L \arctan\theta_{pa} \tag{4.7}$$

Considering the mission targets small-sized debris, in the range of 1 to 10 cm, the spot size is constrained to be larger than the debris object. This is considered as smaller spot sizes are infeasible at long ranges, and considering all the debris objects can be covered entirely by the beam simplifies de-orbiting simulations. The pointing accuracy, θ_{pa}, determined by the pointing accuracy of the laser gimbal and the accuracy of the LiDAR detection system, determines the potential divergence of the beam from the target at a given range. Thus, to cover a debris object for the duration of a shot, the necessary spot size is calculated using Equation (4.7), where d_d is the debris diameter, for which the worst-case value of 10 cm is used. For clarity, δ is multiplied by 2 considering the laser can diverge in either direction in any arbitrary axis. It is useful to use this minimum spot size as this reduces the required pulse energy, and thus power output of the laser, which reduces the laser mass as well as associated EPS mass. The disadvantage of using a smaller spot size is the mirror diameter, and thus mirror mass, necessary to focus the laser on a smaller area is increased.

By specifying this d_s, the necessary mirror diameter D_{eff} can be calculated simply from equation (4.6). A challenge presented earlier is that the fluence of the beam at the target object must be kept relatively constant at the optimal fluence. From (4.2), it is shown that fluence varies with range and effective mirror diameter, as these parameters influence spot size. Thus, to maintain a small spot size as the range of the target decreases, the effective diameter of the mirror must also continuously decrease to keep a constant ratio between the two. This could be done by morphing the secondary mirror to disperse the beam on an incrementally smaller fraction of the primary mirror throughout the shot based on the changing range of the detected debris fragment.

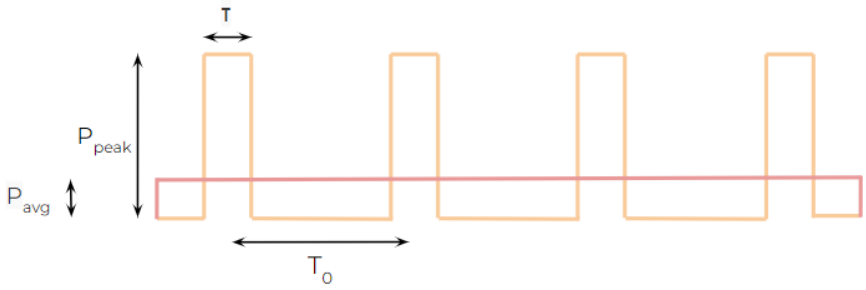

Figure 4.2: Labelled diagram of pulse parameters.

4.2.5 Pulse Geometry

Optimising the laser characteristics beyond this point is a difficult process, given the plethora of variables to be taken into account. For a given input laser power, other laser pulse parameters may still be fine-tuned for optimal performance. The pulse duration, τ, pulse energy, E_p, defined as the product of τ and the pulse power, P_{peak}, as well as the frequency, f, equal to the reciprocal of the repetition rate, T_0, can all be adjusted. The detailed parameters are labelled in Figure 4.2 for clarity.

The first parameter to be determined is the pulse duration. A shorter duration is more efficient in ablating debris, as this minimises thermal effects both in the laser instrument and the targeted debris, [3,4]. As long as the optimal fluence, determined from the pulse duration, is achieved, a shorter pulse duration leaves a longer window between pulses to dissipate generated heat. There is a limit to shortening pulse duration, as the achievable peak power of the laser pulses is constrained. From Phipps (2014, p. 250), data shows that while a shorter pulse duration is desirable, there is no benefit in using $\tau < 100$ ps.

Using Equation (4.2), the pulse energy, E_p, of the laser needed to provide the necessary fluence is derived. Considering $P = E_p f$, either the power P or frequency f must first be found. The pulse frequency is to be derived based on the acceleration imparted on the debris by one pulse with the given E_p and the total time in which a debris fragment is to be ablated. These parameters will be discussed further in Section 4.4.

4.2.6 Debris Material

The laser can only be "optimised" for one type of material, if it is not designed to be configurable remotely. This latter quality of a system is not recommended, given that making a laser perform multiple tasks will degrade the quality of the laser at performing any of those tasks. Previously it was seen that the material C_{m0} considered was taken to be 420 N/MW, which is specific to aluminium. The reason aluminium was chosen is twofold:

- Firstly, it was taken because the relevant literature (which is very difficult to obtain, and generally speaking, experiments are always required to obtain trustworthy values) used (Phipps, 2014) gave the C_{m0} for aluminium when it is singly ionised for a given atomic mass. Both the ionisation state and atomic mass of the material, when subject to the laser, are parameters that influence C_{m0}; thus, between different materials, the C_m and the associated ablation rate will vary. This said, the laser will still perform for materials that have a higher threshold fluence, but not at that material's optimum rate. For example, (Hodgson et al., 2019) shows that using steel's optimum fluence level on BK7 still achieves a comparable ablation rate, but this is not equal to BK7's maximum ablation rate (which is at a higher fluence).
- Secondly, focusing on the removal of aluminium debris is representative of the challenge in space. SS-TL-STK-US-REQ-G-005 shows that the STS (space shuttle) missions determined aluminium to make up the largest proportion of space debris, while Satellite Orbital Debris Characterisation Impact Test (SOCIT) showed that, actually, plastic makes up the largest proportion of space debris. This could be due to limited detection techniques when STS missions were still flown. In either case, plastics are part of the "low density" materials, while aluminium is part of the "medium density" materials. For debris of a given size, a higher density results in a higher mass, and a higher kinetic energy. Thus, aluminium debris can be considered more critical to remove, as it can do more damage to a spacecraft. However, eventually the mission should be able to remove all types of debris (because even the low density plastic debris has a high kinetic energy), and for this the C_{m0} of plastics used on spacecraft must be known. If this is known, the laser can be designed optimally to perform well against both aluminium, and plastic debris (which make up about 80% of space debris (Opiela, 2009)). Chapter 14 explains how research on debris materials will take place.

4.2.7 Incident Angle, Shape- and Spin-Effects

The discussion of the laser thus far has assumed a head-on interaction with the target debris fragments. However, the incident angle with which the laser hits the debris with respect to the debris velocity vector varies substantially per

[3]Personal communication Fabio Di Teodoro (senior engineer, raytheon), email dd. 02-06-2022
[4]Personal communication Laurens Siebeles (management assistant, TU Delft), meeting dd. 31-05-2022, 16:30-17:30

interaction. From literature, it is determined theoretically that "the mass ablation rate scales with the 4/3 power of the cosine of the laser ray incidence angle relative to the target normal".

It was decided that a limit of 20° would be used as a targeting range for further simulations. To reduce processing time, an efficiency of $\cos(20°)^{4/3} = 92\%$ was applied to the laser as a conservative estimate for its performance. At this small angle, the laser pulses only contact the Earth at operational altitudes below 450 km, for which the 20° limit can be reduced due to the substantially lower power requirements at lower altitudes. However, it is nonsensical to apply a lower filter for the worst-case-scenario of 100 0km operational altitude.

Furthermore, the shape of the target debris fragment is expected to have a considerable impact on the transverse momentum induced through ablation. However, the exact impact is highly dependent on the exact shape in orientation of the object, and experimental data on the subject is sparse (Liedahl et al., 2013, p.896). A similar conclusion can be drawn for the effect of spin on laser ablation. While Mason et al. (2011) suggests "target spin will tend to average the specular reflection component to zero, and do not treat off-beam momentum transfer" (Liedahl et al., 2013, p.896), Phipps shows that in the case of ablation, as opposed to reflective photonic momentum transfer, a component of the transverse transmitted momentum is retained. Again, experimental data in this field of research is limited. In Phipps' later published paper (Phipps, 2014), the effects of spin are seemingly neglected and a head on interaction is assumed with targeted debris objects, assuming a flat surface orthogonal to its respective motion. While the angle of incidence of the beam is treated in further calculations, the effects of spin and shape of debris objects considered is not. The assumption that the laser beam envelops the entire targetted debris object, as explained in Subsection 4.2.4, is expected to justify this neglection. However, these aspects are important to establish before detailed payload development can commence, and are to be researched in a dedicated research phase, which will be detailed in Chapter 14.

4.3 Debris Detection Payload

An active detection device is required, due to the dependency of passive devices on lighting conditions, and their poor performance in long-distance situations. In this section, a method to calculate the required power for active detection methods is shown. The results from this method are then used to size the active detection system, and to estimate its performance.

4.3.1 Detection Method

A lidar is the only method, as compared to radar and passive optical methods, that can provide the necessary performance for the Space Sweeper mission. Firstly, passive optical methods are not suitable for the mission, as they cannot be used during eclipse, drastically decreasing the available time for debris removal. Secondly, an accurate detection is required to detect the debris during or right before the ablation mode, which cannot be done with a radar, due to its long wavelength. Lidars use smaller wavelengths, so are better suited for this. In an atmosphere, a small wavelength propagates less far than a large wavelength, but in space (vacuum), this is not the case. In other words, using a lidar is possible and necessary. It is thus more efficient to use this same lidar also for broad detection, instead of having to add a radar as well. Furthermore, an ablation laser is already on board of the spacecraft, so it was initially thought that the same laser could also be used for detection. However, it is uncommon and inefficient to do this[5], so the lidar is designed separately from the ablation laser.

For wide FoV searching, there are two lidar technologies to be considered: narrow beam scanning lidar, and flash lidar (Christian et al., 2013, pp.2-4) (Dissly et al., 2012, p.1). The former consists of a collimated beam, and a single-pixel sensor. After the beam is swept along a certain pattern, the data is combined to form a single image. The latter makes use of optics to give the laser beam a nonzero Field of View (FoV), and uses a multi-pixel sensor array to immediately form the image. Flash lidars are therefore better suited for large FoV searching, and for the tracking of moving debris[5].

A suitable wavelength for the lidar should first be determined, as this value is needed for the background noise calculation in the next section. Several lidar systems, specifically designed for space debris detection, employ 532 nm (green light) Nd:YAG (Neodymium-doped Yttrium Aluminum Garnet) lasers by means of frequency doubling (Zhang et al., 2019, p.691) (Steindorfer et al., 2020, p.5) (Kirchner et al., 2013, p.21). The ICESat-2 mission[6], and CALIPSO mission (Winker et al., 2004, p.4), also use this wavelength. This wavelength also reflects well off aluminium (Shanks et al., 2016, p.400, fig.6).

4.3.2 Extragalactic Background Noise

The 'empty' sky is chosen as the background radiation, as this is the minimum threshold that should be surpassed. Brighter factors such as the Sun and Earth albedo can be avoided by not pointing directly at them, and stars can be recognised by using an on-board catalogue, similar to the functioning of star trackers[7]. The intensity of the extragalactic background is dependent on wavelength, and is shown in Figure 4.3 (Cooray, 2016, p.3). The y-axis is λI_λ: the wavelength multiplied with the intensity. The lidar transmitter wavelength is 532 nm, where the value of the y-axis is approximately 10 $\text{nWm}^{-2}\text{sr}^{-1}$. Dividing this by the wavelength, yields $I_{532nm} = (10 \cdot 10^{-9})/(532 \cdot 10^{-9}) = 0.0188\ \text{Wm}^{-3}\text{sr}^{-1}$. Assuming that this value is constant for wavelengths near 532 nm, integration can be done by multiplying it with the receiver bandwidth, to get the total intensity per solid angle. Finally, this value is to be multiplied by the solid angle of the

[5]Personal communication Fabio Di Teodoro, meeting dd. 24-05-2022, 17:00-18:30

[6]URL: https://icesat-2.gsfc.nasa.gov/sites/default/files/page_files/ICESat2missionBrochureFINAL1.pdf [Accessed 04/06/2022]

[7]URL: https://www.esa.int/Applications/Telecommunications_Integrated_Applications/Alphasat/Advanced_Star_Tracker [Accessed 04/06/2022]

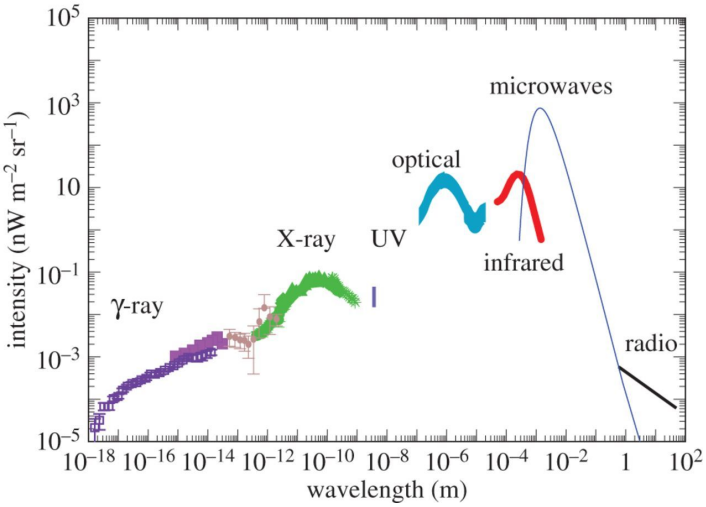

Figure 4.3: Extragalactic background irradiance per wavelength (Cooray, 2016, p.3). The y-axis is λI_λ: the wavelength multiplied with the intensity.

detection system, in steradians. The solid angle relates to the FoV[8] as shown in Equation 4.8, where A_{cone} is the surface area projected onto the sphere, for which the expression is found with a triple integral[9], resulting in Equation 4.9.

$$\Omega = \frac{A_{cone}}{R^2} = 2\pi \left[1 - \cos\left(\frac{FoV}{2}\right)\right] \tag{4.8}$$

$$A_{cone} = 2\pi R^2 \left[1 - \cos\left(\frac{FoV}{2}\right)\right] \tag{4.9}$$

Multiplying the background intensity by the solid angle, yields the final value of the extragalactic background irradiance where B_{sensor} is the bandwidth detected by the receiver:

$$I_{back} = 0.0188 B_{sensor} \Omega = 0.0188 B_{sensor} \cdot 2\pi \left[1 - \cos\left(\frac{FoV}{2}\right)\right] \tag{4.10}$$

4.3.3 Distance and Field-of-View Performance

Given a certain background noise, a desired Signal-to-Noise Ratio (SNR), debris distance, and transmitter FoV, the required transmitter power can be calculated. An active detection system is assumed to work as follows, and this sequence is also shown in Figure 4.4. The transmitter antenna sends an electromagnetic (EM) wave with a certain FoV to the distance at which the debris is. The total power of the transmitter is thus spread out over a larger area as it propagates in space. Part of this power is received by the debris, and assumed to reflect in a Lambertian manner, with a certain reflection coefficient, resulting in a hemispherical power propagation. Part of this power reaches the receiver antenna. Only if this received power flux has a high enough SNR with respect to the background radiation, it can be detected.

The following calculation is done 'backwards' with respect to the aforementioned sequence, to find the required transmitter power, based on the desired end result. First, the area of the hemisphere that is reflected by the debris to the spacecraft, is calculated in equation (4.11) where R is the distance between the spacecraft and the debris. Next, the total power, that should be present over this hemispherical area, is calculated. Equation (4.12) represents the total power to be reflected by the debris.

$$A_{hemi} = 2\pi R^2 \tag{4.11}$$

$$P_{debris} = \frac{SNR \cdot I_{back} A_{hemi}}{\eta_r \eta_q} \tag{4.12}$$

where I_{back} the power flux of the background noise, η_r the efficiency of the receiver optics, and η_q the quantum efficiency of the detection sensor. Then, the power flux to be received at the debris is:

$$I_{debris} = \frac{P_{debris}}{A_{debris}\rho} = \frac{P_{debris}}{\pi\left(\frac{D_{debris}}{2}\right)^2 \rho} \tag{4.13}$$

where A_{debris} is the frontal area of the debris, ρ the fraction of the received light that is reflected by the debris in a Lambertian manner, and D_{debris} the debris diameter. Specular reflection cannot be relied upon for detection, as this is fully dependent on the debris shape and orientation. It is assumed that the debris has a circular frontal area. Next, the area of the spherical cone of EM waves emitted by the spacecraft is calculated with equation (4.9). Finally, the required power by the transmitter can be found:

[8]URL: https://spie.org/publications/fg11_p02_solid_angle [Accessed 02/06/2022]
[9]URL https://mathworld.wolfram.com/Sphere.html [Accessed 01/06/2022]

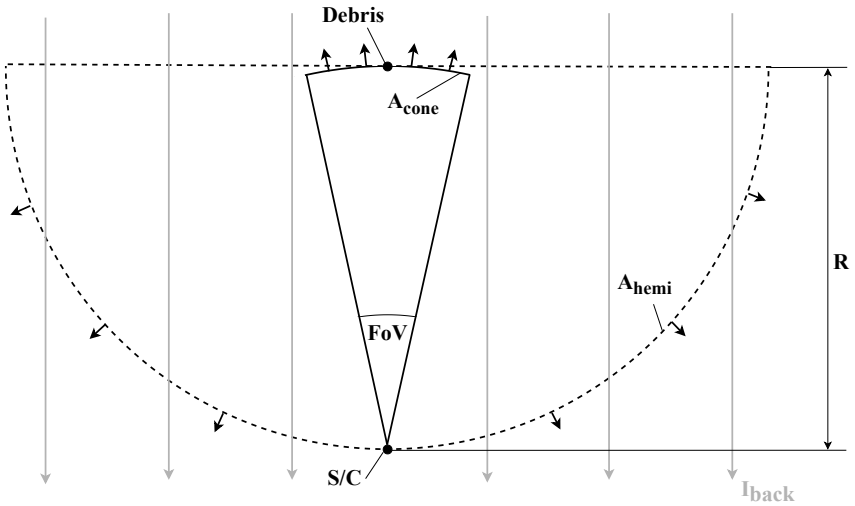

Figure 4.4: Sequence of events for active debris detection. The spacecraft sends out a signal in a FoV over a distance R, after which the debris reflects part of this power in a hemispherical direction. A constant background noise with power flux I_{back} is present.

$$P_{pulse} = \frac{I_{debris} A_{cone}}{\eta_t} \tag{4.14}$$

where η_t is the efficiency of the transmitter optics. The complete aforementioned calculation results in Figure 4.5a, where the parameters from Table 4.3 were used. A detailed explanation on how these specifications were determined, is discussed in Subsection 4.3.4. Next, instead of calculating the required power for a given distance and FoV, the pulse power can be set constant at 10 MW. Based on this power, all possible combinations of FoV and distance can be calculated. An explicit expression for the distance R can be found by combining equations (4.9)-(4.14):

$$R = \sqrt[4]{\frac{P_{pulse} A_{debris} \rho \eta_t \eta_r \eta_q}{4\pi^2 SNR \cdot I_{back} \left[1 - \cos\left(\frac{FoV}{2}\right)\right]}} \tag{4.15}$$

of which the result is the blue, dotted line in Figure 4.5b, using the parameters from Table 4.3.

Since the FoV for broad searching is too low for long distances, the effective FoV should be increased by incorporating a scanning pattern. This entails steering the lidar such that a larger area can be scanned. The scanning can be done by moving mirrors or prisms (Li et al., 2021)(Lu et al., 2014). The scanning pattern is assumed to have 30% overlap between each image, since 'perfect' scanning, with no overlap, is impossible when the projected area is a circle. The maximum area drawn by the searching pattern now increases to:

$$A_{pattern} = t_{pattern} f_{rep} A_{cone} \left(1 - overlap\right) \tag{4.16}$$

where $t_{pattern}$ is the time to perform the scanning pattern once, and f_{rep} is the pulse repetition rate. The overlap between images is estimated at 30%. The corresponding total scanning FoV is then calculated with an alternative form of equation (4.9):

$$FoV = 2 \arccos\left(1 - \frac{A_{pattern}}{2\pi R^2}\right) \tag{4.17}$$

The result of this additional calculation is shown in Figure 4.5b. Again, the blue, dotted line indicates no scanning pattern, and the other lines show the drastic improvement by implementing a scanning pattern. The point where the lines stop at 360 degrees FoV, indicates that the entire spherical area can be scanned within the given scanning time. These results are used as an input for the mission simulation, to find the optimal combination of distance, FoV, and scanning time, for which the debris removal speed is maximum. The scanning time is subtracted from the available ablation time of the debris, as a long searching pattern may result in taking longer to detect the debris once it enters the total FoV, as compared to a stationary wide FoV.

4.3.4 Lidar Specifications

As an iterative procedure, making use of the previously outlined calculation schemes, the lidar is designed in more detail. This sections discusses the most relevant characteristics of the lidar system.

First, the pulse repetition rate is determined. The detection distance should be maximally 300 km, since the ablation distance is 250 km. This 50 km of play in distance allows for pointing of the ablation laser before starting the ablation.

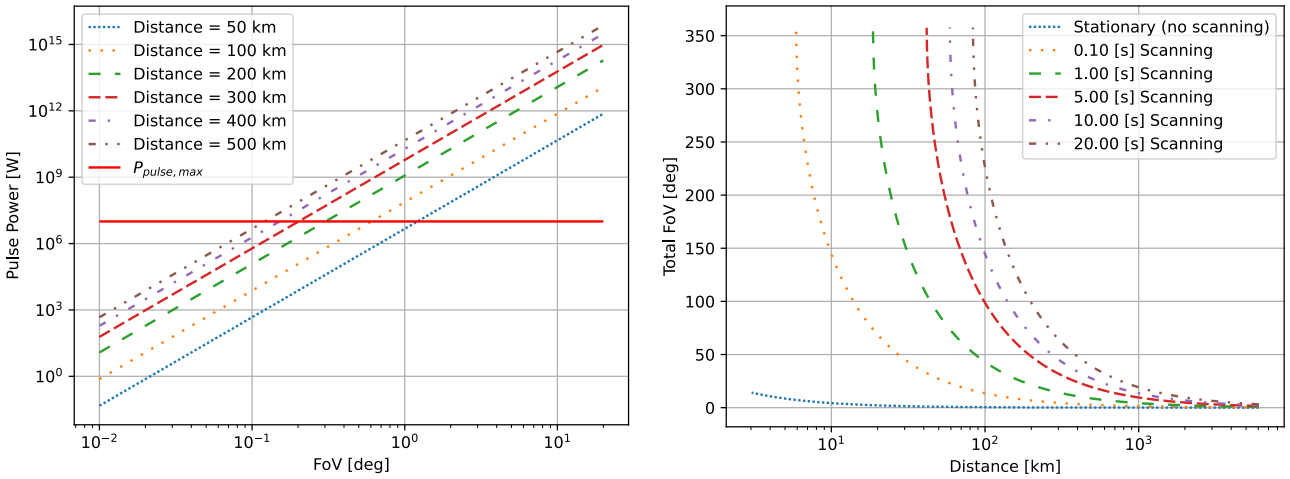

(a) Required power for a FoV and debris distance. The red line is the laser pulse power, so the required power cannot exceed this.

(b) Given the maximum pulse power of 10 MW, the compatible distances and FoVs, including different scanning times.

Figure 4.5: Performance for SNR 2 against an extragalactic radiation background, a debris diameter of 1 cm, with a maximum pulse power of 10 MW. The values from Table 4.3 are used.

For a debris distance of 300 km, an EM wave takes $2 \cdot 300,000/c = 600,000/(2.99792458 \cdot 10^8) = 2.00$ ms to travel from the transmitter back to the receiver. The maximum repetition rate of the lidar would be $1/(2.00 \cdot 10^{-3}) = 499.7$ Hz, which turns out to be too low to achieve a large FoV based on scanning patterns. The scanning is explained later in this section. To allow for higher repetition rates, the transmitter shall dynamically vary the characteristics of each pulse, such that different pulses can be distinguished from each other. This could entail varying the pulse duration, pulse shape, pulse phase, or pulse-to-pulse interval[10]. A repetition rate of 10 kHz is chosen, since it allows for fast sampling and thus fast searching patterns, and since this value is proven feasible by the ICESat-2 mission[5].

Next, the pulse duration and pulse energy are determined. The pulse duration for lidars is usually in the order of nanoseconds[10] (Kirchner et al., 2013)(Steindorfer et al., 2020), so one nanosecond is chosen. The pulse energy should not be too large, since the debris should not be ablated by the lidar. A pulse energy of 10 mJ is chosen, since it is in the same order of magnitude as other lidars (Kirchner et al., 2013)(Steindorfer et al., 2020), and since it results in sufficient pulse power during the nanosecond pulse duration. Combining the pulse energy and duration, the peak pulse power is $(10 \cdot 10^{-3})/(1 \cdot 10^{-9}) = 10$ MW. Combining the pulse energy and repetition rate, the average operating power of the lidar is $(10 \cdot 10^{-3}) \cdot 10,000 = 100$ W.

The received bandwidth by the antenna can be controlled by adding a band-pass filter in front of the sensor[10]. A bandwidth of 0.17 nm can be achieved with a filter from AHF analysentechnik AG[11].

The accuracy with which the receiver can detect the time-of-flight of the laser pulses is assumed to be 800 picoseconds ([6]). This corresponds to a distance resolution of $(2.99792458 \cdot 10^8) \cdot (800 \cdot 10^{-12})/2 = 12$ cm. The division by two comes from the fact that the laser travels both to the debris and back to the receiver. The angular detection resolution depends on the FoV, and should be designed for the situation right before/during ablation. It is not commonly done to change the lidar FoV in-flight, but it is possible by using moving optics[12]. However, this technology has not yet been applied in combination with a scanning beam. To allow for both a variable FoV, and a scanning FoV, a new mirror architecture should be developed. The details of this are explained in Chapter 14. The angular resolution is therefore variable, and can be increased by narrowing the FoV, if needed. Based on the orbital simulation of the Iridium-Cosmos collision, the maximum velocity of the debris with respect to the spacecraft is 1.72 km/s. In a single pulse of $1/f_{rep} = 1 \cdot 10^{-4}$ s, the debris travels 17.2 cm. The stationary FoV should thus be larger than this, so about 1 m diameter at the debris, such that the debris does not leave the FoV within the time of a single pulse. To have a resolution of 5 mm, which should be sufficient for the ablation laser, the resolution of the sensor should be 200x200 pixels.

To estimate the total power, mass, and volume of the lidar system, data from the CALIOP lidar system on-board the CALIPSO spacecraft is used, as it shows the relation between the laser transmitter size, and entire lidar system size (Winker et al., 2004, p.4). The CALIOP laser itself uses 99 W of power, almost identical to the proposed lidar for Space Sweeper. The entire CALIOP lidar system has the following properties (Winker et al., 2004, p.4): a total power of 241 W, a mass of 283 kg, and a volume of 3.59 m^2 (Winker et al., 2004, p.4). Scaling these to 100 W of laser power, yields a total power of 243 W, a mass of 286 kg, and a volume of 3.63 m^2. One difference between the two lidar systems is that CALIOP has many additional instruments attached to it, such as infrared cameras, star trackers, and an additional

[10]Personal communication Fabio Di Teodoro (senior engineer, Raytheon, email dd. 03-06-2022, 18:06

[11]URL:https://www.ahf.de/en/products/spectral-analysis-photonic/optical-filters/individual-filters/ultra-narrow-bandpass-filters/sub-nanometer-bandpass-filters/3356/sub-nanometer-bandpass-filter-532-079/0-17?c=558 [accessed 04-06-2022]

[12]URL https://www.edmundoptics.com/knowledge-center/application-notes/imaging/understanding-focal-length-and-field-of-view/ [accessed 02-06-2022]

Table 4.3: Specifications of the lidar detection system.

Symbol	Property	Value
-	Material	Nd:YAG
λ_{lidar}	Wavelength [nm]	532
τ_{lidar}	Pulse Duration [ns]	1
$E_{pulse_{lidar}}$	Pulse Energy [mJ]	10
$P_{pulse_{lidar}}$	Pulse Power [MW]	10
$f_{rep_{lidar}}$	Repetition Rate [kHz]	10
B_{sensor}	Detection Bandwidth [nm]	0.17
ΔR	Distance Resolution [m]	0.12
N_{pixels}	Sensor Resolution [pixels]	200x200
$P_{avg_{lidar}}$	Total Average Power [W]	243
M_{lidar}	Mass [kg]	286
V_{lidar}	Volume [m^3]	2.383

camera. These are located on the sides of the system, resulting in a large volume increase as opposed to solely the lidar system. However, as the Space Sweeper lidar shall have moving optics to allow for wide FoV scanning, some additional volume shall be needed for this. Taking the previously mentioned factors into account, the Space Sweeper lidar CAD model has dimensions of 1.3x1.3x1.41 metres, and a volume near 2.383 m^3. The mass will still be assumed the same, as a conservative estimate, since the masses of the individual elements of CALIOP cannot be estimated.

4.3.5 Verification of 'DetecTool.py'

DetecTool.py takes all lidar, debris, and background characteristics as an input, performs the calculations from Subsection 4.3.2 and 4.3.3, and returns Figure 4.5a and 4.5b. The goal of this tool is to assess the combinations of FoV and distance, for which a certain debris is detectable. Keeping this goal in mind, the code verification was performed as follows:

1. Walk-through testing: The main focus lies on checking the input values, and the formulas. The values were checked with the previous sections, which were also checked with their corresponding references. The formulas were checked in a similar way, and they were derived manually as a final verification.
2. Degenerate testing: The most important sanity check to be performed, is to see how the performance changes as the input parameters change. For example, an increase in receiver bandwidth should increase the possible FoV, since the received intensity of the background radiation decreases.
3. Analytical testing: A reference case was calculated by the program, printing all intermediate values, and by hand, and they were checked for equality. These values were identical up to seven digits behind the decimal point. The main source of error here is the calculator used for the manual computation.
4. Convergence testing: The only input array for the programme is the FoV; all other inputs are scalars. When decreasing the step for the FoV array, the plots all converged to their expected results. However, it was found that the length of a NumPy array is limited by the computer running the program. For a step size of $1 \cdot 10^{-9}$ degrees, over an interval of [0.01, 20), the error was: *"numpy.core._exceptions.MemoryError: Unable to allocate 149. GiB for an array with shape (19990000001,) and data type float64"*. Therefore, if an extremely small step size is desired, the interval for the FoV should be decreased. However, this only occurred at step sizes in the order of $1 \cdot 10^{-9}$ degrees.
5. Extreme value testing: The following three cases were tested: negative values, null values, and values tending to infinity.
    - Most constant parameters, such as the debris diameter, cannot physically have negative values. Assigning these values anyway, resulted in errors, such as division by zero, or an invalid argument for the arccosine. For the debris diameter, and debris distance, the negative sign disappears through a squared operation. A negative overlap value is possible, as this would just mean that there is an empty space between each image during the scanning mode. For a negative FoV, which is technically possible, Figure 4.5a mirrors about the y-axis, although the plot should be changed from a logarithmic X-axis to a linear X-axis.
    - For most parameters, assigning a null value results in infinite values for other parameters. For example, a zero debris diameter reflects zero power, so the power required by the laser would be infinite. The exact same happens for zero reflectivity, and zero efficiency. A FoV of zero is physically possible, representing a collimated beam. However, a collimated beam has the same energy density along its entire path, in vacuum, as opposed to a nonzero FoV, which loses energy over distance. Since the calculation aims to find the combination of FoV and distance to yield the required output power, such a distance cannot be found. To account for this zero FoV, a special case for collimated beams could be included in the code, where it simply states that the required energy can or cannot be achieved. This implementation is not done, since the purpose of this code is to find combinations between distance and FoV.
    - Extremely large debris diameters run flawlessly, as well as all efficiencies. A high bandwidth yields no errors, but it should be realised that this bandwidth relates to Figure 4.3, where the y-value was taken constant, since

Table 4.4: Change in outputs in percentage for changes in the main input parameters of the lidar system. The input parameters that are varied are shown in the leftmost column, while the output parameters are the stationary FoV and scanning FoV.

Inputs	**Output 1: Stationary FoV**		**Output 2: Scanning FoV**	
Percentage change	+10%	-10%	+10%	-10%
Debris Diameter	+4.86	-5.11	+4.91	-5.15
Debris Reflectivity	+2.43	-2.58	+2.45	-2.60
Sensor Bandwidth	-2.33	+2.68	-2.35	+2.70
Pulse Duration	-2.33	+2.68	-2.35	+2.70
Pulse Energy	+2.43	-2.58	+2.45	-2.60
Repetition Rate	0.00	0.00	+4.93	-5.18
Efficiency of Transmitter Optics	+2.43	-2.58	+2.45	-2.60
Efficiency of Receiver Optics	+2.43	-2.58	+2.45	-2.60
Quantum Efficiency of Receiver	+2.43	-2.58	+2.45	-2.60
Image Overlap	-2.17	+2.12	-2.19	+2.14
SNR	-2.33	2.68	-2.35	2.70

the bandwidth was assumed to be small. For larger bandwidths, a full integration of the graph is needed, and the simplified multiplication does not hold anymore. However, lidar bandwidths are always small enough to justify the simplified integration. nalytical function, after which a numerical integration should be performed. This is completely outside of the scope of this code, as a large bandwidth results in worse performance, so is undesirable. Lastly, the FoV was set to large values. As the FoV was increased beyond 360 degrees, which is physically impossible, an interesting phenomenon occurred. Figure 4.5b appeared to be the same, but the data points, as the FoV kept increasing, were actually travelling back and forth along the same path. In Figure 4.5a, this means that the required power oscillates with a period of 720 degrees FoV. This is because the FoV is divided by two before entering the cosine function. Since such large FoV values are physically impossible, this oscillating behaviour will have no impact on using the DetecTool for real-life applications.

6. Sensitivity testing: an elementary sensitivity analysis for all non-constant parameters was performed, to find the values that have the largest impact on the output. The stationary FoV, FoV with five seconds of scanning, at 300 km distance, are used as the output values. The reference values, using the parameters from the previous sections as input, are 0.169 degrees for the stationary FoV, and 37.9 degrees for a five second scanning period. The results are shown in Table 4.4. Note that the values in the leftmost column are the inputs to be varied, while the Stationary FoV and Scanning FoV are the reference outputs. The debris diameter is the most driving parameter, since it affects both the stationary FoV and the scanning FoV, since it takes a factor of two when converting it to debris area. Furthermore, the repetition rate drives the scanning FoV to a large extent, but has no impact on the stationary FoV.

4.4 Debris Removal Payload

Based on the conclusions drawn from Section 4.2, the ablative laser payload can be sized for the required altitude reduction for de-orbiting. The relevant calculations were performed for the worst-case scenario, assuming a debris altitude change from 1000 km to 340 km.

4.4.1 De-orbiting

The thrust that the laser imparts on a debris object is calculated as follows, (Pieters, 2020, p. 33).

$$F_{thrust} = C_m P_{out} = C_m \Phi A_{target} f \tag{4.18}$$

Here, P_{out} is taken to be equal to the laser pulse energy on the target area in one second (thus, multiplied by the frequency). A_{target} refers to the area absorbing the laser energy. It should be noted that this value typically represents the area of the laser at the target. However, given the small-size of the debris targets considered, the laser beam will cover the entire debris object so A_{target} refers to the debris area in this context. A_{target} specifically indicates the cross-sectional, 'silhouette', area of the debris object; an average area of the debris is taken given that the area orthogonal to the laser beam is unpredictable.

The deceleration of the debris fragment from the given thrust, a_{debris} is simply calculated by:

$$a_{debris} = \frac{F_{thrust}}{m} = \Phi \frac{A}{m} C_m f \tag{4.19}$$

where m is the debris target mass. Equation (4.19) clearly illustrates that the area to mass ratio, hereafter referred to as the AMR, of the debris fragments is a critical factor in the de-orbiting effectiveness. Thus, a minimum AMR of debris targets considered must be determined to size the laser. From literature, (Pieters, 2020), it is expected that AMR scales with mass, assuming that for a given fragment density, the mass of a particle should scale with the volume (m^3) as opposed

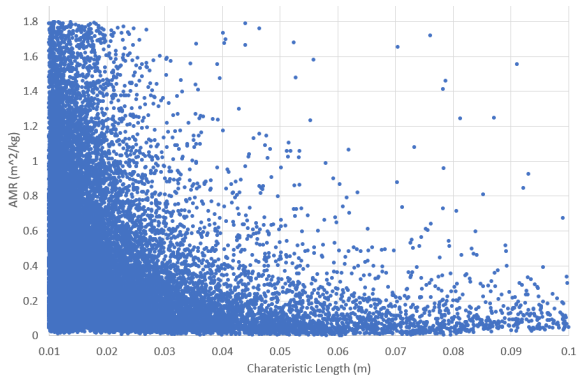

(a) Relationship between characteristic length and AMR for sample of fragments from the Kosmos-Iridium dataset (Schuhmacher, 2021)

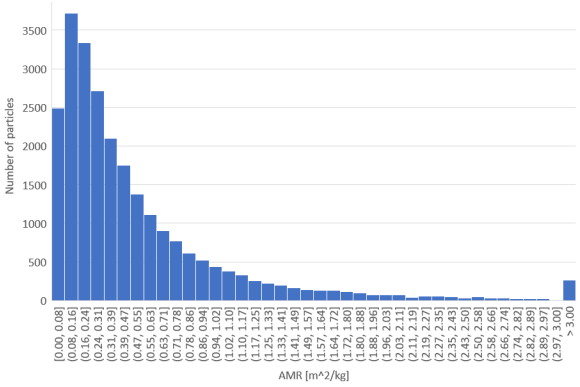

(b) Histogram of AMR Distribution from Kosmos-Iridium dataset (Schuhmacher, 2021)

to the area (m^2), resulting in fragments with more mass having a lower AMR. However, figure Figure 4.6a shows that, from the Cosmos-Iridium collision data, this correlation is not as strong as anticipated. While there is a general trend that particles with a high AMR are likely to be smaller, many small-sized particles, in the order of cm's.

The distribution of AMR for the reference sample of debris objects in Figure 4.6b shows a peak in the number of objects in the AMR range of 0.08 - 0.16 m^3/kg. Thus, by neglecting the 10% of debris objects with the lowest AMR (up to 0.7946 m^3/kg), the power requirements of the payload would be dramatically tempered, allowing the system to remove more objects in the grand scheme of the mission. Further optimisation of the selection of such an AMR threshold is recommended in further studies.

Referring back to Equation 4.19, the acceleration of the debris should be constant for a given fluence, AMR, coupling coefficient and laser frequency. The change in velocity, ΔV, imparted on the debris object throughout the ablation process, is given by the integral of the acceleration over the ablation time, t_a.

$$\Delta V = \int_{t_0}^{t_{end}} a_{debris}\, dt = a_{debris} t_a \tag{4.20}$$

For a given ΔV, calculated from the desired change in orbital altitude for de-orbiting, the required ablation time per particle can be derived.

It should be noted that the debris removal system must be able to fully de-orbit any targeted debris object in one pass. If the laser were to ablate a debris fragment for less time than the required ablation time per fragment, the laser would impart a lower ΔV on the fragment, and would be unlikely to see the fragment again for another shot in its mission. This would effectively cause scattering of debris fragments throughout the LEO altitude band below the spacecraft altitude, which is undesirable.

It is unfavourable to have a high t_a for many reasons. For one, this requires the laser to point at the debris object accurately for a longer period, increasing risk of de-orbiting failure. Furthermore, a longer t_a leaves less time for recharging of the EPS capacitors. Finally, the time window in which debris objects pass the laser's shooting range is limited; thus, a higher t_a results in a loss of system performance in terms of percentage of debris objects removed in six months.

4.4.2 Mass and Volume Estimation

Given the novelty of the debris removal payload, estimation of the mass and associated volume of the system is highly uncertain. A distinction can be made between the mass of the laser and the mass of the mirror system, including the primary mirror "dish" and the secondary mirror extension. From literature describing a similar mirror configuration (Soulard et al., 2014), a 3 m diameter mirror dish is sized at 400 kg. The following scaling formula was used for estimating mirror mass.

$$M_{mirror} = \frac{D}{3m}^2 \cdot 400kg \tag{4.21}$$

Similarly, it is assumed that the mass of the laser can be scaled with input power, taking Phipps' 125 kW Nd:YAG laser with a mass of 2500 kg as a reference case (Phipps, 2014). This assumption was backed up by Fabio di Teodoro [13], who suggests 10-20 kg/kW is a good rule of thumb for laser sizing. Additionally, 10-20 l/kW is used for the volume estimation.

[13] Personal communication Fabio Di Teodoro (senior engineer, Raytheon), email dd. 03-08-2022

Table 4.5: Change in outputs in percentage for changes in the main input parameters.

Outputs	**Range**		**Ablation time**		**AMR**		**C_m**		**Φ**	
Percentage change	+10%	-10%	+10%	-10%	+10%	-10%	+10%	-10%	+10%	-10%
Change power input	4.04	-3.96	-9.09	11.1	-9.09	11.1	-9.09	11.1	0.00	0.00
Change pulse energy	4.04	-3.96	0.00	0.00	0.00	0.00	0.00	0.00	-0.10	0.10
Change pulse frequency	0.00	0.00	-9.09	11.1	-9.09	11.1	-9.09	11.1	11.1	9.09
Change laser mass	4.04	-3.96	-9.09	11.1	-9.09	11.1	-9.09	11.1	0.00	0.00
Change mirror mass	16.3	-15.7	0.00	0.00	0.00	0.00	0.00	0.00	0.00	0.00

4.4.3 V&V of 'Laser_parameters.py'

In this section, the verification plan detailed by Teixeira et al. (2022b) is applied to the tool used for the research presented in the section. The most important input parameters on which the degenerative, extreme value and sensitivity testing was applied are the ablation time, range and AMR. The results are presented in the following list:

1. Walk-through testing: the equations used sequentially in the program were first checked by inspection. Comparison with the equations provided above in this section was performed, and the implementation came out as identical. This type of verification has a low reliability and simply serves to spot the most obvious errors.
2. Degenerate testing: The variables output from the program are comparable to those from literature. For example, Phipps' L'ADROIT (Phipps, 2014) requires 48 kW for operation, and values from the simulation output are of a similar order of magnitude with a similar laser design. Any discrepancies are likely due to using a second-harmonic laser with a more accurate efficiency estimate and varying assumptions between the approaches (e.g. spot size, AMR limitations, etc.)
3. Analytical testing: a reference case was computed by hand and compared to the obtained intermediate values. All values came out as accurate up to the 7th decimal. Eventual inaccuracies could arise from the calculator or computer machine inaccuracy. This test is very reliable as it directly checks that the intended model was implemented as intended.
4. Convergence testing: from the nature of the presented code, the convergence test was found to be inadequate. The program is used as a sequence of scalar equations, rather than a nodal simulation, where the number of nodes can be increased to improve the accuracy.
5. Extreme value testing: was first performed on the three driving parameters mentioned above by attributing negative, null and physics defyingly high values. For the null value, the code broke after the value was used, indicating a warning for divisions by zero (which is a desired output). The null value testing was also applied on other parameters, and a physical behaviour of the code was found. For instance, giving a value of zero to the C_m parameter yields a requirement for infinite power, which is expected as this parameter express the transfer in momentum of the ablated particle (if it is zero, no momentum change arises).
   Testing for negative values of ablation time and AMR yielded negative outputs for the power input and laser mass, which is obviously physics defying. This was expected as both those parameters cannot be physically negative, furthermore, such behaviour was found for most parameters. A more concerning result was however found when applying the test to the range, as physical outputs were obtained. This was found to come from the d_s equation, where its formulation was changed to the absolute value of the range instead, such that similar typing errors would have no effect.
   Testing for physics defyingly high values also yielded the expected behaviour. For example, increasing the range by a factor of 10^{10} yielded an extremely high required power and laser mass. Similarly, increasing the ablation time to multiple days, decreased the required power to extremely small values.
6. Sensitivity testing: the sensitivity of the most critical parameters of the tool was investigated by varying its value by 10% and considering the change in the output. The results are shown in Table 4.5. From those results, the mirror mass is deemed to be more sensitive than average

4.4.4 Final Debris Removal Payload Design

The final specifications from the design process are outlined in Table 4.6. An extensive research and technology development program will be established in Chapter 14, outlining the development strategy to produce an ablation payload with the specifications listed. Similar programs will be implemented for the development of the detection payload system.

Given that the fluence at the target location is maintained throughout the de-orbiting shot, the key variables that were optimised to determine the required power, and thus mass, of the subsystem are the range and the ablation time of the laser. From Figure 4.7 and Figure 4.8, it is evident that higher ranges increase the associated power and mass. There is also an inverse exponential decay in these parameters with increasing shooting time. It should be noted, however, that decreasing the range of the laser intuitively has negative implications for performance, as this leaves a shorter window to shoot debris objects. Similarly, increasing shooting time makes it more difficult to keep the laser locked on debris objects and objects that do not pass the range of the laser for more than the required shooting time cannot be de-orbited.

Table 4.6: Final debris removal payload specifications.

Symbol	Property	Value
-	Material	Nd:YAG
Φ_{opt}	Optimum Fluence [J/m^2]	8,500
τ	Pulse Duration[ps]	100
C_m	Coupling Coefficient [N/MW]	91.1
λ	Wavelength [nm]	532
η	Total Efficiency [%]	25.2
M^2	Beam quality factor [-]	2
a_l	Diffraction constant [-]	1.7
T_eff	System loss factor [-]	0.9
E_p	Pulse Energy [J]	116
f	Repetition Rate [Hz]	55.8

Symbol	Property	Value
L	Range [km]	250
Θ	Max. Incidence Angle [°]	20
d_s	Spot Size [m]	0.125
D	Mirror Diameter [m]	4.02
AMR_{min}	Minimum AMR [kg/m^2]	0.0795
t_a	Ablation Time [s]	50
P_{in}	Total Input Power [kW]	27.7
m_{laser}	Laser Mass [kg]	564
m_{mirror}	Mirror Mass [kg]	581
m_{total}	Total Mass [kg]	1150

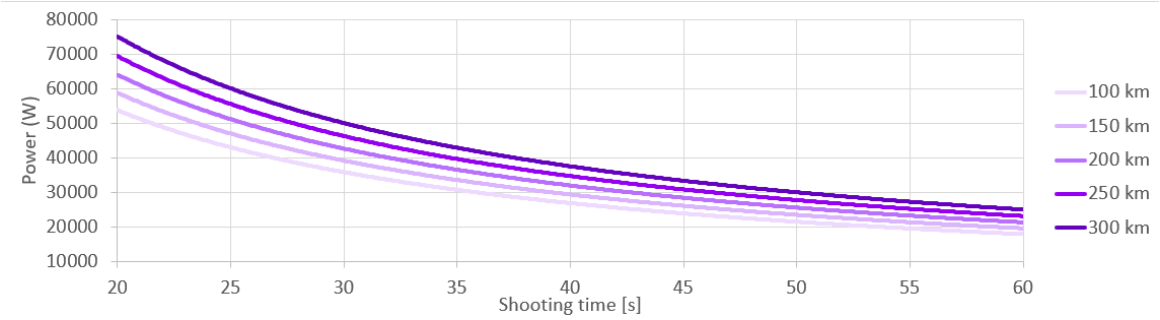

Figure 4.7: Required average input shooting power as a function of ablation time for various shooting ranges.

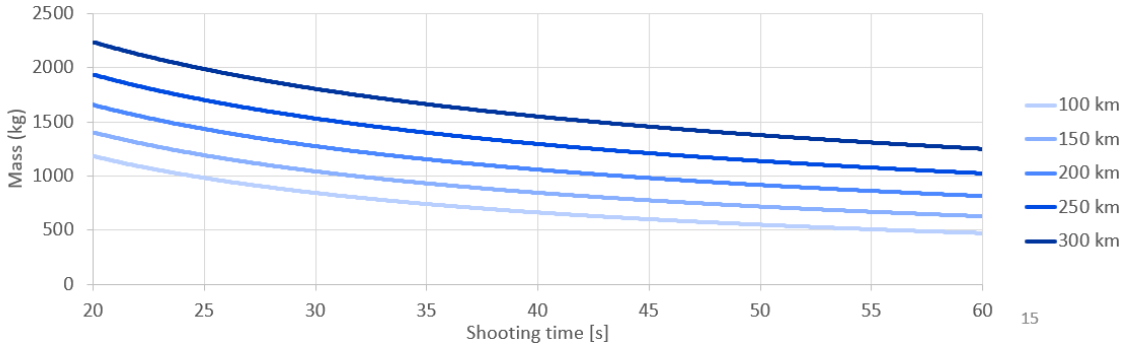

Figure 4.8: Debris removal payload mass as a function of ablation time for various shooting ranges.

The optimisation of the laser involved simulating the system with combinations of increments of ablation time and range, using the debris removal simulation in Section 3.6. The optimal combination of parameters, that successfully removes 50% of targetted debris in less than a year while minimising mass and power, is a 50 s ablation time at 250 km range. It may be noted that the performance of the laser would be improved for a higher range and ablation time. However, the primary mirror diameter greatly increases with increasing shooting range, which became a limiting factor given the mirror diameter directly defines the required dynamic envelope of the selected launcher fairing. Reiterating, the shooting time was minimised to reduce risk of failed locking onto target debris during shooting procedures.

The total mass of the payload, including the ablation laser and the lidar tracking system, exceeds the estimated budget of 1000 kg by roughly 400 kg. The preliminary budget was vastly underestimated for the given subsystem, given its complexity and shooting power required for ablation. Given that the performance of the system would be jeopardised by reducing the mass, it was decided to reconsider the mass budget. The gain in performance substantially outweighs the added mass, given the associated cost is minor.

Guidance, Navigation and Control 5

The design of a Guidance, Navigation and Control subsystem, capable of meeting the imposed requirements, is discussed in this chapter. First, the requirements for this subsystem are detailed in Section 5.1. Next, the manoeuvres that require navigation are briefly outlined in Section 5.2. In Section 5.3, a target orbit with respect to the collision orbit is selected. How the spacecraft determines its position and velocity is explained in Section 5.4. Following this, everything that relates to the Attitude Determination and Control System (ADCS) can be found in Section 5.5. The filtering and calibration needed for the selected sensor suit is summarised in Section 5.6. With all necessary components laid out, their interrelations are shown in Section 5.7. Hereafter, the verification and validation can be found in Section 5.8. Finally, the chapter is concluded in Section 5.9.

5.1 Subsystem Requirements

The subsystem requirements of the GNC subsystem that are the results of the analysis performed in this chapter are introduced in Table 5.1.

Table 5.1: GNC initial requirements.

Requirement ID	Description	Rationale
SS-SYS-GNC-REQ-001	The mass of the GNC subsystem shall not exceed 355.97 kg.	Allocated mass budget.
SS-SYS-GNC-REQ-002	The size of the GNC subsystem shall not exceed 0.337 m^3.	Allocated volume budget.
SS-SYS-GNC-REQ-004	The power used by the GNC subsystem shall not exceed 388 W during nominal operations.	Allocated power budget.
SS-SYS-GNC-REQ-005	The power used by the GNC subsystem shall not exceed 880 W during non-nominal operations for duration of 50 s.	Allocated power budget.
SS-SYS-GNC-REQ-006	The GNC subsystem shall be operational between the temperature range 253 < T < 333 K.	This temperature range is encountered during the mission and thus the GNC subsystem should be able to deal with it.
SS-SYS-GNC-REQ-007	The GNC subsystem shall provide an attitude determination accuracy of $4.52 \cdot 10^{-05}$ rad around all axes with 3 σ.	The satellite needs to determine attitude with some accuracy within given probability.
SS-SYS-GNC-REQ-008	The GNC subsystem shall provide a pointing accuracy of $4.52 \cdot 10^{-05}$ rad around all axes with 3 σ.	The satellite needs to control attitude with some accuracy within given probability.
SS-SYS-GNC-REQ-011	The drift of the GNC subsystem shall not cause an error larger than $4.52 \cdot 10^{-05}$ rad over <50> s.	The drift of the satellite needs to stay within some bounds over some period of time in order to determine attitude accurately.
SS-SYS-GNC-REQ-013	The GNC subsystem shall be able to withstand a disturbance torque of at least 0.012 Nm.	Disturbance torques are constantly acting over the spacecraft, so they need to be counteracted.
SS-SYS-GNC-REQ-014	No single point of failure in the GNC subsystem shall be present.	GNC subsystem is critical for the operations, hence it needs to be redundant.
SS-SYS-GNC-REQ-015	The spacecraft's position shall be determined with an accuracy of 0.12 m with 1 σ.	The estimated position of the spacecraft must be more accurate than the distance resolution of the lidar system, such that the debris is catalogued as accurately as possible.

SS-SYS-GNC-REQ-017	The actuators shall be able to dump 65.1 Nms of angular moment per orbital period.	Angular momentum is accumulated due to external disturbances and needs to be dumped.
SS-SYS-GNC-REQ-018	The actuators shall be able to rotate the spacecraft with angular acceleration of 0.056 rad/s^2.	Actuators need to rotate spacecraft fast enough such that the laser can ablate the space debris.
SS-SYS-GNC-REQ-019	The control and determination performance must be met at any altitude within 19 °of nadir.	Performance of GNC may vary depending on attitude, so it is important the requirements are met for operational attitude.
SS-SYS-GNC-REQ-020	The control and determination performance must be met at any rotational rate below 0.314 rad/s.	GNC may have limitations on rotational rate, therefore it cannot be exceeded during operation.

5.2 Navigation Manoeuvres

During several phases in the mission, the spacecraft shall be navigated to different orbits. First, as will be shown in Section 13.2, the launch vehicle will be able to perform the orbit insertion, such that no orbital manoeuvre is needed at the very start of the mission. During the operational phase, station keeping is required, to maintain the target orbit, which will be done once per orbit. This will be elaborated upon in Chapter 7. Furthermore, collision avoidance manoeuvres may be needed, depending on whether a potential collision is detected. Whenever the spacecraft is unable to detect the endangering debris, this detection can be done using the catalogues provided by the US Space Surveillance Network (SSN) or ESA's Space Surveillance and Tracking (SST), where Conjunction Data Messages (CDM) will be sent to the ground operators. Subsequent detailed calculations will indicate if a collision avoidance manoeuvre shall be performed (Rongzhi et al., 2020). Finally, at EoL, the spacecraft will be re-entered into the atmosphere, by entering an elliptical orbit with a perigee at a 100 km, as determined in Section 3.5. This manoeuvre will be activated by the ground station, who will send a command to the spacecraft to initiate the manoeuvre.

5.3 Target Orbit

In the Midterm Report (Teixeira et al., 2022b, pp.18-20), an orbital altitude was selected, namely 40 km above the collision altitude, with the other orbital parameters remaining unchanged compared to the collision orbit. This decision is now revisited, as a more accurate simulation is available, described in Section 3.6, which can be used to find a more optimal value.

Building on the reasoning provided in the Midterm Report, where a trade-off was performed for the target orbit, the co-planar orbit with an increased semi-major axis compared to the collision orbit, is still considered to be the best choice. However, the 40 km was not substantiated, and is therefore now reconsidered. For the current consideration, a semi-major axis equal to the collision altitude plus an additional range of 0 to 100 km is considered. This is also to satisfy the requirement to focus on the debris with an increased semi-major axis, which have a longer natural decay time. In the simulation, a significant percentage of the debris will have a sufficiently low perigee, namely lower than 340 km, immediately after the collision. For the reference dataset used in the simulation, this corresponds to the removal of around 33% of the debris, thus skewing the remaining data to the higher altitudes. Therefore, an optimum is expected to be found at a significantly higher altitude, where the performance will scale non-linearly with the spacecraft's altitude, due to the approximate normal distribution of the debris around the collision orbit (Kelso et al., 2009).

Running the simulation for nine different relative altitudes, that is, the increase in semi-major axis with respect to the collision orbit, results in the table shown in Table 5.2. It should be noted that the given removal time in days, is only indicative, used for comparison, and does not represent the final performance of the system. This is because the cooldown time is set equal to zero, to minimise the simulation time, which does not impact the relative visibility of the debris for the different altitudes, and is therefore valid for comparison. Here, also the percentage of the removed debris with an increased semi-major axis is provided, as a higher percentage is desirable. From this data, it is determined that 30 km is the optimal altitude for the best performance, while mainly removing debris with a relatively long natural decay time.

This optimisation has been done specifically for the reference dataset, namely the Kosmos fragments originating from the Iridium-Kosmos collision, where the original collision altitude was equal to 789 km. For different altitudes, the distribution of the debris is rather similar, considering the orbital velocities in the targeted altitude of 350 to 1000 km are in a close range. However, at lower altitudes, say 400 km, a larger fraction of the debris decays by itself in a sufficiently short amount of time, and would therefore not need to be removed by the system. Thus, in that case, a higher relative altitude would be beneficial, but is not further considered for the current discussion, because this mission is aiming to remove 50% of a certain orbit and should thus target the bulk of the debris. Yet, it is recommended to analyse the performance

Table 5.2: Debris removal performance for different relative altitudes.

Relative altitude [km]	Removal time [days]	Fraction increased semi-major axis
0	45.5	61%
10	45.0	62%
20	44.8	66%
30	43.6	69%
40	46.4	72%
50	56.8	73%
60	60.7	74%
80	84.6	77%
100	571	91%

also for these lower altitudes, by considering different reference collisions, to derive an optimal spacecraft altitude for each different collision altitude. A weak dependency on collision altitude is expected, based on the fact that the debris is heavily concentrated around the collision orbit (Wang, 2010). Furthermore, for lower altitudes, it is recommended that the 50% removal requirement is renegotiated with the customer, to target the space debris with a longer natural decay time. This corresponds to debris in higher orbits, where the distribution is more scarce, and thus a lower percentage of the debris will be removed by the system if those fragments are targeted specifically.

5.4 Position and Velocity Determination

The position and velocity of the spacecraft need to be estimated for the spacecraft to be operated successfully. One method to achieve this is by tracking the spacecraft from the ground and uplinking the orbital parameters, to thereafter propagate these by onboard processing (Wertz, Everett, et al., 2011). This avoids the need for additional components, but does require additional onboard computational power. Alternatively, the spacecraft position and velocity can be obtained from onboard GNSS antennas. This method has been used on numerous spacecraft over the last decades, with the first GPS antenna flown already in 1982 (Fang et al., 2012). Especially for LEO, this is regarded as the most effective method for real-time navigation (Gong et al., 2019). Also, it has the particular advantage that it can also serve as a (redundant) attitude determination system, in case at least three additional antennas are installed, by relating the measured phase difference of the received signals to the associated attitude angles (Speretta, 2020). Four antennas are needed, because the attitude shall be determined for the three axes, for which three antennas are needed, but also a references signal is used for the computation of the phase difference, hence the fourth antenna.

To accurately catalogue the detected space debris, the state of the spacecraft should be known with reasonably high accuracy, considering the position of the debris will be estimated relative to that of the spacecraft. However, it should be noted that the removal of the space debris is irrespective of this, as both the detection and the pointing of the removal laser will be done relative to the spacecraft such that the absolute positions are not needed. Therefore, the accuracy of the position, velocity, and angular rates of the spacecraft are mainly of importance for the secondary mission. Compared to ground-tracking methods, GPS receivers perform relatively well in terms of accuracy, with a standard precision that can go to even a few centimetres, while for ground-tracking methods this is in the order of a hundred metres (Chiaradia et al., 2013).

For the aforementioned reasons, a GNSS receiver is used for state determination, and will also be considered for attitude determination in Section 5.5. A commercially available component is selected, namely the PODRIX GNSS Receiver, developed by RUAG . This receiver has a position measurement accuracy of below 20 cm, which can be further improved up until a few centimetres if on-ground post-processed dual-frequency receiver data is used, and thereby satisfying SS-SYS-GNC-REQ-014. To benefit from this high accuracy, the spacecraft shall make use of Galileo's High Accuracy Service (HAS) on the E6 signal. The velocity measurement accuracy is less than 1 mm/s. Furthermore, this component is selected because of its flight heritage (more than 80 successful flight models), and is manufactured in Europe.

5.5 ADCS

As can be observed from Table 5.3, the accuracy required strongly drives the selection of its components, and has an impact on the spacecraft.

[1]URL: https://satcatalog.s3.amazonaws.com/components/1216/SatCatalog_-_RUAG_-_PODRIX_GNSS_Receiver_-_Datasheet.pdf [Accessed on 08-06-2022]

Table 5.3: Effects of Control Accuracy Requirements on Sensor Selection and ADCS Design (Starin et al., 2010).

Required accuracy (3σ)	**Effect on Spacecraft**	**Effect on ADCS**
>5°	-Permits major cost savings -Permits gravity gradient (GG) stablisation	Without attitude determination - No sensors required for GG stablisation - Boom motor, GG damper, and a bias momentum wheel are only required actuators With attitude determination: - Sun sensors & magnetometer adequate for attitude determination at >2° - Higher accuracies may require star trackers or horizon sensors
1° to 5°	-GG not feasible -Spin stabilisation feasible if stiff, inertially fixed attitude is asseptable -Payload needs may require despun platform on spinner -3-axis stabilisation will work	-Sun sensors and horizon sensors may be adequate for sensors, especially a spinner -Accuracy for 3-axis stabilisation can be met with RCS deadband control but reaction wheels will save propellant for longer missions -Thruster and damper adequate for spinner actuators -Magnetic torquers and (and magnetometer) useful
0.1°to 1°	-3-axis and momentum-bias feasible -Dual-spin stabilisation also possible	-Need for accurate attitude reference leads to star tracker or horizon sensors & possibly gyros -Reaction wheels typical with thrusters for momentum unloading and coarse control -Magnetic torquers feasible on light vehicles (magnetometer also required)
<0.1°	-3-axis stabilization is necessary -May require articulated & vibration-isolated payload platform with separate sensors	-Same as above for 0.1° to 1° but needs star sensor and better class of gyros -Control laws and computational needs are more complex -Flexible body performance very important

Only certain sensors and actuators can meet the accuracy criteria, which therefore needs to be determined in Subsection 5.5.1. The required torques for control of the spacecraft needs to be established in Subsection 5.5.2. Furthermore, the disturbance environment needs to be quantified, including the momentum to be dumped per orbit, which is shown in Subsection 5.5.3. With all this data available, correct sensors are chosen in Subsection 5.5.4, while actuators are selected in Subsection 5.5.5.

5.5.1 Required Accuracy of Attitude Determination

The accuracy required for attitude determination and debris detection should not be underestimated. The former is required for determining the position of the spacecraft relative to known reference frame, while the latter determines the position of the debris with respect to the spacecraft. The payload has its own space debris detection device described in Section 4.3, which can very accurately detect the relative position of the debris with respect to the spacecraft. It can be used for aiming the laser, and consequently the accuracy of the Attitude Determination required for the primary mission may stay low as it is only required for the antennas and the solar array. However, for the secondary mission, space debris needs to be accurately detected in an absolute reference frame. Therefore, the attitude of the spacecraft also needs to be known with very good accuracy and more accurate Attitude Determination is required. This can be quantified by deriving a simplified 2D model of determining the debris orbital parameters from its relative position with respect to the spacecraft and its absolute position. It can be assumed that both the spacecraft and the debris follow circular orbits with radii of R_{SC}, and R_D, respectively as shown in Figure 5.1.

The spacecraft position in in Cartesian coordinates is $\boldsymbol{R}_{SC} = \begin{bmatrix} R_{SC}\cos(\nu_{SC}) \\ R_{SC}\sin(\nu_{SC}) \end{bmatrix}$, while debris position is $\boldsymbol{R}_d = \begin{bmatrix} R_d\cos(\nu_d) \\ R_d\sin(\nu_d) \end{bmatrix}$.

The position of debris with respect to the spacecraft is:

$$\vec{R_{d/SC}} = \vec{R_d} - \vec{R_{SC}} = \begin{bmatrix} R_d\cos(\nu_d) - R_{SC}\cos(\nu_d) \\ R_d\sin(\nu_d) - R_{SC}\sin(\nu_d) \end{bmatrix} = \begin{bmatrix} x_{d/SC} \\ y_{d/SC} \end{bmatrix} \tag{5.1}$$

This relative position vector can be transformed to radial coordinates:

$$R_{d/SC} = \sqrt{x_{d/SC}^2 + y_{d/SC}^2} \tag{5.2}$$

$$\theta_{d/SC} = \arctan(\frac{y_{d/SC}}{x_{d/SC}}) \tag{5.3}$$

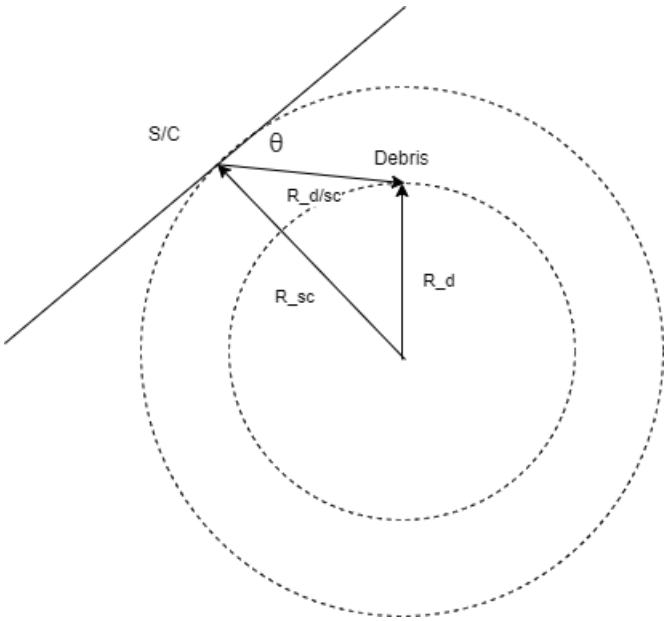

Figure 5.1: Simplified 2D model for determining debris position.

By using lidar it is possible to find $R_{d/SC}$, and the combination of it and ADCS allows to determine $\theta_{d/SC}$. These values can then be used with equations above to find orbital parameters of the debris required for cataloguing it, R_d and ν_d. However, these values can be affected by errors in $R_{d/SC}$ and $\theta_{d/SC}$. The measured and real $\theta_{d/SC}$ can be linked through the accuracy of lidar and ADCS:

$$\theta_{d/SC,\,measured} = \theta_{d/SC,\,real} + \theta_{error,\,lidar} + \theta_{error,\,lidar\ gimbal} + \theta_{error,\,ADCS} \tag{5.4}$$

It is only desired to quantify the impact of the accuracy of ADCS on the measured orbital parameters of the debris, therefore it is assumed that $\theta_{error,\,lidar} = \theta_{error,\,lidar\ gimbal} = 0°$. The accuracy of measured $R_{d/SC}$ depends solely on lidar, therefore it is also assumed it does not have an error. The accuracy of spacecraft position determination with GPS also affects the determined R_d and ν_d, but for similar reasons it is not taken into account in this case. To determine orbital parameters of the debris, Eq.(5.3) can be used to determine $\frac{y_{d/SC}}{x_{d/SC}}$:

$$\tan(\theta_{d/SC,\,real} + \theta_{error,\,ADCS}) = \frac{y_{d/SC,\,m}}{x_{d/SC,\,m}} \tag{5.5}$$

where subscript m stands for measured. Eq.(5.2) can be then used to find $x_{d/SC,\,m}$ in equation Eq.(5.6), after which $y_{d/SC,\,m} = x_{d/SC,\,m}\frac{y_{d/SC,\,m}}{x_{d/SC,\,m}}$, using (5.1) and spacecraft position, $\boldsymbol{R}_d$ can be found using equation Eq.(5.7).

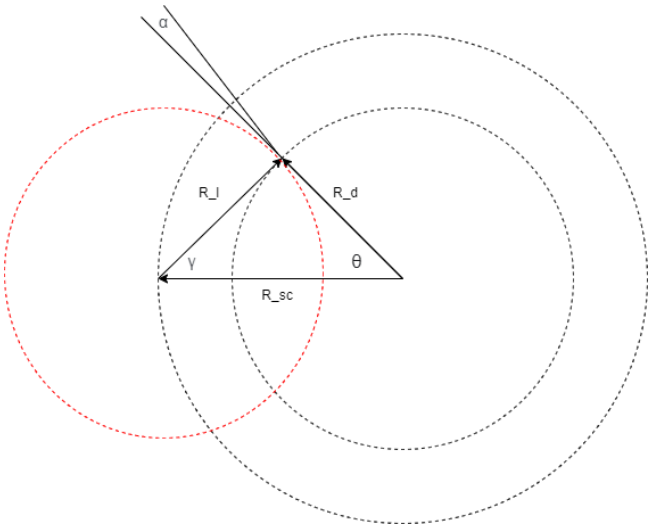

Figure 5.2: Spacecraft and debris position for determining error in orbital radius.

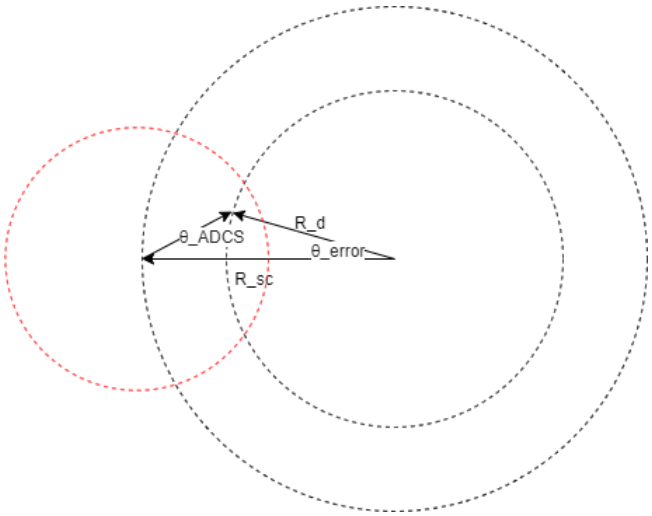

Figure 5.3: Spacecraft and debris position for determining error in true anomaly.

$$x_{d/SC} = \frac{R_{d/SC}}{\sqrt{1 + (\frac{y_{d/SC,\,m}}{x_{d/SC,\,m}})^2}} \tag{5.6}$$

$$\vec{R_d} = \vec{R_{d/SC}} + \vec{R_{SC}} \tag{5.7}$$

The spacecraft and debris motion can be simulated, and the error between real and measured $\boldsymbol{R}_d$ can be found to assess the impact of ADCS accuracy. Unfortunately, Eq.(5.5) would cause division by zero in the simulation, which would then introduce large numerical errors. It was therefore decided for a simplified model, where the error in true anomaly and orbital radius of the debris is determined at the positions where they would be the largest. The spacecraft and debris position for determining error in true anomaly $\Delta\theta$ is introduced in Figure 5.3.

It can be observed from it that:

$$(R_{SC} - R_D) \cdot \sin(\theta_{error,\,ADCS}) = R_D \cdot \sin(\Delta\theta) \rightarrow \Delta\theta = \arcsin(\frac{(R_{SC} - R_D) \cdot \sin(\theta_{error,\,ADCS})}{R_D}) \tag{5.8}$$

The result will be the biggest for the smallest $R_D = 300$ km (with $R_{SC} = 330$ km as described in Section 5.3). In Subsection 8.3.3 it is determined that the accuracy of debris' orbit detection needs to be 10 m for orbital radius and 0.01°for true anomaly. To meet latter requirement, $\theta_{error,\,ADCS}$ needs to be at least $5.17 \cdot 10^{-3}$ rad. A similar approach can be used for determining error in orbital radius, however this will result at the edge of view of the satellite as shown in Figure 5.2. The cosine rule can be used to calculate θ and γ:

$$\theta = \arccos(\frac{R_L^2 - R_{SC}^2 - R_D^2}{-2R_D R_{SC}}) \tag{5.9}$$

$$\gamma = \arccos(\frac{R_D^2 - R_L^2 - R_{SC}^2}{-2R_L R_{SC}}) \tag{5.10}$$

Then $\alpha = \gamma + 90° - \theta$. The difference in measured orbital radius is then:

$$\Delta R = \cos(\alpha) R_L \sin(\theta_{error,\,ADCS}) \tag{5.11}$$

It will be again the biggest for $R_D = 300$ km. The required $\theta_{error,\,ADCS}$ to meet 10 m accuracy on orbital radius is then $4.52 \cdot 10^{-05}$ rad or 9.32 arcsec. This is a significantly larger accuracy than that of a lidar presented in Chapter 4, hence the assumption that it does not contribute to the orbital parameters determination can be considered accurate.

5.5.2 Manoeuvre torques

Relative angular acceleration of the debris is required to calculate manoeuvre torque. The required angular acceleration can be preliminary obtained by differentiating Eq.(5.3) twice. Since analytical solution is very long, it was decided to differentiate the result numerically. The results of the simulation are introduced in Figure 5.4 for a moment in time when particle passes the spacecraft.

The maximum angular acceleration between the spacecraft when the debris comes into its range and leaves its field of view (around t = 2717 s) is 5.7 °/s^2, which was used during preliminary analysis. Later in the design, more advanced simulation of debris removal described in Chapter 3 was available, which statistical results for relative angular acceleration are introduced in Figure 5.5. It can be observed that to meet SS-TL-STK-US-REQ-G-003, the angular acceleration of the spacecraft needs to be at least $3.2°/s^2$, which is less than preliminary results in Figure 5.4 that presented conservative case.

The obtained value for relative angular acceleration can be used with spacecraft Mass Moment of Inertia (MMOI) to determine torques required. It should be noted that this is a high rate of angular acceleration, therefore it may be advisable

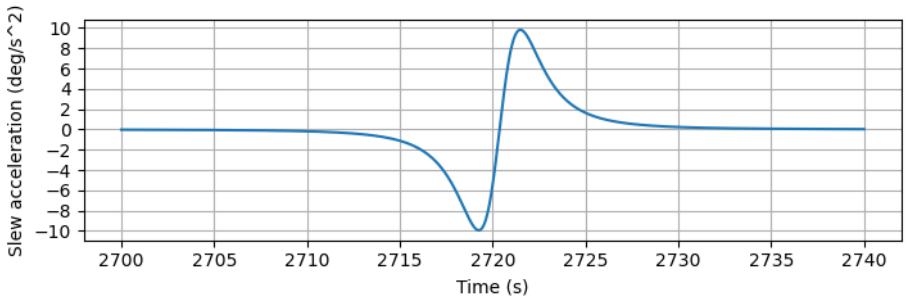

Figure 5.4: The output of the ADCS sizing tool for relative angular acceleration between spacecraft and debris.

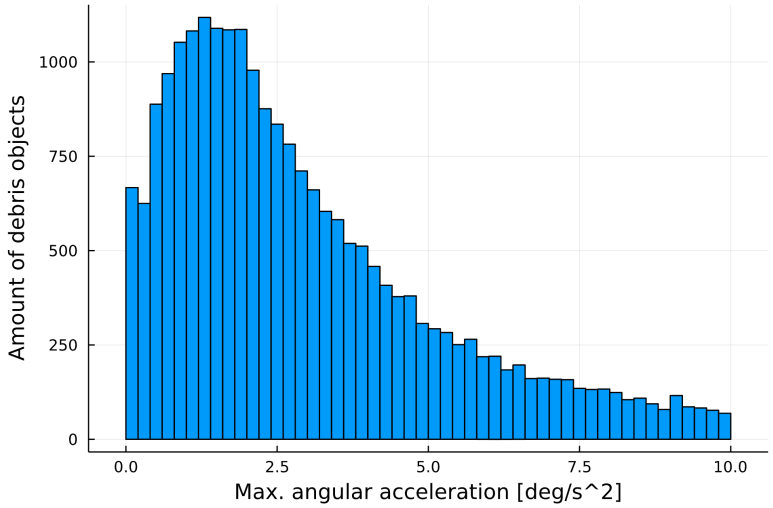

Figure 5.5: Angular accelerations of space debris particles with regards to the spacecraft.

Table 5.4: MMOI of assemblies of the spacecraft.

Assembly name	Mass (kg)	CG location (m)	I_{xx}(kg ·m^2)	I_{yy}(kg ·m^2)	I_{zz}(kg ·m^2)
Laser head	1297,380	4,300	1676,984	923,549	923,549
S/C main body	1559,620	1,605	3539,861	2650,979	3009,785
Total S/C	2857,000	2,829	5216,845	6146,196	6331,939

for a laser to be gimbaled. In this case, angular acceleration needs to be only multiplied with MMOI of the gimbal to obtain its torque. The first estimate of spacecraft MMOI can obtained from manual diagrams. The known masses and sizes of the individual components can be then assigned, while the rest is lumped into the main body of the spacecraft. Eq.(5.12) can be used to calculate MMOI for each axis.

$$I = \sum (I_c + m_c d_c^2) \tag{5.12}$$

where c is a subscript for component, I is mass moment of inertia and d is a distance of the component CG from CG of the assembly. Once the CAD is available, the results can be obtained from the tools itself. Table 5.4 introduces these results for three assemblies - laser head, spacecraft main body, and the whole spacecraft. With the data from Table 5.4 and angular accelerations from Figure 5.5 it can be calculated that the greatest torque required to rotate the whole spacecraft is 353.64 Nm, however it is only 51.58 Nm if it is gimbaled.

5.5.3 Disturbance environment

The external disturbance torques acting on the spacecraft are gravity gradient, atmospheric drag, magnetic and solar pressure torques. Meanwhile, the internal disturbance torques may come from leaks, propellant sloshing in the tanks, outgassing of the materials, flexible structures, thermal shocks or thruster misalignment (Starin et al., 2010). The latter are hard to quantify, so only external torques will be analysed.

The gravity gradient torque due to uneven mass distribution (such as when spacecraft is tilted with the respect to the attitude reference frame) is (Zandbergen, 2021):

$$\boldsymbol{T_g} = \frac{3\mu}{2R^3} \begin{bmatrix} I_{zz} - I_{yy} \\ I_{zz} - I_{xx} \end{bmatrix} \sin(2\theta) \tag{5.13}$$

Table 5.5: Criteria for Magnetic Properties Control (Blackburn et al., 1969).

	Class I	**Class II**	**Class III**
Design	Formal specification on magnetic properties control; approved materials and parts lists; cancellation of moments by preferred mounting arrangements and control of current loops.	Advisory specifications and guidelines for material and parts selection. Avoidance of "soft" magnetic materials or current loops and awareness of good design practices.	Nominal control over current loops; guidelines for avoidance of "soft" magnetic materials.
Quality Control	Complete magnetic inspection of parts and testing of subassemblies.	Inspection or test of suspect parts.	Test of subassemblies that are potentially major sources of dipole moment.
Test and compensation	Deperming either at subassembly or spacecraft level; test of final spacecraft assembly and compensation if required.	Deperming and compensation frequently used.	Test and compensation optional.

It has been assumed that $\theta = \frac{\pi}{2}$, as it results in the greatest torque. Only 2D case is preliminary assumed, hence the biggest component of that torque moment is chosen. The atmospheric drag torque is (Zandbergen, 2021):

$$T_a = 0.5\rho C_d A_r V^2 (r_{cp,\,a} - r_{cm}) \tag{5.14}$$

where C_d is drag coefficient, A_r is ram area, $r_{cp,\,a}$ is a centre of atmospheric drag pressure and r_{cm} is a centre of mass. The most conservative estimate for A_r is when the solar array is perpendicular to the flight path. For a flat plate C_d is then 3 (Wertz, Meissinger, et al., 2009). $r_{cp,\,a}$ is hard to assess at preliminary stage, hence $r_{cp,\,a} - r_{cm}$ can be then assumed to be a 0.1 m. Once CAD is available, more refined value can be determined from it. If it is too large then, $r_{cp,\,a}$ and r_{cm} can be readjusted to match the value chosen during preliminary design. ρ can be obtained from NLRMSISE-00. Another external torque is magnetic moment (Starin et al., 2010), given by equation (5.15), where D is the spacecraft's residual dipole moment and B is the magnetic field strength in tesla. B can be calculated from (Starin et al., 2010), given in Eq.(5.16).

$$T_m = DB \tag{5.15}$$

$$D = \frac{M}{R^3}\lambda \tag{5.16}$$

where M is a magnetic constant of $7.8 \cdot 10^{15}$ T $\cdot$ m^3 and λ is a unitless function of magnetic latitude ranging from 1 at the magnetic equator to 2 at the magnetic pole. Since the mission needs to operate at all inclinations, $\lambda = 2$ is chosen. Spacecraft's residual dipole moment can be estimated from (Blackburn et al., 1969) depending on class of magnetic properties control. Table 5.5 introduces a table with criteria for magnetic properties control.

For a large and expensive satellite, Class I is preferred. It results in the lowest spacecraft's residual dipole moment per kilogram of $10^{-3}\ \frac{\text{Am}^2}{\text{kg}}$.

The final external torque to include is solar pressure (Starin et al., 2010):

$$T_S = \frac{\Phi}{c} A_S (1+q)(r_{cp,\,s} - r_{cm})\cos(\phi) \tag{5.17}$$

where Φ is a solar constant of $1367 \frac{\text{W}}{\text{m}^3}$ and c is the speed of light of $3 \cdot 10^8 \frac{\text{m}}{\text{s}}$. A_s is a sunlit surface area and q is a reflectance factor. A perfect reflection of 1 was assumed. $r_{cp,\,s}$ is a solar radiation pressure centre. Since solar radiation pressure is a minor disturbance, $r_{cp,\,s} - r_{cm}$ can be again preliminary assumed to be 0.1 m, and more accurate value can be obtained from CAD. ϕ is an incidence angle conservatively assumed to be 0°for conservative results. By summing each of these disturbances, it is possible to get the total disturbance torque as a function of altitude as shown in Figure 5.6. The momentum to be dumped at the lowest operational altitude is 65.1 Nms.

Table 5.6: Typical ADCS Sensors (Starin et al., 2010).

Sensors	Typical performance range	Mass [kg]	Power [W]
Gyroscopes	Drift Rate = 0.003 °/hr to 1 °/hr Drift rate stability varies widely	<0.1 to 15	<1 to 200
Sun Sensors Star Sensors (Scanners & Cameras)	Accuracy = 0.005°to 3° Accuracy = 1 arcsecond to 1 arcminute = 0.0003°to 0.01°	0.1 to 2 2 to 5	0 to 3 5 to 20
Horizon Sensors - Scanner/Piper - Fixed Head (static)	Accuracy: 0.05 °to 1°(0.1°is best for LEO) <0.1°to 0.25 °	 1 to 4 0.5 to 3.5	 5 to 10 0.3 to 5
Magnetometer	Accuracy = 0.5°to 3°	0.3 to 1.2	<1

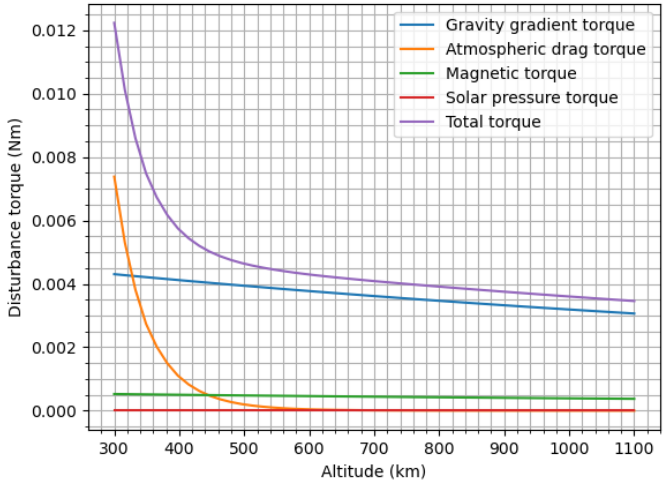

Figure 5.6: Disturbance torque as a function of altitude.

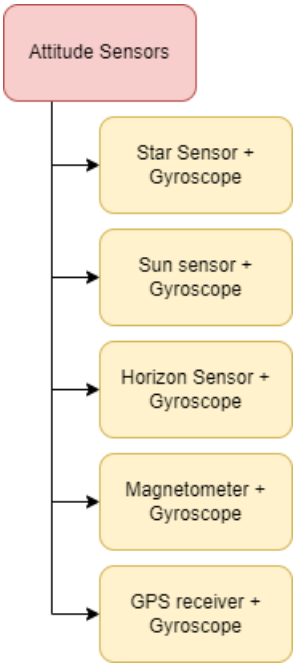

Figure 5.7: Design Option Tree for attitude sensors.

5.5.4 Attitude Determination

Attitude Determination is required for the accurate determination of the spacecraft state. In this subsection, a tradeoff will be performed to decide on the best configuration of sensors and the COTS hardware will be chosen.

Sensors Trade-off

Figure 5.7 introduces the Design Option Tree for attitude sensors. All options have the gyroscope included, as it has significantly higher refresh rate than other sensors. This allows for more accurate manoeuvres, as well as for redundancy during anomalies. However, it cannot be used alone due to drift and the need for regular re-calibration with some external reference. Performance that can be expected from each sensor type is introduced in Table 5.6.

The highest possible accuracy is required for the secondary mission, because the satellite needs to determine the orbit of a debris based on a very short fly time. Only star sensors can meet accuracy obtained from Subsection 5.5.1 as can be seen from Table 5.6. Furthermore, the accuracy of star sensor from Table 5.6 is low enough to be used with accuracy of lidar from Section 4.3.

Therefore, it was simply decided to use the star sensor for low-frequency readings and the gyroscope for high-frequency readings. Furthermore, the gyroscope can be used when the star image is blurred, such as during manoeuvres. Two-star sensors and three gyroscopes are required for attitude determination for each axis. It was decided to use an additional three gyroscopes for redundancy.

It was already decided in Section 5.4 to use GNSS receivers for navigation. Therefore, if three more units are added, GNSS could be also used for less accurate attitude determination. This would allow using it in fail-safe mode, as GNSS

receivers are simpler and less power demanding than star sensors. Furthermore, this would add additional redundancy to low-frequency Attitude Determination during the primary mission, which is more important, but does not require as accurate attitude determination as the secondary mission. Regarding the accuracy of attitude determination using GNSS receivers, it depends on the phase difference, which increases with the distance between the GNSS receivers. Therefore, to achieve attitude determination in an accurate manner, the spacecraft needs to have certain size, where at least 1.5 m between the receivers is recommended, referred to as baseline length, which corresponds to a 0.1°measurement accuracy (Speretta, 2020). Based on the volume of the lidar system determined in Subsection 4.3.4, Table 4.3, the spacecraft is expected to exceed this size, and therefore likely to be able to measure its attitude using the GNSS receivers with an accuracy better than 0.1°. It should be noted, however, that once implemented in practice, many potential error sources could prevent attaining such accuracy. For instance, one of the largest error source is the susceptibility to reflections off the spacecraft, which is also referred to as multipath (Markley et al., 2014, p.138). Other potential error sources include ephemeris errors, satellite clock errors, ionospheric errors, tropospheric errors, and receiver errors (Parkinson et al., 1996). Thus, besides the lengths of the baselines, the accuracy of GNSS attitude determination is dictated by the spacecraft geometry and error sources. This will be taken into account in the final design of the spacecraft, by placing the receivers as far apart as possible, thereby maximising the baseline lengths, by isolating them as much as possible from the other antennas, to minimise interference, and by providing a clear view from the receivers, to minimise the errors due to multipath. The high redundancy and accuracy of the chosen sensor package allows to avoid using sun sensors for aiming solar arrays.

Choice of Attitude Determination Hardware

ASTRO XP Autonomous Star Sensor[1] and ASTROgyro[2] by Jena-Optronik GmbH were chosen for star sensors and gyros combination, mainly because they are manufactured by a European company, which is a part of reputable Airbus Group, and have a flight heritage. Furthermore two ASTRO XP sensors can be connected with ASTROgyro, which already includes 2x 3-axis Coriolis Vibratory Gyrscopes (CVGs), to create together a sensor package with the following benefits[3]:

- Availability of both raw and merged data
- Full redundancy (2x star sensors and 6x gyroscopes)
- Outage ability
- Facilitation of Fault Detection Identification and Recovery

The additional GPS units are again PODRIX GNSS Receivers by RUAG. Properties of these items are introduced in Table 5.7.

Table 5.7: Parameters of the chosen Attitude Determination sensor models.

	Mass [kg]	**Dimensions [mm x mm x mm]**	**Power [W]**	**Error**
ASTRO XP Autonomous Star Sensor (2x)	13.8	215x215x601	11	0.5 arcsec
ASTROgyro (6x)	7.8	230x230x170	30	0.005 $°/\sqrt{(h)}$
PODRIX GNSS (4x)	12	280x240x81	60	<0.1 °

5.5.5 Attitude Control

Once the attitude is determined, it also needs to be controlled with the required accuracy by Attitude Control. Furthermore, Attitude Control needs to be able to rotate the spacecraft with required acceleration.

Actuators trade-off

The Design Option Tree of attitude actuators is introduced in Figure 5.8. There are two main choices available - either the laser is fixed and the whole spacecraft rotates with it, or the laser is gimbaled, while the rest of the spacecraft maintains attitude. In the second case, spacecraft can be stabilised actively or passively depending on the gimbal torque. Changes

[1]URL: https://www.jena-optronik.de/products/star-sensors/astro-xp.html [Accessed on 08-06-22]
[2]URL: https://www.jena-optronik.de/products/star-sensors/astrogyro.html [Accessed on 08-06-22]
[3]URL: https://www.jena-optronik.de/products/star-sensors/astrogyro.html [Accessed on 13-06-22]

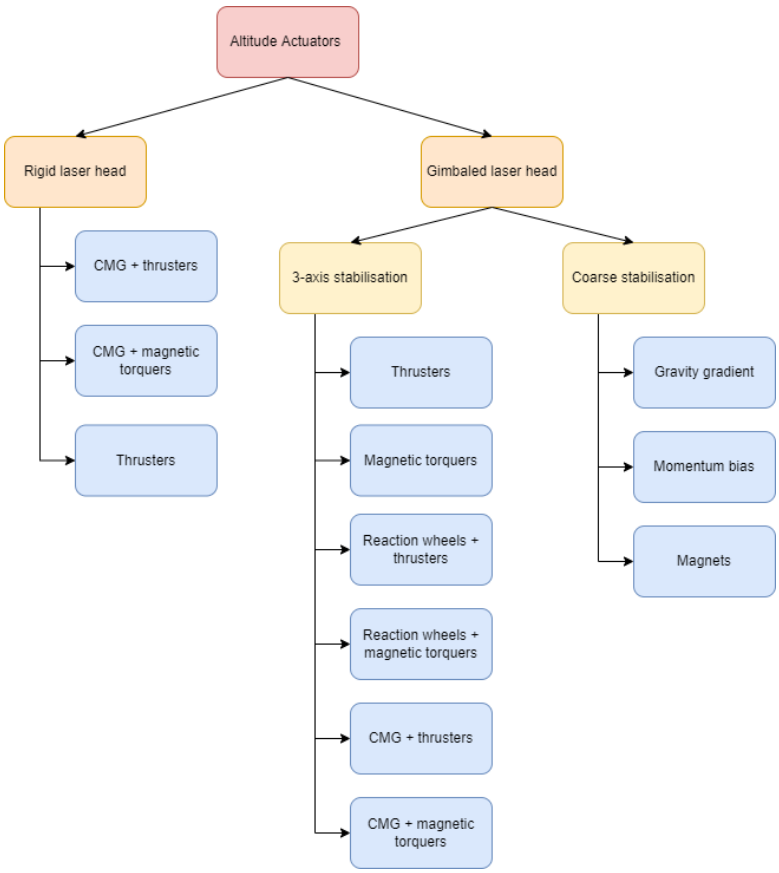

Figure 5.8: Design Option Tree of attitude actuators.

Table 5.8: Typical Attitude Actuators (Starin et al., 2010).

Actuator	**Typical Performance Range**	**Mass [kg]**	**Power [W]**
Thrusters Hot Gas (Hydrazine) Cold Gas	Thrusters produce force; multiply by moment arm for torque 0.5 to 9000 N <5 N	Mass and power vary	
Reaction and Momentum Wheels	Maximum torques: from 0.01 Nm to 1 Nm Practical momentum storage capacity: 0.4 to 3000 Nms	2 to 20	Varies with speed: 10 to 100
Control Moment Gyros (CMGs)	Max. torques: 25 to 500 Nm	>10	90 to 150
Magnetic Torquers	1 to 4000 Am^2	0.4 to 50	0.6 to 16

in internal momentum can be used to change the attitude of the spacecraft, but dumping accumulated momentum is also required. Internal momentum changes can be done either with reaction wheels or Control Moment Gyros (CMGs). External momentum can be dumped through thrusters or magnetic torquers. Thrusters and magnetic torquers can also be used alone, instead of internal momentum changes, to affect the position of the spacecraft. Furthermore, they are necessary for detumbling the spacecraft after launch vehicle, as CMGs are not rotating then yet.

The capabilities of different actuators are introduced in Table 5.8.

By comparing the data from Table 5.8 with required manoeuvring torques from Subsection 5.5.2 it can be noticed that only CMGs and thrusters can achieve required values. However, using thrusters alone would require extremely large amounts of propellant as spacecraft needs to slew constantly to scan the space for the debris. Therefore, CMGs are preferable for primary method of actuation, as they do not use propellant, but also do no require a lot of power.

CMGs can be used in two ways as indicated in Figure 5.8. They can either rotate the whole spacecraft to aim the laser or stabilise it while laser is gimballed. Gimballing the whole spacecraft requires 6 times more torque, and therefore extremely heavy CMGs would be needed. No COTS CMGs with such torque could be found, so gimballed laser head was chosen. CMGs on the spacecraft can still rotate it though during less demanding manoeuvres. The additional benefits of

Table 5.9: Slewing Requirements That Affect Control Actuator Selection (Starin et al., 2010).

Slewing	Effect on spacecraft	Effect on ACDS
None or Time-Unconstrained	Spacecraft constrained to one attitude (highly imrpobable), or reorientations can take many hours.	-Reaction wheel, if planned, can be smaller -If magnetic torquers can dump momentum, reaction control thrusters may be not needed
Low Rates From 0.05 °/s to 0.5 °/s	Minimal	-Depending on spacecraft size, reaction wheels can be fully capable for slews -If reaction wheels not capable, thrusters will be necessary -Thrusters may be needed for other reasons, i.e. stationkeeping
High Rates >0.5 °/s	-Structural impact on appendages -Weight and cost increase	-Control moment gyros or thrusters needed. -If thrusters needed for other reasons, two thrust levels may be needed.

lower slew rates for the main body of the spacecraft are introduced in Table 5.9.

The last remaining option is whether thrusters or magnetic torquers should be used to dump momentum due to external disturbances and to desaturate CMGs. Using thrusters to desaturate CMGs could require significant amount of propellant (Starin et al., 2010). Furthermore, thrusters are a more complex and failure prone system. Consequently, magnetic torquers are chosen. Although they cannot create torque in the direction of magnetic field, the changing magnetic field direction as satellite orbits the Earth allows to store the momentum in CMGs and dump it with magnetic torquers during convenient moment. This effect is called cross-orbit coupling and can be the most efficiently used with 3 torquers in different orientations [4].

Choice of Attitude Control Hardware

The CMGs were chosen to be CMG 75-75S [5] and Newton CMG package [6]. Components from Airbus were again chosen due to their flight heritage of 1000000 hours in orbit without failure. Furthermore, using Newton CMG package allows to conveniently combine all CMGs into a single cluster. This guarantees:

- Avoidance of CMG singularities
- Command with 3D torque commands
- Integration of saturation on the commands

4x 75-75S CMGs were chosen for redundancy. CMGs are assembled in the cluster, which according to Newton CMGs package datasheet results in smaller torque output than the sum of individual CMG torques. Unfortunately, available cluster torques were given only for CMG 15-45S which has the torque of just 15 Nm in comparison to 75 Nm of CMG 75-75S. It was therefore assumed that cluster torque can be simply scaled by the ratio of CMG 75-75S and CMG 15-45S torques, which results in the minimal torque:

$$\boldsymbol{T}_{cluster,\,75-75S} = \boldsymbol{T}_{cluster,\,15-45S}\frac{T_{75-75S}}{T_{15-45S}} \tag{5.18}$$

For the smallest component of $\boldsymbol{T}_{cluster}$ this results in the torque of 64 Nm, thus meeting the required torque established in Subsection 5.5.2. No other CMG found was able to satisfy this condition.

For sizing magnetic torquer, momentum obtained from Eq.(5.15) can be used. This results in graph of required torquer dipole versus altitude Figure 5.9.

One of the companies that produces torquers large enough is Cayuga Astronautics [7]. The company was chosen due to its flight heritage and manufacturing of the torquers more efficient than competition. Series L of their torquers was chosen due to smaller mass and power. It produces torquers large enough to have a dipole moment of $465\,\mathrm{Nm}^2$ as dictated by Figure 5.9. However, the largest torquer was conservatively chosen as magnetic field direction is not always favourable to dump momentum. It is MT-800B-28V [8] had a design dipole moment of $800\ \mathrm{Am}^2$, which can generate torque up to 0.021 Nm to counteract disturbance at the lowest altitudes. To ensure that the moment is able to reach design value, torquer should operate at room temperature and the constant voltage of 28V. According to the simulation described in Chapter 9, the magnetic torquer is at 308 K, thus close to the temperature requirement. EPS can keep voltage constant

[4] URL: https://www.cayugaastro.com/pages/product_pages/MTBs/mtb_choosing.html [Accessed on 14-06-2022]

[5] URL: https://www.airbus.com/sites/g/files/jlcbta136/files/2022-02/AVIONICS-CMG75-75S-v6_2022.pdf[Accessed on 13-06-20222]

[6] URL: https://www.airbus.com/sites/g/files/jlcbta136/files/2022-03/AVIONICS-NEWTON%20CMG%20PACKAGE-v3_2022.pdf[Accessed on 13-06-22]

[7] URL: https://cayugaastro.com/assets/products/MTBs/MTB.pdf[Accessed on 13.06.2022]

[8] URL: https://www.cayugaastro.com/assets/products/MTBs/tables/MTB_table_4.pdf [Accessed on 13.06.2022]

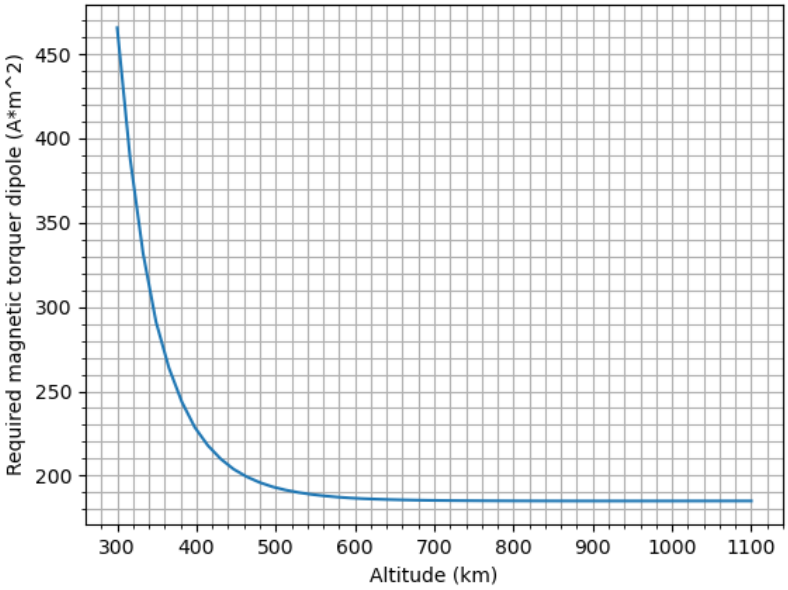

Figure 5.9: The dipole of magnetic torquer as a function of altitude.

with converters as specified in Section 6.4, therefore also specifying voltage requirement. Even if these temperature is higher and the voltage is lower, the minimum guaranteed torque is $771\,\mathrm{Nm}^2$, thus still satisfying the requirement on dipole moment. The magnetic torquer only consumes 4.95 W at 28 V DC due to its large length of 1.7 m. Therefore, no issues from ADCS areas are estimated with EPS.

Table 5.10 summarises the properties of the chosen actuators. Peak power for CMGs was given.

Table 5.10: Chosen actuators parameters.

Actuator	**Mass [kg]**	**Power [W]**	**Size [m]**
4x 75-75S CMGs with NEWTON architecture	284	820	0.78 m x 0.5 m x 0.175 m for 4x CMGs 0.310 m x 0.3 m x 0.15 m for drive electronics 0.23 m x 0.16 m x 0.2 m for processing unit
3x magnetic torquers MTB-800-L-28V	41.19	14.85	Length of 1.7 m; diameter not given

5.6 Filters and Calibration

The functioning of the GNC subsystem is heavily dependent on the accuracy of the state determination, which includes both the position and velocity, and the attitude of the spacecraft. This determination process is corrupted by measurement errors and random noise. Therefore, filters shall be applied to improve the state determination from the sensor measurements. Also, it is crucial that the system is properly calibrated before launched into space.

As explained in Subsection 5.5.4, star trackers and gyroscopes will be used for attitude determination. Gyroscopic measurements are very accurate for high frequencies, but once integrated over time to find the attitude angles, suffer from drift. Star trackers, instead, do not drift over time and provide relatively accurate measurements at low rotation rates, and thus are more suitable for low frequency attitude motion. To find an accurate state estimation from the combined measurements, an Extended Kalman Filter (EKF) is used. This filtering method has widely been used, is relatively simple, and can deal with a great variety of measurements (Crassidis et al., 2007). Other available filtering techniques that can deal with the non-linearities present in the spacecraft's dynamics, are the Unscented Kalman Filter (UKF) and Particle Filter (PF). However, both methods have a higher computational load than the EKF, and show similar measurement accuracy (LaViola, 2003). Thus, an EKF is considered more suitable for this application. Next to using the EKF for accurate attitude determination, the EKF is also used for the position and velocity determination. These are highly coupled and are therefore done by the same EKF. The three inputs from the selected GNSS receivers is used to determine accurate position and velocity estimations, and can also be used to estimate the trajectory of the spacecraft. The filter can fit, using a measurement model that estimates the orbital parameters, the measured positions and velocities to find the trajectory.

The different sensors on board as part of the GNC subsystem shall be calibrated before being launched into space, to minimise constant measurement errors. First, the star trackers are optical sensors that estimate the star vectors, based on images. The geometric defection of such star trackers, the so-called camera parameters, such as the lens alignment inaccuracy and distortion, should be estimated using calibration. On ground, the calibration is usually done in a lab environment. However, due to the nature of the mission, where the system shall be launch ready in a number of days, it is desirable to have a less demanding calibration procedure that can be performed shortly before the launch. Also, to improve accuracy during the mission lifetime, also calibration on orbit shall be performed. Both the on ground and on orbit calibration can be done by analysing the images captured by the star trackers and the star catalogue (Vaz, 2011). The proposed approach minimises the difference between the angular distance of pairs of imaged and catalogued stars. Using this method, the constantly drifting camera parameters can be determined, and the offset can be compensated for. Ground tests have been performed to validate this method. Furthermore, for the gyroscopes, calibration before launch is essential to ensure accurate rate measurements. Again using an EKF, calibration for the gyro's can be performed, where sensor misalignments, which are usually present to at least some extent, are determined and can be accounted for during operational attitude determination. Furthermore, biases and scale factors can be estimated by means of this calibration (Markley et al., 2014, p.235). Also, during operations, the gyro measurements are recalibrated using the star trackers frequently, which means that the drift is compensated for by resetting the gyro measurements using the star tracker measurements every few time steps. For the selected gyroscopes, the ASTROgyro, this happens at a frequency of 10 Hz for an update frequency of 30 Hz.

5.7 GNC Architecture

In the previous sections, all the individual elements of the GNC subsystem are detailed, and specific components are selected. To show how all of these are connected, a high-level overview is provided next. In Figure 5.10, the aforementioned components and the main processes are included.

In this schematic, the control algorithms are not further elaborated, which requires extensive simulation and tuning of control parameters. In general, classical Proportional-Integral-Derivative (PID) is still most commonly used, but it is recommended that more advanced control algorithms are explored as well. PID has the advantage that it is relatively simple and therefore computationally inexpensive. However, employing other methods, such as adaptive control, can provide the spacecraft with higher pointing accuracy and stronger robustness, and is therefore worthwhile to be explored (Xie et al., 2016). Also, the orbit control and attitude control work at different frequencies. Typically, the attitude control operates at an order of magnitude higher frequency compared to the orbit control, due to the fact that attitude changes faster than the orbit, and is therefore controlled on a smaller timescale.

Furthermore, it is reiterated that the GNSS receivers only serve as a redundant system, in terms of attitude determination. Thus, in Figure 5.10, only the position and velocity are determined based on the GNSS receivers. The output from the EKF includes both the position and velocity, which are used to compose the estimated state vector, and the estimated trajectory. These are then combined with the attitude to find the estimated spacecraft state. Additionally, the current states are sent to the database, because they are used to calculate the absolute positions of the space debris, which are used to compute the orbital parameters of the fragments. These can then later be communicated to the TT&C subsystem, via de CDHS.

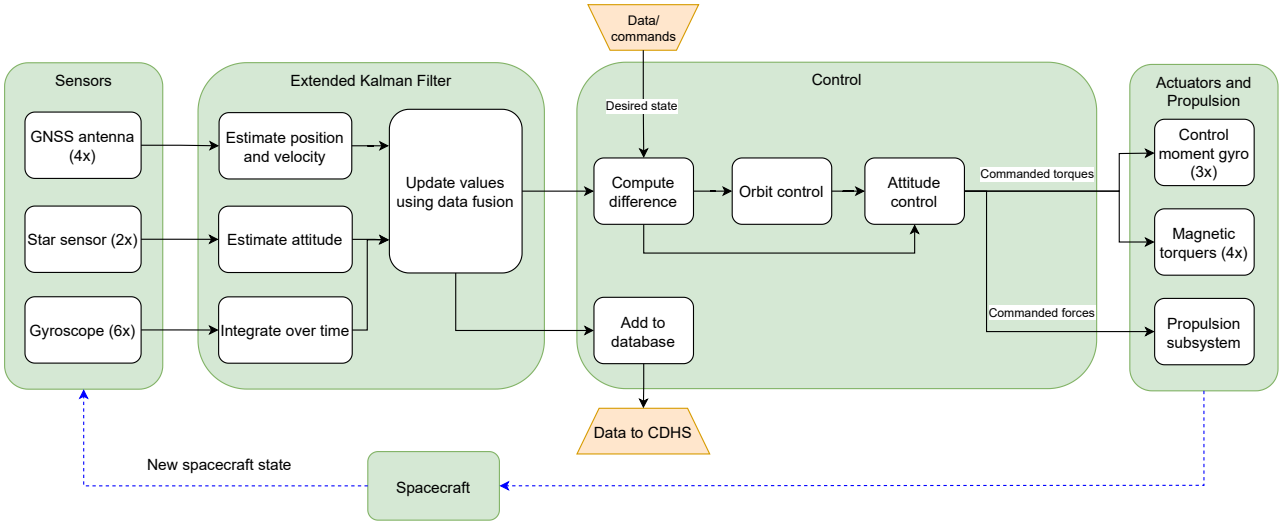

Figure 5.10: High-level GNC subsystem architecture.

Table 5.11: The sensitivity analysis for the output of 'ADCS.py'

		Outputs		
Inputs	**Input percentage change**	Accuracy required	Manoeuvre torque	Disturbance torque
$r_{cp,\,a} - r_{cm}$	+10	+0	+0	+6.03
	-10	-0	-0	-6.03
$r_{cp,\,s} - r_{cm}$	+10	+0	+0	+0.02
	-10	-0	-0	-0.02
Removal and detection range	+10	+11.27	+0	+0
	-10	-9.17	-0	-0
I_{xx}	+10	+0	+0	-4.13
	-10	-0	-0	+4.13
I_{yy}	+10	+0	+0	+0
	-10	-0	-0	-0
I_{zz}	+10	+0	+10	+7.65
	-10	-0	-10	-7.65
Drag area	+10	+0	+0	+6.03
	-10	-0	-0	-6.03
Adsorption area	+10	+0	+0	+0.02
	-10	-0	-0	-0.02
Residual magnetic dipole	+10	+0	+0	+0.43
	-10	-0	-0	-0.43
Field of View	+10	+0	+0	+2.91
	-10	-0	-0	-3.06

5.8 Verification of 'ADCS.py'

'ADCS.py' used for creating figures in Section 5.5 and sizing of ADCS uses analytical formulas and time arrays instead of numerical time propagation, therefore it is easy in verification. The following tests were performed:

1. Walk-through testing: the code was checked line by inspection. Comparison with derived equations was performed. This method of testing was mainly performed during code development, as it is fast but unreliable.
2. Degenerate testing: The degenerate testing was hard to perform due to lack of disturbance torque data on a similar satellite. However, the relative strength of different disturbance torques matches the one presented in (Starin et al., 2010). Furthermore, torques have a value on the order of 0.01 Nm at maximum. It has some face validity, as the torque is small like space disturbances tend to be, but it is on the upper envelope of it, which should also happen due to satellite being large.
3. Analytical testing: A reference case was calculated by hand and compared with the results returned from the tool. These values have been accurate up to 10^{-6}, which is the accuracy of the numerical scheme and time-step used in numerically differentiating the relative motion.
4. Convergence testing: A convergence testing was performed first by changing the numerical scheme used in differentiation from 2nd order to 1st order and the accuracy was confirmed to change to 10^{-3}. The step used in differentiation of 2nd order scheme was then increased twice and the accuracy again changed to 10^{-3} as expected.
5. Extreme value testing: A tool was tested for extreme values of altitude. For altitude equal to 0 km the code throws an expected error due to division by zero. For extremely large values of altitude all disturbances except of solar pressure go to zero as expected in the deep space.
6. Sensitivity testing: A change of 10% was introduced in the input values and the corresponding change in the output was obtained to record the impact of each variable on the sizing of ADCS. The sensitivity analysis was only performed for the final design method, so the part of the code that produced Figure 5.4 used during preliminary sizing was not part of it. The sensitivity analysis was done for the lowest altitude as disturbances torques are the biggest for it. The results are introduced in Table 5.11. Firstly, the results that should not depend on some inputs indeed do not depend on them. Secondly, it can be noticed that for determined sensor accuracy and manoeuvre torque required the output is respectively close and approximately linear around the design point. Therefore, any change in input will have a proportionate impact on the output. The non-linear impact of removal and detection range on sensor accuracy required is to be expected as the result depends on trigonometric functions. The directly proportional impact of the biggest MMOI on the required manoeuvre torque should be directly proportional, which is indeed reflected in the result of this sensitivity analysis. For disturbance torques, there is no input variable to which the output would be overly sensitive, as all changes are limited to below 10%. Therefore, the design point can be considered to be fairly stable. Furthermore, the disturbance torque is proportional to all inputs except of deflection as expected.

5.9 Conclusion

To summarise this chapter, firstly the requirements about GNC are established. The orbit is then determined to be 30 km above the orbit of the space debris. Furthermore, GNNS module with accuracy below 11 cm is chosen for position and velocity requirements. A set of star sensors and gyroscopes with bias error on the order of 0.5 arcsec is chosen as these are the only sensors that meet the requirements on space debris orbit determination for the secondary mission. 75 Nm CMGs are chosen for attitude control to stabilise the spacecraft while laser is gimbaled to ablate the space debris. Furthermore, 800 Am^2 magnetic torquers capable of producing 0.021 Nm of torque are chosen to dump the momentum due to external disturbances. The total mass of GNC is 355.8 kg and the nominal power is 388 W. Finally, a verification and sensitivity analysis of the design is performed to prove its correctness and that it is not overly sensitive.

Electrical Power 6

This chapter aim to explains the procedure to design the Electrical Power Subsystem of Space Sweeper and to outline its components and performance characteristics. The chapter starts with the analysis of the subsystem requirements in Section 6.1, followed by the relevant trade-offs in Section 6.2. Then, the initial estimation for the subsystem characteristics can be found in Section 6.3, and Section 6.4 explains the component selection and the final sizing. Section 6.5 displays the spacecraft's electrical block diagram, ending the chapter with a conclusion in Section 6.6.

6.1 Subsystem Requirements

As for the rest of the subsystems, the first step is to analyse the requirements that will drive the design. Specifically for the Electrical Power System (EPS), these requirements come from the allocated budgets by the systems engineering department and the payload performance for the average and peak powers. It is believed that the peak power will occur during nominal operation, since, as seen in Chapter 4, operating the shooting laser will require a power larger than 20 kW, considerably more power than the estimated power for de-tumbling, orbit reinsertion, or EoL de-orbiting.

To obtain the average payload power required during nominal operation, the payload power should be divided into searching power (P_{search}, the power used by the lidar), which is assumed to be working at all times, and the shooting power (P_{shoot}, the power used by the laser), which is required a total of n_{tot} times per day, during the shooting time. The shooting time, t_{shoot}, equals 50 s, as stated in Chapter 4. using the debris removal simulation from Section 3.6, n_{tot} equals 320 during the first days of the mission (the worst case). Thus, the average power equals:

$$P_{av} = \frac{P_{search} \cdot 24 \cdot 3600 + n_{tot} P_{shoot} t_{shoot}}{24 \cdot 3600} \tag{6.1}$$

From this value, using the relationship from Wertz, Everett, et al. (2011), the total power of the spacecraft can be preliminarily estimated using Equation (6.2), to which then the margins and contingencies are added to make the power budget. This value will be updated once the specific components for each subsystem are chosen and their power consumption is known. Lastly, the peak power can be obtained just by adding together the bus power (Equation (6.3)), the searching power, and the shooting power.

$$P_{sc} = 1.85 P_{av} \pm 35\% \tag{6.2}$$

$$P_{bus} = P_{sc} - P_{av} \tag{6.3}$$

Table 6.1 shows the required power of the laser for different three different altitudes. This information allows for a modular design with varying payloads. This chapter will assess the possibility of making the EPS subsystem modular as well.

Having estimated the average and peak powers of the system, Table 6.2 displays the preliminary requirements used for the initial detailing of the subsystem. Throughout the design, new and more specific requirements will be found from other subsystems, and requirements will arise from the EPS towards the manufacturer and the future project design stages.

6.2 Subsystem Options and Trade-off

Starting with the Design Option Tree (DOT) for the EPS, all relevant decisions will be performed in this section. The chosen trade-offs are: power generation, energy storage, power distribution, bus voltage level, and the solar array structure.

6.2.1 Design Option Tree

To choose an appropriate architecture of the subsystem to fulfil the aforementioned requirements, an extensive Design Option Tree (DOT) has been generated and is displayed in Figure 6.1. It shows numerous available options to generate, store, and regulate the spacecraft's power.

Several of the solutions for energy storage have already been discarded from the trade-off due to their clear unfeasibility and unsuitability. Namely, generative fuel cells cannot be used because they are still in development (with very low TRL), and their efficiencies do not surpass 60% (Wang et al., 2016). Moreover, flywheels are unfeasible due to the torques induced when charging them (by making them spin), that will de-stabilise the spacecraft. Specifically, the amount of energy required to maintain the spacecraft's attitude parameters constant would be the same amount of energy that is stored, due to the conservation of angular momentum, thus not actually storing any energy. Then, hydraulic accumulators are not considered because, even though their power densities are higher than supercapacitors, they show energy densities

Table 6.1: Shooting laser power requirements for several altitudes.

Altitude [km]	Power Required [kW]
500	8.2
750	17.6
1000	27.4

Table 6.2: EPS initial requirements.

Requirement ID	Description	Rationale
SS-SYS-EPS-REQ-001	The EPS subsystem shall provide an average power of 12.5 kW during nominal operation.	Estimated worst case power from subsystems and payload lidar searching at a height of 1000 km.
SS-SYS-EPS-REQ-002	The EPS subsystem shall provide a peak power of 34 kW.	Estimated worst case power from subsystems and payload lidar searching at a height of 1000 km.
SS-SYS-EPS-REQ-003	The EPS subsystem shall ensure that each component receives the appropriate power, current, and voltage levels.	For effective component performance.
SS-SYS-EPS-REQ-004	The mass of the EPS subsystem shall not exceed 600 kg, with a target value of 417 kg.	Allocated mass budget.
SS-SYS-EPS-REQ-005	The power of the EPS subsystem shall not exceed 1 kW at EoL, with a target value of 0.74 kW.	Allocated power budget

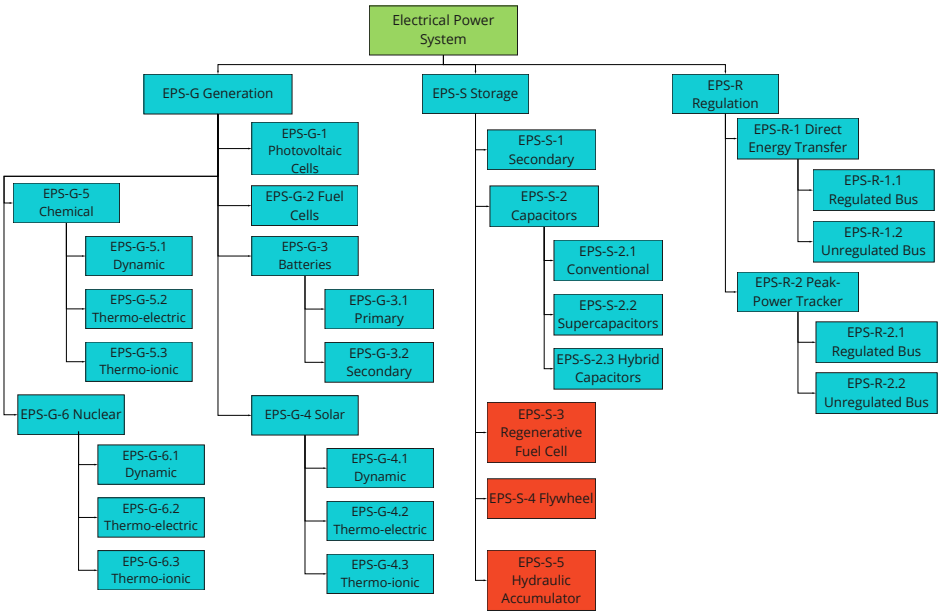

Figure 6.1: Design Option Tree for the EPS subsystem. Note that the crossed out concepts do not enter the trade-off.

three orders of magnitude lower than batteries (Leon-Quiroga et al., 2020), and even one order of magnitude lower than supercapacitors, making them unfeasible for the mission due to its long eclipse times (up to 40 minutes) and the required shooting energy ($P_{shoot}t_{shoot} \approx 300$ Wh).

6.2.2 Energy Source Trade-off

Starting with the energy storage, to find the best option, one can make use of past missions data and check what kind of energetic solution they used. For each of those missions, an extensive trade-off on the EPS was performed to find the most appropriate solution, of which we can take advantage. In addition, the capabilities of newer technologies should also be included. This information is all collected in Figure 6.2 (Wertz, Everett, et al., 2011), from which, depending on

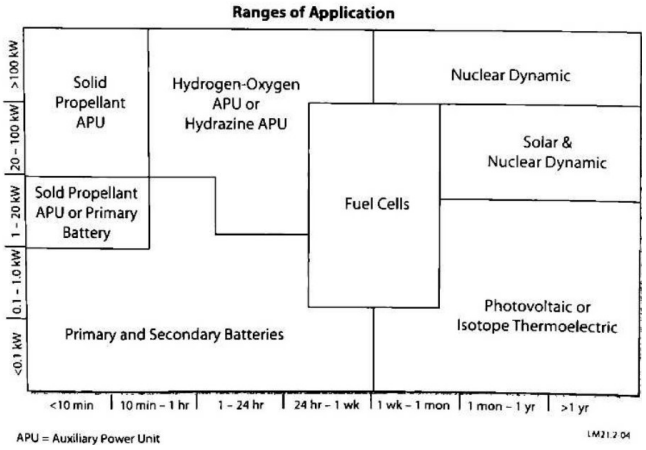

Figure 6.2: Ranges of application of various power generating technologies (Wertz, Everett, et al., 2011, p.648).

Table 6.3: Trade-off between power generation options.

	Specific power (High)	**Sustainability (High)**	**Cost (Moderate)**	**Heritage (Moderate)**
Photovoltaic Cells	H	H	L	H
RTG	L	L	H	H
Solar Thermal Dynamic	L	H	L	L
Nuclear Dynamic	M	L	H	M

the required average power of the system and the mission duration, one can obtain the feasible power generation options. Having a lifetime of at least 1 year, according to Requirement SS-TL-STK-US-REQ-MI-002, all technologies based on fuel cells, chemical reactions, or batteries can be disregarded. Then, from Requirement SS-SYS-EPS-REQ-001, it is evident from the figure that photovoltaic and RTG are the most suitable options. Nevertheless, the power requirement, even though it is for the worst case scenario, is very close to the threshold between these two and solar and nuclear dynamic, thus, they are worth considering.

The chosen four criteria to evaluate the solutions are: specific power, with a high importance due to the high estimated mass of the spacecraft, sustainability, also with a high importance due to Requirement SS-TL-STK-US-REQ-STB-001, cost, with moderate importance since it is not as limiting as the previous two, and heritage. Heritage has moderate importance as well, since it plays a big role in the reliability of the system, but it can still be increased by extensive testing in later stages of the project. Manoeuvrability is not part of the trade-off, since the system does not need to manoeuvre too much during nominal operation(as explained in Chapter 5). In addition, durability is not an issue due to the short duration of the mission.

Using the table provided by Wertz, Everett, et al. (2011, p.659), it can be seen that the specific power of the photovoltaic cells can reach an order of magnitude greater than the rest, being nuclear dynamic the best of the remaining three. From the same table, it can be concluded that a solar array is also the best option costwise (800-3,000 $/W vs. 400k - 700k $/W for nuclear dynamic). Regarding sustainability, it is evident that RTG and nuclear dynamic do not comply with Requirement SS-TL-STK-US-REQ-STB-001 because of the plutonium/uranium isotopes being used. Lastly, the heritage is highest for the solar panels and the RTG, only around 30 spacecraft used nuclear dynamic generators [1], and the TRL of solar dynamic systems is still between six and seven (Jaffe et al., 2019).

From Table 6.3, it is evident that a solar array is the best solution, since it is better than the rest in every aspect. The only way another source of power would be considered is if the power required is at least doubled, and even then, according to the aforementioned table from Wertz, Everett, et al. (2011, p.659), it would still be possible to use solar panels. Nevertheless, considering that Requirement SS-SYS-EPS-REQ-001 is the worst case scenario for the average power, going as low as 6.4 kW, is definitely the cheapest, most reliable, lightest, and most sustainable option, followed by solar dynamic. As a plus, using solar array as a power will allow the EPS subsystem to be modular since, depending on the collision orbit, more or less array area will need to be sent with the system, since at higher altitudes the power required by the laser is considerably higher (recall Table 6.1).

6.2.3 Energy Storage Trade-off

Following the same procedure as for the energy generation trade-off, Figure 6.3 (NASA, 2021) displays the energy and power densities of the available energy storage technologies. From these two parameters, the range of application, reflected in the figure by the discharge time, can be computed (dividing one by the other). To power the bus, the best option

[1] URL https://world-nuclear.org/information-library/non-power-nuclear-applications/transport/nuclear-reactors-for-space.aspx [Accessed 09-06-2022]

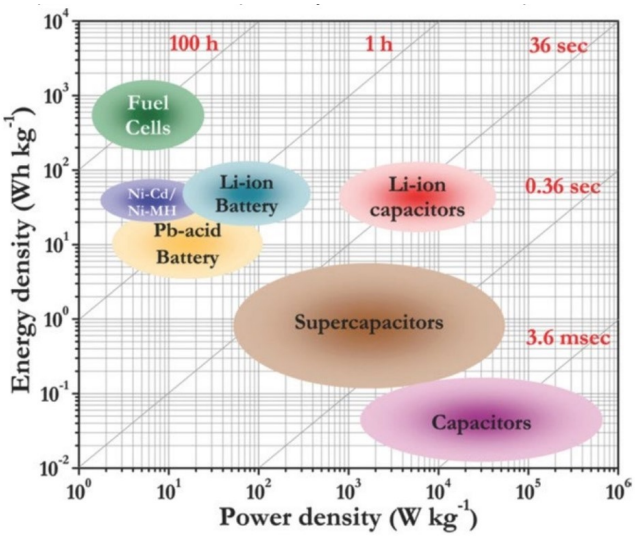

Figure 6.3: Energy density to power density comparison for various power storage technologies (NASA, 2021, p.40).

is to use secondary (rechargeable) batteries, since the eclipse time in LEO can go up to 40 min (Zandbergen, 2021). No trade-off is required to choose the battery type other than choosing the best (the one with the largest energy and power densities), which is Lithium-Ion (Li-Ion).

On the other hand, as seen in Table 6.1, a power of 27 kW is required during 50 s to shoot effectively. Achieving these power values with conventional batteries would not be ideal, since, from Figure 6.3, one would need roughly 120 kg of batteries due to the slow discharge times, and a lot of storage capacity would be wasted since the shots only last 50 s. Thus, for powering the lasers the best solution is to use hybrid capacitors (Li-Ion capacitors), which combine the technology of Li-Ion batteries with capacitors. Although they are not as available in the market as batteries or supercapacitors, and they are slightly more expensive, they are by far the best option for this application. Only if the shooting time was decreased to the order of seconds, the use of supercapacitors for this purpose would be considered. Nevertheless, these shooting times would be unfeasible for the mission as described in Chapter 4.

Furthermore, by separating the bus and lidar power from the laser power in batteries and hybrid capacitors, respectively, the idea of modularity in the EPS subsystem can be further extended. Not only can the solar array area change with the laser, but also the capacitors to power it, without changing the battery mass or structure. Having thus a laser-capacitors module that can be changed depending on the mission.

6.2.4 Bus Regulation Trade-off

Since solar panels were chosen in the first trade-off, with a power output dependent on the load, the power output will change over time depending on the voltage of the batteries, being at its lowest right after eclipse, when the batteries are empty (Wertz, Everett, et al., 2011). Thus, before choosing the level of regulation in the bus, a solution for this issue should be found.

In spacecraft, two types of Solar Array Regulators (SAR) are used: Peak Power Trackers (PPT) and Direct Energy Transfer (DET) using Sequential Switching Shunt Regulators (S3R). As described in ESA (2021), the latter, even though more efficient, less complex, and lighter, cannot ensure that the maximum power is extracted from the solar panels at all times, and the power output is difficult to estimate, having to be compensated with extra solar array area. Since the payload power availability is critical for this mission (the shooting windows are narrow) and the solar array area is bound to be very large due to Requirement SS-SYS-EPS-REQ-001, performance prevails over any other criterion, making the use of PPTs the best solution. Moreover, basing the design of the power switches on GaN switches instead of the classic Silicon Power Mosfets, mass, volume, and efficiency can be improved, reducing the disadvantages with respect to S3R (ESA, 2021).

On the other hand, the level of regulation of the bus should be determined. Following the approach from ESA (2021), a fully regulated bus includes Battery Charge Regulators (BCRs) and Battery Discharge Regulators (BDRs), standardised voltage levels, current limiters, and better Electromagnetic Cleanliness Control (EMC). Due to the high power requirements and the long eclipse times because of the LEO orbits at which the system operates, a large amount of batteries can be expected, for which BCRs are very convenient to ensure correct charging of the batteries. Leaving the charging of so many batteries unregulated will decrease their lifetime, dissipating valuable power into heat and not fully charging them. Furthermore, since the hybrid capacitors and the batteries are charged and discharged separately, at different voltages, and at different rates, the use of BCRs and BDRs is a must to ensure that no power is dissipated and that the capacitors are charged and ready to shoot in the allocated recharging time from Chapter 5. As a plus, the current limiters, the standardised voltage levels, and the improved EMC will add reliability and efficiency to the system. Thus, from the aforementioned reasons, a fully regulated bus needs to be chosen for the mission to be successful, even though the mass, volume, cost, and complexity of the Power Conditioning and Distribution Unit (PCDU) will increase.

Table 6.4: Trade-off between different bus voltage levels.

	Reliability (High)	**Efficiency (Moderate)**	**Component Availability (Moderate)**	**Heritage (Moderate)**
100V	L	H	L	L
50V	M	M	L	L
28V	H	L	H	H

6.2.5 Bus Voltage Level Trade-Off

Large spacecraft use bus voltage levels of 28V, 50V, and 100V, being the 28V the most common, for which most spacecraft components are designed (ESA, 2021). The disadvantage is the power dissipation through the distribution unit, since, for the same amount of power, the current intensity would be larger. Nevertheless, since the great majority of the subsystem components will require somewhere near 28V, numerous buck converters with high voltage ratios will be needed to adapt the voltage levels, which decreases efficiency and adds complexity, provided a bus 50V or 100V is chosen. If 28V are selected instead, it is safe to assume that only a few boost converters may be needed (for the payload and the ADCS actuators, mainly).

In addition, the safety of the system may be threatened by a higher voltage, since, due to the fact that the payload generates a small amount of data (Chapter 8), the OBC components will be rather small, requiring very low voltage levels (as it is becoming more and more common in the industry (Wertz, Everett, et al., 2011)), being very sensitive to voltage spikes that are more severe the higher the voltage. This can be solved by adding remote sensing to the boost-buck converters, which adds complexity and reduces reliability.

From the above explanation, Table 6.4 can be generated, in which reliability has the highest weight due to the fact that this mission will be carried out during space emergencies. Thus, from the table, it is safe to conclude that 28V is the best option for the bus voltage. This decision may change if during design it is found that many components require high voltages.

6.2.6 Solar Array Structure Trade-Off

Solar array structures are usually either rigid or flexible. The solar array, due to the high power requirements, will not be mounted in the body. In addition, to ensure that the sun-rays are always perpendicular to the panels' surface, two degrees of freedom must be added to the panels via Solar Array Drive Actuators (SADAs), for which rigidity is desired to avoid oscillations in the structure. Due to these reasons, the use of a flexible solar array is not feasible. However, rigid solar panels are much heavier than their flexible counterparts, which will influence the mass of the spacecraft significantly.

Airbus (Zimmermann et al., 2017) offers a suitable solution to find a middle ground between rigidity and solar array weight. By using a semi-rigid solar array configuration, the power density of the structure will increase from the usual 65 W/kg to 95 W/kg. Since it uses a combination of rigid panels for the core structure, surrounded by semi-rigid panels, rigidity during actuation can be ensured (although extensive testing should be performed during future development phases).

These panels were implemented in the Eurostar Neo, which was scheduled to launch in 2021, proving the high TRL of the system. By the time the *Space Sweeper* mission starts, in 2028, the power density of these structures is predicted to increase to 146 W/kg, which will further decrease the weight of the structure, if implemented.

6.3 Initial Sizing

Now that the general architecture of the subsystem has been fully defined, the solar array, the batteries, the hybrid capacitors, and the PCDU can be sized. From this, the initial subsystem mass can be estimated. For the sake of modularity, this analysis was done at altitudes of 500 km, 750 km, and 1000 km. Since the payload power varies per altitude (Table 6.1), and it was used to estimate P_{bus}, the bus power in the worst case (1000 km) is considered for all of them due to the fact that the bus components will not change with altitude, and they are sized for the worst scenario.

6.3.1 Solar Array Sizing

Starting with the solar array, the power that needs to be generated at all times during sunlight can be estimated via the following equation, where n_e is the number of times the system is designed to shoot during eclipse, n_{orb} the number of times it shoots per orbit, t_e is the eclipse time per orbit, and t_d the sunlight time per orbit. η_d is the power transmission efficiency from the solar array to the spacecraft bus, whereas η_e is the one from the solar array to the batteries and then to the bus. Using the estimations from Wertz, Everett, et al. (2011, p.643), and having decided to use a PPT to regulate the power generation, the values of η_d and η_e are 0.8 and 0.6, respectively. Since the power transmission is more efficient during the day, the ideal case would be to only shoot once during eclipse, also lowering the required storage capacity of the hybrid capacitors. Nevertheless, this will increase the number of shots during sunlight (in order to complete the mission), which may be constraint by the thermal subsystem, and n_e may thus change in the next iteration.

$$P_{SA} = \frac{\frac{(P_{bus}+P_{search})t_e+n_e P_{shoot}T_{shoot}}{\eta_e} + \frac{(P_{bus}+P_{search})t_d+(n_{orb}-n_e)P_{shoot}t_{shoot}}{\eta_d}}{t_d} \tag{6.4}$$

For the eclipse time, the worst case scenario was considered, in which the orbital plane is parallel to the Earth's orbital plane around the Sun. Following the procedure in Sumanth (2019), which is valid for low altitudes, Equation (6.5) computes the fraction of the orbit in which the spacecraft is in eclipse, where h_{sc} is the height at which the spacecraft is flying, R_e is the average radius of the Earth (6371 km), β is the angle between the Sun and the spacecraft's orbital plane (0°for the case considered), and a is the semi-major axis. To obtain the eclipse time, this fraction is multiplied by the orbital period (Equation (6.6)), in which μ_E is the gravitational parameter of the Earth, with a value of $3.98600{\cdot}10^{14}$ m^3/s^2).

$$f_e = \frac{1}{\pi}\cos^{-1}\frac{\sqrt{h^2+2R_E h}}{a\cos\beta} \tag{6.5}$$

$$T = 2\pi\sqrt{\frac{a^3}{\mu_E}} \tag{6.6}$$

Having computed the required power to be delivered, it is the next step to compute the power that can be generated by the solar array per m^2. Being η_{sp} the solar cell efficiency, Φ_{Sun} the solar constant (1353 W/m^2), and I_d the inherent degradation factor of the solar array, the power generated by the array at BoL is shown in Equation 6.7. The EoL performance can be estimated via the Equation 6.8. D_{sp} is the percentage of degradation of the cells per year, and $t_{mission}$ is the mission duration in years (1 year).

$$P_{BOL} = \eta_{sp}\Phi_{Sun}I_d. \tag{6.7}$$

$$P_{EoL} = P_{BoL}e^{-Dt_{mission}} \tag{6.8}$$

For the estimation being carried out, initial estimating values for the parameters can be taken from Wertz, Everett, et al. (2011). Namely, η_{sp} equals 0.3, I_d is 0.72, and D is roughly 0.5% for triple junction solar cells. All these values will be updated once the specific components are chosen. After this, the solar array area can be computed simply by using Equation (6.9).

Lastly, the total mass of the array is obtained, as shown in Equation 6.10, by dividing the power that the solar array needs to generate at BoL to meet the power requirement at EoL by the power density of the solar array. Since the semi-rigid structure was chosen, as explained in Section 6.2, it is safe to assume a $P_{\rho_{SA}}$ of 95 W/kg.

$$A_{SA} = \frac{P_{SA}}{P_{EOL}} \tag{6.9}$$

$$M_{SA} = \frac{(1+e^{-D_{sp}t_{mission}})P_{SA}}{P_{\rho_{SA}}} \tag{6.10}$$

6.3.2 Capacitor and Battery Sizing and Subsystem Mass

Since the Li-Ion capacitors will only charge the shooting laser, the required storage capacity is simply the energy per ablating shot times the number of times the system is meant to shoot during eclipse (one time, for now). In addition, the required capacitance is described by Equation (6.12), where V is the bus voltage, with a value of 28 V (as chosen in Section 6.2).

$$E_{cap} = n_e P_{shoot} t_{shoot} \tag{6.11}$$

$$C = \frac{2E_{cap}}{V^2} \tag{6.12}$$

Then, the energy storage required for the batteries would follow Equation (6.13), where η_{bat} is the efficiency of the battery, taken as 0.9 (Wertz, Everett, et al., 2011, p.653), and DOD is the allowed depth of discharge of the battery, which is usually 0.6 for short missions (Wertz, Everett, et al., 2011). A too high depth of discharge may degrade the battery too fast. Then, for both batteries and capacitors, the mass is obtained by dividing the storage capacity by the energy density of the component. As an initial estimate, this density is 0.1 kWh/kg for Li-Ion capacitors (NASA, 2021) and 0.22 kWh/kg for the Li-Ion batteries (ESA, 2021).

$$E_{bat} = \frac{(P_{bus}+P_{search})}{\eta_{bat}DOD} \tag{6.13}$$

$$M_{bat/cap} = \frac{E_{bat/cap}}{E_{\rho_{bat/cap}}} \tag{6.14}$$

To conclude the analysis, the estimated total EPS mass, accounting for the PCDU through a relationship from Zandbergen (2021), would be:

$$M_{EPS} = 1.3(M_{SA}+M_{cap}+M_{bat}) \tag{6.15}$$

6.3.3 Initial Values

Following the described analysis, with the specified preliminary parameters, the lower and upper values for the EPS subsystem are shown for three different altitudes in Table 6.5. These values will be iterated when the power usage of all subsystems is defined and the specific components for the EPS are chosen (Section 6.4).

Table 6.5: EPS range of values for three different orbital altitudes.

	Solar Array Area [m^2]	**Solar Array Mass [kg]**	**Battery Energy [kWh]**	**Battery Mass [kg]**	**Capacitor Capacitance [F]**	**Capacitor Mass [kg]**	**Total EPS Mass [kg]**
500km	21 - 74	64 - 228	1.5 - 9	6.6 - 41	1050	1.2	93 - 307
750 km	32 - 83	98 - 254	1.4 - 8.9	6.5 - 40	2250	2.5	138 - 342
1000 km	42 - 91	130 - 280	1.4 - 8.8	6.5 - 40	3870	4.2	183 - 380

Table 6.6: Subsystem power overview.

	Payload	TT&C	EPS	GNC	CDHS	Thermal	Structures & Mechanisms	Propulsion
Power [W]	5300	3.1	100	880	25.64	23.5	500	72

6.4 Component Selection and Final Sizing

Using the final power estimations from each subsystem displayed in Table 6.6, the previous analysis can be redone to obtain the final values for the EPS. It can be seen from the table that the spacecraft power is well within the budget, so the values from Table 6.5 will tend towards the lower bound. In addition, since the first iteration, the value of 320 particles to be ablated per day during the first day of the mission was decreased to 243, from the simulation from Section 3.6, drastically decreasing the power required. Note that the powers required for ablation at different altitudes did not change.The EPS power is low since for most components the power usage is taken as an efficiency of the component, already taken into account in the sizing. Moreover, the fact that the required powers are this low supports the decision made for a bus voltage of 28V.

6.4.1 Solar Cells

For the solar cells, no trade-off is required, the best available in the market should be chosen, which, according to ESA (2021), the QJ Solar Cell 4G32C - Advanced [2] from AzurSpace is the most promising. It has an AM0 efficiency of 31.8 %, an area of 40x80 mm^2, and a maximum power voltage of 3.025 V. Due to the cells usually being at 65°C at LEO (Wertz, Everett, et al., 2011), the voltage gets reduced to 2.681 V, and the power decreases by a factor of 0.88, being thus the new inherent degradation factor (I_d) 0.756.

6.4.2 Batteries

Following the same procedure as for the solar cells, the best option is the VL10-ES from SAFT (ESA, 2021). They have a voltage of 4 V, a capacity of 12 Ah, an energy storage of 47 Wh, a mass of 213 g, and a volume of $8.81 \cdot 10^{-5}$ m^3.

6.4.3 Hybrid Capacitors

Regarding the hybrid capacitors, firstly capacitors with high power and energy densities were chosen, but, when analysing the performance of the configuration, it was seen that the required currents would catastrophically damage the capacitors, so the required amount of capacitors in parallel would need to be tripled. Due to the low availability of hybrid capacitors, larger capacitors which can withstand the high currents with worse energy power and energy densities were chosen. Since the required capacitance is low, this added mass and volume should not dramatically affect the design. The chosen hybrid capacitor is the LIC Cell 3300F Prismatic [3], with a capacitance of 3300F, a voltage of 3.8 V, a mass of 350 g, and a volume of $2.21 \cdot 10^{-3}$ m^3. When sizing the capacitors, the lowering in capacitance due to having capacitors in series was taken into account.

6.4.4 PCDU

When choosing the PCDU, it was found that there are no off-the-shelf units capable of handling the 27 kW required for shooting the laser. Thus, it was decided to choose an available PCDU for the 4.03 kW required to power the spacecraft bus and the lidar, to which a pseudo-independent one (still connected to the solar array) would be added just for the capacitors and the laser. This added component would need to be designed specifically for this mission. This is, of course, one of the possible solutions, another one would be to fully design the PCDU from the ground up. Nevertheless, for the purpose of sizing the spacecraft and have an initial design available, the first solution is selected, although it will be further investigated in future iterations.

The chosen PCDU is the Airbus EVO PCDU [4], which is scalable, has the option of a fully regulated bus of 28 V and of using PPTs, and has an efficiency of 95%. Regarding the weight, similar sized PCDUs weigh around 22 kg [5], to which a factor of 3 is added for the component in charge of the laser and capacitors, leading to an estimated mass of 70 kg.

6.4.5 Final Sizing

With these new specifications for the components, the final values for the EPS can be obtained. These are displayed in Table 6.7, entailing a significant reduction in the initial EPS size. As discussed before, the solar array and capacitor values are given for three different altitudes: 500 km, 750 km, and 1000 km, implementing modularity in the design.

As a sensitivity analysis for the solar array area (the most critical for the rest of subsystems), both the laser power and the shooting cooldown time were varied 10% to see the effect. For the former, the area ranged between 32.4 m^2 and 37.2 m^2. For the latter, it ranged between 32.7 m^2 and 37.1 m^2. This proves the robustness of the decision of choosing solar panels.

[2] URL: https://satsearch.co/products/azur-space-qj-solar-cell-4g32c-advanced [Accessed 15-06-2022]
[3] URL: https://www.electrostandards.com/esl703301-lic-cell-3300f-prismatic-jsr-cpp3300s-2273.html [Accessed 15-06-2022
[4] URL: https://satsearch.co/products/airbus-defence-and-space-evo-pcdu [Accessed 15-06-2022]
[5] URL: https://satsearch.co/products/airbus-defence-and-space-high-power-pcdu Accessed: 15-06-2022]

Table 6.7: Final EPS sizing for three different altitudes. *Not relevant for the analysis.

	Power [kW]	Energy [kWh]	Cells in series [-]	Cells in parallel [-]	Area [m^2]	Mass [kg]	Volume [m^3]
Solar Array	6.61-8.92-9.54	-	11	490-662-832	20.4-27-35	70-94-119	-
Batteries	-*	2.07	7	7	-	10.5	$4.32 \cdot 10^{-3}$
Capacitors	-	0.12-0.25-0.42	8	3-6-10	-	8.4-16.8-28	$5.3 \cdot 10^{-3}$-0.011-0.018

6.5 Electrical Block Diagram

To conclude the subsystem design, the electrical block diagram is displayed in Figure 6.4. It includes all electrical components used in the spacecraft, flowing from the energy supply (blue), through the PCDU (red), to every subsystem (green).

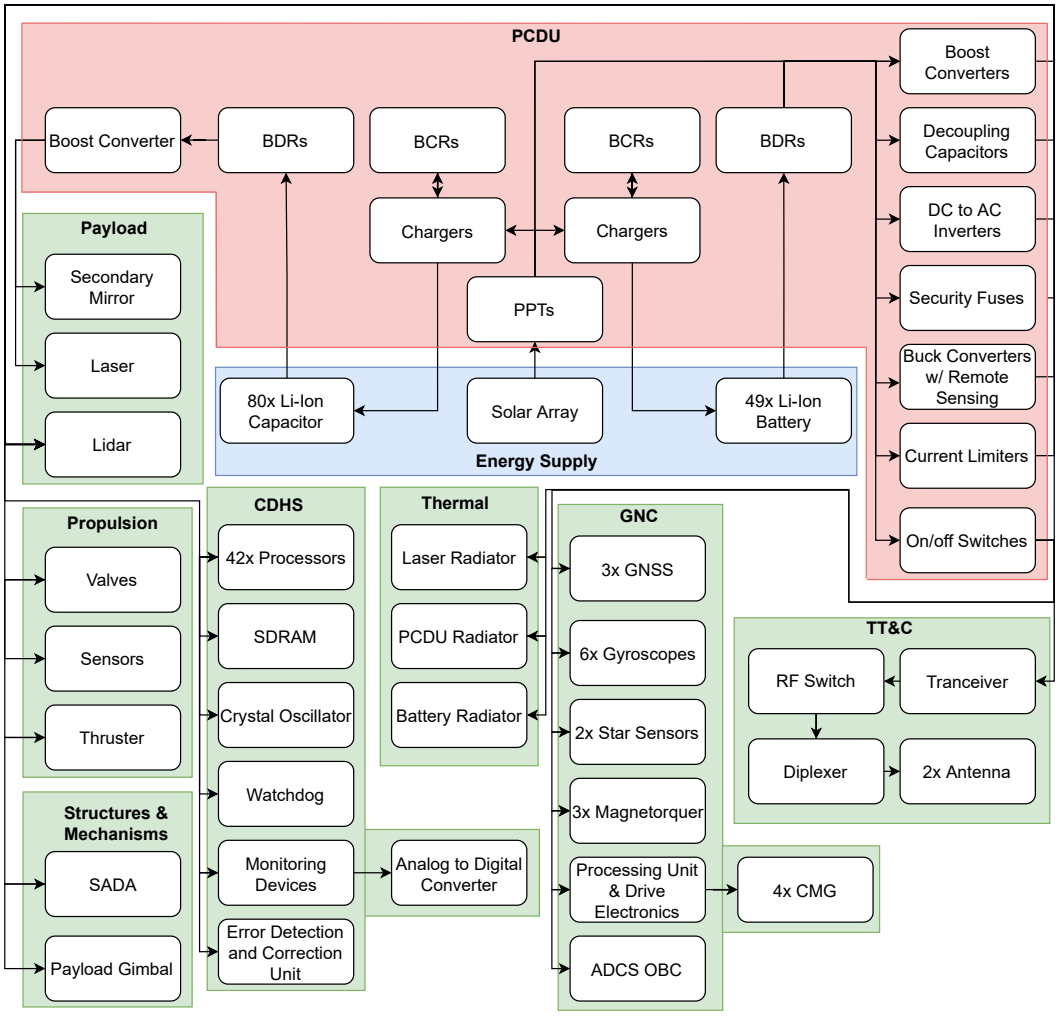

Figure 6.4: Electrical Block Diagram of the spacecraft.

6.6 Conclusion

These calculations lead to a total EPS mass ranging from 100 kg to 166 kg, depending on the altitude, thus staying well within budget (Requirement SS-SYS-EPS-REQ-004). The biggest point of concern in this subsystem is the design of the PCDU to withstand the very high loads, other than that, this optimised design (after multiple iterations) is believed to be able to fulfil the requirements. All equations used are adaptations of the ones provided in Wertz, Everett, et al. (2011). This book offers an extensive overview of how to design a spacecraft, validating the procedure with numerous missions. The results obtained in the equations were thus compared with these missions to identify any possible mistakes. It is also assumed that these equations apply perfectly to the EPS of this mission, since the power subsystem has a conventional architecture, widely used in the industry.

7 Propulsion

The propulsion subsystem will be designed in detail in the following chapter. Starting at a very top level, Section 7.1 explains the procedure undergone to arrive at the final concept to be designed in detail, as seen in Section 7.2. Note that the possible propulsion required for attitude control is treated in Chapter 5.

Table 7.1: Propulsion Subsystem Requirements.

Requirement ID	Description
SS-SYS-PROP-REQ-01	The mass of the Propulsion subsystem shall not exceed 86 kg
SS-SYS-PROP-REQ-02	The power used by the Propulsion subsystem shall not exceed 126 W during nominal operation
SS-SYS-PROP-REQ-03	The power used by the Propulsion subsystem shall not exceed 126 W during non-nominal operations
SS-SYS-PROP-REQ-04	The Propulsion subsystem shall be operational between 0 K and 55 K
SS-SYS-PROP-REQ-05	The Propulsion subsystem shall provide a ΔV of 249 m/s
SS-SYS-PROP-REQ-06	The Propulsion subsystem shall provide thrust pulses lasting a minimum of 0.53 s
SS-SYS-PROP-REQ-07	The Propulsion subsystem shall be able to perform 5720 manoeuvres
SS-SYS-PROP-REQ-08	The Propulsion subsystem shall be able to accelerate the spacecraft by a minimum of 0.037 m/s^2 for 0.53 s
SS-SYS-PROP-REQ-09	The Propulsion subsystem shall not use toxic or radioactive propellants.

7.1 Top-Level Concept Selection

As a first step for the selection procedure of the propulsion subsystem design, a design options tree (DOT) was generated, aiming to arrive at the highest possible number of possible options. This OR tree differentiates between cold gas, chemical, nuclear, electric and advanced propulsion methods at its top level. These main branches are then expanded to yield a plethora of design options to be analysed.

7.1.1 Elimination of Non-concepts and Unfeasible Concepts

The next step in this design process was the elimination of both the non-concepts and the unfeasible concepts, where the former refers to concepts that, for example, violate the laws of physics or do not yet exist, and the latter refers to concepts which exist, but are not considered useful regarding the specific mission objectives. This aims to decrease the total amount of designs to be further considered for the final trade-off procedure.

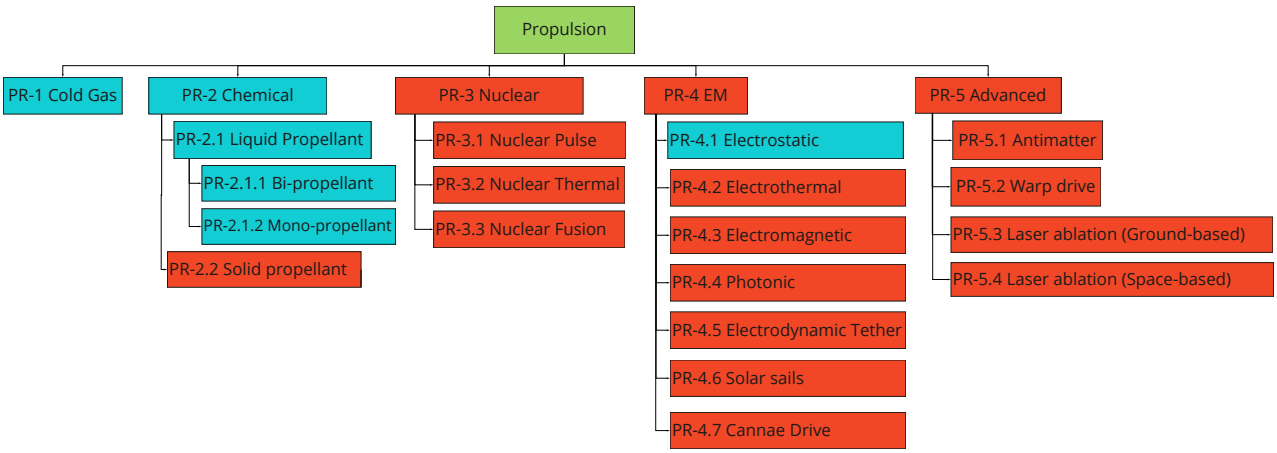

Figure 7.1: Propulsion subsystem DOT. Note that red cells indicate the concepts which are deemed unfeasible.

Table 7.2: List of neglected design options.

Concept Name	Concept ID	Reason for elimination
Solid Propellant	PR-2.2	Solid propellant thrusters cannot be stopped once they start, making them unfeasible for orbital maintenance. The need for a completely new system also makes them unfeasible for EoL.
Nuclear	PR-3	Requirement SS-TL-STK-US-REQ-STB-001 states that the maximum toxicity level allowed in the spacecraft is zero.
Photonic	PR-4.4	The thrust per kilowatt of power is four orders of magnitude lower than electrostatic propulsion (Levchenko et al., 2018). Using photonic propulsion would result into an extreme power requirement that lies outside of the preliminary budget allocation.
Electrodynamic Tether	PR-4.5	The thrust per kilowatt of power is two orders of magnitude lower than electrostatic propulsion. Also, a tether of several kilometers length is required to produce this thrust force (Bilen et al., 2010). There will be a risk of this tether colliding with debris.
Solar Sail	PR-4.6	The drag is higher than the thrust force provided by the solar sail below 700 km (Giovanni Vulpetti, 2015). The orbital altitude range for the Space Sweeper mission is between 350 and 1000 km.
Cannae Drive	PR-4.7	The Cannae Drive does not produce any measurable thrust (Tajmar et al., 2021).
Antimatter	PR-5.1	Technology readiness level is too low (TRL = 1) for now [1].
Warp Drive	PR-5.2	Warp drives do not exist yet.
Laser ablation (Ground-based)	PR-5.3	Too many stations would be needed to have full coverage for orbital maintenance.
Laser ablation (Space-based)	PR-5.4	The TRL of this propulsion method is 3 (Meyer et al., 2012). This method of propulsion will not be available in time.

7.1.2 Evaluation of Chosen Trade-Off Criteria

The third step was to then come up with the trade-off criteria that will be used for the final selection procedure. These were selected based on the criticality of each concept towards the overall system design, keeping in mind that the concepts must differ significantly with regards to each criteria, which is the case. Following a typical trade-off process, these criteria were then assigned weights relative to their effect on the system, from low (L) to high (H) importance. The reasoning for these weights is explained in Table 7.3. After these criteria were set in stone, a preliminary design of each selected option (described in Table 7.4), based on the criteria, was done so that the different concepts can be ranked from low to high with respect to the chosen criteria. This will lead to a concept that is declared the winner of the trade-off, and that will be further analysed in detail.

To evaluate the chosen concepts on the selected trade-off criteria, one needs to first estimate the required propellant mass that the spacecraft needs to carry, due to the total ΔV required for the entire mission. A spacecraft typically requires propellant for two main procedures, station keeping, and EoL. The former depends on many different disturbances that act on the spacecraft in its lifetime, with the main ones being the drag and the J2 effect (Montenbruck et al., 2000, p.55). The latter relates to the procedure chosen by the design team to end the life of the spacecraft, for example, the decay orbit chosen, and the number of burns required for the transfer. The total ΔV required due to these two procedures was estimated for a range of three altitudes; 380 km, the lowest altitude the spacecraft will orbit at, 650 km, and 1000 km, the point after which atmospheric drag is negligible (Wertz, Everett, et al., 2011, p.210). This was done because at each altitude, there are worst and best case scenarios related to station keeping and EoL; for example, at 1000 km, the drag is negligible however the ΔV required for EoL is obviously higher, due to the larger altitude change needed.

The ΔV for station keeping was estimated for the two main perturbations, drag and J2, assuming one burn is done per orbit, using the tool seen in Section 3.5, with the estimated dry mass from Subsection 3.4.1, and the worst case scenario area, as seen in Section 6.3, as inputs. After careful consideration, taking into account minimal propellant use and fastest re-entry possible, so as to not contribute to the problem we are trying to solve, the following EoL procedure was chosen: an incomplete Hohmann transfer, lowering the perigee to an altitude of 100 km, in which a number of burns will be done to control the S/Cs re-entry intro Earth's atmosphere. Note that this simulation was done assuming a maximal solar cycle. The simulation was also ran for a perigee of 120 km, yielding a lifetime of three hours, confirming the fact that the spacecraft will immediately re-enter at 100 km. Following the common guidelines for the sizing of this subsystem, and to account for the other orbital perturbations, which are nearly negligible (Montenbruck et al., 2000), such as the third body

Table 7.3: Explanation of chosen trade-off criteria.

Criteria	Weight	Reasoning
Propellant Mass	High	Yields the largest difference between concepts.
Power	High	Very limiting power budget for this subsystem as seen in Table 3.6.
Volume	Moderate	The differences in volume between the different concepts are significant.
Complexity	Moderate	All propulsion system options in the trade-off have been extensively tested in space, however it is still crucial to ensure a high reliability of the subsystem.

Table 7.4: List of selected design options.

Concept Name	Concept ID	Concept Description
Cold Gas	PR-1	Pressurised gas is expanded through a converging-diverging nozzle, creating thrust.
Liquid bi-propellant	PR-2.1.1	Propellant consists of an oxidiser and a fuel that come together in the combustion chamber, exhausting through a converging-diverging nozzle and creating thrust.
Liquid mono-propellant	PR-2.1.2	Propellant is combusted and creates thrust by being exhausted from a converging-diverging nozzle.
Electrostatic	PR-4.1	Uses electric fields to accelerate ionised particles to propel the spacecraft.

Table 7.5: Delta V required per parameter at 380 km for a duration of one year, using the orbital decay simulation, explained in Section 3.5.

	Altitude
Parameter	**380 km**
Drag/J2 Compensation	117 m/s
EoL	81.8 m/s
Total	198 m/s
Total with 25% margin	249 m/s

perturbations of the Moon and Sun, a safety factor of 1.25 is applied to the total ΔV (Mani et al., 2018, p.5). Note that collision avoidance is also considered in this safety factor, as simulations show that no debris piece will orbit within a 100 m radius of our spacecraft. The propulsion system was then designed for the worst case scenario, the altitude at which the total ΔV required for both station keeping and EoL is the highest, which was 380 km, for which the values are seen in Table 7.5.

A typical fuel, as well as its specifications, was selected for each of the chosen concepts to evaluate the criteria of this trade-off. These are; gaseous Nitrogen for cold gas, Hydrazine for mono-propellant, N2O4-MMH for bi-propellant, and Krypton for electrostatic propulsion (Wertz, Everett, et al., 2011, p.534-538).

Power

Using the data available in (Wertz, Everett, et al., 2011, p.550) for the two most typical types of electrostatic propulsion systems, ion and Hall effect, statistical relationships were made to estimate the power required by this concept, with an R value of 0.9462 and 0.9917, respectively:

$$T_{ion} = 0.02P + 32.575 \quad (7.1) \qquad T_{Hall} = 0.054P + 19.884 \quad (7.2)$$

Rearranging these equations to yield a power requirement, and using the total thrust needed for station keeping and EoL, the ion system would require 3087.53 W, and the Hall effect system 1151.35 W. As seen in the preliminary power budget in Subsection 3.4.1, the power values required for electrostatic propulsion systems is over one order of magnitude larger than what is allocated. For this reason, electrostatic propulsion systems were immediately eliminated from the trade-off, and since power was only added as a criteria due to the fact that it was only critical for electrical systems, it will not be analysed for the rest of the concepts.

[1] URL: https://www.nasa.gov/directorates/heo/scan/engineering/technology/technology_readiness_level [Accessed on 02-06-2022]

Table 7.6: Propellant mass required by type of system. Note that average values of specific impulse are used here (Zandbergen, 2021, p.142).

System	Propellant	Isp [s]	Propellant Mass [kg]
Cold Gas	GN2	61	1473.38
Liquid Mono-propellant	Hydrazine	221	347.5
Liquid Bi-propellant	N2O4/MMH	269	282.55

Table 7.7: Volume required by type of system.

System	Propellant density [kg/m^3]	Propellant volume [m^3]	Subsystem Volume [m^3]
Cold Gas	300	4.9	6.78
Liquid Mono-propellant	1020	0.34	0.47
Liquid Bi-propellant	1060	0.27	0.37

Propellant Mass

To calculate the preliminary propellant mass, the rearranged Tsiolkovsky's rocket equation, as seen in Equation (7.3), is used for the three remaining concepts, using the same dry mass value used for the determination of the ΔV for drag compensation. Looking at Table 7.6, we can clearly see an important difference between the mass required for the three concepts. Using these results, the cold gas concept is given a high score, while the other two concepts are both given low scores, due to the order of magnitude difference.

$$M_p = M_{dry}\left(e^{\Delta V/I_{sp}g_0} - 1\right) \tag{7.3}$$

Volume

To calculate a preliminary estimate of the total volume for each concept, a factor of 1.2 is applied to the propellant volume to account for the expansion of the propellant due to temperature and density related variations (Wertz, Everett, et al., 2011, p.543). A further 15% is added, accounting for other components, such as piping and thrusters (Zandbergen, 2021, p.154). Examining the results, one can see a similar relation as with the mass. The cold gas concept will clearly be given a high score, while the others will be given a low score in this case.

Complexity

The complexity of the three concepts wildly differs. Cold gas propulsion concepts require relatively simple engineering knowledge, needing simple valves, filters, and regulators to connect the thruster to the high pressure gas storage tank. Furthermore, its advanced TRL value and the amount of flight-proven missions it has undergone proves the high reliability of such a system. A low complexity score will therefore be given to this concept. As their name suggests, mono-propellant systems only require one type of propellant, avoiding combustion instabilities which may arise with the mixing of two propellants. They are more complex than cold gas systems as they require more intricate systems to combust the propellant, which includes the need for catalytic beds. Typically hydrazine is used for these systems, which decomposes into hydrogen and ammonia. To control the specific impulse of the system, the further dissociation of ammonia must be limited, adding extra overall complexity to the system. Due to the added complexity, reliability decreases compared to the cold gas system, however extensive testing has also been done. A score of moderate will then be given for this concept. It can be argued that bi-propellant systems can achieve higher levels of reliability compared to mono-propellant ones due to their possibility to achieve hypergolic combustion, negating the need for ignition systems. However, due to the much larger amount of components such as valves, filters, and pressure transducers, the overall complexity is typically much higher than the other two concepts. Also, very precise calculations must be done to ensure the correct oxidiser to fuel ratio is used at all times, and the propellants must undergo a larger amount of chemical processes. It will therefore be given a high score in this aspect. (Wertz, Everett, et al., 2011, p.533-535)

7.1.3 Trade-Off Results

The trade-off results are presented in Table 7.8, where the weights of each criteria are represented by the width of each column. We can clearly see that the only benefit that cold gas systems would have for this mission would be the low complexity, whereas it has the worst performance regarding the other two criteria. The liquid mono-propellant and bi-propellant systems perform very well with regards to propellant mass and volume required, however they differ in complexity, as bi-propellant systems are always the more complex of the two. Analysing this graph yields a clear winner, the liquid mono-propellant system, which is more than capable of providing the total ΔV required in the spacecraft's lifetime, and will be designed in detail in the next section.

7.2 Detailed Design

The detailed design of the propulsion subsystem will be explained in this section. By means of a trade-off that was explained above, a monopropellant system was chosen. For the detailed design of this subsystem, hydrazine was chosen,

Table 7.8: Trade-off between top-level propulsion system options.

	Propellant Mass (Highly important)	**Volume (Moderate)**	**Complexity (Moderate)**
Cold Gas	H	H	L
Liquid Mono-propellant	L	L	M
Liquid Bi-propellant	L	L	H

Table 7.11: Thruster options.

Name	**Thrust [N]**	**Specific impulse [s]**	**Massflow [kg/s]**	**Minimum pressure [MPa]**	**Minimum impulse bit [Ns]**	**Minimum pulse duration [s]**	**Burn cycles**
Ariane-1N[2]	1	222	0.00044	2.20	0.043	0.043	59000
Ariane-20N[2]	20	222	0.0032	2.40	0.685	0.034	93100
MONARC-90LT[3]	90	232	0.0396	1.62	1.80	0.020	50000
MONARC-90HT[3]	116	234	0.0506	1.62	1.16	0.010	70000
MONARC-445[3]	445	234	0.194	1.90	11.52	0.026	12000

Table 7.9: ΔV budget breakdown for thruster sizing and detailed propulsion subsystem sizing.

Component	**ΔV [m/s]**
Total drag and J2	117
Drag and J2 per burn	0.0205
EOL	82
Margin	50
Total	249

Table 7.10: Mass and power target budget for the propulsion subsystem.

Component	**Mass [kg]**	**Power [W]**
Target value	57	91
Contingency	15	12
Margin	14	23
Total	86	126

due to its heritage in space, and the wide range of available COTS components. The sizing of this subsystem starts with the ΔV budget that is required for the mission. The breakdown of this budget can be seen in Table 7.9. This section has the following structure: first, the pressurisation system will be chosen in Subsection 7.2.1. Second, the thruster will be selected by means of a trade-off in Subsection 7.2.2. This is followed by trading off different propellant tanks in Subsection 7.2.3 and pressurant tanks in Subsection 7.2.4. Finally, the plumbing, sensors and actuators will be chosen in Subsection 7.2.5. The design of this subsystem must stay within the allocated mass and power budget shown in Table 7.10.

7.2.1 Pressurisation system selection

Propellant must flow to the thruster during the operational lifetime of a spacecraft. This can be achieved by using several methods: pump fed systems, often used for bipropellant systems, and pressure systems, often used for monopropellant systems. Pressurised systems were considered for this mission, due to the use of a monopropellant. There are two types of pressurised systems: the blow-down system, and the pressure regulated system. An advantage of using a blow-down system is that there are no moving parts, thus the system reliability is higher. However, blow-down systems have a major flaw: the thrust force is not constant throughout the mission duration. Using such a system on our mission would require significant pressurant mass and volume, due to the EOL manoeuvre which requires a ΔV of 82 m/s. Another point of consideration is the significant number of small manoeuvres that the mission must perform. Designing a blow-down system that can deliver the right amount of thrust, with changing burn times per manoeuvre is complicated. A final disadvantage of blow-down systems is that a larger pressurant volume, and thus a larger tank, is required. Pressure regulated systems can deliver a constant thrust force throughout the mission duration and allow for maximising propellant volume in the tanks (Wertz, Everett, et al., 2011, p.545). A major downside of using such a system is that extra weight is required for the pressure regulators. When considering all above mentioned advantages and disadvantages, the pressure regulated system is chosen.

7.2.2 Thruster selection

Five thrusters are included in the trade-off. These thrusters deliver a thrust force between 1 and 445 N. This wide range of thrust force was chosen to see what the impact would be on the total propellant mass required, and as a result the total mass of the propellant tanks. A preliminary sizing for each thruster option was performed, assuming a pressure regulated propellant system. Details about the selected thrusters can be found in Table 7.11.

[2]URL: https://www.space-propulsion.com/brochures/hydrazine-thrusters/hydrazine-thrusters.pdf [Accessed on 08-06-2022]

[3]URL: https://www.moog.com/content/dam/moog/literature/Space_Defense/spaceliterature/propulsion/moog-MonopropellantThrusters-Datasheet.pdf [Accessed on 08-06-2022]

Table 7.12: Margins for propulsion subsystem (Wertz, Everett, et al., 2011).

Component	Value
Trapped propellant	0.03
Loading uncertainty	0.005
Feed system	0.2

The preliminary sizing of the propulsion subsystem was performed using the following method. The starting point is the specific impulse (I_{sp}), the mass of the thruster (M_{th}), and the dry mass (M_{dry}). As mentioned in the introduction, the manoeuvre to compensate for the drag and J_2 effect is performed every orbit. The required change in velocity per orbit was determined using the program explained in Section 3.5. Using this value, combined with the value of the Isp, and plugging them into the rewritten form of the rocket equation, Equation (7.4), gives a value for the propellant mass required per manoeuvre. This calculation is performed for all orbits during the lifetime of the spacecraft whilst ensuring that the new final mass (M_{fin}) in Equation (7.4) includes the propellant mass of all previously performed manoeuvres. All values of the required propellant mass were summed, and the propellant mass required for the EOL manoeuvre was added. The total mass was multiplied by two margins: a margin for trapped propellant and a margin for propellant loading uncertainty. This gives the value for the loaded propellant mass ($M_{p_{loaded}}$). The values for these margins can be found in Table 7.12. Dividing the loaded propellant mass by the density of hydrazine (at 293 K) results in the total volume required for the propellant (V_{pl}). The usable volume (V_{p_u}) of propellant is calculated by using the total propellant mass, excluding margins for trapped propellant and the loading uncertainty, and dividing this by the density of hydrazine. The required propellant tank volume ($V_{tank_{prop}}$) is equal to this usable volume (V_{p_u}). The mass of the propellant tank ($M_{tank_{prop}}$) is estimated using Equation (7.5). This equation is used, since pressure regulated systems require a boundary between the propellant and pressurant, which is present in diaphragm tanks.

$$M_{p_{man}} = M_{fin}(e^{\frac{\Delta V}{Isp \cdot g_0}} - 1) \tag{7.4}$$

$$M_{tank_{prop}} = 2.36 \cdot 10^{-7} V^3_{tank_{pro}} - 2.32 \cdot 10^{-4} V^2_{tank_{pro}} + 0.131 V_{tank_{pro}} + 0.264 \tag{7.5}$$

The preliminary design of the pressurant tank is initiated by picking a volume for this tank, a material that the tank is made of, and by assuming that the tank is spherical. In this case, a volume of 0.040 m^3 was chosen, as well as aluminium 7075-T6 for the material. This material has a yield strength (σ) of 503 MPa and a density (ρ) of 2810 kg/m^3. The crucial point is to calculate what the required thickness of the tank must be to withstand the pressure that is present inside the pressurant tank at BOL ($p_{pre_{BOL}}$). This pressure is calculated by using Equation (7.6), where V_1 is the volume of the pressurant tank, V_2 is the volume of the pressure tank and propellant tank combined, and $p_{min_{req}}$ is the minimum required pressure at EOL for nominal operation of the thruster. It must be noted that this equation is the rewritten form of the ideal gas law, by assuming that the mass, and temperature of the pressurant stays constant throughout the mission duration. With this pressure at BOL knows, the minimum required thickness of the pressurant tank (t_{min}) can be calculated using Equation (7.7), where r is the radius of the tank. The mass of the pressurant tank ($M_{tank_{pre}}$) can be calculated by using Equation (7.8) Also, the mass of the pressurant (M_{pre}) can be calculated by using the ideal gas law, as shown in Equation (7.9), where M the molar mass of nitrogen at 293 K in kg/mol, R the universal gas constant, and T the temperature in the tank in K.

$$p_{pre_{BOL}} = p_{pre_{EOL}} \cdot \frac{V_2}{V_1} \tag{7.6}$$

$$t_{min} = \frac{p_{pre_{BOL}} \cdot r}{2 \cdot \sigma} \tag{7.7}$$

$$M_{tank_{pre}} = \rho \frac{4}{3} \pi ((r + t_{min})^3 - r^3) \tag{7.8}$$

$$M_{pre} = \frac{p_{pre_{BOL}} \cdot V \cdot M}{R \cdot T} \tag{7.9}$$

Finally, the mass of the feed system (M_{feed}) can be calculated using Equation (7.10), where it is assumed that this mass is 20% of the total dry mass of the propulsion system. A summary of the results of the preliminary sizing for each thruster is shown in Table 7.13. The wet mass of this sizing will be part of the trade-off for the thruster.

$$M_{feed} = margin_{feed} \left(\frac{M_{th} + M_{tank_{prop}}}{1 - margin_{feed}} \right) \tag{7.10}$$

The trade-off cannot be based solely on wet mass. Other factors are important when choosing a thruster. Four other factors have been taken into account for the final trade-off. Each of these will be briefly explained below, starting with the minimum pulse duration.

The minimum pulse duration is the minimum burn time that the thruster can burn. It can be calculated using Equation (7.11), where MIB is the minimum impulse bit in Ns, and F is thrust force in N. This value must lower than the minimum required burn time per orbital manoeuvre. This minimum burn time ($t_{b_{min}}$) can be calculated using Equation (7.12), where $M_{p_{man}}$ is the propellant mass required per orbit, and $\dot{m}$ is the mass flow of the engine. It was found that the minimum

Table 7.13: Preliminary sizing of the propulsion subsystem for each thruster option.

Name	M_{th} **[kg]**	$V_{tank_{pro}}$ **[m^3]**	$M_{tank_{prop}}$ **[kg]**	$M_{tank_{pre}}$ **[kg]**	M_{feed} **[kg]**	M_{prop} **[kg]**	M_{pre} **[kg]**	M_{dry}**[kg]**	M_{wet} **[kg]**
Ariane-1N	0.29	0.36	27.6	7.54	8.79	361	10.1	43.9	415
Ariane-20N	0.65	0.36	27.6	8.24	8.96	361	11.0	44.8	417
MONARC-90LT	1.12	0.34	26.7	5.24	7.99	345	7.07	39.9	392
MONARC-90HT	1.12	0.34	26.5	5.24	7.94	342	7.07	39.7	389
MONARC-445	1.60	0.34	26.5	6.15	8.16	342	8.28	40.8	391

Table 7.14: Trade-off table for thruster selection.

Name	M_{wet} **[kg]**	**Burn cycles**	**Propellant throughput [kg]**	**Missions flown**
Ariane-1N	415	59000	67	>500
Ariane-20N	417	93100	>290	>100
MONARC-90LT	392	50000	1540	>10
MONARC-90HT	389	70000	890	>10
MONARC-445	391	12000	2441	>10

pulse duration was lower than the minimum required burn time. It was therefore excluded from the final trade-off. The second factor that is considered is the number of burn cycles that the engine can deliver. This value should be higher than the number of burns required during the mission duration. The third factor that was looked at is the minimum propellant throughput. This value should be higher than the minimum propellant mass required for the mission. The final consideration is the number of missions that the thruster has been successfully deployed on. This gives an indication about the reliability of the engine.

$$Pulse_{min} = \frac{MIB}{F} \tag{7.11}$$

$$t_{b_{min}} = \frac{M_{p_{man}}}{\dot{m}} \tag{7.12}$$

All trade-off criterion and values for each thruster option are shown in Table 7.14. The weights of all trade-off criteria are assumed to be equal. The winner of the trade-off is the MONARC-90HT, which will be explained below. The Ariane-1N is discarded due to the propellant throughput value. This is well below the required propellant throughput. The value of this throughput for the Ariane-20N was found to be higher than 290 kg. This results in uncertainty; whether it is possible to burn the almost 600 kg of propellant. For this reason, the Ariane-20N is also discarded. The MONARC-445 is discarded, because of the amount of the burn cycles. It is possible that the mission will be extended by using in-orbit refuelling. Having only 12000 burn cycles means that the maximum mission duration can only be 2 years (roughly 6000 cycles per year due to the manoeuvre every orbit). This leaves the MONARC-90LT and MONARC-90HT. In all honesty, both thrusters could have been chosen, however only one can be picked. It was decided that the MONARC-90HT was the better option, because of the lower wet mass.

7.2.3 Propellant tank selection

The next step in the design process, after selecting the thruster, is to design the propellant tank. It was decided to use existing propellant tanks for three reasons: the cost of COTS tanks is significantly lower compared to designing a custom tank, COTS tanks are flight proven thus have a higher reliability, and no complex structural analysis, such as vibration and pressure loads, must be performed. The fact that COTS tanks are used results in an immediate exclusion of propellant management devices (PMD) tanks. The reason for this is that the design of these tanks differs per mission profile, thus require a custom design (Wertz, Everett, et al., 2011, p.543). For selection of the propellant tanks, it is determined that it is not possible to pick different propellant tank within the same configuration. It is likely that no configuration of propellant tanks will result in the exact required volume. It must be considered that any additional volume that is not occupied by the propellant must be filled with pressurant before the launch of the mission.

During the preliminary sizing of the propulsion subsystem, different values for ΔV were used. For this detailed determination of required propellant volume, more detailed values will be used including the 25% margin, and updated values for the EOL manoeuvre. These values can be found in Table 7.9. The 25% margin is assumed to be used at the start of the mission, resulting in a worst-case scenario for the required propellant mass. Using the same method as explained in reference to method with the selected MONARC-90HT thruster, a propellant volume of 0.34 m^3, including the margins for trapped propellant and the propellant loading uncertainty, was found.

Six propellant tanks have been selected for the trade-off with volumes ranging from 96 to 331 litres per tank. All tanks have a diaphragm that keeps the propellant and pressurant separate, and have a maximum operating pressure that lies well above the minimum required pressure ($p_{min_{req}}$ = 16.2 bar) for the thruster to operate nominal. For this trade-off, three trade-off criteria have been selected: the total mass of the tank configuration (including pressurant mass required to fill up the empty space), the total volume that the configuration will occupy, and the reliability. The total volume ($V_{tot_{prop}}$) is calculated by assuming that the pressurant tanks occupy a rectangular block, since it is unlikely that the space around

Table 7.15: Propellant tank calculation results.

Name	V_{us} **[L]**	**Dimensions (D x H) [mm]**	$M_{tank_{prop}}$ **[kg]**	**Number of tanks**	$M_{tank_{tot}}$ **[kg]**	$V_{p_{pro}}$ **[m^3]**	$M_{pr_{pro}}$ **[kg]**	$M_{tot_{prop}}$ **[kg]**	$V_{tot_{prop}}$ **[m^3]**
DT180	180	623 x 907.2	21.0	2	42.0	0.02	0.37	42.4	0.70
OST25/3	331	753x 953.5	22.7	2	45.4	0.32	6.00	51.4	1.08
80505-1	134	588 x 723	16.0	3	48.0	0.06	1.15	49.2	0.75
PTD-222	222	608 x 1028	17.1	2	34.2	0.10	1.94	36.1	0.76
PEPT-590GB	204	589 x 1170	17.5	2	35.0	0.07	1.27	36.3	0.81
PTD-96	96	545 x 685	8.20	4	32.8	0.04	0.82	33.6	0.81

Table 7.16: Propellant tank trade-off table.

Name	$M_{tot_{prop}}$ **[kg]**	$V_{tot_{prop}}$ **[m^3]**	**Number of tanks**
DT180	42.4	0.70	2
OST25/3	51.4	1.08	2
80505-1	49.2	0.75	3
PTD-222	36.1	0.76	2
PEPT-590GB	36.3	0.81	2
PTD-96	33.6	0.81	4

the spherical part will be used by any other subsystem. The reliability of the system is directly linked to the number of propellant tanks required. The reason for this is that more propellant tanks require more sensors and actuators, which can fail during the mission.

The details for each propellant tank can be found in Table 7.15. The number of tanks required for the mission is calculated by dividing the total required tank volume ($V_{t_{req}}$) by the usable volume per tank (V_{us}). This number is then rounded up to nearest integer. The total mass of the tanks ($M_{tank_{tot}}$) is then simply calculated by multiplying the tank mass ($M_{tank_{prop}}$) with the number of tanks required. As mentioned before, it is highly unlikely that the propellant volume of the tanks will be exactly equal to the required volume. The space that will not be occupied by the propellant should be filled with pressurant to ensure that the pressure inside the tank will be exactly equal to the minimum required operating pressure of the thruster. The pressurant volume ($V_{p_{pro}}$) required is calculated by subtracting the total required tank volume ($V_{t_{req}}$) from the total tank volume (V_{tank}). This total tank volume is calculated by multiplying the usable volume per tank (V_{us}) with the number of tanks required. The mass of pressurant ($M_{pr_{pro}}$) required to fill the tank can now be determined using Equation (7.9). The total mass of the propellant tank configuration($M_{tot_{prop}}$), including the mass of pressurant, is now calculated by summing $M_{tank_{tot}}$ and $M_{pr_{pro}}$. The results of these calculations are summarised in Table 7.15.

The trade-off results are shown in Table 7.16. The winner of the trade-off is the PTD-96 tank. It can be seen that there are three tanks (DT180, PTD-222, and PEPT-590GB) that have two green and one yellow box. Due to the equal weights that are put on all criteria, either of these tanks can win. The PTD-96 won due to it having the lowest total tank mass. This will impact the resulting dry mass budget in a positive manner, concerning the residual budget for the pressurant tank, and the propellant manifold design.

7.2.4 Pressurant tank selection

The third step in the design process is determining what pressurant tank will be used. Again, it was decided to use a COTS tank for this mission. The reasons for this are similar to the ones for the propellant tank: lower costs, high reliability, and no detailed structural analysis required. This final point is especially crucial for the pressurant tank, due to the high pressures it must withstand.

The starting point for the design of the pressurant tank is the ideal gas law (Equation (7.13)), where m is the mass of the pressurant, R is the specific gas constant for nitrogen (at 293 K), T is the temperature of the pressurant, p is the pressure of the pressurant, and V is the volume of the pressurant. Assuming that the temperature stays constant, and realising that the mass and specific gas constant are constant, since no pressurant is burned, this equation can be rewritten to the form shown in Equation (7.14). In this equation, $p_{min_{req}}$ is the minimum required pressure at EOL for nominal operation of the thruster, $V_{tank_{pre}}$ is the volume of the pressurant tank, and $V_{tank_{pro}}$ is the total propellant volume required. The variable

[4]URL: https://www.space-propulsion.com/brochures/propellant-tanks/180lt-mon-mmh-tank-dt180.pdf [Accessed on 09-06-2022]
[5]URL: https://www.satcatalog.com/component/331-l-biprop-or-hydrazine-tank-ost-25-3/ [Accessed on 09-06-2022]
[6]URL: https://www.northropgrumman.com/space/diaphragm-tanks-data-sheets-sorted-by-volume/ [Accessed on 09-06-2022]
[7]URL:https://satcatalog.s3.amazonaws.com/components/812/SatCatalog_-_MT_Aerospace_AG_-_PTD-222_-_Datasheet.pdf?lastmod=20210709221212 [Accessed on 09-06-2022]
[8]URL: https://satsearch.co/products/rafael-pept-590 [Accessed on 09-06-2022]
[9]URL: https://www.mt-aerospace.de/files/mta/tankkatalog/PTD-96.pdf [Accessed on 09-06-2022]

Table 7.17: Pressurant tank trade-off table[10].

Name	Volume [L]	$M_{tank_{pre}}$ [kg]	$p_{max_{allow}}$ [bar]	$p_{pre_{BOL}}$ [bar]
80314-201	36.1	16.0	372	169
80510-1	36.6	11.9	421	167
80586-1	40.0	8.00	388	154

Table 7.18: Updated mass budget.

Component	Mass [kg]
Thruster	1.12
Propellant tank	33.6
Pressurant tank	8.00

in this equation is the volume of the pressurant tank; changing this value will result into different values of the required pressure in the pressurant tank at BOL.

$$pV = mRT \tag{7.13}$$

$$p_{pre_{BOL}} = p_{min_{req}} \frac{V_{tank_{pro}} + V_{tank_{pre}}}{V_{tank_{pre}}} \tag{7.14}$$

Three pressure tanks were chosen for this trade-off. The criterion for this trade-off is the mass of the tank ($M_{tank_{pre}}$), due to the very limited mass budget that is left after the thruster and propellant tank selection. By following the approach mentioned above for all three tank options, it was found that the pressure inside the tank ($p_{pre_{BOL}}$) is lower than the maximum allowable pressure ($p_{max_{allow}}$) as stated by the manufacturer. The results of this are shown in Table 7.17. The winner of this trade-off is the 80586-1 tank, due to it having the lowest mass.

7.2.5 Propellant feed system selection

Now that the thruster, propellant tank, and pressurant tank has been decided on, it is crucial to ensure that these three components are connected correctly by the propellant feed system. This propellant feed system, also called propellant manifold, consists of multiple parts. This subsection will show a schematic overview of the entire propulsion system and will discuss all components that are present in this manifold. The current mass budget used by the thruster, and tanks is shown in Table 7.18. As for all other components, discussed in previous subsections, the components for the manifold will be COTS components. The reason for this is again due to simplicity of the design, the high reliability due to space heritage of these components, and the lower costs involved by picking COTS components. The schematic overview of the propulsion subsystem can be seen in Figure 7.2.

There are three fill/drain valves present. These fill/drain valves are there to allow for loading and draining of the pressurant (valve 1 and 2), and for loading and draining of propellant (valve 3). Fill/drain valve 2 is present, because pressurant must be loaded inside the unused space of the propellant tanks before launch. There are six filters present. These filters ensure that no contaminants get inside the pressure tank (filter 1), the space for pressurant inside the propellant tank (filter 2), and the propellant tanks (filters 3, 4, 5, and 6). There is a pressure regulator present which ensures that the pressure inside the propellant tanks and feedlines between the regulator, and the thruster, maintain a constant pressure which is equal to the minimum pressure required for nominal operation of the thruster. There are five pressure transducers present, one for each tank. These transducers ensure that the pressurant tank is loaded to the correct pressure required at BOL (pressure regulator 1), and that the propellant tanks maintain the correct pressure for nominal operation of the thruster (pressure regulator 2, 3, 4, and 5). There are nine isolation valves present. These valves can open and close to allow for manipulation of the pressurant and propellant flow. Isolation valve 1 is closed during the loading of the pressurant tank before the start of the mission. Isolation valve 2, 3, 4, and 5 are present to allow for manipulation of the pressurant flow to each of the propellant tanks. This is required, since it is possible that the pressure of one of the tanks might be different compared to the other tanks. This also allows for closing of part of the propulsion system in case of a malfunction. Isolation valves 6, 7, 8, and 9 are present to allow for manipulation of the propellant flow. These valves allow for control of the centre of mass of the propulsion system, since closing valves result in a different propellant mass in each tank during operation. They also allow for equal filling of the tanks at the start of the mission since valves can close when the tank is filled to the required level. The final function of these valves is that they can be closed in case of a malfunction of the propellant feed system. The cavitating venturi that is present provides an upper limit of the mass flow of propellant towards the thruster. This ensures that no propellant mass will be expelled without it being burned. This increases the efficiency of the propulsion subsystem and ensures that a constant thrust force is produced.

The final step of designing the propellant manifold is the design of the feed lines, shown as the connecting lines in Figure 7.2. It is assumed that the pressure drops over the length of the propellant feed lines is negligible, and thus the only pressure drop present in the system is the pressure drop inside the thruster. This assumption can be validated by using the Darcy-Weisbach equation[1] as shown in Equation (7.15), where ΔP is the pressure drop in Pa, λ is the friction

[10]URL: https://www.northropgrumman.com/space/pressurant-tanks-data-sheets-sorted-by-volume/ [Accessed on 09-06-2022]
[1]URL: https://www.engineeringtoolbox.com/darcy-weisbach-equation-d_646.html [Accessed on 13-06-2022]

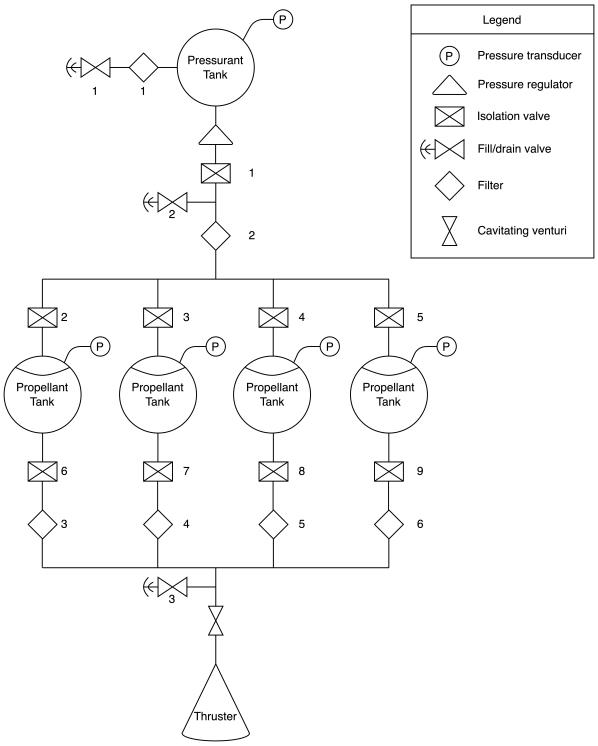

Figure 7.2: Schematic overview of the propulsion subsystem.

coefficient, L is the length of the pipe in m, V is the flow velocity of the propellant in m/s, ρ is the fluid density in kg/m^3, and D is the pipe diameter in m. A diameter of 1/4 inch (6.35 mm) is chosen for easy connection to the thruster. The flow velocity is calculated by using Equation (7.16), where $\dot{V}$ is the volumetric flow, and A_p is the cross-sectional area of the pipe. The friction coefficient can be calculated using the Colebrooke Equation[2], as shown in Equation (7.17), where λ is the friction coefficient, Re is the Reynoldsnumber, k is the absolute roughness, and d_h is the internal diameter of the pipe. The Reynolds number can be calculated using Equation (7.18), where μ is the dynamic viscosity of the propellant. Using all input values, shown in Table 7.19, results in a pressure drop of 1520 Pascals per meter of tubing. This is 0.01 % of the pressure drop inside the thruster, showing that the assumption of neglecting the pressure drop inside the tubing is valid. The total mass of the feed lines (M_{lines}) can be calculated using Equation (7.19), where m_{meter} is the feed line mass per meter, and L_{tot} is the total length of feed lines required.

$$\Delta P = \frac{\lambda \cdot V^2 \cdot \rho}{2 \cdot D} \tag{7.15}$$

$$V = \frac{\dot{m}}{\rho \cdot A_p} \tag{7.16}$$

$$\frac{1}{\sqrt{\lambda}} = -2 \cdot \log_{10}\left(\frac{2.51}{Re \cdot \sqrt{\lambda}} + \frac{k}{3.71 \cdot d_h}\right) \tag{7.17}$$

$$Re = \frac{\rho \cdot V \cdot L}{\mu} \tag{7.18}$$

$$M_{lines} = m_{meter} \cdot L_{tot} \tag{7.19}$$

Table 7.19: Input values for calculating the pressure loss in stainless steel pipes.

Input	**Value**	**Units**
ρ	1010	kg/m^3
k	0.0000008	m
$\dot{m}$	0.01265	kg/s
D	0.00635	m
d_h	0.00635	m
m_{meter} [11]	0.119	kg/m

Table 7.20: Updated mass budget.

Component	**Mass [kg]**
Thruster	1.12
Propellant tank	33.6
Pressurant Tank	8.00
Sensor and actuators	6.38
Feed lines	0.54
Propellant mass	344
Pressurant mass	7.07

An overview of all components, including the mass of each component, is shown in Table 7.21. This is followed by an updated version of the mass budget, as shown in Table 7.20.

[2]URL: https://www.engineeringtoolbox.com/major-loss-ducts-tubes-d_459.html [Accessed on 13-06-2022]

[11]URL: https://www.amazon.com/Stainless-Tubing-Welded-Bright-Annealed/dp/B002VRAVBS [Accessed on 13-06-2022]

Table 7.21: Overview of all components present in the propellant manifold.

Component	Quantity	Mass [kg]	Total Mass [kg]
Fill/drain valve (HP)[12]	1	0.113	0.113
Fill/drain valve (LP)[13]	2	0.68	1.36
Pressure regulator[14]	1	0.94	0.94
Isolation valve[15]	9	0.227	2.043
Filter nitrogen[14]	2	0.076	0.152
Filter hydrazine[14]	4	0.11	0.44
Pressure transducer (LP)[16]	4	0.25	1
Pressure transducer (HP)[17]	1	0.23	0.23
Cavitating venturi	1	0.1	0.1

Table 7.22: Thruster trade-off table for sensitivity analysis.

Name	M_{wet} [kg]	Burn cycles	Propellant throughput [kg]	Missions flown
Ariane-1N	415	59000	67	>500
Ariane-20N	417	93100	>290	>100
MONARC-90LT	392	50000	1540	>10
MONARC-90HT	389	70000	890	>10
MONARC-445	391	12000	2441	>10

7.2.6 Sensitivity analysis

A sensitivity analysis is performed on the trade-offs of the thruster, propellant tank, and the selection of the pressure tank. Starting with the sensitivity analysis of the thruster selection, it was mentioned in Subsection 7.2.2 that it is assumed that all trade-off criteria are assumed to have the same weight. This says that all criteria have the same importance, which can be argued against. For example, the number of burn cycles are all above the number of burn cycles required for the duration of the mission (roughly 6000 burns). This leads to a reduction in weight for this trade-off criterion, since it is unlikely that the mission duration will be extended beyond two years, and if this happens, it will most likely result into a complete redesign of the propulsion subsystem due to the amount of propellant required. Another trade-off criterion of which the weight can be reduced is the number of missions flown. All engines are flight-proven, and thus have a similar reliability. The weights of both these criterion are reduced by 50%. The weights of the preliminary total wet mass of the propulsion system (M_{wet}), and the propellant throughput remains the same, since these values can result in an infeasible design of the propellant system. When the wet mass of the propulsion subsystem grossly exceeds the allocated budget, or the propellant throughput is lower that the minimum throughput that is required, will result in an unfeasible design. The new trade-off table is shown in Table 7.22, where it can be seen that the MONARC-90HT remains the winner.

The sensitivity analysis for the propellant tank, and pressurant tank selection, is done by two methods. The first method is to reduce and increase the total ΔV requirement of the subsystem sizing column, shown in Table 7.9, by 10%. This leads to a total reduction, and increase of 25 m/s which is taken from the value of the margin. The reason for subtracting and adding this 10 % for the margin, is that this is again a worst case scenario, since it was assumed that the margin was used at the start of the mission. By following the calculations, explain in Subsection 7.2.2, a reduction of total required propellant volume of 40 liters, and an increase of 30 liters is found. The consequences of this change in required propellant volume is shown in Table 7.23, and Table 7.24, where the changed values are presented in *italics*. For reduction of 10% leads to a new winner of the trade-off: the OST25/3. However, for the increase of 10%, the PTD-96 remains the best option. Due to the uncertainty, whether or not the ΔV budget will increase or decrease, it is safest to stick with the same tank.

The selection of the pressurant tank is performed using the same method as explained in Subsection 7.2.4. As explained above, the amount, and type, of propellant tank stays the same whilst the propellant per tank decreased due to the lowering of ΔV budget. This decrease in propellant volume required, results in an increase in pressurant gas in the tanks at the start of the mission. Using Equation (7.14), it can be calculated that the pressure required at BOL ($p_{pre_{BOL}}$) decreases, due to the decrease in the amount of propellant required for the mission. This results in selection of the same pressurant tank, the 80586-1.

The second sensitivity analysis method that can be applied to the propellant tank trade-off, and the selection of the pressurant tank, is to change the weights of the trade-off criteria, and see what the result of this change is. The weights

[12] URL: https://satsearch.co/products/vacco-industries-1-4-high-pressure-gas-fill-drain-valve-v1e10430-01 [Accessed on 11-06-2022]
[13] URL: https://satsearch.co/products/vacco-industries-1-2-low-pressure-fill-drain-valve-v1e10401-01 [Accessed on 11-06-2022]
[14] URL: http://www.omnidea-rtg.de/site/images/stories/Downloads/Omnidea-RTG_Catalogue_Feb2016.pdf [Accessed on 11-06-2022]
[15] URL: https://satsearch.co/products/vacco-industries-positive-isolation-valve-normally-closed-130097000 [Accessed on 11-06-2022]
[16] URL: https://satsearch.co/products/bradford-high-accuracy-pressure-transducer [Accessed on 11-06-2022]
[17] URL: https://satsearch.co/products/bradford-standard-accuracy-pressure-transducer-sapt [Accessed on 11-06-2022]

Table 7.23: Propellant tank trade-off table for first sensitivity analysis (-10% ΔV), where changed values are shown in *italics*.

Name	$M_{tot_{prop}}$ **[kg]**	$V_{tot_{prop}}$ **[m^3]**	**Number of tanks**
DT180	*43.1*	0.70	2
OST25/3	*23.3*	*0.54*	*1*
80505-1	*49.9*	0.75	3
PTD-222	*36.9*	0.76	2
PEPT-590GB	*37.0*	0.81	2
PTD-96	*34.4*	0.81	4

Table 7.24: Propellant tank trade-off table for first sensitivity analysis (+10% ΔV), where changed values are shown in *italics*.

Name	$M_{tot_{prop}}$ **[kg]**	$V_{tot_{prop}}$ **[m^3]**	**Number of tanks**
DT180	*66.2*	*1.06*	*3*
OST25/3	*50.8*	0.54	2
80505-1	*48.6*	0.75	3
PTD-222	*35.6*	0.76	2
PEPT-590GB	*35.7*	0.81	2
PTD-96	*33.1*	0.81	4

Table 7.25: Propellant tank trade-off table for second sensitivity analysis.

Name	$M_{tot_{prop}}$ **[kg]**	$V_{tot_{prop}}$ **[m^3]**	**Number of tanks**
DT180	42.4	0.70	2
OST25/3	51.4	1.08	2
80505-1	49.2	0.75	3
PTD-222	36.1	0.76	2
PEPT-590GB	36.3	0.81	2
PTD-96	33.6	0.81	4

of the total propellant tank mass, and the number of tanks will remain the same. The reasoning for this is that the mass of the tanks should stay within the given dry mass budget. The design will become infeasible when it grossly goes over budget. The weight of the number of tanks required will remain the same, since this gives a major indication about the reliability of the subsystem. More propellant tanks will require more filters, valves, and pressure transducers. The drop in reliability will increase the likelyhood of complete failure of the mission. The weight of the total required volume of the propellant tanks can be reduced by 50%. The reasoning for this is that there is sufficient empty space in the spacecraft to allow for an eventual increase of this total volume. The updated trade-off table is shown in Table 7.25. It can be seen that the PTD-96 tank is still the winner of this trade-off. This automatically results in the selection of the same pressurant tank, as explained in the first method of this sensitivity analysis.

7.2.7 Conclusion

This section discussed the methodology used for the design of the propulsion subsystem. The final components chosen are the MONARC-90HT thruster, four PTD-96 propellant tanks, and one 80586-1 pressurant tank. The total dry mass of the propulsion subsystem is 49.6 kg, which is below the target value of 58 kg. The wet mass of the subsystem is 401 kg. The power well within the given power budget. This is a result of the duty cycle of the thruster, resulting in a negligible power requirement. The average power requirement is 5.02 W, which is mainly driven by the required power for the pressure transducers that have to perform continuous measurements of the pressure inside the tanks. Verification and validation of the calculations have been performed by performing all calculations by hand, and comparing them to the scripts written. A sanity check on the iterative use of the rocket equation was performed, to ensure that the amount of propellant required for each burn decreases with the decrease in total spacecraft mass. All requirements, except for requirement SS-SYS-PROP-REQ-09, have been met. The toxicity requirement is not met due to the fact that there is no other propellant currently available that complies with all other subsystem requirements. Further research must be performed on this choice of propellant, since hydrazine will be banned in the near future. This will most likely change the current configuration of the propulsion subsystem, with as minimum a change in thruster. Two other factors that must be considered when continuing the design of the propulsion subsystem, is the use of multiple thrusters for redundancy reasons, and to investigate possible plume impingement with the TT&C antenna.

Command and Data Handling 8

An apt description of the command and data handling system (CDHS) is that it functions as "the brain and nervous system of the spacecraft" (Zandbergen, 2021, p.177). Firstly, the subsystem requirements matrix is given in Table 8.1. Hereafter, a general explanation of the system architecture is given in Section 8.2. Section 8.3 and Section 8.4 detail a dedicated sizing of the CDHS system for the detection payload, and for the remaining subsystems respectively. Special attention is paid to determining the volume of data that is sent to ground (both housekeeping and payload data), as this is leading for the telemetry, tracking and command (TT&C) subsystem. The components that are commercially available and required are chosen in Section 8.5, with a data handling and software block diagram in Section 8.6 to illustrate the system architecture. Verification and validation is not a separate chapter, given the complexity of calculations performed is very low, and were all verified by hand.

8.1 Subsystem Initial Requirements

Table 8.1: CDHS final subsystem requirements.

Requirement ID	Description
SS-SYS-CDH-REQ-01	The CDHS subsystem shall be able to handle a data rate of 10,000,283.6 kbps.
SS-SYS-CDH-REQ-02	The CDHS subsystem shall be able to handle 270 mega instructions per second.
SS-SYS-CDH-REQ-06	The mass of the CDHS subsystem shall not exceed 104 kg.
SS-SYS-CDH-REQ-08	The power used by the CDHS subsystem shall not exceed 1096 W.
SS-SYS-CDH-REQ-11	The CDHS subsystem shall have a memory size of 66,847 MB.
SS-SYS-CDH-REQ-13	The CDHS subsystem shall be able to process the data from the CDHS, EPS, GNC, payload, propulsion, TMS and TT&C subsystem.
SS-SYS-CDH-REQ-14	The CDHS subsystem shall be able to process the code required for the CDHS, EPS, GNC, payload, propulsion, TMS and TT&C subsystem.
SS-SYS-CDH-REQ-15	The CDHS subsystem shall be able to store the housekeeping data required for the CDHS, EPS, GNC, payload, propulsion, TMS and TT&C subsystem.

Table 8.1 gives the requirements for which will be designed. The values in the requirements are all found during the analyses in this chapter, apart from the power and mass requirements, which stem from the target values in Table 3.7. Requirements SS-SYS-CDH-REQ-13 and SS-SYS-CDH-REQ-14 are functional requirements, describing what the subsystem must be able to perform, while the others are objective-oriented.

8.2 System Architecture and Data Types

Before the CDHS system can be sized, and components chosen, a quick overview of the system framework and its functionality is necessary. Zandbergen (2021) concisely lists the key CDHS functions as:

- Handling sensory information from the payload.
- Handling information on the spacecraft's subsystems, including so-called "housekeeping data" and provides "info on health, status [and] internal environment" of the spacecraft.
- Perform decision-making, either by authorising commands (from other parts of the spacecraft, for example), or by generating them.
- Performing so-called "command actions", which include switching instruments on/off or setting parameters to a given value.

For this design stage, it is assumed that the various spacecraft computers can be divided into an external, and an internal bus. The external bus contains the main CDHS system, including the processing unit commonly named the "On-Board Computer" (OBC), TM (telemetry) encoder and TC (telecommand) decoder, as well as storage space for payload and housekeeping (HK) data. The internal bus contains electronics which handle far higher data rates than the external bus, and are not transmitted to ground. One of the functions of these electronics could include servo actuation, which requires very high data rates and computations to be done locally. As not all of this data is important to monitor from the ground, it is not communicated to the CDHS either. Instead, it remains local to the subsystem. Furthermore, for components whose data the ground station is interested in, the data rate necessary for telemetry is most likely not equal to the data rate required for subsystem operation. For example, while the rotation rate of a control moment gyro is not something ground will want to receive in the order of kHz, a sample rate of 1-10 Hz may be appropriate for telemetry. The electronics not part of CDHS, but that still link into it (like a subsystem dedicated computer) are assumed to be contained in subsystem COTS budgets, and are not part of the CDHS subsystem.

As Figure 8.1 shows, the OBC is connected to each subsystem at the top-level, and data is fed to and from it at a low speed data rate. From the payload to the data storage a high speed data rate is used, though this does not impact the

resultant storage capacity. On a deeper level, the OBC contains one or more central processor units (CPU), which may indeed have separate in-and-outputs leading to it, including, but not limited to, the housekeeping board. In the case of the detection payload, it may have a dedicated CPU to run the algorithm necessary to perform detection and tracking. For this, a trade-off between on-board processing or ground-based processing is necessary, given in Table 8.2, and based on the following four criteria:

- Storage required for image saving: for local, on-board processing, images are saved for short periods of time to be analysed, while for ground processing, in the case that the spacecraft is not in contact with a ground station, a larger storage capacity is required to save images between data dumps.
- TM data to transmit: on-board processing would only send down orbital parameters of the debris it has analysed, thus limited to only values, and not whole images. On the other hand, ground image processing requires the full images to be sent down, which are obviously much larger in data than orbital parameter values.
- Processing speed: to be able to process the images on-board, a high processing speed capability on-board is expected. This may, of course, be limiting, but it is expected that it is possible to design for this. Ground image processing would require lower on-board processing speeds, as all the computations are performed on the ground.
- Real-time image processing: during the primary mission, real-time image processing is far more practical than ground image processing, as the ablation laser needs to know where to point and shoot quickly, also when outside of contact with the ground station. Outside contact windows, waiting for ground processing is not feasible. However, in the case of the secondary mission, where only tracking of debris is performed, ground image processing may be viable. Nonetheless, the spacecraft very likely requires the ability to detect and track debris during its primary mission, and so ground imaging processing would only unduly increase TT&C requirements.

Table 8.2: Trade-off for local (on-board) image processing, or downlinking the image and processing it on the ground.

	Local image processing	**Ground image processing**
Storage required for image saving	M	H
TM data to transmit	L	H
Processing Speed	H	L
Real-time image processing	Y	N

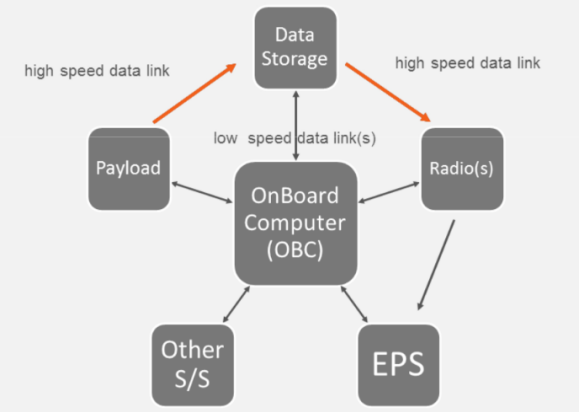

Figure 8.1: CDHS architecture.
[1]

It is immediately obvious that local, on-board image processing is the winner of the trade-off, especially considering real-time processing is absolutely necessary for the primary mission. This implies that it is highly likely that the detection payload will require a dedicated CPU. Note that a dedicated CPU may be contained in the same OBC. A separate CPU only implies that the detection payload algorithm and remaining subsystem operations cannot be run on the same processor, but may be run on the same OBC. The data output from the detection-specific CPU will also be sent to Earth, like the rest of the housekeeping data. All the remaining subsystems, including the high-powered, ablation laser payload, will be operated from a separate CPU. Therefore, in this report, the aforementioned system architecture components that are sized are thus the: payload computer, the subsystem computer that operates the remaining subsystems (both may be combined into one OBC, or a separate OBC and payload computer), any components necessary for data compression (may also be done by the OBC), and the storage space.

8.3 Payload processing and image storage

Image processing is unique to the lidar in this mission, and in general a real-time lidar processing requirement is an advanced application of this technology to spacecraft. The frequency of the lidar system is 10 kHz, which implies a high data rate is fed to the processing units. Therefore, the lidar system requires a dedicated sizing, due to the expected high data rates and processing power.

8.3.1 Debris imaging data rate

Scientific data is that which is collected using the on-board payload. In the case of this mission, the detection system uses lidar to detect debris. This data is fed to the CDHS system, which ensures that appropriate action is taken to allow the ablation laser to remove the particle. Given that lidar outputs images, the digitisation of its information can be estimated using (Zandbergen, 2021, p.182):

$$DR_{image} = N_{images} N_{pixel} n_{bits} \tag{8.1}$$

[1] URL: https://ocw.tudelft.nl/wp-content/uploads/1.0-Command-and-Data-Handling-Lecture-Notes.pdf [Accessed 13/06/2022]

Here DR_{image} represents the data rate, N_{images} is the number of images digitised per second, N_{pixel} is the number of pixels in the image, and n_{bits} is the number of bits per pixel. Given the lidar system, the number of bits is 22 per pixel. This is based on the 12 cm accuracy and 300 km range given in Subsection 4.3.4, which results in:bits $= \log_2(\frac{\text{range}}{0.12})$
Using the lidar frequency of 10 kHz, a resolution of 200 x 200 pixels, and 22 bits per pixel, a data rate of 8,8 Gbps is found. It is assumed that this data rate may not be compressed, though remaining subsystem data can be compressed. The reason for this is that because the lidar payload is so novel, it should not be the case that the mission cannot be carried out if the compression system does not work, or does not work as intended. On the other hand, compression of normal housekeeping data is commonly done, a mature technology, and thus compression can be safely assumed. It is assumed that at any point in time, the pictures of the previous 10 seconds are saved, in case tracking was not possible within 1 second. In other words, nominal operation (with sufficient verification and validation of the algorithm) would result in the program acquiring debris within 1 second. 10 seconds is taken to be the absolute maximum it should take, as this is already ten times higher than nominal operation. This means that for storage, a total of 88 Gb is necessary (data rate multiplied by time). This corresponds to a storage capacity required of 11 GB. Using the Airbus CORECI 2, compression of 3 to 6+ times as much is possible[2], which reduces the storage required to 3.7 GB. Nonetheless, to be conservative, 11 GB is taken, given it is the uncompressed form of the data.

8.3.2 Image processing

The computation speed required to run the software necessary to process the lidar images is vital to correctly determine the hardware necessary. The detection software must be able to process the relative position, velocity and acceleration of the particle in three axes rapidly for fast tracking of the targeted debris fragments during the primary mission. Such a system must be able to process 10,000 images a second, and calculate moving averages of particle trajectories in real-time to keep the particle in view. Given the initial scope of the lidar system, and a 200 x 200 resolution, the software must also incrementally provide zoom commands during tracking to provide the necessary pointing accuracy, while maintaining sight on the target. Rems et al. (2015) provides insight into the processing speed necessary for a more advanced lidar algorithm, which is capable of tracking the position and rotational motion of larger debris objects (satellites). In this algorithm, a lidar takes images at 30 kHz, and creates a point cloud of around 600 to 900 points. A point cloud is the resulting digital mesh, as illustrated in Subsection 8.3.2.

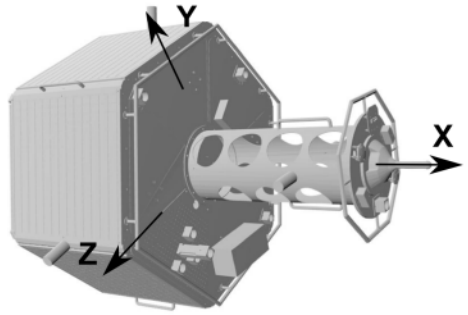

Figure 8.2: Debris object targeted by lidar. (Rems et al., 2015)

Figure 8.3: Mesh generated to depict debris object digitally. (Rems et al., 2015)

To measure orbital parameters of target objects, just one mesh point is necessary. It is estimated that, for a small debris piece, around 10 points is sufficient to achieve a rough estimation of its rotational motion, which is useful for analysis of space debris, and the effectiveness of ablation with rotation and shape effects, discussed in Subsection 4.2.7. Given that, in literature, the code takes in a minimum of 600 points and processes the relative motion between the mesh points at 2.9 GHz, it is expected that the throughput for 10 points is far lower. This algorithm would only need to be modified to target smaller debris objects and calculate their orbital parameters for cataloguing, which is relatively simple compared to the sophisticated motion analysis already achieved. To predict processing-speeds, "lines of code" (LOC) are used, defined as "statements that a programmer writes" (Zandbergen, 2021, p.187). Various types of "LOC" are possible, such as:

- N_{LOC}, number of lines of code processed per unit time.
- I/LOC, number of instructions carried out per LOC. This is dependent on the programming language, but is approximately between five and ten for higher languages like C++ or JAVA.
- $SLOC$, source lines of code. This is "the number of lines in the text of the program's source code" .

Using these parameters, the throughput (how much data can be processed per second) can be calculated, which is often expressed in Mega Instructions Per Second (MIPS). The unit of MIPS corresponds to processing speed in MHz. As an example, if the system is to process 50 MIPS, a processor of at least 50 MHz is necessary. The throughput, is given by:

$$\text{Throughput} = N_{LOC} \cdot I/LOC \tag{8.2}$$

[2]URL: https://www.airbus.com/sites/g/files/jlcbta136/files/2022-05/DS_Payload_Datahandling-CoReCi-2-2022.pdf [Accessed 14/06/2022]

In the case of the lidar algorithm processing, Rems et al. (2015) gives a size estimate of 27 MB. Using the estimate that software "typically requires 2-4 kB of memory size (depending on a.o. the programming language used) for each 1,000 lines of code (LOC)" (Zandbergen, 2021, p.188), it can be found that 27 MB of code corresponds to 9 million LOC (assuming an average of 3 kB per 1,000 LOC). This is very likely an overestimate, given that the storage of an algorithm is not only LOC, but may also contain things like data structures (which are not run in the same manner as the algorithm). However, an overestimate is conservative, and will not jeopardise the mission. The number of instructions per LOC is conservatively estimated to be ten, with an estimated frequency of 1 Hz. By considering the highest possible I/LOC, running the program once a second is deemed appropriate, given a debris particle remains in the lidar FoV for far longer. Using equation (8.2), the throughput is 90 MIPS, and thus requires at least a 90 MHz processor.

8.3.3 Cataloguing Communication Data

The payload data to be communicated to ground requires more detailed calculations. As mentioned prior, detection data is to be provided for ablated particles to verify both the success of the mission, and allow for further investigation of ablative propulsion in practice (providing experimental results). The same data is provided for cataloguing tracked debris objects for the secondary mission. Using the algorithm discussed in Subsection 8.3.2, the software will generate values for the debris characteristic length and area detected, the orbital parameters, and the angular rates in three axes. The number of debris in view and the time stamp of the sample are important parameters to transmit to ground as well.

The characteristic length of the calculated parameters are limited to particles ranging between 1 mm and 100 mm. Similarly, the area is limited to the range of 1 mm^2 to 10,000 mm^2, assuming an accuracy of 1 mm for the lidar camera, and a square area, to be conservative. Additionally, the orbital motion of the detected debris objects can be defined by six parameters: semi major axis, eccentricity, inclination, right ascension of the ascending node, argument of the perigee, and true anomaly. While the UN suggests only the apogee, perigee, inclination, and nodal period are required to register space objects[3], it is necessary to have a complete overview of the orbital motion of each detected particle for effective cataloguing of orbital debris. ESA recommends orders of accuracy for the catalogued initial orbital parameters (Musci et al., 2005), which are shown in Table 8.3. Finally, the detection algorithm is able to measure the angular rate of motion in three axes. It should be noted that this rotation is measured using ten points, as discussed in Subsection 8.3.2. Therefore, effective spin measurements of particles significantly smaller than 10 mm cannot be achieved, given the detection accuracy of 1 mm. However, this should not be an issue, as the spin data for catalogued particles is only provided for supplementary research and investigation. The number of bits needed to downlink each parameter value is calculated, assuming a base-10 floating point numbering system is adopted by the processor. Such a numbering system is described using the following expression on the left side, and the number of bits required for such a system is given by equation (8.3) on the right.

$$(-1)^s m 10^e \qquad\qquad b = \log_2 10^{SF_m} + \log_2 e + b_{sign} \tag{8.3}$$

where s is the sign digit, allowing for representing positive or negative numbers of necessary. Also, m is the mantissa, taking the value of $9.\dot{9}$ with a given number of significant figures, SF_m determining the achievable precision of the number. Finally, e is the exponent of the number, assuming base-10. The number of bits, b, for each parameter is determined by equation (8.3), where b_{sign} is 1 if a sign bit is necessary and 0 otherwise. The calculation of the number of bits needed to represent each payload sample to be communicated is shown in Table 8.3. An accuracy for each variable had to be estimated for this. For the timestamp, the accuracy considered was 1/10,000 given an imaging rate of 10,000 Hz. Similarly, as the lidar can detect up to 1mm, the characteristic length and area are to be downlinked with mm and mm^2 accuracy respectively. Finally, the orbital parameter accuracies are taken from (Musci et al., 2005) and the angular rate accuracy is taken as 0.01°/s.

The total data per sample is calculated to be 300 bits. Assuming one sample is computed each second, the payload TM data rate is simply 300 bps. This is a remarkably low data rate, which is expected considering on-board processing is implemented, and thus only numbers have to be downlinked for the mission. However, assuming the information to be downlinked may be made much more advanced for more extensive research and more accurate cataloguing, a very high safety factor of 10 is applied, resulting in an estimated TM data rate of 3,000 bps.

8.4 On-board computer and storage

The OBC will run the software that determines (top-level) subsystem operation, and as such, is influenced by the total work it has to perform per second - the same as the aforementioned IPS. These IPS flow down from the lines of code the OBC has to run, precisely like the payload computer detailed before. To determine the total number of LOC, the $SLOC$ per subsystem is required. Determining the $SLOC$ can be done using SMAD (Wertz, Everett, et al., 2011, p.614), which gives Table 8.4, where averages were taken when $SLOC$ ranges were given. Input from each subsystem lead engineer resulted in determining what functions are required, and the necessary $SLOC$ was determined. The three subsystems with code present in the spacecraft (thus neglecting structures), but not given in SMAD, are propulsion, and obviously the detection (already discussed) and ablation subsystem. For the propulsion subsystem, 800 $SLOC$ was deemed appropriate, given the relatively low complexity of the system (similar to the TMS for example) compared to, e.g., GNC. The ablation laser is more complex to determine, given the novelty of the system. It is assumed that 4,000 lines of code should exceed

[3]URL: https://www.unoosa.org/oosa/en/ourwork/spacelaw/treaties/registration-convention.html [Accessed 13/06/2022]

Table 8.3: Data breakdown of one detection sample.

Data Variables	**Max Value**	**Accuracy**	SF_m	**e**	b_{sign}	**total bits**
Boolean	1	1	-	-	-	1
Number of Debris Found [-]	1,000	1	3	3	0	12
Time Stamp [s]	31,536,000	10^{-4}	11	7	0	40
Characteristic Length [mm]	100	1	3	2	0	12
Area [mm^2]	10,000	1	4	4	0	17
Semi Major Axis [m]	10,000,000	10	7	7	0	27
eccentricity [-]	1.00	10^{-6}	7	0	0	24
Inclination [deg]	180	10^{-5}	8	2	0	29
RAAN [deg]	360	10^{-5}	5	2	0	19
Argument [deg]	360	10^{-5}	5	2	0	19
True anomaly [deg]	360	10^{-5}	5	2	0	19
Euler Angular Rate 1 [deg/s]	10,000	10^{-2}	7	4	1	27
Euler Angular Rate 2 [deg/s]	10,000	10^{-2}	7	4	1	27
Euler Angular Rate 3 [deg/s]	10,000	10^{-2}	7	4	1	27
Total data per sample [bits]						300

Table 8.4: Total SLOC per subsystem.

Subsystem	**SLOC sum**	**Source**
CDHS	19,750	SMAD
EPS	1,200	SMAD
GNC	27,000	SMAD
Detection	-	-
Ablation	8,000	Estimate
Propulsion	800	Estimate
TMS	800	SMAD
TTC	4,500	SMAD

Table 8.5: Table indicating the throughput the OBC must provide (at least 6.3 MHz) for subsystem operations (excluding the detection subsystem), and the storage size required to save all the lines of code (0.19 MB).

	OBC Throughput			
Subsystem	**SLOC**		**I/LOC**	**Throughput**
CDHS	19,750	197,500	10	1,975,000
EPS	1,200	12,000	10	120,000
GNC	27,000	270,000	10	2,700,000
Detection	*Payload CPU*	*Payload CPU*	*Payload CPU*	*Payload CPU*
Ablation	8,000	80,000	10	800,000
Propulsion	800	8,000	10	80,000
TMS	800	8,000	10	80,000
TT&C	4500	45,000	10	450,000
		IPS		6,205,000
		Clock Speed [MHz]		6.30
		Memory size [MB]		0.19

what is required, given the laser functions include turning it on and off, monitoring its state, and morphing the mirrors to achieve the spot size at the debris distance. Given the notorious unreliability of software estimation, on top of the predicted overestimation of the LOC needed, a factor two is multiplied by the $SLOC$ to ensure the processing power necessary will not be underestimated. This yields 8,000 $SLOC$. Table 8.4 gives the total LOC per subsystem.

As a general estimate, N_{LOC} is estimated to be ten (Zandbergen, 2021, p.187). This seems reasonable, given that it represents some average processing rate. In other words, taking the GNC system as an example, there are some parameters that are determined with a high frequency (like angular velocity during debris tracking for example), while parameters like orbital velocity require a lower rate of calculation during nominal operation. The I/LOC parameter was kept at ten, to ensure a conservative estimation of processing power. Using the aforementioned N_{LOC}, $SLOC$ and I/LOC parameters, Table 8.5 is generated. The subsystem code (excluding detection subsystem) requires a storage of 0.19 MB (3 kB per 1,000 LOC), and a throughput of at least 6.3 MHz (rounded upward from 6.205 MHz).

Table 8.6: Data rate per subsystem, determined from the number of TM points, and frequency per subsystem.

Subsystem	Number of TM points	% Servo Regulation	% Vital Control	% Planning	Resultant Frequency [Hz]	Total Data Rate [bps]
CDHS	10	0	50	50	5.5	880
EPS	40	10	80	10	18.1	11,584
GNC	80	10	80	10	18.1	23,168
Detection	50	20	60	20	26.2	23,960
Ablation	50	20	70	10	27.1	21,680
PROP	20	30	50	20	35.2	11,264
TMS	80	30	60	10	36.1	46,208
TTC	20	0	95	5	9.55	3,056
					Sum [bps]	141,800

8.4.1 Subsystem Data Rates and Storage

Each subsystem transmits data from a set amount of variables (TM points) to ground, in order to allow for adequate monitoring of each subsystem's performance and health information. The number of TM points per subsystem were estimated by looking at system complexity. For example, the complexity of GNC requires more data points (position, velocities, angular rates, etc.) to be transmitted compared to propulsion, where most of the data is related to health information and whether, as an example, a valve is open or shut. The payload systems both have a high number of TM points relatively speaking, due to the novelty of the systems. Given this is the first mission of its kind, precise monitoring of the payload systems is required, to allow for adequate performance analysis. The frequency range at which system types operate is broken up into three categories: servo regulation at 1,000 Hz, vital control at 2 to 100 Hz, and planning at 0.1 to 1 Hz (Ley et al., 2009, p.364). These frequencies do not correspond to the rate at which data is collected for telemetry, but they give a general indication of what parameters operate at a higher rate than others. Every subsystem is predicted to require 16 bits (using a mantissa with m is 4 digits, base-10, and e is 4 digits), which is sufficient to provide data to 4 significant figures - enough to show, e.g., "Battery 1 Voltage = 6.2 V". For the TM data rates, the collection rate of: servo regulation/ moving parts is 100 Hz, vital control/ general subsystem operations is 10 Hz, and planning is 1 Hz.

Table 8.6 includes HK and scientific data for the detection system, where the scientific data (3,000 bps) is added onto the HK data in the "Total Data Rate" column. These data rates may be compressed to be as storage efficient as possible. This is akin to creating a .zip file on a Windows computer, where "data compression reduces the number of bits to the most essential ones" (Zandbergen, 2021, p.185). Compressing the data by values up to fifty are "well possible" according to Zandbergen, and can occur in two ways: lossless and lossy. In lossless compression, as the name implies, no data is lost, as only "statistical redundancy" is removed. Contrary to this, lossy compression actually removes information that is deemed unnecessary. The data rate using a compression factor of fifty is merely 2,836 bps.

8.4.2 Data storage

Storage for the TM data is necessary in between data dumps. In this regard, the longest possible duration in between dumps is considered, given this is the minimum storage capacity the satellite must have. From the TT&C ground network, discussed in Chapter 10, it is determined that the longest time between dumps is 200 minutes. Thus the TM data collected, assuming a compression factor fifty, can be worked out by multiplying the total data rate by time, giving 4.25 MB, while uncompressed (worst case) data will be require 212.70 MB. Assuming that, for adequate failure diagnosis, data should be stored for the previous five data dumps, this would require a maximum storage capacity of 1.06 GB uncompressed, or 21.27 MB for compressed data. Data compression is a common technology, and thus the compressed data volume (21.27 MB) is used to determine off-the-shelf components later, while TT&C is expected to send 4.25 MB. A more reasonable, expected storage value is 1.7 MB, given that a time between dumps of, on average, 80 minutes is expected.

8.4.3 Data rate compared to existing missions

The housekeeping data rate of 2,836 bps is not very comparable to existing spacecraft, given the difference in mission type. While the majority of space missions may perform missions that include "doing science", and thus sending down, e.g., images or signals, this mission only sends down orbital parameters in terms of scientific payload. However, the housekeeping rate may be compared to literature to ensure feasibility. Wertz, Everett, et al. (2011, p.629) states up to 10 kbps can be considered for housekeeping downlink rate, and up to 5 Mbps for scientific data. From TT&C, five minutes is considered the worst case time to downlink data. Downlinking the 4.25 MB in 300 seconds would require 113.4 kbps downlink, while downlinking 1.7 MB requires 45.4 kbps downlink. These values are thus too high compared to conventional spacecraft for housekeeping data, but fall well within scientific data downlink rates. Thus, while the data rates of this spacecraft are definitely feasible, they are high. This is due to three factors: overestimation of the frequency at which housekeeping will be collected (100 Hz for servo actuation is extremely high, and the real spacecraft will likely use less; however, for this stage in the design process it ensures the design remains robust), the novel payloads used (around 33% of the housekeeping data comes from purely payload monitoring), and the fact that later on in the mission, when nominal functioning of the spacecraft is establish, the housekeeping data is collected at lower rates.

8.4.4 Operating System and Protection Systems

As the project is commissioned by ESA, the operating system mainly used will be RTEMS, a "Real-Time Executive for Multiprocessor Systems". It is open source, which means it is free to use by any person, and does not come with high licensing costs. The reason RTEMS is used, as opposed to something like Windows for example, is that "real-time" operating systems negate any delays caused by blocked cores[4]. Due to its open source nature, it can also be customised to work exactly as desired, without running into scheduling problems like NASA's OS of choice: VxWorks[5]. The way VxWorks was developed meant that "a programmer is stuck with a preemptive priority-based scheduler for tasks with differing priorities and a round-robin when multiple tasks have the same priority. It can't be changed."[5] RTEMS can also be optimised to run on LEON, ESA's processor, with services provided by Gaisler Research[6]. RTEMS is still being qualified for the most safety-critical functionalities (it is currently level B[5]), so where it is not possible to use RTEMS, another operating system used by ESA should be implemented, like "ObjectAda real-time RAVEN", which is the highest level: level A[1].

A firewall is, of course, necessary to protect against hacking. Though the detailed design of this falls outside the scope of the DSE, some solutions for security are analysed. To prevent hacking, the CDHS system could include a firewall similar to a BGAN firewall, which "effectively blocks all traffic except what you provide Ground Control in a whitelist of allowed IP addresses."[7] Authentication systems are similar to this where, if a signal is not authenticated before it leaves ground, it is ignored by the satellite[8]. Encryption, with changing encryption keys, is necessary too. Quantum encryption is likely the future for this, given the high processing power results in an advantage in computing encryption keys over hackers decrypting them[9]. Should it be impossible to communicate with the satellite (due to jamming for example) after a certain number of orbits, the laser will be inoperative until communication is restored. The satellite will focus on trying to regain communication during this period (by better pointing of the antenna, for example).

8.5 Component Selection

Now that the storage and processing power for the detection and remaining subsystems has been determined, off-the-shelf components can be selected. Table 8.7 gives the bare minimum in terms of requirements, and thus safety margins need to be incorporated. SMAD states that, as a rule of thumb, it is recommended to use less than 70% of the available throughput (Wertz, Everett, et al., 2011, p.615). All the storage requirements (for code and TM/paylaod data) are multiplied by three, to allow for bit flip correction. A bit flip is when a binary 1 becomes a 0, and vice versa, which may occur due to the harsh space environment. Up to ten a day may be expected (Ley et al., 2009, p.362).

8.5.1 Detection Payload Specifications

Given the novelty of the implementation of the detection system to track space debris, it can easily be argued that twice as much throughput (so 180 Mhz instead of the required 90 MHz) is necessary to choose. As the algorithm is a standalone piece of software, the processing requirements will be specified with a high level of confidence, so a factor above two is not necessary. Therefore 180 MHz is set for the detection processing speed. In terms of storage, a factor two is applied, thus 22 GB of data will need to be able to be stored. The algorithm size will not suddenly be higher or lower, given literature already gives a value of 27 MB. When considering the changes that have to be applied for compatibility with space debris, the storage size will likely be lower than those 27 MB, given its reduced complexity (10 cloud points instead of 600-900), and likely simplified data structures. Regarding its performance in space, the storage an algorithm takes up is already set - it will not suddenly alter in orbit. That said, should it change during further development of the spacecraft, 27 MB is very little compared to the 22 GB necessary, so it should not pose any problems. A factor two is assumed adequate for further development, giving 54 MB. All the data is saved three times, including the housekeeping data, thus 66 GB and 162 MB for the images and algorithm respectively are the requirements. Regarding data rate, given a certain number of pixels (resolution), bits per pixel, and frequency, this cannot alter. It is not possible, with set camera parameters, to get a higher data rate. Therefore, this should remain at 8.8 Gbps. Any fluctuation in this already incredibly high data rate should also be carefully monitored during further development - and is likely a killer to feasibility - and for this reason, the maximum data rate is set to 10 Gbps.

8.5.2 Remaining Subsystems Specifications

For the remaining subsystems, 6.3 MHz is required, which yields a minimum processing speed of 9 MHz if following the same 70% rule of thumb as before. However, unlike the detection algorithm, a factor five to ten is suitable, given the overall (computational) performance of the spacecraft is unknown at this point. As such, a maximum of 90 MHz is desired. Regarding storage, the subsystem HK data storage was previously set to 21.27 MB. As with the throughput, this may be increased by a factor ten due to the unknown performance of the spacecraft at this point (the subsystem performance is a

[4]URL: https://www.esa.int/Enabling_Support/Space_Engineering_Technology/Software_Systems_Engineering/RTEMS [Accessed 13/06/2022]

[5]URL https://arstechnica.com/features/2020/10/the-space-operating-systems-booting-up-where-no-one-has-gone-before/ [Accessed 13/06/2022]

[6]URL https://www.esa.int/TEC/Software_engineering_and_standardisation/TECLUMKNUQE_0.html [Accessed 13/06/2022]

[1]URL https://www.esa.int/TEC/Software_engineering_and_standardisation/SEM5T7XIPIF_0.html [Accessed 13/06/2022]

[7]URL: https://www.groundcontrol.com/en/products/inmarsat/bgan-range/bgan-firewall/ [Accessed: 21/06/2022]

[8]URL: https://trustedcomputinggroup.org/cyber-security-in-the-skies-protecting-satellites-from-attack/ [Accessed 21/06/2022]

[9]URL: https://www.esa.int/Applications/Telecommunications_Integrated_Applications/Quantum_communication_in_space_moves_ahead [Accessed 21/06/2022]

Table 8.7: Requirements for CDHS off-the-shelf components, including bit flip correction for storage capacities.

	Processing Speed [MHz]	**Storage [MB]**	**Maximum Data Rate [kbps]**
Detection Payload	90 (algorithm processing)	11,000 (image storage) 27 (algorithm storage)	8,800,000 (lidar images pre-processing)
Remaining Subsystems	6.3 (subsystem processing)	21.27 (TM data storage) 0.19 (LOC storage)	141.8 (HK + detection data output)
Combined with Safety Factors	180 (algorithm processing) + 90 (subsystem processing)	66,000 (image storage) 162 (algorithm storage) + 638.1 (TM data storage) 1.14 (LOC storage)	10,000,000 (lidar images pre-processing) + 283.6 (HK + detection data output)

larger unknown than the standalone algorithm), and updates to subsystem code may be required in orbit. This gives 212.7 MB. For further development of the subsystems code, a factor two is applied, as with the detection algorithm. A higher factor is not applied, as cost will be more limiting than storage space. In other words, before storage becomes a problem (0.19 MB is very low, compared to the storage of lidar images), the cost budget will ensure a simpler subsystem code logic is attained. Again, the storages are multiplied by three to give 638.1 MB of housekeeping storage, and 1.14 MB of code. On the maximum data rate, the 70% rule from SMAD is also treated conservatively, and is rounded up to a factor two, giving 283.6 kbps. This gives Table 8.7, and now components must be chosen to satisfy these requirements.

8.5.3 Commercial, Off-The-Shelf Component Selection

In terms of processing speed, the requirements are easy to fulfil. The next generation of processing power, the High Performance Data Processor (HPDP) from Airbus, can run a total of fourty 250 MHZ processors on one OBC. From the product specification sheet, the HPDP contains "40 ALU Processing Array Elements (PAEs 16-bit) running with 250MHz each", with "2 Harvard type VLIW 16-bit processor cores (FNCs) running at 125MHz".[10] It is therefore possible to run the non-detection subsystem operations (90 MHz) on a single core, and the detection algorithm (180 MHz) on another core. This leaves 38 cores available for any possible secondary payloads, as well as dual connections to the detection system and subsystems, so that if the primary connection between OBC and subsystem fails, a secondary can continue. It could even be decided that each subsystem in Table 8.4 is best operated separately, which, including the detection algorithm, still only requires a maximum of 16 processors used, depending on single or dual connections. Now that processing speed is satisfied, the storage capabilities need analysis.

In general, it is better to allow code to be run from the random-access memory (RAM) than solid state recorder, given the data can be accessed much faster. The detection algorithm + subsystem operation code as defined before require around 165 MB of RAM. The HPDP has a total SDRAM (synchronous dynamic random-access memory) capacity of 5 Gb[8], or 625 MB, which is more than three times what is necessary. For clarity, SDRAM is a type of RAM, so the fact that SDRAM is given instead of RAM does not change the system functionality. The second part of storage refers to data storage, both for the detection system and general housekeeping data. In total, 66.7 GB is required for data storage. This does not include data compression for the lidar images, which is conservative, given that adding a component like the CORECI 2 will only add to power, mass, and volume requirements. The HPDP will be able to do image compression in the future[11], thus it is expected that the spacecraft will include data compression abilities before launch. Thus, to satisfy the storage requirements, Airbus' NEMO-2[12] is chosen, which contains a total of 8 Tb of data when choosing the low-end "2040" model (for comparison, the "2120" model has a 16 Tb capacity). This is around 15 times what is required, and allows for wide flexibility in choosing secondary missions, not only for this mission, but for future missions should different secondary missions be desired. This high storage capacity is also useful for contingencies in case the satellite cannot communicate with ground. The 8 Tb storage capacity allows HK data saving for thousands of ground network passes, should the data not be dumped. While the NEMO-2 contains a "SCOC3 System-On-Chip based on the LEON3 sparc v8 core[9], the processing power of this is limited to 80 MHz (Koebel et al., 2010, p.1346), and therefore the detection algorithm will require a high speed connection to the HPDP to allow for adequate processing.

Lastly, the data rate for the detection subsystem and remaining subsystems must be able to be processed. The 10 Gbps required by the detection algorithm is possible using a single slice, of the two total slices, of the "2040" NEMO-2 model, which contains four high-speed 2.5 Gbps ports[9] (which combine to 10 GBps). This would, however, require that the lidar images be broken up into four quarters, to allow each quarter to be transferred to the processing unit separately. The same slice of the NEMO-2 allows for four times two 200 Mbps power and two 100 Mbps data rate input, which is enough to allow for the housekeeping data rate, while the HPDP allows for four times 1.1 Gbps. Routing all the

[10] URL: https://www.airbus.com/sites/g/files/jlcbta136/files/2021-11/publication-sce-payload-hpdp-12-2020.pdf [Accessed 14/06/2022]

[11] URL: https://indico.esa.int/event/225/contributions/4251/attachments/3379/4428/OBDP2019-S05-05-Airbus_Helfers_HPDP-40_High_Performance_Data_Processor_A_New_Generation_Space_Processor_in_Demonstration.pdf [Accessed 14/06/2022]

[12] URL: https://www.airbus.com/sites/g/files/jlcbta136/files/2022-05/datasheet-datahandling-nemo2-2022.pdf [Accessed 14/06/2022]

Table 8.8: CDHS component specifications from literature.

	Power [W]	Mass [kg]	Size LxHxW [mm]	Operating Temperatures [°C]	Reliability	Lifetime [years]
Airbus NEMO-2	22	8	365x220x170	-25 to +60	0.995	12
Airbus HPDP	1.82	-	-	-55 to +125	-	20

housekeeping data to the HPDP will simplify the CDHS architecture, and thus this option is chosen. The housekeeping data, once assembled by the HPDP, is saved in the NEMO-2, in the same slice as the lidar data. This means that the secondary slice in the NEMO-2 "2040" model is completely unused, and becomes available for detection system and housekeeping data redundancy, should the first slice fail. Thus, to conclude, the CDHS system will require one Airbus NEMO-2 "2040" model, and two Airbus High Performance Data Processors. The reason for only one NEMO-2 is that it is extremely reliable, as will be shown in Subsection 8.5.4, while an OBC failure is more probable given the new state of the HPDP technology. This configuration complies with all requirements from Table 8.1.

8.5.4 Component Budgets and Specifications

With the components determined, important characteristics to determine are: reliability, power usage, mass, volume, and operating temperatures, given in Table 8.8. Data on the HPDP was lacking, given that the component is very novel and under continued development. The first step in the next design phase would be to contact the developers of the module, to check the component really does fulfil all requirements. Assuming that HPDP mass and size scale with NEMO-2s power, the HPDP specifications become 0.67 kg (1.34 kg in total) and a cube with volume of 0.001 m^3, thus a length of around 11 cm per side. In total, the power budget then becomes (for one NEMO-2 and two HPDPs) 25.64 W, with a mass budget of 9.32 kg, and a combined volume of 0.016 m^3. Given the overall CDHS budgets of 104 kg and 1096 W, these components fit well within the budget. Some comments can be made on the remaining NEMO-2 parameters, such as operating temperatures, which are limited for the CDHS by the NEMO-2, giving operation between -25 and 60°C. The NEMO-2 is also extremely reliable, with a reliability of 0.995 over 12 years, thus practically no failures should occur in the mission duration of one year. The lifetime of the overall CDHS system is also limited by the NEMO-2, to give 12 years, which is still above the mission duration considered.

8.5.5 CDHS Sensitivity Analysis

A sensitivity analysis is required to indicate whether major system changes would be required, should any inputs into the CDHS system vary (e.g., data rate doubles). In the case that the "Combined with Safety Factors" parameters (Table 8.7) should halve, the COTS chosen should remain. This is because the processing power required by the algorithm should not change, and including safety factors, the processing speed required cannot be provided by a single LEON3 chip, for example[2]. It is, therefore, practical and useful to remain with the state-of-the-art Airbus HPDP, given it provides exceptional processing speed, and has the "ability to meet the increasing requirements of future payloads regarding flexibility, processing power and re-programmability"[9]. In other words, the Airbus HPDP is future proof, and does not require much in terms of power, mass, and volume (given mass and volume are estimated appropriately) from the spacecraft. The same reasoning can be used for the NEMO-2, where the performance benefits (in terms of storage, but more importantly data rate) outweigh the selection of other components. This is especially true because this project is performed for ESA, and close cooperation with Airbus (the components selected are two of the four that Airbus' CDHS department provides) is beneficial, as opposed to a US-based company for example. In the case that the requirements are doubled, the following performance must be met: 540 MHz processing capabilities, 495 MB of RAM, 133.4 GB of storage capacity, 20 Gbps data rate for the image processing, and 567.2 kbps for the housekeeping data.

The HPDP has the potential for 40 times 250 MHz, therefore 540 MHz will not be a problem, and does not need a different component. Similarly, the 625 MB of SDRAM available on the HPDP will allow for 495 MB to be saved, thus code saving is not a problem. Clearly, the NEMO-2 storage capacity of 8 Tb will also be able to save the 133.4 GB of data. Housekeeping data rates of 567.2 kbps will be able to be routed into the HPDP (which allows for four lots of 1.1 Gbps input). The data rate of 20 Gbps would, however, require a slight CDHS redesign, and the "2080" model must be chosen. This is because it has three slices available, so the detection data could be routed over two slices of 10 Gbps each, while still keeping the same redundancy on the last slice like the current design. The overall power and mass of this system would be based on one NEMO-2 "2080" model, and two HPDPs, giving a total mass of 12.34 kg, power of 47.64 W, and volume of 0.019 m^3, which all still remain within the budget provided by the systems engineer.

8.6 Data Handling and Software Block Diagram

Figure 8.4 shows the architecture of the CDHS system, including data rates for the housekeeping data, data flows from the detection system, and shows that the software for the detection and remaining subsystems run on two separate CPUs.

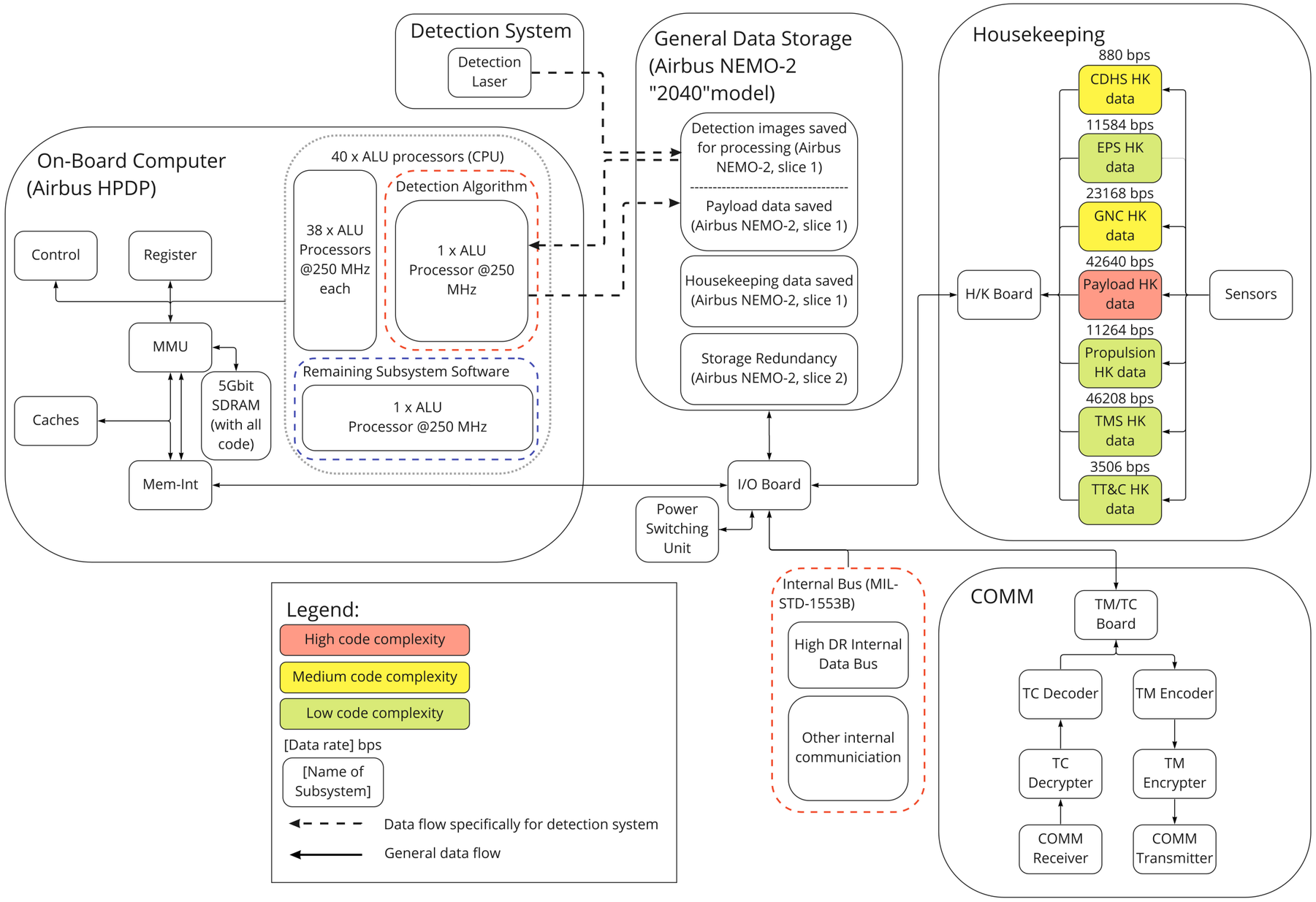

Figure 8.4: Data and software block diagram.

Thermal Subsystem 9

The thermal subsystem is critical for the Space Sweeper mission, mainly due to the high-power laser system. During ablation, the laser requires an average power of 27.8 kW is required, of which about 75% is dissipated as heat. In case of an unpressurised spacecraft bus, convection and conduction via air does not occur, resulting in all dissipated heat to remain concentrated near the heat sources. To trade-off different methods for heat transfer, a distinction is made between intra-spacecraft heat exchange, and heat exchange with the environment.

9.1 Thermal Subsystem Requirements

The following requirements represent the most significant subsystem requirements taken over from the Teixeira et al. (2022a).

Table 9.1: Thermal subsystem requirements.

Requirement ID	Description
SS-SYS-TMS-REQ-001	The Thermal Management System shall maintain the temperature of all components within their operating temperature range.
SS-SYS-TMS-REQ-002	The mass of the Thermal Management System shall not exceed 86 kg.
SS-SYS-TMS-REQ-005	The power used by the Thermal Management System shall not exceed 1506 W.
SS-SYS-TMS-REQ-006	The thermal management system shall be functional throughout the entire mission life.

9.2 Design options and Trade-off

For the design of the TMS for the Space Sweeper mission, only radiators and elements for heat transport were considered. Heaters of any kind were not considered due to the limiting factor being the high dissipative power and a lack of heat is of little concern.

This section first describes the different possibilities for heat transfer within the spacecraft. The main goal is to transport the heat from all heat sources to the heat sinks. The selection of an approach is guided by a trade-off process. The criteria at the core of this process are mass, power consumption, heat flux capability and system complexity. Secondly, the section describes reasoning for the selection of a sub-type of radiator, without elaborate trade-off process due to the similarity of the design options.

9.2.1 Criteria

The system mass is a critical performance parameter for the TMS in order to stay within the limited mass budget of 60 kg. The performance of subsystems can however not be quantified without full detailed design and layout. Nevertheless, the design options can be qualitatively ranked. This criterion was assigned a weight of 33%, primarily due to the low mass budget available to meet very high thermal performance.

Power consumption is the primary differentiator between active and passive heat transport systems. Both heat pipes, as well as thermal straps, are fully passive design options, whereas both kinds of MPFL systems are actively pumped and require input power to drive the pumps to circulate the working fluid.

With peak heat output of higher than 25 kW during ablation laser operation, the maximum heat flux is an important measure that dictates the required size and mass of the heat transport solution. The maximum amount of heat that may be transported widely varies between the design options. In particular, MPFL and heat pipes separate themselves from thermal straps due to their use of convection next to conduction, whereas thermal straps rely solely on conduction through solid material.

Another differentiator between active and passive systems, as well as the different active systems, is the complexity of the system, which is also related to the probability of failure. This criterion is evaluated qualitatively, however the ranking naturally flows from design options that can be seen as increasingly complex versions of one another. The complexity was determined to be relatively less important than the other criteria, and is weighted at 10% as a consequence.

9.2.2 Design Option Performance

Thermal Straps

Thermal straps are the simplest option considered and consist purely of solid material in a mesh structure to provide flexibility. They provide limited conductor capabilities for short distances. A common material for thermal straps is copper, providing a thermal conductivity of 398 W/m^2.

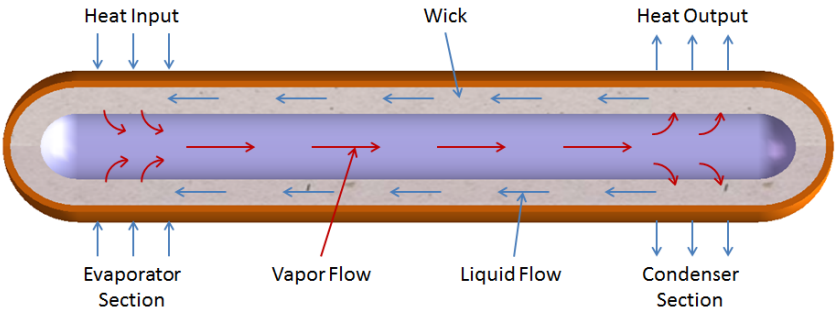

Figure 9.1: Illustration of a heat pipe. The internal fluid is present in two phases, allowing for heat absorption and heat rejection[1].

Figure 9.2: Internal wick structure of an axially grooved heat pipe[2].

Heat Pipes

Heat pipes are a passive way to move a fluid through a tube, thereby transporting heat. A working fluid, usually ammonia or water, is transported through a the tube by means of capillary driving forces. These forces are the result of axial grooves (see Figure 9.2), or sintered material, on the inside of the tube. The working principle of a heat pipe is shown in Figure 9.1. A heat source is placed on the left side, where the working fluid evaporates. A heat sink on the right side takes away heat from the gas, such that it condenses. The hot gas on the left side has a larger specific volume than the cold gas on the right side, resulting in a gas flow from left to right. The fluid then travels from right to left, through the wick, by capillary action (Camañes et al., 2019).

The motion of the fluid is rather slow, resulting in low heat fluxes, as compared to actively pumped loops (Camañes et al., 2019). The main advantage is that heat pipes do not require any pumping power, as it is indirectly provided by the heat source and sink. This also results in a low mass. On an operational level, heat pipes have a low complexity, since no active power input or control is needed. However, integration of heat pipes into the spacecraft is relatively complex, since they are often pre-filled by the manufacturer (Camañes et al., 2019, p.42).

The two most common working fluids are ammonia (where the tubes are aluminium), and water (where the tubes are copper) (Shukla et al., 2015). The former has a heat flux of a few W/cm^2, while the latter has a heat flux of maximally 100 W/cm^2 (Camañes et al., 2019, p.23). The operating range of ammonia is about -60°C to 100°C, and the range for water is about 25°C to 300°C (Shukla et al., 2015, p.11). Considering the high operating power of the ablation laser, and the high expected laser temperature as a result of this, water is expected to be the more suitable fluid. Variable conductance heat pipes can also provide the the necessary control over the radiated temperature by disrupting the function of the heat pipe and thereby limiting the amount of heat transported to the radiators. This however requires some electrical power input for a heating element with a low power draw at approximately 1 W[3].

Mechanically Pumped Fluid Loops

As opposed to thermal straps and heat pipes, a Mechanically Pumped Fluid Loop (MPFL) uses input power to actively pump the working fluid through a set of tubes. MPFLs greatly outperform heat pipes in terms of heat flux, since MPFLs are not limited by capillary movements. The working fluid can either be chosen such that it remains in a single, liquid, phase (1Φ-MPFL), or such that it undergoes a phase change between fluid and gas (2Φ-MPFL) (Camañes et al., 2019, p.16). The latter has a higher heat flux (222 W/cm^2 for Refrigerant-236fa) (Kheirabadi et al., 2016) than the former (170 W/cm^2 for water cooling) (Kheirabadi et al., 2016), as it makes use of latent heat, rather than only sensible heat. A major drawback of MPFL systems is their size. An MPFL system requires large accumulator tanks, both in single phase and two phase systems (Camañes et al., 2019, p.40), resulting in a high mass and volume..

Comparative Heat Transport Performance

In comparison to other design options, heat pipes offer the best mass-specific performance and therefore are also qualitatively rated as the lowest mass. Both multi- and single phase mechanically pumped fluid loops are strong options for extreme powers and their mass scales better to extreme power or far distances, however lose out to heat pipes for the dissipated powers and distances involved. Thermal straps provide comparatively low performance, but due to the use of only solid material conductors, come with a very high mass penalty.

Regarding power consumption, both thermal straps and heat pipes take the top spot due to their passive nature. Fluid loop systems differ based on whether a single phase or two phases are used. Single phase fluid loop systems require better pump performance and thereby also require higher input powers, therefore coming last when compared to other options.

[1] URL https://myheatsinks.com/heat-pipe-solutions/standard-heat-pipes/ [accessed 07-06-2022]
[2] URL https://commons.wikimedia.org/wiki/File:Grooved_Aluminum_Extrusion_for_Spacecraft_Heat_Pipes.jpg [accessed 07-06-2022]
[3] URL https://www.1-act.com/resources/tech-papers/variable-conductance-heat-pipes-for-variable-thermal-links/ [accessed: 14-06-2022]

Table 9.2: Trade-off between top-level thermal control options. The width of the columns represents the importance.

	Mass (High)	**Power Consumption (Moderate)**	**Heat Flux (High)**	**Complexity (Low)**
Heat Pipes	L	L	M	M
Thermal Straps	H	L	L	L
1Φ-MPFL	M	H	H	M
2Φ-MPFL	M	M	H	H

Heat fluxes with both types of MPFL can be almost arbitrarily high, provided pump performance is high enough and the radiators are large enough. They therefore perform best on the criterion. Heat pipes can reach very high performance, however must obey several physical limits due to properties of the working fluid, and the fluid flow speeds within the heat pipe. Lastly, thermal straps perform poorly compared to other options as they cannot make use of convection of a working fluid, but only conduction in solid material.

However, thermal straps are extremely simple structures, while fluid-based systems are far more complex and rely on many more effects than solid material conduction. Single phase fluid loops and heat pipes are operationally somewhat complex, however not as intricate as multi-phase pumped loops. The performance of all options is outlined in Table 9.2, where heat pipes arise as the clear best option for the use case in this mission.

Heat Exchange with Environment

For the heat exchange with the space environment, radiation is the only possible heat transfer method available beside ejecting hot material, making radiators a necessity. Several different forms of radiators may be employed, providing different levels of controllability.

Fixed radiators with no moving parts are the simplest form of radiators, providing no control over the amount of heat radiated away from the spacecraft. The only control over the performance fixed radiators can provide, comes through the use of different materials and adjusting the surface properties, in particular absorbtivity and emissivity. Optical Solar (OSR) materials are advanced radiator materials that provide far higher emissivity-to-absorptivity ratios than paint or coatings, and therefore offer significantly improved heat rejection capabilities when exposed to environmental radiation[4]. For this reason, OSR-based radiators are employed in the design of the thermal management system.

A type of radiator that can provide active control over the amount of heat radiated is the Louvre. Several rotatable sections are placed on top of the radiator to alter the effective surface area of emissive or absorptive material. As a result, the performance of the louvre may follow the usage profile of the payload. Furthermore, it can create space between surfaces that are heated by solar radiation and the rest of the spacecraft and act as a thermal insulator, reducing the incident heat flux as necessary. However, louvre operation also presents a significant reliability concern due to the use of many movable parts. A failure of a louvre panel system in the closed state may disable the primary payload and prevent the spacecraft from fulfilling its primary mission. Hence, louvre use was eliminated on the basis of insufficient reliability.[4]

9.3 Thermal Analysis

To analyse the thermal behaviour of the spacecraft and come to a conclusion about the required radiator areas, as well as the geometry of the TMS, including routing of heat pipes and other conductors, a nodal, lumped model was employed. This was chosen over finite-element-based model and codes like ESATAN-TMS due to the inability to quickly iterate in a concurrent design situation. When parameters of various subsystems, such as mass estimations, materials, as well as estimations of the dissipated power or the subsystem position, change very frequently, constant re-computation of the thermal performance is required. Furthermore, node-based models agree very well with finite-element-based models, which are often only required to evaluate precise thermal gradients in marginal cases.[4] The goal of the thermal analysis is to determine the required area and performance of the radiators, as well as the amount, length and layout of the heat pipes and linear conductors within the spacecraft. Furthermore, the nodal model is used iteratively in cooperation with the development of the spacecraft structures in order to optimise the layout of the subsystems according to not only the functional constraints, but also thermal performance, as the location of subsystems and the proximity of components to one another may have severe implications on the thermal behaviour of the spacecraft.

[4]Personal communication Martin Lemmen (Thermal Engineer, TNO), meeting dd. 09/6/2022, 16:00

9.3.1 Model Assumptions

To make the formulation of a node-based thermal model possible, several assumptions are made:

Table 9.3: List of assumptions used for the nodal thermal analysis simulation.

Assumption ID	Description	Validity
TMS-AS-01	Each node acts as a point source for internal radiative heat transfer, radiating equally in all directions.	The components that are represented by nodes are generally small and have the same surface material and temperature over the entire surface due to their tight internal geometry. This assumption causes a significant error only when nodes represent very large components. When this is the case, these components should be broken down into multiple nodes.
TMS-AS-02	Heat pipe performance is modelled as a weak linear conductor when outside the working temperature range, and as a strong linear conductor when inside the working temperature range.	When the working temperature range is not met, the working fluid does not transport heat and the heat pipe behaves like a linear conductor solely due to the solid pipe material. When inside the working temperature range, heat pipe performance increases drastically and can be approximated using linear conductance.[4]
TMS-AS-03	Radiation from node surfaces exposed to the outside of the spacecraft is assumed to not hit another node surface.	Radiator surfaces can and will be oriented in a way where the outgoing radiation does not irradiate a different part of the spacecraft, but instead will reject all heat into the environment.
TMS-AS-04	The spacecraft keeps the same orientation with respect to nadir and the velocity vector.	The scanning operation requires that the spacecraft keeps its orientation with respect to its orbit constant, with only minor deviations possible during ablation laser operation.
TMS-AS-05	Each node has a constant absorptivity and emissivity across all of its surface area.	The bulk of all components that are represented as nodes are encompassed in a housing structure made of only a single material each.

9.3.2 Model Description

At the core of the model sit nodes, which are connected by linear conductors. Further, radiative heat transfer between different nodes, and between nodes and the environment is modelled. This section will describe the properties of nodes and conductors, and provide insight into how the heat transport between nodes was modeled.

Inputs and Outputs

Nodes are defined by a set of parameters: the position in the spacecraft body frame, the node mass and specific heat capacity, as well as the surface area and the fraction of the surface area that is exposed to the environment, together with the average normal vector of the exposed surface in the spacecraft body frame. Furthermore, a node also contains the effective emissivity and solar absorptivity over the surface and an initial temperature. An internal dissipative heat load is specified for every node as a function of time to allow modelling of the heavily changing thermal load of the ablation laser pulses. Conductors consists only of a minimum and maximum operating temperature, as well as a conductivity values for operation inside and outside the operating temperature range respectively. Nodes are then connected pair-wise with a given number and length of one type of conductor. Finally, nodes are also "connected" in the radiative sense by specifying a view factor from one node to another. Note that this view factor does not need to be equal in both directions of a radiative connection. The only model output is the temperature of each node as a function of time, in addition to the eclipse time and percentage per orbit. Furthermore, the solution is visualised as a set of filterable line graphs, together an indication of minimum and maximum operating temperatures, as well as eclipse periods.

Heat Transfer Mechanisms

Heat transfer into and out of nodes may happen through two mechanisms: through linear conductors, and through radiation. However, the radiative heat flux may come from a variety of different sources. The total heat flux for a node i is modelled using Equations (9.1) through (9.7).

$$\dot{Q}_{\text{i, conductive}} = \sum_{i \neq j} (T_j - T_i) A_{ij} \frac{k_{ij}}{L_{ij}} \tag{9.1}$$

$$\dot{Q}_{\text{i, internal radiation outflux}} = -\epsilon_i \sigma A_i T_i^4 (1 - f_i) \tag{9.2}$$

$$\dot{Q}_{\text{i, internal radiation influx}} = \sum_{i \neq j} \epsilon_j \sigma A_j R_{ij} T_j^4 (1 - f_j) \frac{A_i \alpha_i}{4\pi d_{ij}^2} \tag{9.3}$$

$$\dot{Q}_{\text{i, external radiation outflux}} = -\epsilon_i \sigma A_i T_i^4 f_i \tag{9.4}$$

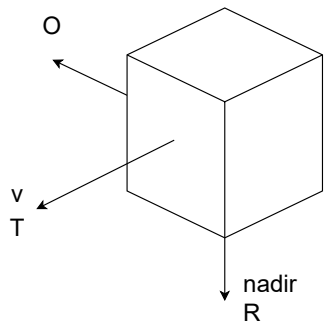

Figure 9.3: Spacecraft body reference frame used for directional computations as part of the thermal model.

$$\dot{Q}_{\text{i, external radiation solar}} = 1371\alpha_i A_i f_i \min(\boldsymbol{n}_s \cdot \boldsymbol{n}_i, 0) S_s \tag{9.5}$$

$$\dot{Q}_{\text{i, external radiation albedo}} = 0.3 \cdot 1371 \cdot 0.5\alpha_i A_i f_i \frac{R_e^2}{(R_e+h)^2} \max(\boldsymbol{n}_z \cdot \boldsymbol{n}_i, 0) S_s \tag{9.6}$$

$$\dot{Q}_{\text{i, external radiation infrared}} = 0.65\alpha_i A_i f_i \sigma 288^4 \frac{R_e^2}{(R_e+h)^2} (0.571 \max(\boldsymbol{n}_z \cdot \boldsymbol{n}_i, 0) + 0.291 \max(\frac{\boldsymbol{n}_z \cdot \boldsymbol{n}_i - cos(\lambda_i))}{cos(\lambda_i)}, 0)) \tag{9.7}$$

where A_{ij}, k_{ij} and L_{ij} are the cross-sectional area, the conductivity and the length of the conductor connecting nodes i and j respectively, σ is the Stefan-Boltzmann constant (5.670374419·10^{-8}[W/(m^{2}K^4])], R_E is the Earth radius, 1371 W/m^2 is the solar constant, 0.3 is the average albedo of the Earth, 0.5 is the ratio of the cross sectional area of Earth and the half-sphere surface of Earth, and finally 0.65 and 288 K are the effective emissivity and the effective temperature of Earth. Furthermore, R_{ij} is the fraction of the emissive area of node j visible from node i, estimated from the internal layout and structure of the spacecraft[4].

The vectors n_s and n_z represent the Sun direction and Earth direction vectors in the spacecraft body frame (RTO) respectively, whereas S_s is a value representing whether the spacecraft is in sunlight, taking the value 1 if the spacecraft is in sunlight, 0 if it is in eclipse. The terms containing the vector dot product are included to take the radiation incidence angle on surfaces into account. Surfaces facing away from the Sun should not receive any influx due to solar radiation, and if they do face towards the Sun under an angle, a cosine relation shall be used. For Earth infrared radiation, additional view factors are included due to the radiation coming from significantly different angles due to the Earth's proximity, such that even surfaces with a normal under an angle of more than 90° from nadir may receive radiative IR heat flux. This effect holds until the surface is at an angle λ_i of $\arctan(\frac{R_e}{R_e+h})$ past parallel with nadir, in the worst case of h = 350 km, λ_i = 43.5° (0.76 rad) from nadir. Under direct nadir pointing of the surface, a view factor of 0.790 should be achieved, and a surface parallel to nadir should receive a view factor of 0.219 [4]. In the model, the IR view factor scales linearly from 0 (43.5° past perpendicular to nadir) to 0.219 (perpendicular to nadir), and then from 0.219 until a maximum of 0.790 (pointing towards nadir). The reference frame used is described in Figure 9.3. The sun direction vector is first defined in an ECI reference frame (and is propagated by 1° per day), then transformed into the RTO frame.

The total heat flux $\dot{Q}_i$ into node i is then formed by the summation of all individual terms, in addition to another heat flux, this time generated by the node itself (for instance dissipated heat from electronic components). The latter, internal, heat flux may vary as a function of time, as required by the pulsed laser operation. It should be noted that these equations by themselves do not guarantee conservation of energy due to possible internal radiation "misses", which is the reason why the view factors R are commonly used to calculate Gebhard factors that express the ratio of of radiation received at node i from j to the total radiation emitted by node j. This enforces conservation of energy, however, due to internal structural components not being modelled, this assumes that no energy gets absorbed and distributed through the structure, but instead wrongly assumes that all outgoing internal radiation is received directly by other components. Instead of the Gebhard factor, a node representing the structure of the spacecraft is introduced to preserve the conservation of energy. When internal radiation is not received by another node, and therefore "misses", the heat flux is applied to the structural node to model radiative heating of the spacecraft structure. This spacecraft structure node is connected to all other nodes through mount points that are modelled as weak linear conductors. This provides a way to enforce conservation of energy with gradual diffusion of heat through the mechanical connection points between the spacecraft structure and each component.

The state variable of each node is the temperature. Using the previously computed total heat flux $\dot{Q}_i$ into node i, a the time derivative of temperature T_i may be evaluated through:

$$\dot{T}_i = \frac{\dot{Q}_i}{m_i c_i} \tag{9.8}$$

This model results in a system of ordinary differential equations that can be numerically integrated. As the system is not very stiff and generally is well-behaved, the common Runge-Kutta 4/5th order integrator was employed. The

sensitivity to the numerical integrator used was checked with several other integrators to avoid integration errors that may not be obvious. The result of the numerical integration is the transient thermal behaviour ($T_i(t)$) of all nodes.

To model the strongly varying internal heat dissipated by each node, Q_{internal} is represented as a function of time. The pulsed laser operation is the primary contributor to the strong variation in dissipated heat, and can be modelled as constant-duration pulses with a constant waiting time between pulses. The average heat load is at its peak in the beginning of the mission, requiring the TMS to be sized for the initial deployment situation, when debris objects very frequently meet the criteria necessary for ablation laser use. Subsystems, like the PCDU and the capacitors, follow this profile, while all other components have constant dissipative power.

9.3.3 Verification & Validation

The implementation of the model was verified in steps by comparing the heat fluxes at various time steps of the model with hand calculations. The conductive term was analysed in a simple test case of two aluminium blocks of 1 kg in mass, connected by a linear conductor with a conductivity of 100 W/(mK), length of 1 m and a cross-sectional area of 1 m^2. Furthermore, the properties of both blocks was set to be equal. One block's initial temperature was set to 330 K, the other to 270 K, resulting in an expected steady-state solution T_{ss} of 300 K. This allows for further checks of the solution, for example that T_1 and T_2 must evolve symmetrically to and must not cross T_{ss}. The gradient of both T_1 and T_2 must also be proportional to $\mid T_1 - T_2 \mid$, i.e. must exhibit the shape of an exponential function. These qualities of the solution are represented perfectly in the numerical solution found by the computational model, shown in Figure 9.4. The radiative terms were verified in a similar way, however with slightly different test cases. For example, a single block radiating heat away to verify the environmental outflux terms, or two plates facing each other to verify the internal radiation terms.

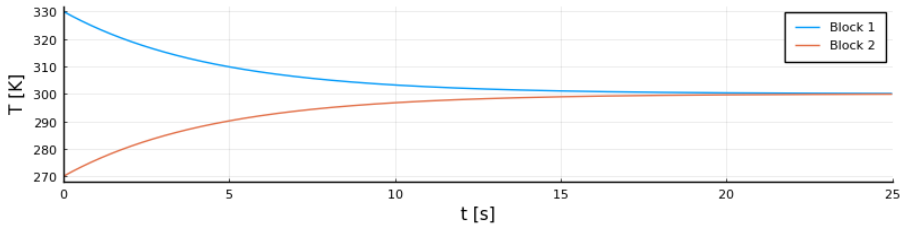

Figure 9.4: Temperature evolution over time for conduction term test case.

Further, the total internal energy of all spacecraft components was evaluated as an additional verification effort. When all interactions with the environment are disabled and , the total energy should stay constant.

The model itself, while it was derived independently from literature, is a very common approach to model the thermal performance of a spacecraft during design stages that have not yet fully converged on a specific geometry and all specific components (as required for thermal models that solve the heat equation using a finite-element approach). The model approach with all its equations was presented to an experienced spacecraft thermal engineer as a step towards validating the model. The model was found to be equivalent and partially more in-depth to the models that are found in thermal software such as ESATAN-ThermXL and can be expected to model the thermal behaviour of the space system to a good degree of accuracy. For further code and model validation, an experiment of a test case shall be conducted and compared to the results of the thermal model for the same test case.

9.4 Thermal Management System Design

After several iterations in collaboration with the structural design process of the spacecraft, the thermal management system has converged to a design solution, indicating required radiator and conductor numbers, dimensions and performance at different stages and different environmental conditions of the mission. In later stages of the mission, the use of the laser is far less frequent than in the beginning, hence the time between pulses, and therefore also the average amount of waste heat generated per unit time decreases sharply. This calls for a mechanism to control the amount of heat that is rejected to avoid cooling of the spacecraft to temperatures below the lower limit of the operating temperature range. This may be achieved both through controlling heat transport to radiators, or through control of the radiators themselves. This is treated in Subsection 9.4.3 and Subsection 9.4.2.

9.4.1 Insulation of Structure and Components

The use of MLI provides much greater control over the distribution of thermal loads, for instance the extreme waste heat during an ablation laser pulse. Heat fluxes into the spacecraft may be reduced to values as low as 0.55 W / m^2 at area densities of only 0.224 kg / m^2 (RUAG Space GmbH, 2020). MLI is also used in the design when a very powerful heat source is located in the proximity of sensitive equipment and instruments to buy the TMS additional time for heat rejection. In order to insulate all outside surfaces except radiators, antennas or the lidar and laser system, an area of 18.27 m^2 must be covered with MLI foils. Using MLI consisting of 10 layers of RUAG COOLCAT 2 NW MLI polyester foil, with area density of 0.224 kg / m^2 for 10 layer-thick MLI, a total mass of 8.1 kg must be used.

Table 9.4: Total Mass and Power required by TMS elements.

Element	Specific mass	Power per unit [W]	$\sum$ Dimension	$\sum$ Mass [kg]	$\sum$ Power [W]
Laser Heat Pipes	0.059 [kg/m]	1	70 [m]	4.13	70
PCDU Heat Pipes	0.059 [kg/m]	1	0.9 [m]	0.053	3
Battery Heat Pipes	0.059 [kg/m]	1	0.3 [m]	0.018	1
Laser OSR Radiator	3.3 [kg/m^2]	0	16 [m^2]	52.8	0
PCDU OSR Radiator	3.3 [kg/m^2]	0	0.9 [m^2]	2.97	0
Battery OSR Radiator	3.3 [kg/m^2]	0	1.5 [m^2]	4.95	0
Total				**64.92**	**74**

9.4.2 Heat Rejection

The fixed OSR radiators were sized using the performance parameters of the Qioptiq "Standard OSR". This OSR surface material offers an emissivity of 0.86, and a maximum solar absorptivity of 0.1. The maximum solar absorptivity was used for sizing to represent a worst-case scenario. The mass per area of the OSR surface (0.5 mm thickness) is $0.5{\cdot}10^3\rho_{\text{OSR}}$ = 1.3 kg / m^2, where ρ_{OSR} = 2600 kg / m^3 [1], while the addition of heat pipe interface points is expected add approximately 2 kg to the total radiator mass per area of 1.3 + 2 = 3.3 kg / m^3.

9.4.3 Internal Heat Transfer

Due to the operating temperature ranges of used components being close to room temperature, the best possible heat pipe performance is offered by aluminium-ammonia heat pipes. For thermal analysis, the performance characteristics of 8 mm diameter ammonia-aluminium variable conductance heat pipes for space use offered by Advanced Cooling Technologies. This heat pipe can achieve a thermal conductivity of 10000 W / mK during unrestricted operation. During restricted operation, the function of the heat pipe is disrupted using a 1 W electric heating element, resulting in conductive heat transfer through the pipe wall being the only mode of heat transfer. The per-length mass was estimated by considering an average wall thickness of 1 mm and an average aluminium density of 2700 kg / m^3, resulting in a per-length mass of $2700\pi((4{\cdot}10^{-3})^2 - (3{\cdot}10^{-3})^2)$ = 59 g / m. The conductance of the heat pipes must be adjusted to the current duty cycle at any point in the mission. This is to be done using a proportional temperature controller.

9.4.4 System Architecture

For the design of the TMS under consideration of control through variable conductance heat pipes, the TMS is designed for the worst case mission within mission parameters: A temporary no-eclipse orbit at an altitude of 350 km, where both the solar influx and the Earth albedo influx is maximised. Other scenarios can also be serviced by varying the conductance of the heat pipes. After several design iterations in parallel with the development of the primary structure and layout of the spacecraft, the TMS design using the thermal model converged on a set of radiators, together with their areas, as well as the number and lengths of heat pipes connecting the radiators to a component. This iterative optimisation process converged to a design using three separate radiators to cool the laser, the PCDU, the battery pack, and the two star sensors with radiators of 16 m^2, 0.9 m^2 and 1.5 m^2 respectively. These radiators are connected to their respective components by 35 2 m, 3 0.3 m and a single 0.3 m long heat pipes respectively. This is tabulated, and their masses and power requirements outlined, in Table 9.4. The temperature evolution for the thermally most critical components (Laser, PCDU, Battery Pack) under the converged TMS configuration for each component considered is presented in Figure 9.5, with a more detailed view of the transient phase shown in Figure 9.6.

Looking back at the subsystem requirements, the TMS fulfills all its core requirements: The power required is far below the budget target value, whereas the mass of the TMS is slightly over the target value, but well within contingency. Both the actual mass and actual power specifications fulfill requirements SS-SYS-TMS-REQ-002 and SS-SYS-TMS-REQ-005. The chosen number of radiators and heat pipes ensures that the spacecraft components stay within their operational temperature range during maximum expected heat loads, fulfilling SS-SYS-TMS-REQ-001. Lastly, the use of VCHP ensures that the TMS can adjust to the change in payload duty cycle, and thereby fulfills requirement SS-SYS-TMS-REQ-006.

9.4.5 TMS Configuration Sensitivity to Inputs

While the design of the thermal system does not heavily influence the design of other subsystems, there are several inputs into the TMS design procedure that can be classified as sensitive. Firstly, the operational temperature of individual components has a severe impact on the performance required from the TMS. Due to the strong relation between radiated power and radiator temperature, low component operating temperatures place far stronger constraints on the TMS design than any other factor. Furthermore, the ablation time and cool-down time indirectly raise the requirements of the TMS due to a higher power requirement. Lastly, the laser input power also has a strong potential to change the design. To evaluate especially this effect, a variation of the input power by 10% up and down was used as an input to the TMS design process,

[1] URL: https://www.excelitas.com/file-download/download/public/58606?filename=Qioptiq_Space-Qualified_Solar_Reflectors_Datasheet.pdf [accessed 14-06-2022]

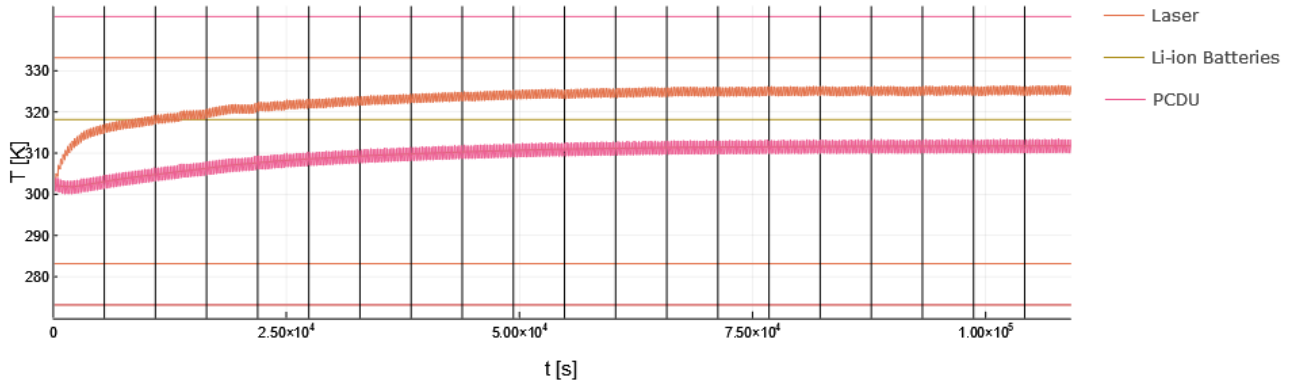

Figure 9.5: Most critical component temperatures as function of time in worst-case orbit scenario, showing the evolution from an initial temperature to the steady-state temperature over 20 orbits (orbits indicated by vertical lines, operational temperature limits shown as horizontal lines).

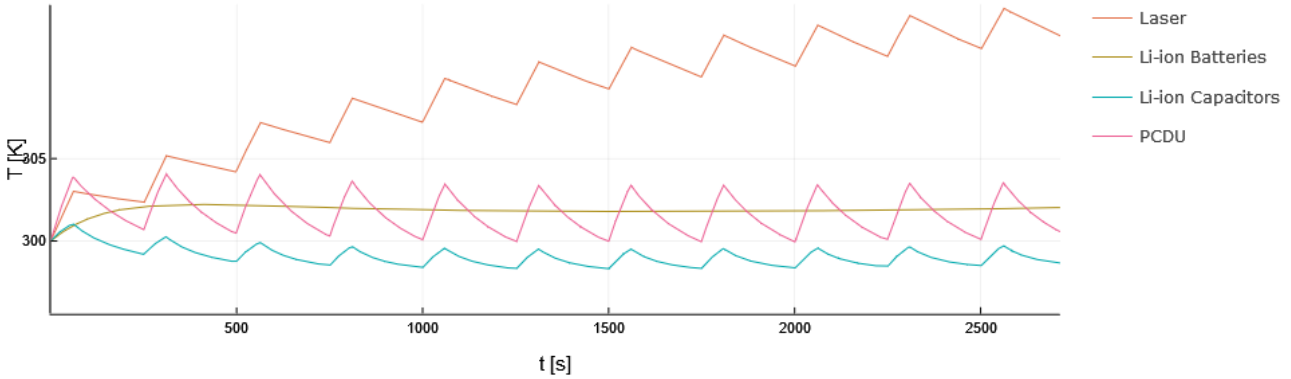

Figure 9.6: Initial transient behaviour as the system starts to move towards steady-state behaviour.

resulting in the generation of a new TMS architecture. In the case of -10% laser power, the radiator area decreased to 16.0 m^2 (-13.0%), and the number of heat pipes was decreased from 39 to 34 (-12.8%). This caused a reduction in mass and power to 56.5 kg (-13.0%) and 65 W (-12.2%) respectively. For the case of +10% laser power, the radiator area increased to 21.2 m^2 (+15.2%), and the number of heat pipes increased to 44 (+12.8%). This caused an increase in mass and power to 74.65 kg (+15.0%) and 83 W (+12.1%). This indicates that particularly the radiator area and the total mass of the TMS are slightly more sensitive than linear to the laser input power.

Telecommunication Infrastructure 10

In this chapter, the telecommunication infrastructure of the Space Sweeper mission will be defined. Given that this mission is Earth orbiting and autonomous, this system is expected to be completely off-the-shelf. This chapter will tackle both the Telemetry, Tracking & Command (TT&C) subsystem design and the required Ground Station (GS) infrastructure.

The structure of this chapter is as follows. First, the subsystems requirements are given and explained in Section 10.1. Second, the design options and preliminary trade-offs are presented by Section 10.2. Third, the ground station network is outlined in Section 10.3. Fourth, the TT&C subsystem design and choice of components is shown in Section 10.4. Fifth, conclusions are drawn on the telecommunication architecture in Section 10.5. Finally, Section 10.6 presents the verification of the tools used.

10.1 TT&C Subsystem Requirements

The requirements relative to the telecommunication infrastructure need to be generated and defined. The following critical requirements were outlined:

- The required **ground station exposure** indicates the length of the contact windows and how often they occur. First, the GS network should provide a complete Low Earth Orbit (LEO) coverage such that any clean-up mission around the Earth can be performed. Following, a minimum contact time of 60 seconds per orbit is assumed to be sufficient to send the complete dataset to Earth, including possible images from the secondary payload (discussed in Chapter 15).
- The **main functions** of the TT&C are to communicate the selected housekeeping and payload data to the ground station.
- The **downlink data rate** is crucial to the mission, as the primary function of the TT&C is to transmit data generated by the spacecraft. From the 60 s of communication time, and the 4.25 MB of data generated per orbit (from Chapter 8), a minimum data rate of 567 kbps is necessary, which is well below the figures provided by (Wertz, Everett, et al., 2011, p.629), of 5 Mbps. The latter is used to allow for a secondary payload.
- The **uplink data rate** is expected to be less critical to the mission than the downlink equivalent, due to the larger Equivalent Isotropic Radiated Power (EIRP) of the GS. Following (Wertz, Everett, et al., 2011, p.629), the largest uplink data rate that can be expected is 1 Mbps, for a memory reload.
- The **Bit Error Rate (BER)** defines the number of wrongly transmitted bits, on average, per bit. The spacecraft is mostly autonomous, and the information could be retransmitted if a corrupted bit arises, meaning that this requirement is no stronger than most past missions. According to (Speretta, 2020), the BER of most missions is in the order of 10^{-6}.
- The **link margin** is set to be at least 5 dB as recommended by (Speretta, 2020) for missions with crucial reliability or experimental technology, as the Space Sweeper mission.
- Data **encryption** is a crucial part of the telecommunication architecture due to the weapon-potential of a laser station in orbit to take down other satellites or shoot towards this Earth (Teixeira et al., 2022b). The TT&C will therefore comprise a data encryption unit.
- The **technical budgets** attributed to the subsystem arose from the preliminary budgets shown in Chapter 2 and further refinements from the iterations performed in the design. This includes mass, power, and volume. Additionally, the cost budget is also driving.

Those requirements are reported in the VALID format in Table 10.1.

10.2 Design Options

A Design Option Tree (DOT) of the telecommunication architecture and technology can be generated. Note that those only aim to outline the types of components or software, rather than selecting a precise component, however.

10.2.1 Telecommunication Technology Options

Starting with the technology, Figure 10.1 shows the technology options for the TT&C system. The crossed options are explained below:

- The wire system was discarded as it is fundamentally unfeasible.
- VHF and UHF are used for amateur radio satellites and microsats when it comes to Earth orbiting satellites (Wertz, Everett, et al., 2011, p. 631). The Space Sweeper is expected to be a large spacecraft, therefore those bands were discarded.
- The C-band is mostly dedicated to commercial applications such as communication satellites (Wertz, Everett, et al., 2011, p. 631), rather than scientific applications such as the Space Sweeper. This option was therefore discarded.
- The use of the V-band and higher has a low Technology Readiness Level (TRL), as they have never been used for satellite communications[1]. Those were then discarded.

[1] URL: https://interactive.satellitetoday.com/via/january-2017/beyond-ka-supporting-future-telecommunications/_fragment.html [Accessed on 02-06-2022]

Table 10.1: TT&C requirements

Requirement ID	Description
SS-SYS-TTC-REQ-001	The TT&C subsystem shall ensure a ground contact time of 60s per orbit.
SS-SYS-TTC-REQ-005	The TT&C subsystem shall modulate and demodulate the signals.
SS-SYS-TTC-REQ-009	The TT&C subsystem shall be able to send telemetry and payload data to the ground station.
SS-SYS-TTC-REQ-010	The TT&C subsystem shall be able to receive ground commands.
SS-SYS-TTC-REQ-012	The TT&C subsystem shall polarise the emitted signal.
SS-SYS-TTC-REQ-016	The TT&C subsystem shall encrypt the data.
SS-SYS-TTC-REQ-017	The mass of the TT&C subsystem shall not exceed 57 kg.
SS-SYS-TTC-REQ-020	The power used by the TT&C subsystem shall not exceed 1130 W.
SS-SYS-TTC-REQ-022	The telecommunication link shall have a link margin of at least 5 dB.
SS-SYS-TTC-REQ-023	The telecommunication link shall have a Bit Error Rate of at most 10^{-6}.
SS-SYS-TTC-REQ-024	The TT&C subsystem shall be able to handle downlink data rates up to 5 Mbps while in communication with a ground station.
SS-SYS-TTC-REQ-025	The TT&C subsystem shall be able to handle uplink data rates up to 1 Mbps while in communication with a ground station.
SS-SYS-GS-REQ-001	The Ground station network shall permit a contact time of 60s per orbit.
SS-SYS-GS-REQ-006	The Ground station network shall provide a full LEO coverage.

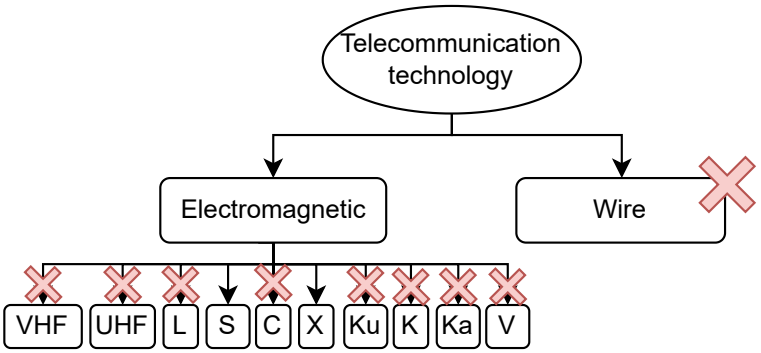

Figure 10.1: Technology design option tree. The letters refer to the frequency bands.

Table 10.2: Trade-off between S and X frequency bands. H=high, M=moderate, L=low. Based on (Speretta, 2020)

	System Cost (moderate)	Data rate (low)	COTS availability (important)	Availability (low)
S-band	L	M	H	L
X-band	H	H	M	M

- The Ku-band is mostly used for commercial applications and for missions that have requirements for near continuous ground contact.
- The L and K-bands were discarded for compatibility with the available ground station network (see later).

This therefore leaves the S and X-bands, which are traded-off below. The criteria are as follows: system cost (moderate due to the mission budget), typical data rate (from legacy mission; low as this is related to an efficient use of the frequency band, but any would be physically possible), availability of Commercial Off-The-Shelf (COTS) components (important from SS-TL-STK-US-REQ-STB-004), spectral availability (low as the licence is still obtainable if the request is initiated early enough and the fee can be paid).

The system cost is an important aspect of such high level decision, and the S-band is less complex and expensive than the X-band for satellite communication in near Earth orbits (Speretta, 2020). This is also related to the efficiency of the devices related to those bands: the S-band permits a high efficiency implementation, while the X-band relies on limited efficiency devices.

The data rate of the mission was estimated to be moderate compared to other missions. The X-band is usually used for high data rate communications, meaning that its use would result in an over-design for the purpose of the present communication architecture. The S-band is usually used by medium data rate missions (Speretta, 2020; Wertz, Everett, et al., 2011).

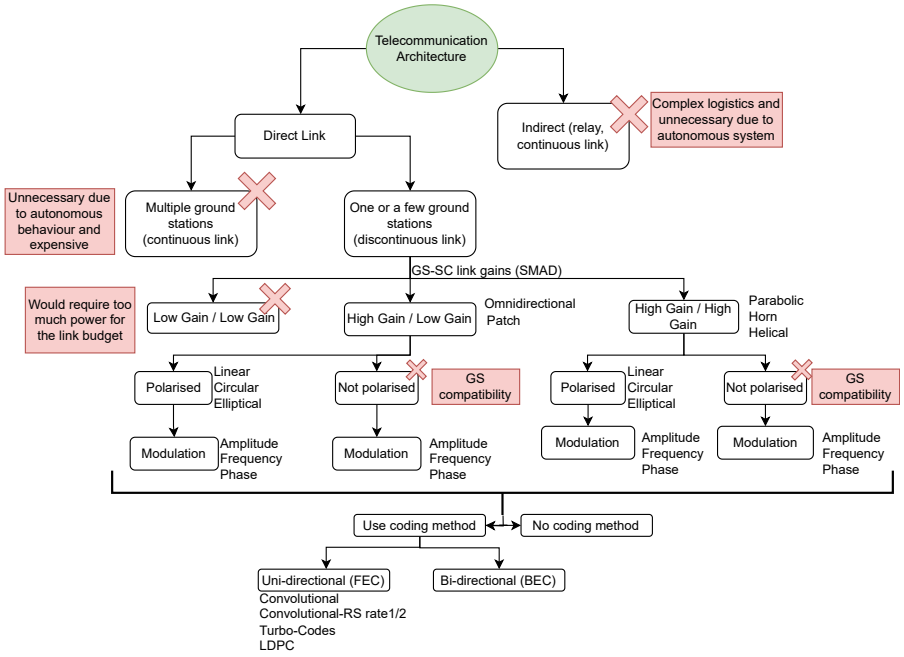

Figure 10.2: Architecture design option tree of the telecommunication system

Table 10.3: Trade-off between high and low gain spacecraft antenna. H=high, M=moderate, L=low. Based on (Speretta, 2020)

	Pointing requirement (important)	**Complexity (low)**	**Data rate (moderate)**
High Gain	H	M	H
Low Gain	L	L	L

Following SS-TL-MI-REQ-015, COTS components shall be preferred. The S-band has been much more used by past missions, stimulating the market and resulting in a variety of high performance and cheap off-the-shelf components. This is less the case for the X-band.

Finally, the spectrum availability of both bands is to be considered, as this might rise the cost of the mission (to obtain a licence) or delay the mission if the licence is not issued early enough. The S-band is much more crowded than the X-band, and therefore has more problems in terms of bandwidth than the latter.

From this trade-off, the S-band can be chosen with confidence (2.3 GHz is assumed for the following analysis as the exact attribution will be performed by the International Telecommunication Union (ITU) or other relevant agency, and the GS band presented below is between 2.2 and 2.3), despite its low spectral availability. The latter might result in an increase in cost and a waiting time to obtain the licence. Furthermore, a special licence could be considered to treat the Space Sweeper mission as an emergency satellite could be considered, enabling the use of the chosen frequency a few days following a collision or explosion to clean up.

10.2.2 Telecommunication Architecture Options

Following, the DOT for the telecommunication architecture is presented in Figure 10.2. The non-concept and concepts which can be ruled out right away are directly indicated on Figure 10.2. As can be seen in the figure, the first main trade-off to perform in terms of architecture relates to the Spacecraft (SC)-GS antenna gain relation, comparing the use of a high gain and a low gain antenna onboard the spacecraft. A trade-off is performed to select whether a high gain or low gain antenna will be required on the spacecraft. The following criteria were taken into account: antenna pointing requirement (important, as it is conflicting with both the payload and Electrical Power Subsystem (EPS) pointing requirements), complexity (low, a high gain antenna would need a deployment procedure), and data rate (moderate, a higher data rate is desirable for logistics with the GS). Note that a low gain antenna is considered to have a gain lower than or around 6 dB (Wertz, Everett, et al., 2011, p. 638).

The payload has critical pointing requirements, which are directly conflicting with eventual telecommunication pointing requirements. Therefore, lower pointing requirements from the antenna are better for the design, if it still fits the downlink and uplink data rate requirements. A lower gain antenna focuses the radiated power less and therefore has a lower pointing requirement.

Considering the complexity, the criteria was considered due to the large difference between the two options on this matter. A low gain antenna often comes in the form of a patch, which is better in terms of size and is less complex than a fully deployable antenna.

The data rate of the mission was indicated to be medium in downlink, according to requirement SS-SYS-TTC-REQ-024 above. A higher data rate capability permits to send more data, which is preferable. However, a low gain antenna expected to be sufficient for the data budget considered in this case.

From this trade-off, it is clear that a low-gain / low pointing requirement antenna needs to be selected for the design.

10.2.3 Remaining Design Points

This overall leaves the following variables to investigate:

- The bandwidth,
- The spacecraft antenna gain,
- The modulation scheme,
- The coding method.

The three last will be balanced between each other to reach an optimal telecommunication infrastructure design, which is compatible with the ground station network and the ITU regulations. The polarisation is chosen as Left Handed Circular (LHC), Right Handed Circular (RHC) for compatibility with the ground station network, as shown in Tables 10.4 and 10.5.

10.3 Ground Station Network

An already established ground station network is selected for the mission. The aim is to select a network with full LEO coverage such that the mission can tackle any collision occurring between 350 and 1,000 km orbital altitude. The project being contracted by the European Space Agency (ESA), the European ground station network dedicated to LEO coverage, will be used for the mission. The advantage of using the ground station network from a single institution relies on the central Network Operations Centre (NOC), which permits a global operation of the entire network from a single location[2]. In order to ensure an extensive Earth coverage, both the core and augmented networks will be considered.

The compliance given in Tables 10.4 and 10.5 are explained in the following: The CORTEX compliance relates to phase modulation or frequency on subcarrier or carrier, BPSK, QPSK, OQPSK, AQPSK, telecommand Modulation (on sinusoidal subcarrier: PCM/PSK/PM) modulations. The IFMS compliance relates to PM on subcarrier or carrier, BPSK, QPSK, OQPSK, UQPSK, GMSK, telecommand Modulation (On sinusoidal subcarrier: PCM/PSK/PM) modulations.

10.3.1 The ESTRACK Core Network

The ESTRACK core network comprises four stations dedicated to satellites and launchers in near Earth orbits [3]: Redu (Belgium, REDU-1), Kourou (French Guiana, KRU-1), Santa Maria (Portugal, SMA-1), and Kiruna (Sweden, KIR-1). Multiple antennae are available in each ground station, therefore, the ones showing the largest gain are chosen for each location. Those stations are compatible with S, and X frequency bands. Table 10.4 gives the key characteristics of each ground station in the core network. Note that each ground station is Telemetry (TM) and Telecommand (TC), and Comms redundant. Furthermore, the SMA-1 ground station can only be used for downlink.

10.3.2 The ESTRACK Augmented Network

The ESTRACK Augmented Network permits to add three ground stations to the core network while keeping all operations at the NOC. Similarly, as for the core network, the GS characteristics given in (Müller, 2008) are given in Table 10.5. Those ground stations are in: Santiago (Chile, AGO-1), Malindi (Keyna, MAL-1), and Svalbard (SG-3).

10.3.3 Contact Windows

Using the core and augmented ESTRACK network, an analysis was performed to assess the GS availability for the mission.

A tool was developed to estimate the contact windows from the spacecraft orbit and the ground station positions, based on the same assumptions as the orbit calculations presented in Chapter 3 (keplerian orbit with J2 perturbations). Furthermore, a communication cone was implemented to check whether communication is feasible at the considered time instants. The communication cone is characterised by a necessary elevation angle, as shown in Figure 10.3.

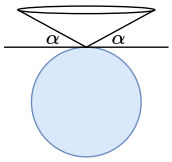

Figure 10.3: Communication one from a ground station. α = elevation angle.

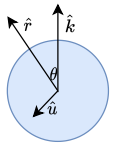

Figure 10.4: Transformation to ground station coordinate frame. **r** = ground station position. **u** the cross product vector. **k** the Z-axis of the ECEF.

To do so, a ground station coordinate system is defined, with the origin on the ground station position (assumed at sea level, spherical Earth) and the upward going axis towards zenith (Z-axis). The transformation from the Earth-centered,

[2]URL: https://www.esa.int/Enabling_Support/Operations/ESA_Ground_Stations/Estrack_ground_stations [Accessed on 07-06-2022]
[3]URL: https://www.esa.int/Enabling_Support/Operations/ESA_Ground_Stations/Estrack_ground_stations [Accessed on 02-06-2022]

Table 10.4: Core ground station key characteristics (Müller, 2008). b = band; CL = convolutional; CC = concatenated; S-SSPA = S-band Solid State Amplifier; SHPA = S-band High Power Amplifiers; comp= compability.

Parameter	**REDU-1**	**KRU-1**	**KIR-1**	**SMA-1**
		General		
Longitude	5°08'43.24"E	52°48'16.79"W	20°57'51.57"E	25°08'08.60"W
Latitude	50°00'01.64"N	5°15'05.18"N	67°51'25.66"N	36°59'50.10"N
Antenna diameter [m]	15	15	15	5.5
Elevation range [deg]	-1 to 181	-1 to 181	-1 to 181	0 to 90
		Uplink		
Polarisation	*S-b:* RHC, LHC	*S-b:*RHC, LHC	*S-b:* RHC, LHC	*S-b:* N/A
	X-b: RHC, LHC	*X-b:* RHC, LHC	*X-b:* N/A	*X-b:* N/A
EIRP [dBm]	*S-b:* 102.5 (S-SSA)	*S-b:* 111.2 (SHPA)	*S-b:* 101	*S-b:* N/A
	X-b: N/A	*X-b:* 112.8	*X-b:* N/A	*X-b:* N/A
Modulation schemes	IFMS comp	IFMS comp	IFMS & CORTEX comp	N/A
		Downlink		
Polarisation	*S-b:* RHC, LHC	*S-b:* RHC, LHC	*S-b:* RHC, LHC	*S-b:* RHC, LHC
	X-b: N/A	*X-b:* RHC, LHC	*X-b:* RHC, LHC	*X-b:* RHC, LHC
G/T [dB/K]	*S-b:* 29.6	*S-b:* 29.1	*S-b:* 27.7	*S-b:* 16
	X-b: N/A	*X-b:* 41	*X-b:* 36.9	*X-b:* 20
Modulation schemes	IFMS comp	IFMS comp	IFMS & CORTEX comp	PCM/FM, BPSK
Coding schemes	R-S, CL and CC	R-S, CL and CC	R-S, CL and CC	R-S, CC

Earth-fixed (ECEF) coordinate system used for the orbital simulation, to the ground station coordinate system, is given by the angle, θ, between the Z-axis in ECEF (**k**) and the position vector of the ground station (**r**). The rotation of the angle θ can be performed around the unit vector from the cross product between the position vector of the ground station and the ECEF Z-axis. The transformation procedure is shown in Figure 10.4.

$$\mathbf{r} \cdot \mathbf{k} = |\mathbf{r}||\mathbf{k}| \cos\theta \qquad (10.1) \qquad \mathbf{u} = u_x\mathbf{i} + u_y\mathbf{j} + u_z\mathbf{k} = \frac{\mathbf{r} \times \mathbf{k}}{|\mathbf{r} \times \mathbf{k}|} \qquad (10.2)$$

$$R_{\mathbf{u}} = \begin{bmatrix} \cos\theta + u_x^2(1-\cos\theta) & u_x u_y(1-\cos\theta) - u_z\sin\theta & u_x u_z(1-\cos\theta) + u_y\sin\theta \\ u_y u_x(1-\cos\theta) + u_z\sin\theta & \cos\theta + u_y^2(1-\cos\theta) & u_y u_z(1-\cos\theta) - u_x\sin\theta \\ u_z u_x(1-\cos\theta) - u_y\sin\theta & u_z u_y(1-\cos\theta) + u_x\sin\theta & \cos\theta + u_z^2(1-co\theta) \end{bmatrix} \qquad (10.3)$$

The angle of rotation can be obtained from the dot product of the rover position vector and the Z-axis unit vector, as seen in Equation (10.1). While the rotation axis is defined by the unit vector given in Equation (10.2). The rotation of the coordinate system is then given by Equation (10.3).

Having rotated the first coordinate system such that it aligns with the intended ground station coordinate system, the satellite position vector can be translated to the GS frame based on $v_{SC}^{GS} = R_{\mathbf{u}} v_{SC}^{ECEF} - \mathbf{r}$. The new Cartesian coordinates can be converted to spherical (r', ϕ', λ'). Finally, checking whether a communication link is possible between the satellite and a given GS comes back to checking if $\alpha_{Comm} < \phi'_{Relay} < \pi/2$. The other parameters can have any value within their bounds.

From this analysis, the availability of the selected ground station network was determined by considering large number of orbits at 350 km altitude (most critical for ground availability). The results presented below are were obtained for circular orbits with different inclination and Right Ascension of the Ascending Node (RAAN) angles to ensure a global satellite passing. This permits to get a first estimate of the ground station coverage. Figure 10.5 gives the ground track of those satellites (in red when the satellite is in communication with a ground station and in blue when not). A full day was simulated such that the J2 effect could be expressed over about 15 orbits. The elevation angle was assumed to be one degree for all ground stations for simplicity (conservative for all but the SMA-1 and MAL-1 ground stations).

The ground availability for those orbits varied between 11.31 and 19.18% (with a median 13.38%). This analysis permits to build confidence in the ground network and a minimum availability of around 10% of the time in LEO at the worst case orbital altitude of 350 km, this fits requirement SS-SYS-TTC-REQ-001. The minimum, yet significant, time to transmit the data during one pass is around five minutes. The passes on average are separated by 80 to 90 minutes at the most. Running the same simulation for an orbital altitude of 1,000 km, the ground availability ranges from 27.18 to 33.89% (with a median 31.34%) and the communication spots on the ground track become larger. This increase in ground availability emphasizes the need for modularity in the secondary payload to be taken onboard of the spacecraft, as larger data rates can be handled in case of higher orbits, due to the larger contact window times.

Table 10.5: Augmented ground station key characteristics (Müller, 2008). b = band; CL = convolutional; CC = concatenated; S-SSPA = S-band Solid State Amplifier; SHPA = S-band High Power Amplifiers; comp= compability; tbc= to be confirmed.

Parameter	**AGO-1**	**MAL-1**	**SG-3**
	General		
Longitude	70°40'W	40°11' 40.24" E	15°24' 28.03" E
Latitude	33°08'S	2°59' 44.00" S	78°13' 47.18" N
Antenna diameter [m]	12/9	10	13
Elevation range [deg]	X/Y Mount	-4 to 90	-5 to 183
	Uplink		
Polarisation	*S-b:* RHC, LHC *X-b:* N/A	*S-b:*RHC, LHC *X-b:* N/A	*S-b:* RHC, LHC *X-b:* N/A
EIRP [dBm]	*S-b:* 115 (9 m) *X-b:* N/A	*S-b:* 98.7 *X-b:* N/A	*S-b:* 98 *X-b:* N/A
Modulation schemes	CORTEX comp	CORTEX comp	CORTEX comp
	Downlink		
Polarisation	*S-b:* RHC, LHC *X-b:* N/A	*S-b:* RHC, LHC *X-b:* RHC	*S-b:* RHC, LHC *X-b:* RHC, LHC
G/T [dB/K]	*S-b:* 27.1 (12 m) *X-b:* 40.0 (12 m)	*S-b:* 21.3 *X-b:* 31.8	*S-b:* 23 *X-b:* 32
Modulation schemes	tbc	CORTEX comp	CORTEX comp
Coding schemes	R-S, CL and CC	R-S, CL and CC	R-S, CL and CC

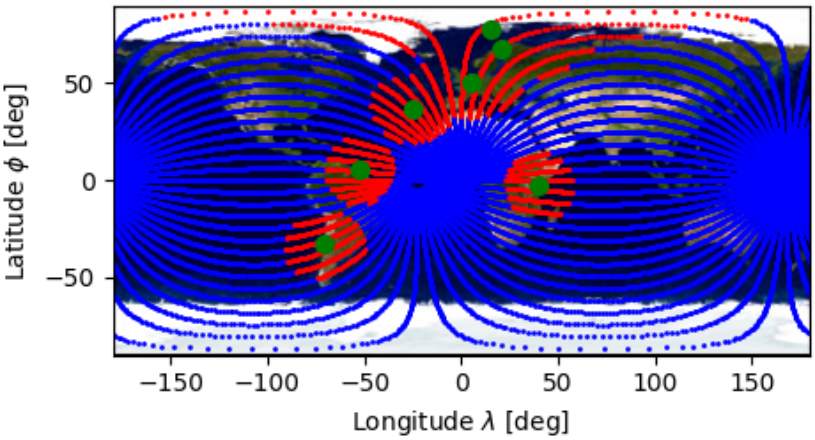

Figure 10.5: Ground track of the satellites used, in circular orbits at 350 km altitude. Red = in communication with a ground station; blue = not in communication with any ground station. Green dots = ground station position.

10.4 TT&C Design

In this section, the bandwidth, necessary antenna gain, modulation scheme and coding method will be determined. The former is first estimated, and the three others are left free and will be optimised between each other to minimise complexity.

The bandwidth, B, is assumed to be 6 MHz as suggested by (Wertz, Everett, et al., 2011, p. 631). This number is mentioned to be indicative, and the real attributed value will be decided by the ITU.

10.4.1 Link Budget Method

A link budget was set up to investigate the design options further. The budget follows the formula given by,

$$\left(\frac{E_b}{N_0}\right) \text{dB} = \left(P + L_l + L_a + L_s + L_{pr} + L_r + \frac{G_r}{T_s} - R - k\right) \text{dB} \tag{10.4}$$

Those parameters are either available from the technical budgets or can be estimated using simple methods presented in (Wertz, Everett, et al., 2011; Speretta, 2020).

- L_a is the atmospheric attenuation, generally consisting of both the rain attenuation and the effect of the atmosphere by itself. The former is considered negligible for the S-band (Thiagarajah et al., 2013) and frequencies below 5

GHz generally (Speretta, 2020). The atmospheric effects can be quantified from the figure 'Total, dry air and water vapour attenuation at zenith from sea level as a function of frequency' in(Recommendation ITU-R P. 676-10, 2013), and a value of 4 10^{-2} dB is used conservatively for the S-band (2 to 4 GHz).

- The free space loss L_s can be estimated from Equation (10.5), where the distance d can be conservatively assumed to be $d = \sqrt{(R_E + h)^2 - R_E^2}$ (zero elevation) for an altitude h of 1,000 km, as the design is performed for worst case scenario. This gives a value of -171.07 dB using a frequency of 2.3 GHz.

$$L_S = \left(\frac{\lambda}{4\pi d}\right)^2 \tag{10.5}$$

- L_l and L_r represent efficiencies of the transmitter and receiver, conservative values of 0.7 are used (Speretta, 2020). This translates to -1.55 dB.
- L_{pr} is first neglected as it would be zero for a low gain antenna on the spacecraft side, which is desired. It would be added if a high gain antenna was found to be necessary to make the telecommunication link viable.
- The transmitter power P is given by the technical budgets, 861 W is used as a starting value.
- G_r/T_s is given by the ground network characteristics. The lowest figure of merit in the network is 16, which will be used as a starting value for the worst case scenario. Furthermore, the values presented in Table 10.4 will be used subsequently to verify that the GS network is capable enough for the configuration.
- The bandwidth B is assumed to be 6 MHz as mentioned above.
- The downlink data rate, R, follows from SS-SYS-TTC-REQ-024.
- The Boltzmann constant k has a value of -228.6 dB.

Table 10.6 shows a summary of the estimations presented above.

Table 10.6: Link budget parameters.

Symbol	Parameter	Estimation [dB]
P	Transmitter power	29.35
L_l	Loss factor transmitter	-1.55
G_t	Transmitting antenna gain	G_t([4])
L_a	Transmission path loss	10^{-2}
G_r/T_s	GS figure of merit	16
L_s	Space loss	-171.07
L_{pr}	Antenna pointing loss	0
L_r	Loss factor receiver	-1.55
B	Communication bandwidth	60
R	Data rate	66.99

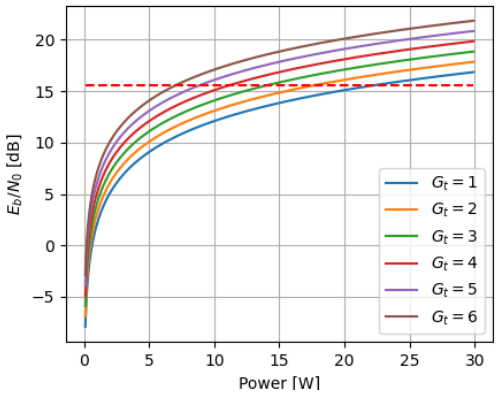

Figure 10.6: Low-gain and S-band configuration viability.

The analysis therefore aims to strike a balance between the used power, antenna gain, modulation method, and coding method such that the Bit Error Rate (BER) specified in SS-SYS-TTC-REQ-023. To confirm the viability of the low-gain antenna and S-band configuration, the link budget curve for an antenna gain of 2 dB is given by Figure 10.6. The dashed lines present E_b/N_0 threshold for a BER of 10^{-6} or smaller for the commonly used BPSK modulation scheme and a link margin of 5 dB. It is further noted that the BPSK line is the best one available [5], showing that a strong coding method will likely be necessary to ensure proper link budget (as low gain antennae usually have a low power limit).

10.4.2 Antenna

The main impact on the link budget comes from the antenna through the G_t parameter. As a COTS low-gain antenna is to be chosen, a list is set up below and a trade-off is performed. Table 10.7 gives multiple COTS antennae eligible for the mission, and their characteristics. The link budget tool was run on those possibilities to obtain the resulting E_b / N_0 for each case. This will permit to preliminarily determine the required modulation and coding methods associated to each antenna. The different antenna types are then traded-off between each other.

[4]Will be considered in the analysis, no value attributed

[5]URL: https://www.gaussianwaves.com/2010/04/performance-comparison-of-digital-modulation-techniques-2/ [Accessed on 09-06-2022]

Table 10.8: Trade-off between different antenna types. H=high, M=moderate, L=low. HPBW=Half Power Beam Width.

	TRL (important)	**E_b/N_0 (highly important)**	**HPBW (important)**
EnduroSat	M	H	L
ISIS	M	L	H
SATREVOLUTION	M	H	L
AnyWaves	H	M	M

Table 10.7: Off-the-shelf S-band low gain antennae. TRL=Technology Readiness Level. RF=Radio Frequency. HPBW=Half Power Beam Width.

Characteristics	**EnduroSat**[6]	**ISIS**[7]	**SATREVOLUTION**[8]	**AnyWaves** [9]
Type	Patch	Patch	Patch	Patch
Frequency range [GHz]	2.025-2.110	2.20-2.29	2.20-2.29	2.025-2.290
Gain [dBi]	7	6.5	7	6.5
HPBW [deg]	70	100	70	90
Max RF power [W]	4	2	4	3
Mass [g]	81.5 ± 0.5	50	10	132 ± 2
Dimensions [mm x mm x mm]	98 x 98 x 14.3	80 x 80x 8	67.3 x 78.4 x 1.6	79.8 x 79.8 x 12.1
TRL	8	8	8	9
E_b / N_0 [dB]	16.42	12.91	16.42	14.68

Those antennas can be traded-off, resulting in the most optimal one for the given mission. It is first noted that each antenna considered has a specific frequency range, which will result in different requests to the ITU. The larger the range, the better in terms of planning, as there is a largest probability that the selected range is approved. Furthermore, all the options are patch antennae, which will be placed on the outer structure of the spacecraft, on the pre-defined side that will be facing Earth during the mission. Additionally, all considered antennae are circularly polarised, which is compatible with the considered ground station network.

The following trade-off criteria are used to determine the selected antenna: TRL (a higher TRL requires less Reseach and Development (R&D)), E_b/N_0 (which characterises the link budget and comprises the information of the gain and RF power; this also will determine the complexity of the coding and modulation methods), and Half Power Beam Width (HPBW) (as this characterises how much low level pointing is required). The mass and volume are not taken into account as criteria, as both are very low for all options and are virtually negligible with respect to the rest of the spacecraft. The cost was not taken into account for similar reasons. This results in Table 10.8.

In this case, the labels H, M and L were used in a ranked fashion rather than an absolute assessment of the capabilities. The ranking directly follows from Table 10.7. The AnyWaves option clearly comes out as the most optimal option from the four considered, as it has no red categories. The downside on the energy per bit sent can be tackled through a careful choice of the modulation and coding method. Furthermore, this antenna provides the most complete set of parameters in the datasheet, allowing to build some more trust on the component provider.

10.4.3 Modulation and Coding Methods

Three general methods are used for the modulation of an electromagnetic signal to represent the data that is to be sent: amplitude, frequency and binary phase shift keying (Speretta, 2020). According to Wertz, Everett, et al. (2011, p. 632), the Binary Phase Shift Keying (BPSK) (or higher order versions of this modulation scheme) is the most common modulation scheme as it has the highest theoretical power efficiency of the three options. Modulation methods considering changes in the phase of the signal are also the only ones supported by the chosen ground network. Therefore, phase modification is chosen for this architecture, without trade-off (only viable option). However, multiple orders exist, as shown in Table 10.9, where each modulation scheme is given with the minimum related E_b/N_0 for a BER of 10^{-6} (theoretical values)[10], OPSK value from (Adly et al., 2010). Note that the 5 dB link margin mentioned in SS-SYS-TTC-REQ-022 is yet to be added.

The BPSK modulation method is chosen for the Space Sweeper mission. According to (Wertz, Everett, et al., 2011, p. 633), this method is often used for moderate downlink data rates as well as high data rate uplinks. The method is very widely used due to its relatively simple implementation on spacecrafts. Higher order alternatives would permit to transmit twice the data rate on the same bandwidth, however, the data rate is not constraining for the Space Sweeper missions.

[6]URL: https://satsearch.co/products/endurosat-s-band-antenna-commercial [Accessed on 09-06-2022]

[7]URL: https://satsearch.co/products/isis-s-band-patch-antenna [Accessed on 09-06-2022]. Further note that the dimensions are derived from the envelope dimensions.

[8]URL: https://satsearch.co/products/satrev-s-band-patch-antenna [Accessed on 09-06-2022]

[9]URL: https://satsearch.co/products/anywaves-s-band-antenna [Accessed on 13-06-2022]

[10]URL: https://www.gaussianwaves.com/2010/04/performance-comparison-of-digital-modulation-techniques-2/ [Accessed on 13-06-2022]

Table 10.9: Phase modulation options and required E_b/N_0 for a BER of 10^{-6}.

Method	BPSK	QPSK	4-QAM	OQPSK	D-BPSK	D-QPSK	8-PSK
Required E_b/N_0 [dB]	10.6	10.6	10.6	10.8	11.2	12.7	14

Table 10.10: Coding schemes options.

Method	**Coding gain [dB]**	**Rate**	**Improved E_b/N_0**	**Complexity**
Convolutional codes	5 - 6	1/2	16.66	Low
Convolutional-RS	7 - 8	1/2	18.66	Moderate
Turbo-codes	10	1/6	16.9	High
LDPC	10	3/4	23.42	Very High

Furthermore, higher order alternatives require a higher E_b/N_0 ratio for the same BER, as seen in Table 10.9, and add to the complexity of both the ground and space segments of the mission.

This overall results in a required energy per bit of 15.6 dB (including margin) for a BER of 10^{-6}, while the link budget analysis performed for the chosen antenna resulted in a link budget of 14.68 at max RF power. This can be tackled through an appropriate coding method, resulting in a coding gain in the link budget. Either Backward Error Coding (BEC), resending the data if an error is detected, or Forward Error Coding (FEC), adding redundancy to the data such that errors can be corrected without resending, can be used to minimise the BER. The latter is generally preferred to avoid time delays (which lead to increased expenses for the ground infrastructures)[11]. According to (Speretta, 2020), the following coding gains are representative of the main coding schemes available:

The complexity rankings were obtained from (Hajiyat et al., 2019; Speretta, 2020; Andrews et al., 2007), and the coding gains and rates from (Speretta, 2020). Furthermore, according to (Speretta, 2020), rates higher than 1/2 are to be preferred for small bandwidth channels of communication (LDPC, Convolutional, Convolutional-RS). Additionally, only Convolutional and Convolutional-RS are available for the complete ground station network. The minimum E_b/N_0 required is 15.2 dB for a BER of 10^{-6} with a link margin of 5 dB. This overall only leaves the Convolutional codes and Convolutional-RS possible for this mission under the given constraints. The former, Convolutional codes, is selected as it is suitable and involves less complexity (note that this trade-off is quite sensitive to the data rate, as will be discussed below, and is to investigate again when less uncertainty on it is present). In a following iteration, the data block size used by the coding should be traded-off and determined.

10.4.4 Final Architecture

Having selected the antenna, the modulation and the coding method, the following components need to be considered, and their necessity is evaluated. If the component is deemed necessary to the telecommunication architecture, an appropriate COTS component is chosen. Finally, the complete architecture of the subsystem is given.

- **Transponders/transceivers** are responsible for the modulation and de-modulation of the method determined earlier, and for the control of the overall subsystem. According to (Wertz, Everett, et al., 2011, p. 636), the transceiver is generally simpler and of lower cost than the transponder alternative, but is only viable for missions relying on alternative orbit control than Doppler shift measurements from communications with the ground stations. In the case of the Space Sweeper mission, the orbit control is handled by a GNSS receiver (see Chapter 5), and a transceiver can be used. The SSTRX-1000 Satellite Transceiver([12]) supports the BPSK modulation scheme and has a modulation data rate ranging from 10 kbps to 4 Mbps, capable of handling a RF power between 100mW and 5W. This fits all the needs of the previous design decisions, except SS-SYS-TTC-REQ-024, which was chosen quite arbitrarily and is not expected to be necessary for the mission, therefore 4 Mbps is considered to be enough. Additionally, the transmit frequency range is between 2200 and 2290 MHz, and the receive frequency range is between 2025 and 2110 MHz (both of those being compatible with the antenna and the ground network respectively).
- A **diplexer** can be used to use the same antenna for both transmitting and receiving functions. Such component will be used to reduce the mass of the system. One is already present in the SSTRX-1000 Satellite Transceiver, resulting in an implementation loss lower than 1 dB.
- A **power amplifier** was not found to be necessary, as the RF power used up until now in the analysis was proved to be sufficient.
- A **RF switch** will be used to enable the possibility to design a fully redundant system, as it permits to connect different antennae with different transceivers.

The final architecture of the TT&C subsystem is then shown in Figure 10.7, where a fully redundant system was chosen to ensure reliability of the subsystem, while still fitting the technical budgets. Using two antennas, two transceivers, two diplexers and cables, a total mass of 6.784 kg is found (assuming 3 kg of cables, of a yet to be determined cable component). The total subsystem mass is estimated to be 23.5 W.

[11] URL: https://headendinfo.com/forward-error-correction/ [Accessed on 13-06-2022]

[12] URL: https://satsearch.co/products/stt-systemtechnik-sstrx-1000-satellite-transceiver [Accessed on 13-06-2022]

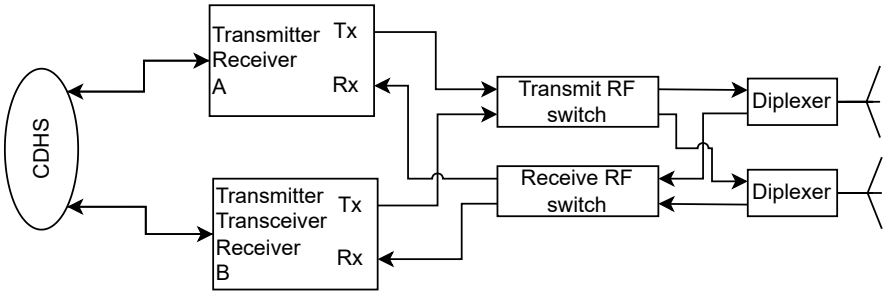

Figure 10.7: Final architecture of the TT&C subsystem.

10.5 Sensitivity and Conclusions

This chapter presented the telecommunication infrastructure designed for the Space Sweeper mission. In this section, the sensitivity of the trade-offs performed in above are discussed and the uplink capabilities of the system are shortly considered.

The first two trade-offs, determining the frequency band and the type of antenna, were performed on a high-level, basing the gradings and weights on the mission definition rather than on uncertain budgets which could change over time. Provided that the mission does not change significantly (like transmitting large amounts of data rather than the small expected budget), the decisions taken at that point are not subject to change. Furthermore, the ground station network was selected based on the contract the team has with ESA, the core and augmented possibilities are used to increase the contact time such that emergency scenarios are picked up quickly.

The combination of the modulation method (BPSK), the coding scheme (Convolutional codes) and the chosen antenna might be sensitive to the data rate used for the sizing (5 Mbps). To consider that, the data rate is both multiplied and divided by two to consider if the chosen architecture would still be valid. For a required energy per bit of 15.2 dB (including margin), for a BER of 10^{-6}, doubling the communication data rate (10 Mbps), gives E_b/N_0=13.64 dB and halving it yields E_b/N_0=19.66 dB. In the latter, the architecture performs as intended, while in the former, the communication link would not meet the requirement SS-SYS-TTC-REQ-022. However, it is to be noted that the figure of merit G/T used for the ground station in the link budget analysis is the lowest of the network (while the second lowest is 21.3 dB). Excluding the SMA-1 ground station would result in a minimum energy per bit of 18.94 dB for twice the design data rate, and the ground station exposure would be reduced to 8.83% of the time minimum (19.19% maximum) at 350 km altitude, which is acceptable following requirement SS-SYS-TTC-REQ-001. However, note that any data rate higher than 4 Mbps would require another transceiver, however this is rather unexpected.

Overall, this shows that the architecture designed in this chapter can be considered as robust and suitable for a wide range of possibilities. Only the coding method could be reconsidered at a later stage if simple convolutional code would be sufficient, however, it is better to consider a more complex one at this stage in the design to be conservative.

10.6 Tools Verification and Validation

In this section, the tools used in the analysis and design presented in this chapter are verified and (if possible) validated. First, the link budget tool is assessed, then the ground station coverage tool is considered.

10.6.1 Link Budget Tool

The link budget tool was verified three main methods due to the nature of the code (which is essentially one formula applied to different cases): walk-through, degenerate and analytical testing. They are shortly explained in the following:

1. Walk-through: the implementation of the functions was compared to the equations presented in this chapter and their formal definition (such as the decibel). No error was found through this test, which is only aiming to spot obvious mistakes in the code (low reliability).
2. Degenerate testing: sanity checks have been performed on the values obtained from the code, to confirm that the behaviour is physical. First, the outputs obtained (as given in the discussions above) came out as realistic for a LEO mission. Second, the behaviour of the program was found to be realistic as increasing or decreasing some values such as the orbital altitude considered or the signal frequency, yielded expected outcomes. For example, increasing the orbital altitude, decreases the link budget.
3. Analytical Testing: the program was run with an example provided by (Speretta, 2020), which uses similar assumptions. The value from the code was in accordance with the worked out example.

10.6.2 Ground Station Coverage

In the following, the ground station coverage tool is verified and validated. However, as the orbital part of the simulation is built upon the same assumptions and similar implementation as the mission analysis simulation, those aspects were not further verified. The following therefore focuses on the telecommunication cone and ground track implementations.

1. Walk-through: similarly to the above, the implementation of the functions was compared to the equations presented in this chapter and their formal definition (such as the decibel). No error was found through this test, which is only aiming to spot obvious mistakes in the code (low reliability).

2. Degenerate testing: running the simulation for a few orbits and showing the ground track on a map of the planet (in blue when not in communication and red when in communication), the areas where the satellites are in communication with at least one ground station are realistic, as seen on Figure 10.8. The ground stations are indicated by green dots. Note that the North Pole is completely covered due to the curvature of the Earth, which is not represented on such map. As an additional check on the sanity of the results, the orbit of the International Space Station (ISS) was also plotted following the same conventions in Figure 10.9. This is quite close to well-known ground track[13]
3. Analytical testing: an analytical testing could not be performed on the total code due to its nature (numerical integration over thousands of time steps). However, the different functions were tested one at a time and compared to an analytical value. No mistake was found in this manner.
4. Convergence testing: a convergence test was not performed as the method relies on Keplerian orbits, which give an 'exact' value for each time step (no error propagation). Reducing or increasing the time step would only affect the accuracy of the results through the J_2 effect, which is very small on a single time step (10 seconds used in the simulation).
5. Extreme value testing: the altitude and the elevation angle parameters were considered in the extreme value testing, and an error was found in the computation of the percentage of orbit during which the spacecraft is communicating. After correction, an expected behaviour was found in those tests. For example, increasing the altitude increases the telecommunication window up to a physical limit due to Earth's curvature, additionally, an elevation angle of 90 gives no communication time, as expected.
6. Sensitivity testing: the sensitivity of the orbital altitude was already investigated in the main text. The elevation angle sensitivity is investigated by adding and subtracting one degree from the original value of one degree (zero and negative values are possible from the landscape. Adding one degree resulted in an expected lower performance, with a median ground availability of 12.28% (13.37% previously). Removing one degree gives a median ground availability of 14.45%. Those are not extremely sensitive, reflecting a good behaviour of the code.

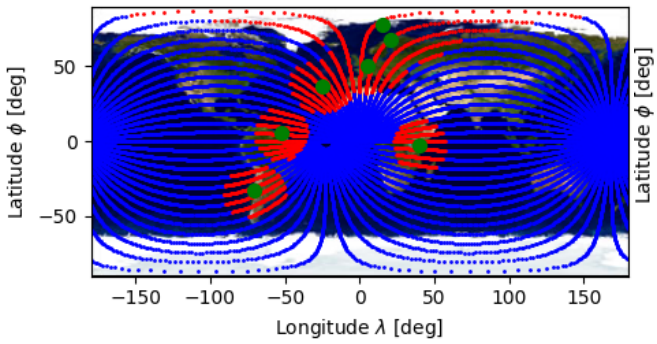

Figure 10.8: Ground track of 29 satellites for 90 minutes.

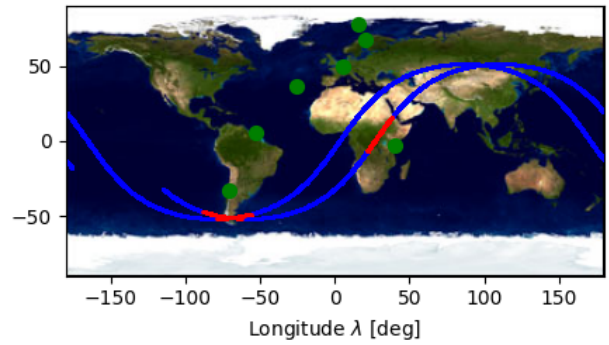

Figure 10.9: Ground track of the ISS as predicted from the tool.

[13] URL: https://spotthestation.nasa.gov/tracking_map.cfm [Accessed on 19-06-2022]

Spacecraft Structure 11

The structures subsystem follows the same layout as the rest of the subsystems. It starts with the initial requirements in Section 11.1, followed by the chosen configuration in Section 11.2, then, the sizing of the cylindrical shell (Section 11.3) and the supporting platforms (Section 11.4, and ending with a top level design of the payload-launcher adapter in Section 11.5 and a conclusion (Section 11.6).

11.1 Subsystem Requirements

After choosing the launcher in Section 13.2, the initial requirements for the spacecraft structure can be obtained, in combination with the mass and power budgets. 11.1 displays these requirements.

Table 11.1: Structures subsystem initial requirements

Requirement ID	Description	Rationale
SS-SYS-STR-REQ-001	The structures subsystem shall withstand longitudinal loads of -6g in compression and 2.5g in tension.	Derived from chosen launcher.
SS-SYS-STR-REQ-002	The structures subsystem shall withstand lateral loads of 1.8g in any direction.	Derived from chosen launcher.
SS-SYS-STR-REQ-003	The structures subsystem shall ensure that the system longitudinal natural frequency higher than 20 Hz.	Derived from chosen launcher.
SS-SYS-STR-REQ-004	The structures subsystem shall ensure that the system lateral natural frequency higher than 6 Hz	Derived from chosen launcher.
SS-SYS-STR-REQ-005	The mass of the structures subsystem shall not exceed 686 kg, with a target value of 500 kg.	Allocated mass budget
SS-SYS-STR-REQ-006	The power of the structures subsystem shall not exceed 126 W, with a target value of 91 W.	Allocated power budget.
SS-SYS-STR-REQ-007	The structure shall withstand the weight of all components	To ensure proper system functioning.
SS-SYS-STR-REQ-008	The structure, along with all components, shall fit inside the launcher	Derived from the chosen launcher.

11.2 Structure Configuration

The first step was to try to fit all components inside the launcher fairing, thus defining the layout and shape of the spacecraft. This configuration can be visualised in Chapter 13. From it, it was concluded that the best structure to act as backbone during launch and carry the loads would be an outer shell surrounding the components, which would be connected to it via platforms and supporting beams. For mounting and integration ease, a squared bus was chosen, whereas, for the backbone, the shape was decided to be cylindrical since it has better buckling resistance, and extensive testing has been performed in this kind of shells.

Aluminium was chosen as a material due to having the best specific-yield-stress-to-cost relation. In addition, it is easy to use in manufacturing due to its convenient mechanical properties, and it has extensive space flight heritage. Composites were not considered due to the lack of verified analytical solutions in complex structures, and the uncertainty added to the Finite Element Method (FEM) simulations. In addition, failure in composites is much more drastic since they do not yield before catastrophic failure, reducing the reliability of the system. Although more expensive, the chosen Aluminium alloy was Al-7075-T6, due to its higher mechanical properties and to how commonly it is used in the industry.

11.3 Cylindrical Shell Sizing

With the chosen configuration of the components, the aim now is to find the required cylinder shell thickness to support the launch loads (Requirements SS-SYS-STR-REQ-001 and SS-SYS-STR-REQ-002). As seen in the renders from Chapter 13, the bus is divided in six shelves. All this shelves will have a supporting cylindrical shell of radius 0.85 m (adapting

Table 11.2: Mass overview of the spacecraft components

	Tanks	**Mirror**	**Laser**	**Lidar**	**CMGs**	**PCDU**	**Solar Panels**
Mass [kg]	385	581	555	286	260	70	118
	Batteries	**Capacitors**	**OBC**	**Gyroscopes**	**Star Trackers**	**Pressure Tank**	**Gimbal**
Mass [kg]	10.5	28	20	13.8	7.8	8	200

Table 11.3: Cylinder shell thicknesses

	Bottom Cylinder	**2nd Shelf**	**3rd Shelf**	**4th Shelf**	**5th Shelf**
Thickness [mm]	3.7	3.1	3.1	1.3	1.4

to the bus size). The thickness of these shells will be varied depending on the loads it would need to withstand, excluding the mass of the shell itself. Nevertheless, the loads inside the fourth shelf are assumed to be fully carried by the gimbal structure of the laser-mirror configuration, since it will be much heavier and robust than a thin cylinder shell (recall that the laser and the mirror have a combined mass of roughly 1100 kg).

For this analysis, the cylinders are assumed to not have any stiffeners, however, if the required thicknesses were to be too high, the use of stiffeners would be considered. To transfer the loads from the platforms to the cylinders, a set of four inclined beams will be used, whose deflection will be checked via FEM analysis. In addition, the weight of the structure itself will be accounted for iteratively, using the initial budget estimation as a starting point. For the axial loads, an evenly distributed stress is distributed. For the lateral ones, the bending force is assumed to act through the centre of mass of all components above the root of the cylinder.

To size the thickness of each cylinder, the compressive stress will be checked both for yield and buckling, any of which can be considered as failure. For the former, the following equation (adaptation of the one in Zandbergen (2021)) can be used. In this equation, σ_{yield} is the compressive yield stress of the material, g is 9.81 m/s^2, m is the mass of all components supported by the cylinder, A is the cross-sectional area of the cylinder, I is the area moment of inertia of the cylinder around the bending axis, and h_{cg} is the height of the centre of mass of all components supported by the cylinder. A qualification factor of 1.25 is added, as well as another one of 1.1 for the analysis of the yield stress, in accordance with Zandbergen (2021). An extra factor of 2 is not required since acceptance testing is expected to be performed. Note that 6 and 1.8 are the g-forces derived from the subsystem requirements.

$$\sigma_{yield} \geq 1.1 \cdot 1.25 \left(\frac{6gm}{A} + \frac{h_{cg} 1.8gm}{I} \right) \tag{11.1}$$

For the buckling analysis, equations from NASA (1975) for cylindrical shells can be used, specifically the equations for combined axial and bending forces, since the shells do not need to be pressurised. Testing has been performed to validate these equations, with promising results, being these commonly used for initial sizing in the aerospace industry. Equations (11.2) through (11.4) display the procedure, where R_c and R_b are the stress ratios between the applied stress (σ) and the critical bucking stress (σ_{cr}) for the axial and lateral direction, respectively. t is the thickness of the shell, r its radius, E the Young's modulus of the material, μ_{pos} is the Poisson's ratio, and η_{plast} is the plasticity coefficient, which is 1 for this case, since the cylinder is in the elastic regime. For this case, only the qualification factor of 1.25 needs to be added to account for possible stress concentrations and imperfections in the structure.

$$\frac{1}{R_c} = \frac{\sigma_{c_{cr}}}{\sigma_c} = \frac{1}{1.25} \frac{1}{\frac{6gm}{A}} \eta_{plast} \left(1 - 0.901 \left(1 - e^{-\frac{1}{16}\sqrt{\frac{r}{t}}} \right) \right) \frac{E}{\sqrt{3(1-\mu_{pos}^2)}} \frac{t}{r} \tag{11.2}$$

$$\frac{1}{R_b} = \frac{\sigma_{b_{cr}}}{\sigma_b} = \frac{1}{1.25} \frac{1}{\frac{h_{cg} 1.8gm}{I}} \eta_{plast} \left(1 - 0.731 \left(1 - e^{-\frac{1}{16}\sqrt{\frac{r}{t}}} \right) \right) \frac{E}{\sqrt{3(1-\mu_{pos}^2)}} \frac{t}{r} \tag{11.3}$$

$$R_c + R_b \leq 1 \tag{11.4}$$

Having explained the procedure, it is time to add values to the equations to find the thicknesses of the cylinders. The considered masses (neglecting several light components), placed in the layout given in Figure 13.1c in Chapter 13, are shown in Table 11.2, and the resulting cylinder thicknesses (after iteration) are displayed in Table 11.3.

Having the weight of all components and the thicknesses of the shell, one can obtain a preliminary estimation of the natural frequencies of the system (which will need to be verified with a vibrational analysis in the future). This is achieved by concentrating the all the mass at the centre of mass, assuming the spacecraft to be a cylindrical shell of constant system, and using Equations (11.5) through (11.7). Here, k_{lon} and k_{lat} are the equivalent spring constants of the spacecraft in the longitudinal and lateral directions, respectively, and h_{cg} is 2.72 m. To be conservative, the thickness was chosen to be the

one of the second and third shelves (3.1 mm), leading to a longitudinal natural frequency of 62.1 Hz and a lateral one of 23.8 Hz, safely complying with Requirements SS-SYS-STR-REQ-003 and SS-SYS-STR-REQ-004.

$$k_{lon} = \frac{EA}{h_{cg}} \quad (11.5) \qquad k_{lat} = \frac{3EI}{h_{cg}^3} \quad (11.6) \qquad f_{nat} = \frac{1}{2\pi}\sqrt{\frac{k}{m}} \quad (11.7)$$

11.4 Yield Analysis of Supporting platforms

Now that it has been verified that all loads can be supported by the cylindrical shell, it is necessary to assess that the component weights are translated to the shell effectively. For this, a simple squared platform (for the ease of assembly) with a set of two beams are welded to the shell. For the estimation of its performance, a yield stress analysis was performed on the structure, applying the appropriate launch loads on top, iterating to find the appropriate thicknesses, and optimise for weight by means of holes in the beam. It should be noted that this structure is still missing the attachments of the components to the platform. To account for these, and any other load concentrations, an additional safety factor of 1.3 was added on top of the 1.25 qualification factor and the 1.1 for yield analysis.

Figure 11.1 shows the load analysis for the final design of the third shelf (using the validated SolidWorks software), in which the platform thickness is 4 mm and the beams' thickness is 6 mm, experiencing a maximum deflection of 2.43 mm (the deflections in the figure are exaggerated for the sake of visualisation). In this simulation, all attachments to the cylindrical shell are taken as fixed surfaces (the deflections of the shell are assumed to be taken into account by the extra safety factor). The same analysis was performed for the rest of the platforms (including the top one supporting the lidar). It should be noted that the supporting structure for the propellant tanks, as well as the actuators, still need to be further analysed and designed in future stages of the project.

11.5 Payload-Launcher Adapter Design

During launch, apart from supporting the spacecraft bus, it would be necessary to also support the laser-dish configuration and the solar array to avoid resonance issues and having to reinforce the joints excessively to avoid extreme deflections. This supporting structure will be designed in future stages of the project, however, as general guidelines, it should make sure to not support the weight of the whole spacecraft through the solar array or dish support. It should guarantee that the spacecraft weight is carried by the attachment to the bus, and only deflections and oscillations are supported by the rest of the attachment points. This can be achieved by determining the deflections in the supporting structure accurately and sizing it according to these estimates. Another option could be to use rubber-like materials or others with similar properties (spring-damper system) that allow for a certain deflection only in the solar array and the dish.

On the other hand, this supporting structure will need to be connected to the Ariane 62 launcher vehicle to ensure a successful launch. This launcher offers a variety of standard launch vehicle and payload adapters (*Ariane 6 User's Manual* 2021). Due to having the spacecraft weight distributed over a circumference of 1.7 m in diameter (the cylindrical shell) and to the fact that a large supporting structure will be needed, the payload and launcher adapters with the biggest diameter were chosen. Therefore, the PLA6 1666 (diameter of 1.666 m) payload adapter and the vehicle launcher adapter of the same diameter will work in combination with the supporting structure to transmit the loads from the Space Sweeper to the launcher.

11.6 Conclusion

The outcome of this analysis lead to a structural mass of 298 kg, including the cylindrical shells and structural interfaces, but excluding the gimbal and the SADA, thus staying well within Requirement SS-SYS-STR-REQ-005. Components such as the payload-launcher adapter, the SADA, the gimbal, and the connection between the tanks and the supporting platforms still require another iteration to be designed in detail. The equations used in this subsystem are assumed to be valid since they are taken from NASA (1975), a NASA report checked with extensive experiments, widely used to design for buckling in the industry. In addition, the FEM analysis was performed via the SolidWorks software, which has proven to be applicable to any conventional structure, especially when using aluminium metal alloys (SolidWorks, 2019).

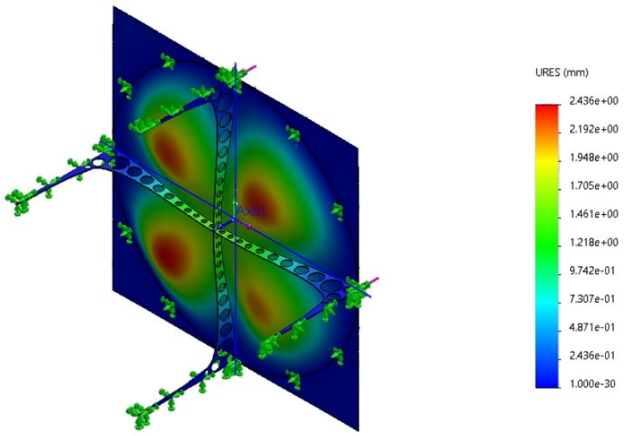

Figure 11.1: Strain plot of the supporting platform under the estimated loads.

System Analysis 12

All the subsystems have been designed, and this chapter aims to analyse the system in its entirety. This is done by first performing a sensitivity analysis on system level, in Section 12.1. Then, the final technical budgets are presented in Section 12.2. Following, the compliance with the requirements is checked in Section 12.3. Next, the risks of the system are discussed in Section 12.4, accompanied by mitigation strategies in Section 12.5.

12.1 System Sensitivity Analysis

A sensitivity analysis is performed to investigate the robustness of the design. It is of interest to see how the design is influenced by the different design parameters, particularly those that are found to be critical in the sensitivity analyses of the subsystems. Furthermore, many uncertainties are introduced in this, still preliminary, design process. These uncertainties can flow down to other design decisions, and should not affect critical decisions, in case the final design is robust. Also, it is analysed how the different important parameters affect the debris removal efficiency.

12.1.1 Design Sensitivity Analysis

For each of the subsystems, an individual sensitivity analysis is performed. However, these individual analyses of course do not take into account the uncertainties that result from combining the subsystems. Therefore, the most critical parameters, that affect subsystems the most, affect multiple subsystems, or are highly uncertain, should be considered. Essentially, those variables are included for which the multiplication of its uncertainty and impact on the design are the largest.

The different relations, illustrating how the identified uncertainties in the design propagate between the subsystems, are shown in Figure 12.1. In this chart, it can be observed that the CDHS and TT&C subsystems are not included. This is done on purpose, because those subsystems are deemed to be relatively isolated, and are less impactful on the overall system. For example, the debris diameter and repetition rate were found to be the most sensitive parameters for the payload detection system in Table 4.4, influencing the FoV the most. This FoV, and its uncertainty, meaning its range of values, serves as an input for the GNC subsystem, because a larger FoV requires more torque delivered by the magnetic torquers. A different, rather far-reaching identified path of data flow, is starting at the payload removal system (the laser). For the laser, if the range at which the debris is first ablated, and the time during which the ablation shall take place, is changed, both the angular rates and the power required change drastically. The power required, referring to the power distribution as a whole, almost completely determines the TMS. Continuing, the required power also largely sizes the EPS. The solar array area, in turn, scales directly with the required power, which has a strong relation with the atmospheric drag. Consequently, as the atmospheric drag changes, the disturbance torques change, influencing the design of the GNC, and the required ΔV delivered by the propulsion subsystem changes.

This clearly illustrates how interrelated the different subsystems are, and how changing a certain value in one part of the design directly affects all the other subsystems. The individual subsystem designs have been shown to be robust, therefore, to show robustness of the chosen complete design, it is checked that the uncertainties of those connected parameters do not result in a different design. To start, the power required, as an output from the payload removal subsystem, was shown to vary from -9.1% to 11.1%, on a change in inputs of $\pm$ 10%. The TMS is highly dependent on this, which was also concluded in the TMS chapter. A new laser power would require a new TMS architecture, but this can be done with relatively minor changes to the overall design. Furthermore, the EPS obviously depends on the laser power required. In the EPS sensitivity analysis, it was shown, however, that the solar array area only changes by $\pm$ 6% with a change of $\pm$ 10% in the laser power. This is a rather favourable result, considering that both the GNC, and the propulsion subsystem have proven in their respective sensitivity analyses that the designs are robust with changes of the solar array area (or total area for the GNC) of $\pm$ 10%. With these changes, the propulsion system would remain identical, no new propellant tanks would have to be selected, and the mass of the system (excluding propellant mass) would stay the same. The structure would thus not change as a result of this. Additionally, for the payload detection subsystem, it was shown that the FoV changes at most from -5.2% to 4.9%, for all the input parameters considered. This FoV influences the GNC subsystem, but as was determined in the corresponding chapter, the chosen GNC architecture is able to deal with such changes. As was shown in the payload removal sensitivity analysis, the mirror mass is observed to be rather sensitive to change in target range. This mirror mass in turn highly influences the design, and therefore also the mass, of the structure. The overall design of the structure would not change, however, mainly reinforcements would be changed, that have to support the mirror, mainly affecting the mass of the structure.

The overall design of the system is found to be robust, while mainly the TMS has shown to have a high sensitivity. It is thus recommended, in a next iteration, to consider a wide range of input parameter values, specifically for those that impact the TMS subsystem.

12.1.2 Mission Efficiency Sensitivity Analysis

The mission analysis simulation presented in Section 3.6 will be used to determine the effects of the following key parameters on the removal efficiency of mission:

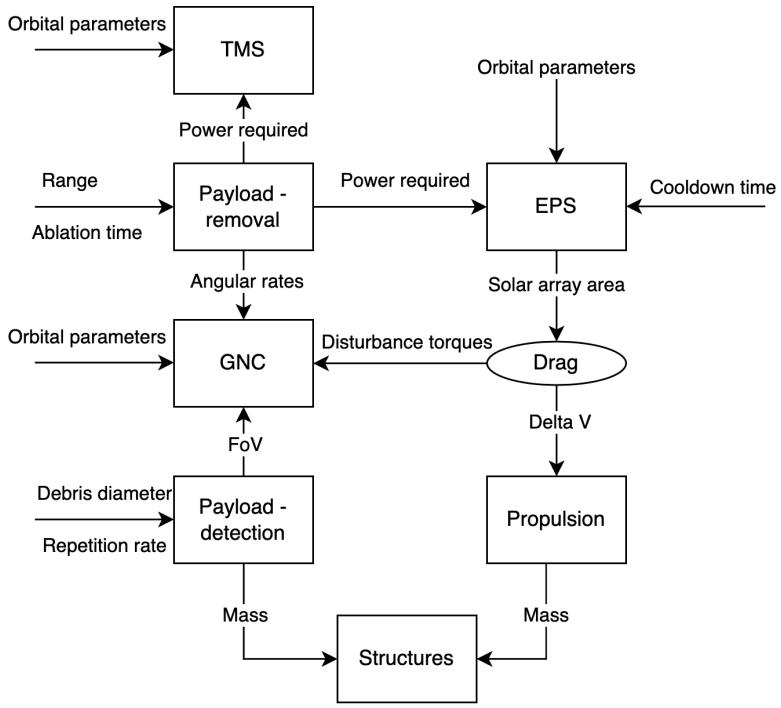

Figure 12.1: Flow diagram showing critical input and output variables for the different subsystems.

Table 12.1: Time to remove 50% of the debris as a function of the detection configuration.

Scan time [s]	FoV [deg]	Removal days
1	17.13	145.299
2	24.25	72.057
3	29.72	53.237
4	34.35	48.665
5	37.91	45.429
6	42.15	55.84
7	45.57	56.545
8	48.77	53.379
9	51.78	53.239
10	54.63	52.711
15	67.23	112.56

- The **cooldown time**, which is the minimum time between two debris ablation procedures. This figure is important for recharging the shooting capacitors and permitting a cooldown of the laser for thermal management.
- The **detection configuration**, quantified by scanning time of the spacecraft and the related FoV, as discussed in Chapter 4.
- The **payload range**, which characterises at what distance the payload is able to detect and ablate a particle.
- The **ablation time**, which is the time necessary to ablate a debris, under the assumption that it is made out of aluminium only.

The objective of such sensitivity study is then to vary those parameters within their realistic bounds and determine if an optimum exists in terms of efficiency of debris removal, and how quickly the system deviates from this.

First, the detection configuration is investigated through Table 12.1, where a simulation using 1,000 debris fragments and a shooting range of 250 km. The combination of scan time and FoV were set by the payload subsystem, as they are dependent variables. Clearly, a scan time of around five seconds, and a FoV 37.91° results in the best overall performance. However, this number is quite sensitive on the right side (from 5 to 6 seconds), meaning that by design, a value of 5 seconds scanning time or less should be aimed for.

Following, an optimal payload range / cooldown time combination is investigated through Table 12.2, note that the combinations of 200 km and larger cooldown times were not computed as they would all be larger than 500 days (which is already too high). Such results, are indicated by N/A, and do not need to be considered as a realistic value. The aim being to come as close as possible to 180 days, to limit the constraints on the other subsystems as much as possible. Meaning that a cooldown time of 190 s and a range of 300 km is chosen.

A number of payload range / ablation time combinations are given in Table 12.3. Again, N/A indicate unrealistically high values, and are consequently not further considered. It was seen in Chapter 4 that the debris removal payload is

Table 12.2: Time to complete the mission as a function of range and cooldown time combinations.

R \t$_{cool}$	**70 s**	**100 s**	**130 s**	**190 s**
200 km	500	N/A	N/A	N/A
250 km	34.65% at 319.58 days	34.05% at 315.74 days	33.67% 323.35 days	33.04% at 321.7 days
300 km	75.0	98.9	129.5	183.3

Table 12.3: Time to complete the mission as a function of range and time to ablate the particles.

Output in days	**20 s**	**30 s**	**40 s**	**50 s**	**60 s**	**70 s**
100 km	>48% in 1000 days	N/A	N/A	N/A	N/A	N/A
150 km	72.761	117.547	N/A (1.8% in 200 days)	N/A	N/A	N/A
200 km	43.036	43.037	52.675	>48% in 900 days	N/A	N/A
250 km	32.975	33.045	34.100	38.955	88.340	N/A
300 km	26.152	26.148	26.148	26.782	32.552	46.976

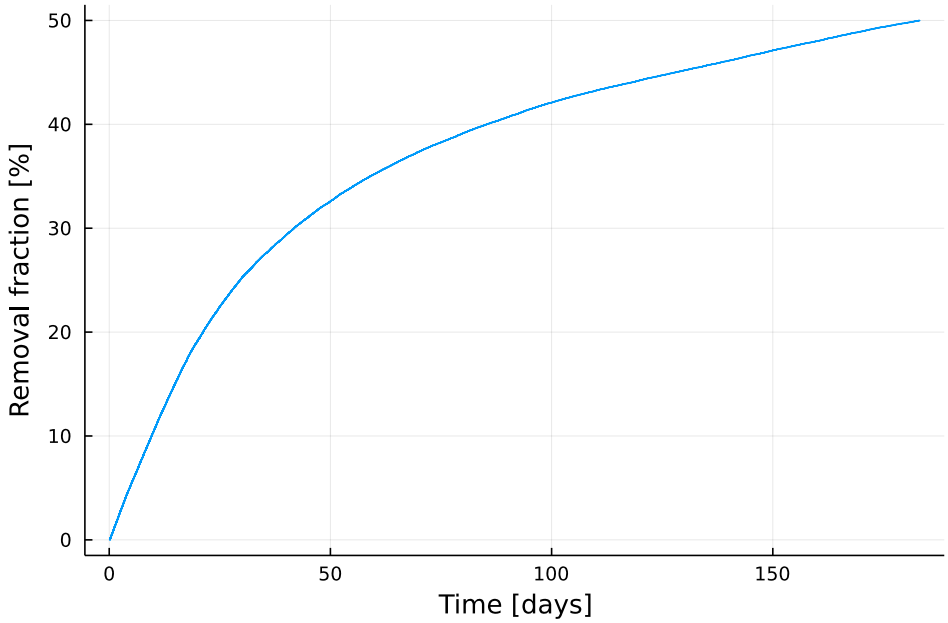

Figure 12.2: Final system debris removal performance.

limited by power and volume: a larger than 300 km range would require a dish too large to fit in the launcher, while an ablation time of less than 40 s would require too much power. Note that the results presented in this table were generated using 1,000 debris, a scanning time of 5 s, a field of view of 38.44°and a lowering of the periapsis to 340 km. This gives 60 s and 300 km range as the main option.

With these values selected, the performance of the final system can be analysed. In Figure 12.2, the removal of the debris, over time, is shown. Indeed, the system removes 50% of the space debris in roughly half a year.

12.2 Final System Mass and Power

The design is set in stone, and final masses and volumes of the subsystems are analysed and related back to the initial budgets as defined in Section 3.4. In this iterative design process, a number of subsystems did not manage to stay within the allocated budget. However, this took place in parallel, where other subsystems did manage to stay well within their respective budgets, thereby compensating each other. The final mass and power characteristics per subsystem is shown in Table 12.4. It should be noted that, the indication of actual mass and volume with respect to the budget is using the absolute total budget, so including the contingencies and margins. As can be seen, the total mass and power of the entire system is within the maximum budget. It can also be observed, however, that especially the initial power budgets were very off. The empirical relations used to get to these numbers clearly did not hold.

12.3 Compliance with Requirements

Now that the system has been analysed in its entirety, all the mission requirements will be revisited, and its compliance will be examined. This is done by means of a compliance matrix, which is shown in Table 12.5. Here, also a section is included for each requirement, where its compliance can be found. The most important requirement is met, namely removing 50% of the space debris. However, modularity is only incorporated in the EPS, and not in the other subsystems. Furthermore, due to the size of the spacecraft, the launch costs could not be minimised. Also, because hydrazine is used as

Table 12.4: Final mass and power per subsystem. In parentheses the value with respect to the allocated budget is indicated, plus indicated over budget, and negative within budget.

Subsystem	**Mass [kg]**	**Power [W]**
Payload	1423.3 (+423.3)	5300 (-600)
Structures & Mechanisms	500 (-186)	0 (-126)
TMS	64.9 (-21.2)	500 (+374)
EPS	166 (-434)	100 (-1030)
TT&C	6.8 (-50.2)	23.5 (-1107)
CDHS	9.3 (-133.7)	25.6 (-1480)
GNC	355.8 (+241.8)	880 (-250)
Propulsion	87.0 (+1.0)	0 (-126)
Other (Balance + Launch)	85.0 (-1.0)	-
Total	2758.7 (-98.3)	6903.1 (-5649.9)

propulsion, the toxicity hazard level is not limited to zero. Finally, no efficient test plan was created, and series production was not considered.

Table 12.5: Requirements compliance matrix.

Requirement ID	**Description**	**Compliance**	**Section**
	General		
SS-TL-STK-US-REQ-G-001	A space-based system shall be designed that can remove space debris in a single orbital band after a collision of two space objects.	✓	Section 12.1
SS-TL-STK-US-REQ-G-002	The system shall be operable at orbital heights between 350 and 1,000 km.	✓	Section 12.1
SS-TL-STK-US-REQ-G-003	The system shall be able to remove at least 50% of the space debris fragments of size larger than 1 cm and smaller than 10 cm, when focusing on the ones with larger orbits.	✓	Section 12.1
SS-TL-STK-US-REQ-G-004	The system shall be equipped with instruments to detect small space debris not visible with ground-based facilities.	✓	Section 4.3
SS-TL-STK-US-REQ-G-005	The system shall be able to deal with a variety of debris materials.	✓	Section 4.4
SS-TL-STK-US-REQ-G-006	Modularity in the design shall allow for optimal performance concerning a variety of space debris (size, composition, mass) and orbital altitudes.	✗	N/A
SS-TL-STK-US-REQ-G-007	The cost of a single system including operation, and launch, shall not exceed M€544.	✓	Section 15.1
SS-TL-STK-US-REQ-G-008	A launcher shall be selected and a design of the interface with the launcher shall be included.	✓	Section 13.2
SS-TL-STK-US-REQ-G-009	A design of the interface with the launcher shall be included.	✓	Section 11.5
SS-TL-STK-US-REQ-G-010	The launch cost shall be minimal; the negotiation of a free launch for the prototype is encouraged.	✗	N/A

SS-TL-STK-US-REQ-G-011	It shall be assumed that both space objects are completely destroyed by the collision.	✓	N/A
SS-TL-STK-US-REQ-G-012	The minimum mass of a single space object to be considered is 350 kg.	✓	N/A
SS-TL-STK-US-REQ-G-013	The system shall detect debris smaller than 1 cm.	✓	Section 4.3
	Mission		
SS-TL-STK-US-REQ-MI-001	The system shall be operational before the end of 2028.	✓	Section 14.4
SS-TL-STK-US-REQ-MI-002	Minimum operation time for the primary mission shall be six months.	✓	Section 12.1
SS-TL-STK-US-REQ-MI-003	Debris detection and removal during nominal system operation shall be autonomous, but some modes for which ground human support is desirable shall be automatic.	✓	Section 13.3
SS-TL-STK-US-REQ-MI-004	The ground-control shall be accounted for in the design.	✓	Section 10.3
SS-TL-STK-US-REQ-MI-005	The minimum operation time for the secondary mission shall be one year.	✓	Section 13.3
	Sustainability		
SS-TL-STK-US-REQ-STB-001	The maximum NASA Toxicity Hazard Level allowed for the system shall be zero.	✗	N/A
SS-TL-STK-US-REQ-STB-002	An efficient test plan shall be set up that meets the reliability goals without wasting resources.	✗	N/A
SS-TL-STK-US-REQ-STB-003	Series production shall be considered to optimise the use of the resources.	✗	N/A
SS-TL-STK-US-REQ-STB-004	Off-the-shelf components shall be preferred.	✓	Chap. 5-10
SS-TL-STK-US-REQ-STB-005	Operation of the space-debris removal satellite shall not increase the space-debris population.	✓	N/A
SS-TL-STK-US-REQ-STB-006	The space-debris removal satellite shall have a clear End of Life (EoL) strategy.	✓	Section 7.1
	Miscellaneous		
SS-TL-STK-US-REQ-MSC-001	A market analysis shall identify the secondary mission objectives to reduce the development and operational costs.	✓	Section 15.2

12.4 Technical Risks

As a detailed design of Space Sweeper has been achieved, the technical risk analysis from (Teixeira et al., 2022b) can be expanded upon. The 'system malfunctions' category is now divided into the specific subsystems: Payload, TT&C, EPS, Thermal, Structures, Propulsion, CDHS, GNC, and the Ground System. Overall, this section aims to restate the important risks that arose in the previous design phases and to determine more specific risks with respect to the different subsystems.

Table 12.6 shows all risks for the Space Sweeper mission. The likelihood is either Very Unlikely, Unlikely, Possible, Likely, Very Likely, while the consequence is either Negligible, Minor, Moderate, Significant, or Severe. All these risks are combined into a single risk map, namely Table 12.7.

Table 12.6: Technical risks.

NB	Risk ID	Description
		Mission Resources
1	SS-TL-MI-RISK-MR-COST-001	**R&D cost overruns** may occur due to the novelty of the spacecraft under consideration. Unexpected difficulties might arise in the design, yielding delays and therefore cost overruns. This is particularly likely for the integration and design of a space-grade laser (never been done before) and the GNC subsystem (higher than usual requirements). *Likelihood:* Likely | *Consequence:* Moderate
2	SS-TL-MI-RISK-MR-COST-002	**Integration cost overruns** can occur for non-COTS components which require recent or usually unused manufaturing processes (and therefore reults in difficulties in the manufacturing process). Due to the innofative character of the mission, this is a possible event, however, its consequence is minor compared to the development cost overruns. *Likelihood:* Possible | *Consequence:* Minor
3	SS-TL-MI-RISK-MR-COST-003	**Operations cost overruns** are a result of extended operational time of the mission. For the Space Sweeper mission, this would be the result of worse than expected capabilities of the system to clean up the space debris. This risk is less likely than R&D cost overruns, however, as careful V&V can be performed on the system. The consequence is always significant as the ground operation contracts and the ground team would need to be extended (violating the cost requirements). *Likelihood:* Possible | *Consequence:* Significant
4	SS-TL-MI-RISK-MR-SCH-001	**R&D schedule overruns** occur in case difficulties arise in the design process, similarly to SS-TL-MI-RISK-MR-COST-001. As this risk is always often linked to the cost overruns described above, this risk is likely due to the novelty of the mission. Furthermore, such delays would have a moderate effect on the mission, as SS-TL-STK-US-REQ-MI-001 ("The system shall be operational before the end of 2028.") might not be satisfied, but the primary objective might still be met with delays. *Likelihood:* Likely | *Consequence:* Moderate
5	SS-TL-MI-RISK-MR-SCH-002	**Integration schedule overruns** can occur from bad project management or a lack in experience regarding performing integration. Those schedule overruns are commonly less significant than the ones presented in SS-TL-MI-RISK-MR-SCH-001 and can be easily avoided using good project management practices, making it unlikely. Furthermore, for the system to be usable within a few weeks time from a collision or explosion, it would need to be produced ahead of time and stored, meaning that small integration schedule overruns would result in less storage time. *Likelihood:* Unlikely | *Consequence:* Minor
6	SS-TL-MI-RISK-MR-SCH-003	**Operations schedule overruns** are directly correlated with SS-TL-MI-RISK-MR-COST-003, as operations cost overruns arise from extending contracts with the ground station, which themselves arise from schedule overruns. They therefore have the same likelihood and consequence. *Likelihood:* Possible | *Consequence:* Significant
		Telemetry, Command, and Tracking Subsystem
7	SS-SYS-TTC-RISK-001	**Loss of contact** would most likely result from a failure of the TT&C subsystem on board rather than on the ground segment. This might in the loss of the spacecraft and a mission failure, which is severe. It is however an unlikely occurrence as the technology (TRL 9) is now well known and COTS components can be used and thoroughly tested. *Likelihood:* Unlikely | *Consequence:* Severe
8	SS-SYS-TTC-RISK-002	**Multipactor discharge** It is a vacuum breakdown phenomenon which can occur at RF power levels of a few watts in the S-band. It is of particular importance for the diplexer, which has a highly resonant nature. *Likelihood:* Unlikely | *Consequence:* Significant
		Electrical Power Subsystem
10	SS-SYS-EPS-RISK-001	**Power lines failure** of either the spacecraft bus or the payload could occur due to vibrations during the launch and would result in a mission failure (severe). This is however very unlikely as those connections can be thoroughly tested, making the risk easily avoidable. *Likelihood:* Very Unlikely | *Consequence:* Severe
11	SS-SYS-EPS-RISK-002	**Electrical battery failure** would result in non-nominal operations of the spacecraft during eclipse times (significant). This is, however, an unlikely scenario due to the high Technology Readiness Level (TRL) of the COTS energy storage devices. Furthermore, this can be controlled through parameters such as the Depth of Discharge (DoD) and prevented using redundancy. *Likelihood:* Unlikely | *Consequence:* Significant

12	SS-SYS-EPS-RISK-003	**Failure of solar arrays** would result in a complete mission failure. Knowing that the solar arrays for the laser station are expected to very large compared to usual satellites, more deployment mechanisms are expected. According to (Tafazoli, 2009, p.8), solar array failures are responsible for 49% of failures of the power subsystem, 48% of those in the first year, mainly due to mechanisms which can be prevented through careful testing. This risk is therefore unlikely, but severe, as (Tafazoli, 2009, p.8) outlines that in 45% of the cases, such power failure results in a loss of mission. Additionally, solar panels degrade significantly in space, however, this risk is well known and can be controlled successfully from the experience of past missions. *Likelihood:* Unlikely | *Consequence:* Severe
13	SS-SYS-EPS-RISK-004	**EPS does not initialise** would result in a complete mission failure as no power would be provided to any subsystem (the spacecraft is lost). This is, however, a very unlikely occurrence. *Likelihood:* Very Unlikely | *Consequence:* Severe
14	SS-SYS-EPS-RISK-005	**Failure of capacitors** results in the loss of the ablation laser, since this is fully dependent on the capacitor discharge. The primary mission objective would be lost, but the secondary mission, related to debris detection, can continue. The likelihood of capacitor failure is low, since they are reliable and often used in spacecraft. The consequence would be significant, but not severe, as the spacecraft's other subsystems are still usable. *Likelihood:* Very Unlikely | *Consequence:* Significant
15	SS-SYS-EPS-RISK-006	**Solar panels not pointing directly at the Sun** Power requirements not being met during a period. low likelihood since SADAs with two DoF are used *Likelihood:* Unlikely | *Consequence:* Significant
16	SS-SYS-EPS-RISK-007	**Batteries or capacitors not fully charged during sunlight** Power requirements not being met during a period. Not very likely since BCRs and BDRs are used to ensure correct charging and discharging. *Likelihood:* Unlikely | *Consequence:* Significant
17	SS-SYS-EPS-RISK-008	**Voltage spikes too high** Sensitive components not receiving enough power or being damaged. Not too likely because a fully regulated bus is used. *Likelihood:* Unlikely | *Consequence:* Significant
18	SS-SYS-EPS-RISK-009	**Severe collision of debris fragments with solar array** Power requiments not met. Simulations show that collision with particles larger than 1 cm is very unlikely considering the solar array area and the time in orbit. *Likelihood:* Very Unlikely | *Consequence:* Severe
		Thermal Subsystem
19	SS-SYS-TMS-RISK-001	**Overheating or overcooling of any subsystem** can occur in the scenario of a failure of the thermal subsystem. Depending on the concerned subsystem, the severity could range from moderate to severe, as all components have specific temperature application ranges. Such failure is generally very unlikely as it rarely happens (Tafazoli, 2009, p.11), however they are significant for a laser station due to the expected large amount of heat to be managed from the use of a laser. *Likelihood:* Very Unlikely | *Consequence:* Significant
20	SS-SYS-TMS-RISK-002	**Leakage of heat pipe systems** A heat pipe grossly exceeding its operating temperature may rupture in an unlikely case, potentially spilling the working fluid on other components, in addition to losing its functionality permanently. In this event, the loss of a single heat pipe may mean failure to control the temperature of a spacecraft component and disabling it too. *Likelihood:* Very Unlikely | *Consequence:* Significant
21	SS-SYS-TMS-RISK-003	**Failure of variable conductance heat pipe heaters** When the spacecraft is not under orbit conditions that represent a worst-case, or is in an advanced mission stage where laser pulses are not frequent anymore, the variable conductance heat pipes must be able to cut off heat transfer from the spacecraft inside to the radiators to avoid running below component minimum operating temperatures. Should a heat pipe's heater fail, the heat pipe can no longer restrict its operation, leading to rapid and uncontrolled loss of heat. *Likelihood:* Unlikely | *Consequence:* Significant
22	SS-SYS-TMS-RISK-004	**Degradation of thermal interface between heat sources / radiators to heat pipes** The TMS heavily relies on a high-conduction interface between the radiators and heat pipes, as well as between heat pipes and components. Should the environment around the interface be unexpectedly hostile and degrade the interface more than expected, a bottleneck in heat conductance may be created. *Likelihood:* Unlikely | *Consequence:* Minor
		Structures Subsystem
23	SS-SYS-STR-RISK-001	**Structural failure during launch** results in the loss of structural integrity, which is significant as it can be mission-critical. NASA reported that this occurs in about 6% of missions for small satellites, which is not very likely (Jacklin, 2018). *Likelihood:* Unlikely | *Consequence:* Significant
24	SS-SYS-STR-RISK-002	**Structural failure in orbit** results in the loss of structural integrity, which is significant as it can be mission-critical. NASA reported that this occurs in about 6% of missions for small satellites, which is not very likely. (Jacklin, 2018) *Likelihood:* Very Unlikely | *Consequence:* Significant
25	SS-SYS-STR-RISK-003	**Material defects** are generally not removable during manufacturing, since the defects are related to the internal structure of a material. This may happen if the half-fabricates are of insufficient quality and that this is not detected during inspection. The consequence may be a decrease in structural rigidity. However, only relatively small defects may be overseen by quality control, and these have little to no significant impact on the system performance. *Likelihood:* Possible | *Consequence:* Minor
26	SS-SYS-STR-RISK-004	**Part manufacturing defects** may occur if improper manufacturing is carried out. Because the system has a low product series, it is possible to perform quality control on every single component in the system. It is therefore very unlikely that defects are not detected. In case a defect is not detected, it can detrimental to the alignment of some components (e.g. a reaction wheel, making it more difficult to manoeuvre), or structural rigidity of the spacecraft (e.g. during the launch). Meaning that an undetected defect has a significant impact on the mission. *Likelihood:* Very Unlikely | *Consequence:* Significant

27	SS-SYS-STR-RISK-005	**Assembly defects** lead to separation of parts in operation, which has moderate structural consequences, especially during launch vibrations. Pointing accuracy of subsystems is also critical and requires a rigid spacecraft, although improper fastening is unlikely. *Likelihood:* Unlikely	*Consequence:* Significant
28	SS-SYS-STR-RISK-006	**Failure of deployment mechanism** mostly results in partial loss of spacecraft or loss of mission, or a negligible effect on the mission performance, according to (Rivera, 2021, p.5). Meaning that the risk is severe (taking worst case scenario). Note that, while the solar arrays' deployment was already considered in SS-SYS-EPS-RISK-003, other mechanisms (such as the antenna deployment) can be as critical. Furthermore, (Rivera, 2021, p.3) shows that the number of failures due to mechanisms has significantly decreased with respect to the increasing number of launched spacecrafts (making the risk unlikely). *Likelihood:* Unlikely	*Consequence:* Severe
		Propulsion Subsystem
29	SS-SYS-PROP-RISK-001	**Propellant leakage** may occur during operations, resulting in the propellant being exposed to vacuum. The propellant may interfere with other subsystems/electronics. It is likely that the majority of the propulsion subsystem will be COTS, drastically decreasing the likelihood of experiencing a leakage. *Likelihood:* Very Unlikely	*Consequence:* Moderate
30	SS-SYS-PROP-RISK-002	**Pressurant leakage** may occur during operations, due to the vaccum of space. The decrease in pressure will affect the total amount of propellant that can be delivered to the thruster at the correct pressure. This will decrease the lifetime of the mission, since less correction burns can be performed. *Likelihood:* Very Unlikely	*Consequence:* Severe
31	SS-SYS-PROP-RISK-003	**(re-)Ignition failure** is very unlikely in most spacecraft propulsion systems, since not all propulsion techniques need a separate ignition system. However, in case this risk is relevant to the spacecraft, the results will be significant, since propulsion a critical system for orbit maintenance and/or momentum dumping, thus decreasing the operational lifetime. *Likelihood:* Very Unlikely	*Consequence:* Severe
32	SS-SYS-PROP-RISK-004	**Isolation valve failure** failure of any isolation valve will result in either propellant, or pressurant not being able to flow. This will decrease the mission duration, since less propellant can be burned. *Likelihood:* Very Unlikely	*Consequence:* Severe
33	SS-SYS-PROP-RISK-005	**Propellant filter failure** failure of any filter can lead to contaminants flowing towards the thruster or propellant tanks. This can result in clogging of the system, resulting in complete failure of the propulsion subsystem. *Likelihood:* Very Unlikely	*Consequence:* Significant
		Command and Data Handling Subsystem
34	SS-SYS-CDHS-RISK-001	**Failure of data storage module** would result in the loss of all on-board data. Usually, the system stores data from the payload, thermal subsystem, ADCS, and general system health on board, and sends this data to the ground segment in batches. If the data storage module is permanently disfunctioning, it means that no data can be sent to Earth anymore. Without any information flow from the system to the ground control, the success of the mission cannot be guaranteed. *Likelihood:* Very Unlikely	*Consequence:* Severe
35	SS-SYS-CDHS-RISK-002	**Transceiver readouts are incorrectly converted** may occur due to a coding error, which is easily avoidable through rigorous code verification. This would lead to a loss of data unless corrective conversion methods are adopted. *Likelihood:* Unlikely	*Consequence:* Minor
36	SS-SYS-CDHS-RISK-003	**Software malfunction** is one of the most difficult problems to deal with, due to the complexity and size of software programs. Since software issues may be difficult to detect, and may have large consequences, this is a critical risk in any engineering project. *Likelihood:* Possible	*Consequence:* Significant
37	SS-SYS-CDHS-RISK-004	**Bit flips** A bit becomes a 1 from a 0 or a 0 from a 1, up to 10 a day occur due to radiation. *Likelihood:* Very Likely	*Consequence:* Moderate
38	SS-SYS-CDHS-RISK-005	**Processing power (throughput) underestimated** processing of lidar images / subsystems may be much heavier than expected *Likelihood:* Very Unlikely	*Consequence:* Severe
39	SS-SYS-CDHS-RISK-006	**Memory/storage capacity underestimated** Storing images / data may be more difficult than expected, or be larger in size than expected (malfunctioning compression) *Likelihood:* Very Unlikely	*Consequence:* Severe
		Guidance, Navigation, and Control Subsystem
40	SS-SYS-GNC-RISK-001	**Failure of an attitude determination sensor** may result in lack of knowledge of the spacecraft's attitude, and thus an inability to point the antenna (if any), solar panels, and the laser. It really depends on the type of attitude determination, though, as a gyroscope is significantly more likely to fail than a Sun sensor or star sensor. However, according to (Tafazoli, 2009, p.7), those failures are around 10% less critical than for other subsystems as redundancy can be used. *Likelihood:* Unlikely	*Consequence:* Significant
41	SS-SYS-GNC-RISK-002	**Failure of an attitude control actuator** is more likely than a failure in attitude determination sensors, due to the often dynamic nature of attitude control actuators (Tafazoli, 2009, p.7). The result is similar to a failure of attitude determination, since the system ends up unable to point itself. *Likelihood:* Possible	*Consequence:* Significant
42	SS-SYS-GNC-RISK-003	**Interference of GNSS receivers with spacecraft** is possible to occur according to Tafazoli (2009); it is generally more likely to occur than other subsystem failures, and results in a 30% chance of a mission failure (Tafazoli, 2009). *Likelihood:* Unlikely	*Consequence:* Significant
		Ground System

43	SS-SYS-GS-RISK-001	**Human error** can occur in various forms; its consequence depends highly on the situation. Designs should always account for human error as it is somewhat inevitable, but risks prone to such error are not severe. *Likelihood:* Very Likely | *Consequence:* Moderate
44	SS-SYS-GS-RISK-002	**Failure in pointing of the GS antenna dish pointing** is very unlikely due to the regular maintenance performed. Furthermore, it also has a minor impact on the mission, as it can quickly be repaired by the ground team. *Likelihood:* Very Unlikely | *Consequence:* Minor
		Payload Subsystem
45	SS-SYS-PL-RISK-001	**Failure of debris detection system** could arise due to damage to the payload sensors or an error in the design. This is an unlikely event due to the extensive V&V and certification procedures that are usually put in place in the design process. The consequence is severe for the laser method. *Likelihood:* Unlikely | *Consequence:* Significant
46	SS-SYS-PL-RISK-002	**Mistaking an active satellite for a debris** (or hitting an active satellite while aiming at a debris) is unlikely, given that ground-operations should check the target object when it exceeds a certain size. This event would result in drastic legal repercussions and failure of not just one, but two space missions. *Likelihood:* Unlikely | *Consequence:* Severe
47	SS-SYS-PL-RISK-003	**Lower capability of debris removal than expected** is possible due to the novel character of the mission and the low TRL of the concept, which is to be raised in the development process. There are however always some uncertainties when a particular function is performed for the first time, and the system might underperform. The consequence depends on the degree of underperformance, however. It is further noted that this type of consequence is of different nature than for other risks, as it directly impacts the capacity of the mission to perform its primary mission, rather than an activity supposed to sustain this primary objective. It is therefore more fundamental to mitigate than other risks. *Likelihood:* Possible | *Consequence:* Significant
48	SS-SYS-PL-RISK-004	**Hacking** may cause the laser to become a weapon aiming at the Earth to injure people on the ground, which could be coveted by hostile parties, yielding a risk of the spacecraft being hacked to misuse the Space Sweeper. This risk is considered severe it would result in a direct mission failure (unable to continue the clean-up mission), and could result in injuries and deaths of the people on the ground. It is, however, unlikely as security will be taken very seriously in the design. *Likelihood:* Unlikely | *Consequence:* Severe
49	SS-SYS-PL-RISK-005	**Ground injuries** could happen by accident (excluding hacking) in case the Earth enters the shooting angle of the laser while tracking a debris. In case ground injuries can be linked to the Space Sweeper, the operating institutions and the mission legitimacy could be put at risk (severe consequence). This is a possible occurrence, depending on the laser type and associated atmospheric attenuation. *Likelihood:* Possible | *Consequence:* Severe
		Environmental Risks
50	SS-TL-MI-RISK-ENV-001	**Environmental Degradation of Hardware Components** occurs in most satellite surfaces due to corrosion and damage from atomic oxygen in LEO, though this is not critical for this short lifetime mission. *Likelihood:* Likely | *Consequence:* Minor
51	SS-TL-MI-RISK-ENV-002	**Single event upset due to magnetic environment** may affect the system's electronics. According to Tafazoli (2009), magnetic storms may occur. In case a system failure occurs due to the environment, it is due to a magnetic storm in 3% of the cases (Tafazoli, 2009). The consequence is a single event effect, e.g., affecting single components in electronic systems. In case there is no solid failure detection system, these issues can have significant consequences. *Likelihood:* Very Unlikely | *Consequence:* Significant
52	SS-TL-MI-RISK-ENV-003	**Electrostatic (dis)charge due to electrical environment** , especially during the assembly, integration, and testing phases, may include the accumulation of electrostatic charge on the system. Once deployed, electrostatic discharge may occur, which can affect electronics and antennas (Mourra et al., 2008). *Likelihood:* Possible | *Consequence:* Significant
53	SS-TL-MI-RISK-ENV-004	**Solar storms** have similar effects as magnetic storms, namely causing single event effects (Tafazoli, 2009). The consequence is therefore the same as for magnetic storms, but the likelihood is higher. According to Tafazoli (2009), solar storms account for eight percent of all environment related failures. *Likelihood:* Unlikely | *Consequence:* Significant
54	SS-TL-MI-RISK-ENV-005	**System collision with debris** is very likely, as the system will be launched in an orbit with high debris density. Furthermore, the consequence can be severe as the space debris originating from a collision or explosion are still large chunks right after the accident and the spacecraft is expected to have a large solar panel area. *Likelihood:* Very Likely | *Consequence:* Significant

12.5 Mitigation Strategies

The risks in the top right corner of the risk map, with the colours orange or red, are critical, and should be mitigated. These mitigation strategies, as well as their impact on the likelihood and consequence, are described in Table 12.8. The risk map post-mitigation is shown in Table 12.9. Note that most of those mitigations are to be implemented at a later stage in the design process, however, some were already considered such as the ones related to the loss of contact, bit flips and attitude control actuator.

Table 12.7: Technical risk matrix pre-mitigation.

	Negligible	Minor	Moderate	Significant	Severe
Very Likely			37, 43	54	
Likely		50	1, 4		
Possible		2, 25		3, 6, 36, 41, 47, 52	49
Unlikely		5, 22, 35		8, 11, 15, 16, 17, 21, 23, 27, 40, 42, 45, 53	7, 9, 12, 28, 46, 48
Very Unlikely		44	29	14, 19, 20, 24, 26, 33, 51	10, 13, 18, 30, 31, 32, 34, 38, 39

Table 12.8: Mitigation of technical risks.

Risk NB	Description & Mitigation Plan
3	**Operations cost overruns:** all operations risks depend on the ability of the system to remove the debris within a given amount of time (depending on the time allocated to the primary and secondary mission). This can be carefully evaluated through simulations (V&V of the laser system to evaluate its capability to remove the 50% of the debris between 1 and 10 cm in the orbit of choice (SS-TL-STK-US-REQ-STB-002). Additional sources of risk linked to operations cost and schedule overruns are directly related to Project Management and Systems Engineering (PM&SE). However, despite good PM&SE practices, most space projects fail to meet the planned budgets and schedules due to the common thinking that those projects are "too big to fail" and that the technological and scientific outcomes outweigh the delays and cost overruns [1]. However, the design team is very aware of the budget and schedule limitations, and all available practices will be put in place to ensure that the Space Sweeper mission is a successful, within the cost and schedule constraints. *Likelihood:* Possible → Unlikely | *Consequence:* Significant → Moderate
6	**Operations schedule overruns:** same strategy as SS-TL-MI-RISK-MR-COST-003. *Likelihood:* Possible → Unlikely | *Consequence:* Significant → Moderate
7	**Loss of contact:** in the case of an on-board communication failure, the mitigation strategy should be applied to the spacecraft, not the ground system. Redundancy in the telecommunication system decreases the consequence of a loss of contact as the backup component could take over and contact would be retrieved. *Likelihood:* Unlikely → Unlikely | *Consequence:* Severe → Moderate
12	**Failure of solar arrays:** shall be addressed by means of extensive testing as standard procedures suggest. However, it can further be mitigated through redundancy (reducing the consequence) and adding additional safety factors in the design (reducing the likelihood). *Likelihood:* Unlikely → Very Unlikely | *Consequence:* Severe → Significant
28	**Failure of deployment mechanism:** same strategy as SS-SYS-EPS-RISK-003. *Likelihood:* Unlikely → Very Unlikely | *Consequence:* Severe → Significant
36	**Software malfunction:** can be tackled through modularisation (to limit propagation), implementing fault detection containments and recovery mechanisms, and software redundancy (reducing the consequence). *Likelihood:* Possible → Possible | *Consequence:* Significant → Moderate
37	**Bit flips:** save data at least three times, so at any point in time, the flipped data can be compared against two healthy sets *Likelihood:* Very Likely → Very Likely | *Consequence:* Moderate → Minor
41	**Failure of an attitude control actuator:** can be made more reliable by introducing redundancy. This decreases the consequence, since one element of the subsystem can fail without obstructing nominal operations. *Likelihood:* Possible → Unlikely | *Consequence:* Significant → Moderate
43	**Human error:** can be mitigated by a form of redundancy. No single person should be the only one to work on any element of the mission. The lead of a mission element shall ensure that quality control (checking the work of colleagues) is performed. *Likelihood:* Very Likely → Possible | *Consequence:* Moderate → Moderate

[1] URL: https://spectrum.ieee.org/gao-warns-of-deteriorating-costs-and-schedules-in-nasas-major-project-portfolio [Accessed on 21-05-2022]

46	**Mistaking an active satellite for a debris:** at the start of the mission, the target orbit should be analysed by the ground segment to check whether any active satellites are present. In the case a satellite is present, the ground segment should monitor it and communicate the location of this satellite to the Space Sweeper spacecraft. *Likelihood:* Unlikely → Very Unlikely | *Consequence:* Severe → Severe
47	**Lower capability of debris removal than expected:** same strategy as SS-TL-MI-RISK-MR-COST-003. *Likelihood:* Possible → Unlikely | *Consequence:* Significant → Moderate
48	**Hacking:** is expected to be a significant risk for the mission due to its potential to become a weapon to either take down satellites from enemies or harm people on the ground. This can be mitigated by putting cybersecurity on the forefront in the communication and software architectures and implementation (using encryption, physically protecting the GS, etc. [2]), which would reduce the likelihood. However, some cases of hacking of satellites occurred through vulnerabilities of computers used in the ground station, meaning that those should be subject to regular maintenance, and be up-to-date with respect to all relevant pieces of software. It is therefore also important that the ground team is aware of this risk. Furthermore, measures ensuring that the spacecraft enters the EoL procedure automatically if an illicit authentication is identified, can be implemented. Additionally, strong passwords to be changed regularly (similar to nuclear codes) should be used to enter any communication with the spacecraft. *Likelihood:* Unlikely → Very Unlikely | *Consequence:* Severe → Moderate
49	**Ground injuries:** can be prevented by avoided by turning the laser off if it detects the Earth in its shooting angle (dropping the likelihood to very unlikely). Another way to cope with the risk is to ensure that atmospheric dissipation is strong enough to render the laser harmless with respect to ground injuries, arguably reducing the severity of the injuries and therefore the consequence (to moderate), as the effects would hardly be noticed and traceable to the operating institutions. *Likelihood:* Possible → Unlikely | *Consequence:* Severe → Moderate
52	**Electrostatic (dis)charge due to electrical environment:** can occur due to improper assembly, integration and testing. One should remove accumulated charge from non-conductive components, or this could also be prevented by implementing electrical grounding in the design. *Likelihood:* Possible → Very Unlikely | *Consequence:* Significant → Significant
54	**System collision with debris:** it is uncommon to purposefully send a spacecraft to a debris-rich orbit, which makes this risk more challenging. However, this risk is very predictable, since it is known from the first day of the design that this will pose an issue for space-based designs. As long as this risk is given priority during the design phase, the likelihood that the design will not be able to withstand this situation reduces to possible (debris avoidance could also be implemented by design). By structurally shielding the spacecraft against debris, the consequence can be reduced to moderate, since the smaller debris particles have no significant consequence any more. *Likelihood:* Very Likely → Possible | *Consequence:* Significant → Moderate

Table 12.9: Technical risk matrix post-mitigation.

	Negligible	Minor	Moderate	Significant	Severe
Very Likely		37			
Likely		50	1, 4		
Possible		2, 25	36, 43, 54		
Unlikely		5, 22, 35	3, 6, 7, 9, 41, 47, 49	8, 11, 15, 16, 17, 21, 23, 27, 40, 42, 45, 53	
Very Unlikely		44	29, 48	12, 14, 19, 20, 24, 26, 28, 33, 51, 52	10, 13, 18, 30, 31, 32, 34, 38, 39, 46

Final Design Characteristics 13

The final layout of the Space Sweeper spacecraft and mission is summarised in this chapter. Firstly, in Section 13.1, the spacecraft internal and external layout is shown, as well as the final mass properties of the spacecraft. Secondly, the launch vehicle selection is discussed in Section 13.2. Thirdly, Section 13.3 elaborates on the operations and logistics of the mission from development to End of Life. Lastly, the reliability, availability, maintainability, and safety (RAMS) characteristics are discussed in Section 13.4.

13.1 Configuration and Layout

This section shows the final layout of Space Sweeper, including the internal and external layout of the whole spacecraft. The main goals when designing the layout are: ensuring that the stowed configuration fits in the launcher; ensuring that the centre of mass (CM) is below the allowed value for the launcher, namely 3.65 metres (see Section 13.2); ensuring that part of the bottom of the spacecraft is kept free, to allow for a connection with the launcher interface; keeping the moments of inertia as small as possible, while ensuring that the centre of mass does not become to high, since this affects structural performance during launch.

The external layout is shown in Figure 13.1a, in the deployed configuration, and in Figure 13.1b, in the stowed configuration. The internal layout is shown in Figure 13.1c, where the cylindrical structure is made transparent. An exploded view, indicating all major components or component groups, is shown in Figure 13.2. The mass properties of the deployed configuration are summarised in Table 13.1. For these values, the axis system from Figure 13.2 is used, where the origin is at the bottom surface of the bus, in the middle. Lastly, a technical drawing, indicating all major dimensions of the spacecraft assembly, is shown in Appendix A.

13.1.1 External Layout

The largest mirror, for the ablation laser, is mounted in the middle of the spacecraft, on a gimbal system, allowing for a FoV of 60 degrees in all directions. The centre location is also ideal for keeping a low moment of inertia. The downside is the large moment that will occur during launch, due to the mirror being outside of the spacecraft. However, this is taken into account during the launcher interface design. Furthermore, a locking mechanism shall be implemented for the gimbal. The lidar needs to look in the same direction as the ablation laser, and must not have the large mirror in its FoV. The lidar is therefore forced on top of the spacecraft bus, since the bottom should house the launcher interface, instead.

The solar panel layout is based on the system from Zimmermann et al. (2017), previously explained in Chapter 6. The four 'middle' solar panels are rigid, while the four 'corner' panels are semi-rigid. They are placed away from the spacecraft bus, to avoid intersecting with the ablation laser. The attachment points to the bus must be as close to the laser mirror as possible, since the solar panels would otherwise exceed the launcher dynamic envelope.

Furthermore, the thruster is placed on the bottom, to make sure that the plume does not interfere with other components, and to still allow it to act through the centre of mass. Since the thruster is used for station keeping, during operations, it provides a thrust in the flight direction, which is 'backwards' with respect to the laser direction. Therefore, the back of the bus is not an option to locate the thruster, since the spacecraft would have to rotate 180 degrees every time an impulse is required. When it is at the bottom, this angle is only 90 degrees.

Lastly, the star trackers are placed on top, as there is no interference with the solar arrays and laser mirror, and as they should not point towards Earth. The communication antennas are placed at the bottom, since that side of the spacecraft points to Earth most of the time. The radiators are placed on the surfaces that point in a direction where the radiation can escape the spacecraft easily. The solar arrays are in front of the two side radiators, but in the deployed configuration, the arrays are perpendicular to the radiators, thereby not obstructing the radiation as much.

13.1.2 Internal Layout

As the lidar is mounted on the top of the spacecraft, the internal layout should change the centre of mass, such that it does not surpass the threshold for the launcher. The fuel tanks are therefore located at the bottom, as they are heavier than all other internal components. The size of the gimbal has a large uncertainty margin, since it has not been designed in detail. It is assumed that it takes up the entire compartment, and has a load-carrying structure. Above this, the CMGs and all accompanying interfaces are present, since they are relatively heavy. All other components, so the batteries, capacitors, PCDU, OBC, and gyroscopes, are located in the floor above.

The magnetorquers are positioned orthogonally to each other. The heat pipes are distributed over the PCDU, batteries, and laser assembly surface, and they are connected to the entire inner surface area of the radiators.

13.2 Final Launch Vehicle Selection

Based on the three preliminary launchers that were chosen in Subsection 3.4.2 a trade-off was done to arrive at a single choice of launcher to have on standby, so that the system can be swiftly deployed once a breakup even occurs.

The trade-off criteria chosen were insertion, limit loads and CG height, reliability, and cost. These were chosen because they impose requirements on the system that are argued to be more driving than others; for example, the CG

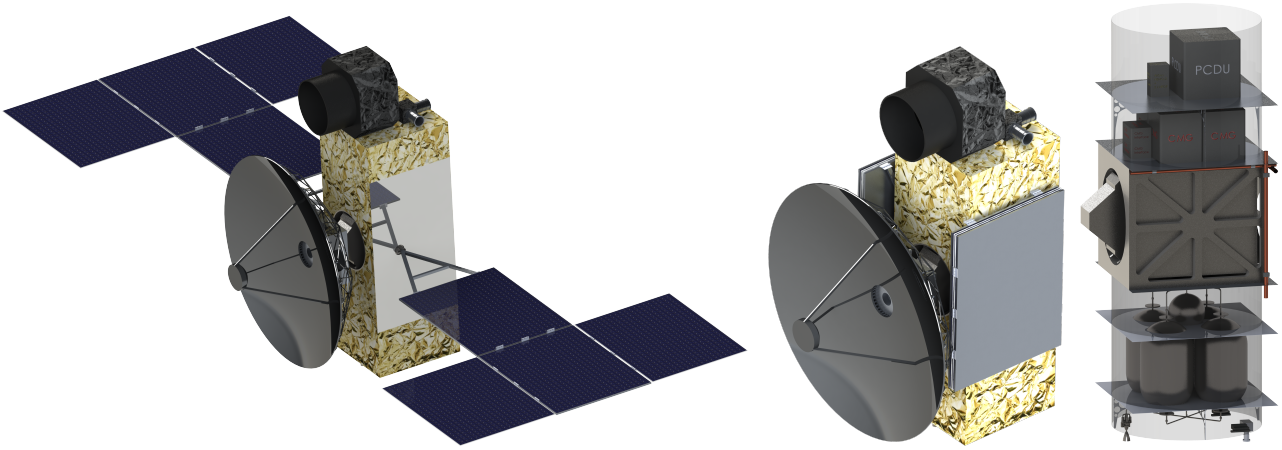

(a) Deployed configuration. (b) Stowed configuration. (c) Internal layout.

Figure 13.1: External and internal layout of Space Sweeper.

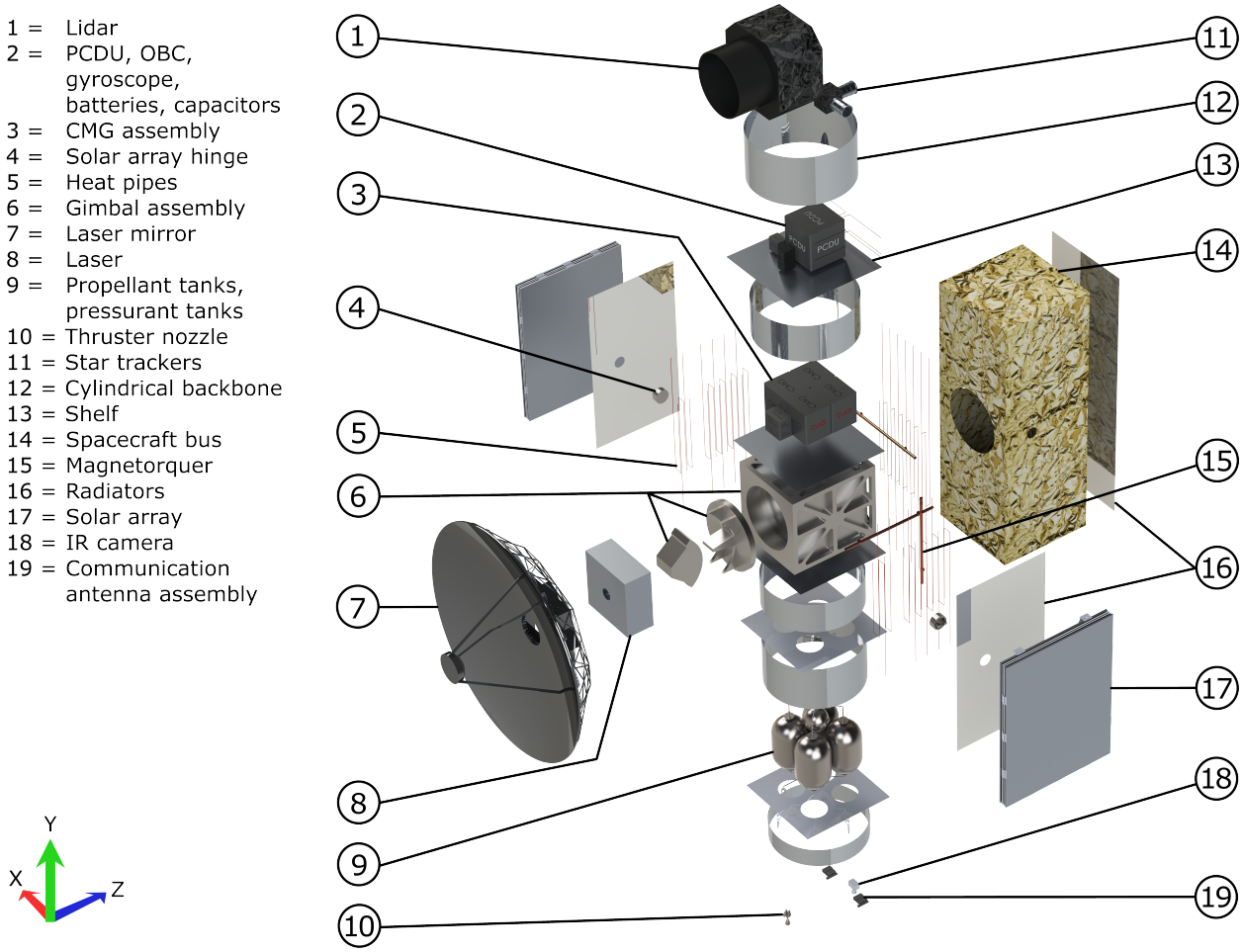

Figure 13.2: Exploded view of the Space Sweeper.

height affects the overall layout of the system much more than the available payload interfaces, which are typically more general in nature. These criteria will be qualitatively evaluated using the data from Table 3.8, as well as other sources found in literature.

The three launchers chosen have quite different insertion capabilities. This criterion is given a high weight for the trade-off as inclination changes lead to high ΔV requirements, and hence the size of the propulsion subsystem depends on how accurately the system is injected into its orbit. A high score for this criterion means that the least amount of ΔV required for insertion by the spacecraft, which is desired. As seen in Table 3.8, the Ariane 62 launcher can reach any inclination. Since our system has to have the capability to work in every orbital inclination, a high score for this criterion is given to this launcher. Due to the extremely high amount of ΔV required for inclination changes, the other

Table 13.1: Spacecraft mass, CM location as seen from the centre of the bottom bus surface, and mass moments of inertia about the CM, for the deployed configuration.

Mass [kg]	CM (x, y, z) [mm]	I_{xx} [kgm^2]	I_{yy} [kgm^2]	I_{zz} [kgm^2]	$I_{xy} = I_{yx}$ [kgm^2]	$I_{xz} = I_{zx}$ [kgm^2]	$I_{yz} = I_{zy}$ [kgm^2]
2,794	(2914, 460.6, 0.2702)	7377	7577	9614	-46.27	-27.92	840.5

Table 13.2: Final key requirements list for the chosen launcher. For more requirements please refer to (*Ariane 6 User's Manual* 2021).

Requirement ID	**Description**
SS-SYS-LV-REQ-01	The cost of the launch shall not exceed 75 million euros.
SS-SYS-LV-REQ-02	The launcher shall be able to deliver the system to the target orbital altitude.
SS-SYS-LV-REQ-03	The launcher shall be able to deliver the system to the target orbital inclination
SS-SYS-LV-REQ-04	The launcher shall be exposed to a maximum axial load of 2.5 Gs in tension.
SS-SYS-LV-REQ-05	The launcher shall be exposed to a maximum axial load of 6 Gs in compression.
SS-SYS-LV-REQ-06	The launcher shall be exposed to a maximum lateral load of 1.8 Gs in compression and tension.
SS-SYS-LV-REQ-07	The launcher shall have a reliability of at least 95%.
SS-SYS-LV-REQ-08	The spacecraft's CG height shall be a maximum of 3.65 m from the payload adapter
SS-SYS-LV-REQ-09	The spacecraft's primary lateral frequency shall be equal to or higher than 6 Hz.
SS-SYS-LV-REQ-10	The spacecraft's primary axial frequency shall be equal to or higher than 20 Hz.
SS-SYS-LV-REQ-11	The launcher shall be able to fit the system.
SS-SYS-LV-REQ-12	The launcher shall be able to support the system's weight.
SS-SYS-LV-REQ-13	The launcher must have an appropriate payload adaptor to ensure the system is carried safely.

Table 13.3: Maximum design launch loads and allowable CG height for each launcher. Note that negative values are from compression loads, positive values are for tension loads, and that CG height values apply to the best fairing available.

	Axial [Gs]	**Lateral [$\pm$Gs]**	**CG Height [m]**
Falcon 9	-6, 2	2	6.2
Ariane 62	-6, 2.5	1.8	3.8
H-IIA202	-4, 1	1.8	3.3

two launchers were given a low score. As mentioned in (*Falcon User's Guide* 2021)(*Ariane 6 User's Manual* 2021)(*H-IIA User's Manual* 2015) all launchers provide 3-axis stabilisation and spin-stabilisation if required.

The limit loads and CG height drive the general layout of the system, earning a moderate importance weight. For the design limit loads, lower values are preferable as this simplifies the spacecraft's design, whereas higher values of maximum CG height are better, as this allows for more freedom in the design layout. The values for both maximum axial and lateral design loads experienced by each launcher are seen in Table 13.3. The Falcon 9 has a slightly lower design loads than the Ariane 62, but larger than the H-IIA202, however it has by far the largest maximum CG height, therefore it is given a score of medium. The Ariane 62 has the highest design loads, and a small maximum CG height, therefore it was assigned a low score. To conclude, the H-IIA202 has the lowest design loads, but also the lowest maximum CG height, therefore, a scored of low was also assigned to it.

A high weight is given for reliability, as even the smallest failure can lead to a complete loss of spacecraft. Two of the launchers in the trade-off have been flight proven tens of times, whereas the other has not yet had its maiden flight at this stage. A high score here means a more reliable launcher, which is what we aim for. The Falcon 9 has had three failures in over 155 launches, a 98% launch success rate [1], clearly deserving a high score in this aspect. The japanese H-IIA202 has launched 45 times and has failed once, leading to another high score. The Ariane 62 however, still has not had its maiden launch. In (*Ariane 6 User's Manual* 2021), Arianespace uses the reliability of their past launchers to prove the reliability of their new vehicle. This cannot be quantified, however it does speak in favour of the manufacturer, therefore a medium score is awarded to this.

Lastly, the cost criterion not only includes the general launch costs, but also a discussion related to the launch site used by each concept, as this will affect the amount of fuel required by the launcher, leading to more, or less, costs. The closer the launch site is from the equator, the more advantage can be taken from Earth's rotational speed, meaning less

[1] URL: https://impulso.space/report/operators [Accessed on 07-06-2022]

Table 13.4: Trade-off results between preliminary launch vehicles chosen in Subsection 3.4.2.

	Criteria			
Concept	**Insertion (High)**	**Loads/CG (Moderate)**	**Reliability (High)**	**Cost (Moderate)**
Falcon 9	L	M	H	H
Ariane 62	H	L	M	H
H-IIA202	L	L	H	M

Figure 13.3: Preliminary S/C structure fitting inside the payload fairing.

propellant is required on board. It will be given a moderate weight due to the limiting cost budget available, and the fact that the launch costs of all three options are relatively similar, noting that high scores for this criterion mean cheaper options. Starting with the Falcon 9, depending on the inclination required, two launch sites can be used; Cape Canaveral Space Force Station (CCSFS) and Vandenberg Space Force Station (VSFS). The launch cost for this vehicle is around 63 million Euros, and the sites sit relatively close to the equator, therefore a high score will be given to it. The Ariane 62 launches from the Guiana Space Center, in Kourou. It is the closest of the three concepts to the equator, and it has a not so expensive launch cost of around 72 million Euros, deserving a high score too. Finally, the H-IIA202 launches from the Tanegashima Space Center (TSC), the furthest from the equator, costing roughly the same as the Ariane 62. It will therefore be given a score of medium.

Using the results shown in Table 13.4, the chosen launcher for the Space Sweeper is the Ariane 62. This launch vehicle can be used for both single or dual launches. The latter is made possible by the dual launch structure (DLS) designed by Arianespace, seen in (*Ariane 6 User's Manual* 2021, p.86). For single launches, both a short and a long fairing are available. As seen in Figure 13.3, the short fairing is enough to take the SpaceSweeper to the desired orbit, therefore the long fairing is excluded as it just adds more weight to the LV, requiring more propellant and subsequently costing more money. Four payload adaptors are available, that can be used in both the single and dual launch configurations, with interface diameters of; 0.937 m, 1.19 m, 1.66 m, and 1.67 m.

13.3 Operations and Logistics

The operations and logistics concept of the mission is presented below. The concept is split among the different high-level phases of the mission, as presented by Figure 13.4. Those phases were already presented in Chapter 3. In the following subsections, the operations and logistics of the different phases are detailed.

Figure 13.4: Mission Phases

Table 13.5: Number of days required (from clean up start) to clean up 50% of the debris larger than 1 cm as a function of the starting day timed from collision / explosion event.

Starting day	5	7	10	15	20	25	40	50	70	100
Days for 50% removed	30.37	30.83	30.43	28.53	27.75	26.69	26.64	36.20	58.94	216.73

13.3.1 Development

During the development, engineers and managers will work in offices in parallel to a workshop to make the necessary prototypes and test the current designs. The need for specific testing facilities will be investigated in the next iteration, when more details are known about the testing needs of the mission. However, it can already be argued that the facilities ran by ESA in Europe will be preferred to facilitate the logistics and reduce the cost aspects of testing (the latter due to the contract the design team has with ESA directly).

13.3.2 Manufacturing and Transport

Once the complete development process of the spacecraft came to a final design (including thorough testing), the spacecraft will be produced by considering different lines of production for the main sub-assemblies: the solar panels, ablation laser, lidar, and the main bus. The main-bus production will mostly consist of the integration of the different off-the-shelf components together, while the production of the ablation laser and lidar. The solar panels are completely off-the-shelf, however, the mechanism will be manufactured and attached to them in the dedicated assembly line.

The four main sub-assemblies are then transported by truck and aircraft towards Kourou, where the main sub-assemblies will be stored and assembled at a later stage. The transportation implies that the sub-assemblies can be fixed on the transporting vehicle (through specific attachment on the bus and solar panels for example), and that the transportation loads are to be taken into account in the design, which will be investigated in the next iteration.

13.3.3 Pre-Launch

One of the main difficulties of the mission resides in the ability of the spacecraft to be launched very quickly in the specified orbit to clean up the debris. Due to the dispersive effect of the J_2 disturbance, it is preferable to launch the Space Sweeper very shortly after the collision or explosion occurred (Teixeira et al., 2022a). This can be compared to a fire truck that needs to stay ready in case it is called for an emergency. Using the mission analysis simulation presented in Chapter 3, the efficiency of the system was evaluated for several clean up starting times (in days after the collision). The simulation was run for 1,000 debris (therefore the absolute number of days is not representative of a real collision, but the relative increase or decrease is) and yielded the results shown in Table 13.5.

Note that those results are also very dependent on the starting position of the spacecraft in orbit relative to the cloud of debris at the start of the mission. The initial decrease is due to the spread of the debris in the initial orbit (desirable such that the spacecraft sees more debris), the following increase in time required is linked to the aforementioned J_2 effect. It can therefore be conservatively assumed that the mission could start up to 30 days after the break-up event, without losing removal efficiency. Assuming an early operational phase of ten days, as discussed below, the launch needs to happen within the first 20 days of the collision or explosion. This is stated in the following requirement:

ID	**Description**
SS-TL-MI-REQ-016	The Space Sweeper spacecraft shall be launched at most 20 days after the collision event.

Storage

To satisfy the requirement to be launched within 20 days of the detection of the collision, the main sub-assemblies of the spacecraft will be stored near the Kourou launch site. Additionally, a main assembly line facility needs to be made available to integrate the remaining sub-assemblies together shortly before launch. It is further more advised that two or more Space Sweeper spacecrafts are constantly available for launch in case both debris orbits arising from a collision are desired to be cleaned.

Furthermore, storage of such spacecrafts (sub-assemblies) prior to an unknown launch date requires careful maintenance, which will be discussed in the following section. First, an overall system state assessment will be performed, consisting of health checks on the separate sub-assemblies, inspections of the most critical parts of the spacecraft, and some eventual non-destructive testing. Following, repairs will be performed if deemed necessary from the spacecraft health assessment. To ensure a quick launch readiness, such maintenance will be performed on a bi-weekly basis. Storage can pose some serious degradation to the spacecraft, according to (Zandbergen, 2021). Therefore, a careful analysis on the rate of collisions in the horizons of 2028 (start of mission operations) should be performed to adapt the batch size and lead time for production, to limit the storage time.

Additionally, the storage conditions need to respect the clean room conditions as specified by the ESA standards (ESA, 2002), commonly used for spacecrafts. No specific part was found to require special storage conditions. This also requires training of the personnel in parallel to the final steps of the development process.

The phase ends as soon as a collision was detected or predicted to happen shortly (the latter being preferable to buy some time). The launch preparation team would then take over to perform the last sub-assemblies health assessment and conduct the last steps towards a successful launch of the Space Sweeper.

Launch Preparations

The launch vehicle needs to be made available very quickly close to the launch site. This is, however, very uncommon, as launchers are generally not kept in storage for very long. A special contract should then be issued with the launch vehicle provider, following a 'fast lane' concept, meaning that in case a collision occurs, the next Ariane 62 produced will be used for the Space Sweeper mission and the previously scheduled spacecraft to be launched would have to wait for the next one. Despite the inconvenience for the other missions, this is likely to be the only solution with respect to logistics, to ensure that space stays clean in near Earth orbits.

When a significant enough collision is detected, the main remaining sub-assemblies are transferred to the main assembly line to put the spacecraft in its assembled, launch configuration. The collision or explosion orbit is then analysed to determine the required EPS and thermal sizing, which were designed to be modular with those respects. First, the ablation laser and the Lidar are mounted, on the main bus, followed by the necessary amount of solar panels, batteries and radiators.

Once the spacecraft has been fully assembled, the procedure presented in Chapter 3 is followed, instruments are re-calibrated and final health checks are performed. The spacecraft is then mounted on the launcher in the dedicated facilities of the Kourou launch site.

While the spacecraft is mounted, waiting for lift-off, the engineers on the ground monitor the spacecraft health at all times prior to lift-off. The phase ends at lift-off, right after the data umbilical between the spacecraft and the launcher is dropped.

13.3.4 Launch and Early Operational Phase

During the launch, the spacecraft operations engineers (responsible for the various parts of the spacecraft [1]) are all present to monitor follow the procedure and prepare the early operational phase. However, The launch vehicle provider is fully in charge of the launch phase, while the spacecraft is in safe mode but cannot communicate housekeeping data through the launcher any more. Furthermore, the cooperative ESA network will be used until the end of the EOP to ensure a near-constant communication between the ground team and the spacecraft (Müller, 2008).

Upon separation, the spacecraft automatically enters the first part of the EOP, such that ground communications can be ensured. This includes: switching to using battery power, activating the on-board transmitter, deploying the solar arrays, de-tumbling and orienting the spacecraft as designed, and switching to a 'wait' mode until the ground station sends the first commands.

The Early Operational Phase will last about ten days[2], starting from the first contact with the spacecraft being in orbit. The launcher provider gives full control of the spacecraft to the Space Sweeper ground control team, who will follow the prepared procedures to ensure a proper functioning of the spacecraft during the following operational phase. The ground team might require to upload some software to correct any detected issues, or send complex commands initiating the following actions of the spacecraft.

The end of the early operational phase is decided by the ground operations, when all systems were verified to work correctly and potential problems were solved. The spacecraft is ready to enter the operational phase and operate the primary mission payload.

13.3.5 Operational Phase

The operational phase requires operations on a day by day basis from the ground team. The mission only then requires the ground station network and a room in the European Space Operations Center (ESOC) as facilities (whereas the main room was used for the early operational phase). Two types of operations and logistics can be detailed for this phase: day-to-day, and single-time management.

Day-to-Day

On a day-to-day basis, the most important operations concern the health state of the spacecraft and the science data that needs to be transmitted to the ground. From this information, the ground operators can take careful decisions on the mission timeline and any type of contingency plan (which becomes a single-time event). The necessary operations performed by the spacecraft are further divided in two:

- **Near-continuous operations**. As shown in Chapters 3 and 8, the functioning of the spacecraft can be seen as an ever repeating loop which takes 100 ms per iteration (10 Hz). The functions performed in the loop are fundamental to the survival of the mission, comprising the basic functions: pointing of the solar panels and production of electrical power, controlling the spacecraft attitude and position in space, operate primary or secondary payload, control the

[1] URL: https://www.esa.int/Enabling_Support/Operations/Who_does_what_in_the_OCC [Accessed on 13-06-2022]

[2] Conservative estimate based on URL: https://www.esa.int/Enabling_Support/Operations/Nonstop_LEOP_full_stop and URL: https://www.esa.int/About_Us/ESOC/Liftoff [Accessed on 14-06-2022]

thermal environment. Following, the housekeeping data for each subsystem is gathered, and evaluated by the CDHS to detect any system faults. All the telemetry and payload data is stored on a hard driven, waiting for the next pass over the ground station to be transmitted. The spacecraft being mainly autonomous in those operations, the ground segment is not solicited.

- **Once per orbit**. A few actions need to be performed once per orbit to ensure a correct functioning of the spacecraft on the long term. First, the data needs to be transmitted during every pass over the ground station network, which implies checking if the low-gain antenna is facing the Earth. Furthermore, it is also required to perform the orbital maintenance procedures to counteract the drag and other disturbances which accumulated over the orbit. This requires the spacecraft to point the thrusters, fire them, and rotate back to its idle position.

Those actions are rather autonomous and are not designed to need any ground support other than operators checking whether the housekeeping data is nominal (low staffing level, following (Wertz, Everett, et al., 2011, p. 905)). The ground operators are then responsible for going through the housekeeping data from the previous orbit to ensure that no fault occurred without alarming the system, and to process the (primary or secondary) payload data. Additionally, the Space Sweeper mission requires a high level of cybersecurity due to the potential threat of the payload to other near-by missions and ground safety. This therefore requires an encrypted and password protected communication, those passwords are to be changed on a daily basis to ensure a reliable and safe operation of the spacecraft.

Furthermore, the ground operations are also responsible for a set of daily tasks to be performed to ensure correct operations of the spacecraft at all times. The most important ones are given below[3]:

1. Power management, in case any limitations arise, to assign the power manually to some components.
2. Data management, in case of restrictions on the storage volume, to choose what data will be stored.
3. Attitude management, put restrictions on the spacecraft pointing in case a spacecraft comes close to another, or for Earth safety.
4. Switching on/off instruments, putting restrictions on which instruments can be used.
5. Fuel management, through minimisation of fuel expenditure to extended the satellite's lifetime as much as possible.

Single-Time

The following single time events could occur during the mission, requiring specific operation procedures:

- **Hacking** would result in a catastrophic failure of the mission and a great threat to ground and space safety. Therefore, the EoL procedure should be initiated if an illicit connection to the spacecraft is found, with a certain delay time (after which the sequence will start). During this delay time of a few hours, the ground team will aim to retrieve the spacecraft.
- **Software**: Memory reload, and firmware and software updates can be initiated by the ground team if necessary.
- **Safety decisions** issued by the ground operations team, in case of a faulty subsystem, resulting in risks for the mission objectives or safety of other nearby spacecrafts.
- Initiate **switch to secondary mission**, as will be discussed below.
- **Collision avoidance**. If a collision is detected by the ground station (based on debris database and satellite data) between the Space Sweeper and a debris or other spacecraft. In which case the spacecraft will initiate a manoeuvre to avoid the debris.

Additionally, the phase ends if it is deemed appropriate by the ground operations team, based on the housekeeping and science data being received. Alternatively, as mentioned above, the mission could end prematurely in case the spacecraft gets hacked, or it needs to be de-orbited for safety concerns.

Flow of Mission Objectives

As explained in Chapter 2, two main missions are on-board of the Space Sweeper:

1. The primary mission consists of the ablation of the detected debris above 1 cm, and starts right after the end of the early operational phase.
2. The secondary mission consists of detecting 1 mm or higher particles, and to catalogue them. Additionally, another payload will be taken on-board to extend the market size of the mission, as will be investigated in Chapter 15. This secondary payload will perform its operations for a duration of one year.

Rather than a sharp change between the two missions, the primary mission will slowly merge into the secondary one, as fewer particles larger than 1 cm are found with time. If less than 25 particles per day are found during three consecutive days, the lidar will reduce the intensity of the noise filtering algorithm such that particles larger than 1 mm or higher. The secondary mission will then start and the tertiary payload will turn on. However, any particle with a predicted size larger than 1 cm will still be ablated, although this will happen less and less regularly with time. This threshold is expected to take around 110 days to be reached, according to the mission analysis simulation.

[3]URL: https://www.esa.int/About_Us/ESOC/Routine_operations [Accessed on 15-06-2022]

13.3.6 End of Life

The end of life can be initiated at any time under decision of the flight operations (either at the end of the planned operational phase, or at if a catastrophic failure occurred), or automatically if the spacecraft identified that it was hacked. A controlled EoL sequence was chosen, meaning that a steep re-entry angle should be followed and the position of the spacecraft at all times during the re-entry to ensure that it falls in the chosen area. It is desirable that the debris fall in an ocean, where the population density is the lowest on Earth, in case the complete structure does not burn up as expected. The cooperative ESTRACK network will again be used to ensure a near constant communication with the spacecraft during the manoeuvre, for the few hours required to perform the de-commissioning.

After the spacecraft burn up, the whole clean-up mission will carefully be documented. The different departments of the mission will analyse the obtained performance and draw lessons learned to possibly improve the design for a next iteration. In this final part of the mission, only the team offices will be used.

13.4 RAMS Characteristics

The reliability of the spacecraft is a crucial measure for the chances of a successful mission. This reliability has an inverse relationship with the technical risks during the mission duration, as reliability decreases with increased odds of failure. The reliability of the spacecraft is analysed by taking the product of the separate reliability values of all subsystems. The reliability (R_i) of each subsystem is calculated using Equation (13.1), where λ_i is the failure rate of the subsystem, and t is the mission duration in years. A margin of 30% is taken on top of failure rates, due to the uncertainty of the applicability of these values on our mission (Zandbergen, 2021). Another reason for such a safety factor is the uncertainty of how the storage time of the vehicle will effect the failure rates. Results of this reliability analysis can be found in Table 13.6.

Table 13.6: Failure rates per subsystem and complete spacecraft (Zandbergen, 2021).

Subsystem	Failure rate	Failure rate (with margin)	Reliability	Reliability (with margin)
Propulsion	0.012	0.0156	0.9881	0.9845
GNC	0.0248	0.03224	0.9755	0.9683
EPS	0.0092	0.01196	0.9908	0.9881
Struc & Mech	0.0078	0.01014	0.9922	0.9899
TT&C	0.0085	0.01105	0.9915	0.9890
TMS	0.0064	0.00832	0.9936	0.9917
Total	-	-	0.9336	0.9146

$$R_i = e^{-\lambda_i \cdot t} \qquad (13.1)$$

$$A_i = \frac{\mu_i}{\lambda_i + \mu_i} \qquad (13.2)$$

$$A_{tot} = 1 - \prod_{i=0}^{6} (1 - A_i) \qquad (13.3)$$

The availability can be described as the proportion of total time that the vehicle is operation. This depends on the failure rate, and the recovery rate for each subsystem. The availability per subsystem can be calculated by using Equation (13.2) (Smith, 2014), where μ_i is the recovery rate. The recovery rate is the reciprocal of the average recovery time, which is assumed to be 60 seconds per subsystem failure. The total availability of the spacecraft can be calculated by using Equation (13.3) (Wertz, Everett, et al., 2011). The results of this calculation are shown in Table 13.7.

Table 13.7: Availability per subsystem and complete spacecraft.

Subsystem	Recovery rate	Failure rate	Availability
PROP	0.0167	0.0156	0.517
GNC	0.0167	0.0322	0.341
EPS	0.0167	0.0120	0.582
Struc & Mech	0.0167	0.0101	0.622
TT&C	0.0167	0.0111	0.601
TMS	0.0167	0.0083	0.667
Total	-	-	0.993

The maintainability has several components: the maintenance of the spacecraft before launch, the maintenance of the on-board software programs, and the maintenance of the ground segment. It is crucial that research will done on how the storage of the vehicle effects the reliability of all subsystems. Spacecraft also have a significant amount of lines of code,

in which small bugs are present. Maintenance on these software programs must be performed during the mission when bugs are founds. Furthermore, the software must be maintained, by means of updating models, and protection against cyber attacks.

The last thing that is considered in this section is the safety during the different stages of the mission. Unsafe situation shall be avoided at all cost. Examples of situations like this are pointing the laser towards Earth, and spacecrafts being in intersecting orbits between the laser and the particle that is ablated. The laser shall not ablate particles when these situations occur, due to the risk of damaging active satellites, or worse, potentially injure humans on Earth. Another unsafe situation that should be taken into account, is the possibility of the spacecraft being hacked. The spacecraft shall perform a full reboot and changing of passwords credentials when such an intrusion of the system is detected.

Development Strategy and Planning 14

The following chapter details three aspects to a successful further development of the mission. Firstly, the production plan is explained in Section 14.1, which includes manufacturing, assembly, and integration. Secondly, the two development plans, one for the ablation laser development, and a second to develop the mirror technologies required, are given in Subsection 14.2.1 and Subsection 14.2.2 respectively. Lastly, the program's sustainability strategy, which includes the mission itself, production, and a life cycle assessment, is explained in Section 14.3.

14.1 Production Plan

The production plan of the satellite is vital for its success. Components needs to be bought, while some parts need to be machined. Some other materials need to be bought before manufacturing can happen in the first place. In the end, parts need to be integrated into subsubsystems, and these need to be integrated into subsystems. In the end, final system is assembled and validation tests are performed. Only if passed, spacecraft can be launched. Otherwise, fault needs to be found, isolated and resolved, which may require going back to some step. Consequently, delays can happen and production plan is needed to visualise bottlenecks in the production. The Manufacturing, Assembly, Integration Plan is introduced in Figure 14.1. Figure 14.1 indicates that the majority of the satellite's subsystems are COTS. The only subsystems that needs to be manufactured are the payload, which consists of a lidar and an ablative laser, and structures. Structures is a relatively simple system to manufacture and assembled due to being aluminium. However, there is a large uncertainty in lidar and laser as removal of space debris is a novel application for these systems. Consequently, it is unknown what materials will be required for and how exactly they will be manufactured. This will be the focus of Design and Development Plan outlined in Section 14.2.

14.2 Design and Development Logic

The design and development resources needed for this spacecraft are plentiful, considering how novel the concept is. Generally speaking, the subjects for design and development are the ablation laser, the mirrors, and the tracking ability of the detection system. Therefore, this chapter will present an initial estimation of the development scale necessary, specialised facilities required, and any other industries that may profit from laser developments.

14.2.1 Ablation Laser Development

The development of the laser includes both the desire for a better theoretical understanding of ablative properties of shapes, materials, and rotational effects, as well as optimisations of the mirror structure necessary. Of course, the actual laser itself must also be custom-built to fulfil the exact requirements desired. Therefore, the distinction can be made between two categories of laser development: debris ablation testing, and secondary structures.

To start with, the theoretical research of ablative propulsion requires investigation. Though Phipps states that rotational velocities of the debris are "beneficial", and result in "the overall effect tending toward the mean" (C.Phipps et al., 2012, p.1295), a more precise quantification of such effects is necessary for practical implementation in space. More importantly, and as is easily understood from research by Coherent (Hodgson et al., 2019), each material requires different laser parameters to result in optimum ablation. It should not be the case that the laser is optimised for ablating one material, but breaks down other materials into smaller fragments, contributing to more space debris. Lastly, the laser itself must, of course, be tested with the appropriate facilities, and must show experimentally to be able to fulfil all the requirements necessary before implementation in space.

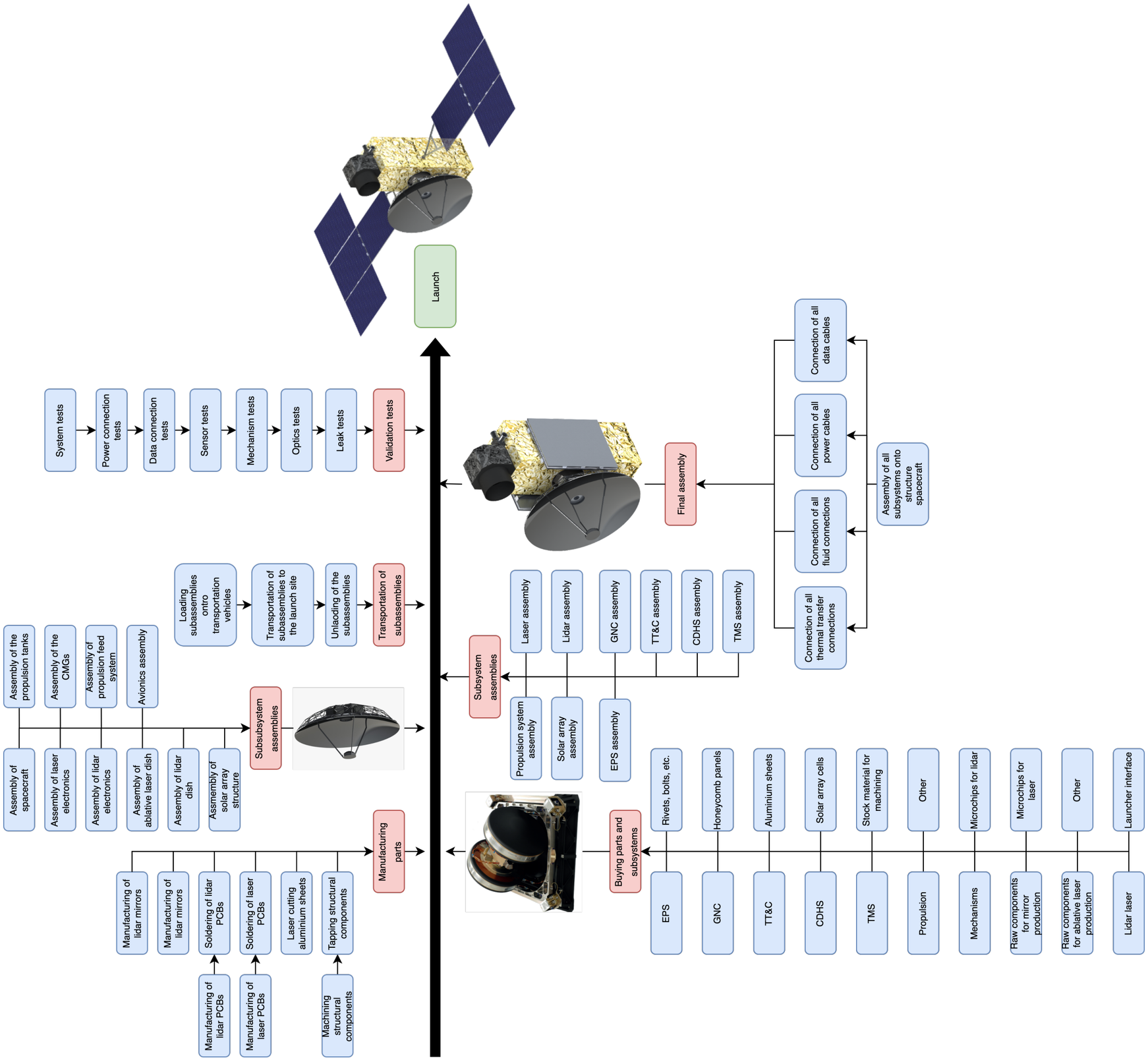

Figure 14.1: Manufacturing, Assembly, Integration Plan.

Specialised facilities

While there are facilities around the world that would allow for testing of ablative properties of materials, these are usually relatively limited in laser properties. As an example, take the experiment performed by Coherent (Hodgson et al., 2019). In this experimental set-up, 100 W lasers were used. This is orders of magnitude below the laser design of this report, and which is lower still than that proposed by Phipps in his L'ADROIT concept (Phipps, 2014) (maximally 40 kW during shooting). It would be logical to develop the laser in parallel the quantifying of material and rotational effects, such that the final iteration of the laser can be tested on the various debris sizes, shapes, materials, and rotations. Therefore, some other facilities look more promising to facilitate the experiments required. Depending on whether development takes place in the EU or US (or both), three facilities are selected. In the US, the Lawrence Livermore National Laboratory (LLNL) is one of the two locations that seems promising. In this facility alone, the "solid-state heat capacity laser" was built in the 2000s, and is capable of an average power above 10 kW (C.Phipps et al., 2012). Straight away, it becomes obvious that such a facility is more apt at providing a testing ground than that of Coherent. A secondary facility in the US would be the Los Alamos National Laboratory (LANL), where Phipps himself conducted a program investigating "mechanical and thermal coupling of pulsed lasers to targets using high-energy-laser facilities" (Phipps, 2014, p.255), thus proving that the facilities required exist. In the EU, the company "HiLASE" would be an ideal partner, given their research into state-of-the-art laser systems. Even more inviting is their "Open Access" program, where since 2017 "beamtime is free of charge", and "successful proposals will get access to the HiLASE Centre research infrastructure." [1] In 2021, their "BIVOJ" laser achieved pulse energies and durations of 145 J and 10 ns respectively[2], both of which are comparable to the laser system desired for the spacecraft. The BIVOJ wavelength of 1030 nm and repetition rate of 10 Hz, however, are not comparable, and especially the repetition rate requires further development. A detailed estimation of the associated costs for relevant labour, components, and facilities for prototyping, development, and testing will be included in Chapter 15.

Cost sharing and external applications

With this novel payload concept comes an extremely high cost, shown in Chapter 15. While some of the budget required is present in the original M€400, it is useful to investigate other industries and applications of laser technology, as they may want to become a research and development stakeholder. The crux of the research is not actually focused on removing space debris. On a more fundamental level, the bounds of laser technology would be pushed to heights never reached before, and with an understanding of photonics to match that. While space debris may be an exciting new application of ablation, the principle already exists in industries such as manufacturing, but may also prove interesting to ever-developing fields, such as medicine.

In medicine, the principle of ablation exists in cardiac treatment[3], where, for certain heart conditions like arrhythmia, either heat (radio frequency energy) or extreme cold (cryoablation) is applied to heart tissue, aiming to disturb the conduction of electrical signals around the heart (which leads to unwanted muscle contractions) by creating scar tissue. This treatment often results in only temporary symptom relief, and is only as good as the surgeon performing the procedure. Imagine the possibilities that a small laser could bring to such a procedure. Instead of applying the heat or cold manually, a laser with an incredibly small spot size could be used to precisely ablate the necessary heart tissue, resulting in a minimal invasive procedure. A secondary use of laser technology could be in treating scar tissue, where laser surgery "involves using a laser to remove the top layers of skin".[4] It is thus clear that any research on ablative properties - something very lacking today - would be useful to treat scar tissue, especially considering that ablation on space debris aims to minimise energy losses into the surrounding 'heat affected zone'. This is perfectly similar to healthcare, where one wants to retain as much healthy tissue as possible during treatments. Though only two applications have been discussed, many more fields, such as ophthalmology, exist in healthcare that would profit from advances in laser technology.

Given the application of lasers in the debris-removing payload, one particular challenge is to create a small spot size (order of cm) at a very large distance (hundreds of km). This particular feat of laser applications could prove extremely useful in laser (optical) communication. Laser communication is becoming increasingly desired, as a way to transmit "huge amounts of data from satellite to satellite", and "provide low latency, secure data".[5] Particularly military applications could benefit from such a system, given secure communication methods are vital to ensuring the safety of a spacecraft, armed forces, or even country. As a quick note regarding military applications of lasers, in the past laser technology has been attempted to be used on an airborne platform called the YAL-1 to shoot down ICBMs[6], and Israel recently claimed to have a working prototype of a laser defence system, capable of shooting down drones and missiles[7]. Hence, it is not

[1] URL: https://www.hilase.cz/en/a-new-world-record-for-bivoj-laser/ [Accessed 11/06/2022]
[2] URL: https://www.hilase.cz/wp-content/uploads/HiLASE-_BIVOJ_world-record-2021_Press-Release.pdf [Accessed 11/06/2022]
[3] URL: https://www.mayoclinic.org/tests-procedures/cardiac-ablation/about/pac-20384993 [Accessed 11/06/2022]
[4] URL: https://www.nhs.uk/conditions/scars/treatment/ [Accessed 11/06/2022]
[5] URL: https://spacenews.com/dod-space-agency-to-launch-laser-communications-experiments-on-spacex-rideshare/ [Accessed 11/06/2022]
[6] URL: https://minutemanmissile.com/abl.html [Accessed 12/06/2022]
[7] URL: https://www.nytimes.com/2022/06/03/world/middleeast/israel-laser-rockets.html [Accessed 12/06/2022]

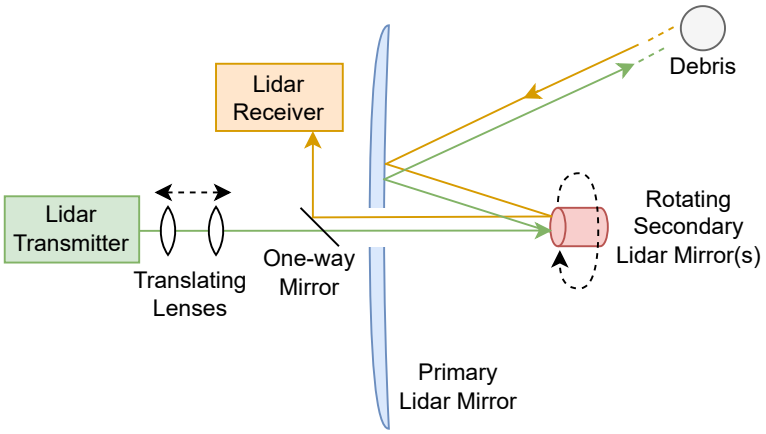

Figure 14.2: Diagram showing the desired development of translating lenses and a rotating secondary mirror to achieve directional lidar sensing. The lenses achieve a variable FoV, while the rotating secondary mirror achieves large FoV scanning.

surprising that the development of laser technology in general could be wholly sponsored by governments or third parties interested in the military applications of such technology.

Lastly, one very interesting application of laser technology is in the field of energy creation, specifically laser-fusion. The aforementioned Lawrence Livermore National Laboratory in California contains the so-called "National Ignition Facility", whose goal it is to "produce more energy than it consumes in a sustained fusion reaction."[8] As of 2021, it was possible to achieve an output of 70% of the energy input, which is supposedly almost enough to achieve ignition[8]. These reactions function by using high powered laser to hit a target, in this case a gold cylinder, with the goal to "unleash a cascade of particles that leads to more fusion and more particles, thus creating a sustained fusion reaction."[8] The laser development programs contributes to this by further enhancing the understanding of energy transfer to objects (to the gold cylinder), the creation of (small) spot sizes (to make the energy losses as small as possible), and the ablative properties of various materials (to understand at what fluence level energy is no longer used to ablate a material, but is absorbed instead). Though the National Ignition Facility is aimed at developing the science needed for nuclear weapons, advances in understanding fusion could play a leading role in combating climate change. Fusion has the potential to become a safe, cheap, and effective power source by[9]:

- Mitigating harmful atmospheric emissions.
- Using abundant resources, mainly hydrogen and lithium.
- Avoiding the creation of any long-lived radioactive nuclear waste (unlike nuclear energy production).
- Being inherently safe, given the process is not a chain reaction, but requires plasma to be above a threshold temperature. Below this temperature, the reaction comes to a halt automatically.

14.2.2 Mirror Development

The mirrors used in both the ablative, high powered laser and lidar detection system require further development. The development of the mirror technologies, though somewhat different for either application, will be combined in one development program. The reasoning behind this is simple, as it keeps the costs as low as possible (efficient use of manpower, sharing of office space and facilities to the extent that it is possible), as well as results in a time-efficient program, as much knowledge is expected to be shared between the applications. The mirror development required for the lidar system is multifaceted, and its implementation is illustrated in Figure 14.2. Two main points can be distinguished, which are:

- Developing a rotating mirror, or multiple mirrors, to create a spiral pattern of light. This includes both the mechanism required to create a rotating pattern of light, but also finding the optimal shape of the mirror to perform said function.
- Developing an optics system that ensures rapid changing of FoV is possible.

The mirror development for the ablative laser consists of designing a secondary mirror that allows for a variation in spot size, such that fluence can remain constant given a non-zero relative velocity (changing distance). This is best illustrated in Figure 14.3, where it can be seen that changing the secondary mirror position allows for a different spot size on the primary mirror, and thus spot size at the debris. The parameters that will need research are a mechanism to change the shape of a fragile structure like a mirror (fragile in the sense that the mirror material may not break), and research into the optimum material that will allow for reliable prediction of light reflection (using phase conjugation mirrors, perhaps), efficient reflection (low absorption), high reliability (not immediately broken when hit by debris), etc. The primary mirror will require less development, given it does not morph but acts like a traditional mirror.

[8] URL https://www.nature.com/articles/d41586-021-02338-4 [Accessed 11/06/2022]
[9] URL:https://www.iaea.org/topics/energy/fusion/faqs [Accessed 11/06/2022]

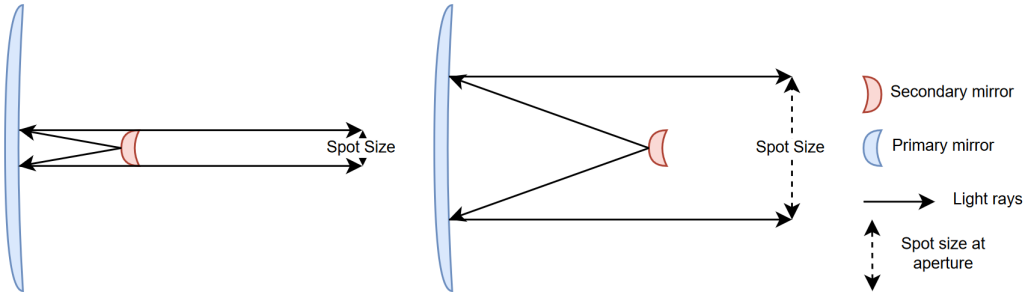

Figure 14.3: Diagram demonstrating different positions of the secondary laser to create a different spot size.

Specialised facilities

As with the laser development plans, the facilities required are first selected. Unlike the laser, where specialised facilities are needed to test high-powered equipment, material research can first take place in lower-scale facilities before implementation is tested in more advanced facilities. Within the TU Delft for example, research into shape-morphing materials is already performed in the emerging materials lab[10]. TU Berlin's optics and atomic physics department may also be one of the best facilities to start research into mirrors, especially considering Dr. Eichler's research into conjugate mirrors (Eichler et al., 2001), which was performed at TU Berlin. However, while some experiments may take place in facilities comparable to those of most large universities, facilities where the laser itself is developed may be necessary to ensure adequate scenario testing. If mirror development takes place in the EU, then HiLASE's facilities would, indeed, be optimal. Otherwise, the Los Alamos National Laboratory or Lawrence Livermore National Laboratory may be viable candidates.

Cost sharing and external applications

Mirror development, in contrast to laser technology, does not necessarily function as a standalone feat. Instead, enhanced mirror technology can result in, as in this report, other systems (the laser) achieving results that were previously not possible. Not only the uses discussed in this report benefit from being able to alter the spot size of the mirror. Just like the James Webb Space Telescope, ground-based telescopes would benefit from enhanced mirrors, that would create more detailed and precise images. Specifically the morphing mechanism may prove useful, in ensuring that the optimal position of the telescope mirrors is achieved.

Apart from space-exploration applications, development in wide FoV lidar systems may prove useful for a plethora of commercial or military, ground-based applications. Self driving cars, "laser altimetry, contour mapping, and digital terrain models"[11] are only some of the existing applications of lidar systems. As an example of a potential commercial application, lidar imaging may prove useful in the maritime or aviation industry. Just like with self driving cars, a manner to avoid collisions during busy night operations could be using lidar to detect obstacles (other, especially smaller, ships) in port, because it provides a higher resolution than radar does. Similarly, in the development to achieve autonomous air travel, lidar imaging could be an addition to Airbus' Autonomous Taxi, Take-Off and Landing (ATTOL) project, where currently image recognition is used[12], while lidar would be able to provide a depth element (extra dimension). This depth sensing could be very useful during taxi operations, where other aircraft, baggage carts, follow-me vehicles, pushback trucks, buildings, and remaining obstacles could be mapped, and thus allow for precise manoeuvring without a wing striking an obstacle.

14.3 Sustainability Strategy

This section explains how the mission contributes to sustainability, and addresses the way sustainability is taken into account in the design. First, the mission sustainability will be given in terms of characterisation factors for space sustainability. Secondly, a strategy will be given for system production, and lastly, the life cycle assessment to be done is planned.

14.3.1 Mission Sustainability

According to (Secure World Foundation, 2018), space sustainability is: *"Ensuring that all humanity can continue to use outer space for peaceful purposes and socioeconomic benefit now and in the long term."* In 2019, the World Economic Forum proposed the development of a so-called Space Sustainability Rating (SSR)[13]. To assist the SSR development, (Letizia et al., 2021) proposed a framework on sustainable space design. This framework is the basis of the following sustainability aspects. The goal is to reach a platinum certified rating for the SSR, the highest possible rating[14]. In case

[10] URL: https://www.tudelft.nl/io/onderzoek/research-labs/emerging-materials-lab/shape-morphing-products [Accessed 12/06/2022]
[11] URL: https://circuitstream.com/blog/what-is-lidar/ [Accessed 12/06/2022]
[12] URL: https://www.airbus.com/en/newsroom/press-releases/2020-06-airbus-concludes-attol-with-fully-autonomous-flight-tests [Accessed 17/06/2022]
[13] URL: https://www.weforum.org/projects/space-sustainability-rating [Accessed on 27-04-2022]
[14] URL: https://spacewatch.global/2022/04/space-sustainability-rating-to-launch-in-june/ [Accessed on 13-06-2022]

any item from the framework is irrelevant to this mission, it is not included. Furthermore, additional items specifically related to the mission objective are added to the list.

Space Traffic Footprint: Relates to the likelihood, and consequence, of creating space debris, either due to the spacecraft breaking, or performing an inadequate End-of-Life (EoL) strategy. This category relates directly to User Requirement SS-TL-STK-US-REQ-STB-005. Specifying this aspect further, one should consider:

1. System mass: a higher satellite mass results in larger consequences in case of a collision. A lower mass is therefore preferred.
2. System size: Larger satellites are more likely to cause a collision. A smaller size is therefore preferred.
3. System durability against collisions with space debris: since the system shall be sent to an orbit which is highly populated with debris, the durability of the system has a high priority.
4. System EoL strategy: to avoid creating more space debris, the system needs to have an EoL strategy that guarantees that the system itself will not act as space debris after its operational lifetime.

Detectability, Identification, and Tracking: If an object in orbit is not detectable, identifiable, or trackable from the ground, there is a larger sustainability issue than when the object is clearly identified and traced. The satellite should comply with these requirements during the entire lifetime. The three aforementioned items are further explained here:

1. Detectability: the ease with which the satellite can be detected from the ground without prior information.
2. Identifiability: the ease with which the satellite can be uniquely distinguished from other objects in space.
3. Trackability: the ease with which the future trajectory of the satellite can be predicted from the ground.

Ideally, the system complies with all these three principles. This helps keeping track of the system, in case the system cannot communicate to the ground station due to a failure. According to (Letizia et al., 2021), knowing the shape and planned orbit of the system aids in complying with these three items.

Collision Avoidance Capabilities: Points one, two, and three in the space traffic footprint are of less relevance in case the system is equipped with a collision avoidance system. However, there are numerous issues with this approach. Firstly, due to the destination orbit of the mission, an orbit crowded with debris, it is likely that the system would be continuously avoiding space debris during its entire operational lifetime, which requires a lot of fuel. Secondly, it is probably more efficient to design a system that can survive debris impact, rather than avoid it. Thirdly, the system is supposed to remove the debris from the orbit, and avoiding the debris is thus disadvantageous in case of contact-based removal methods.

Data Sharing: Relates the amount of information that a business is willing to share with other companies in the space sector. The more open a company is about their mission, the more robust a global satellite database can be, and the more sustainable spaceflight is. A line between confidential and public data should therefore be drawn.

Operation Standards: The Inter-Agency Space Debris Coordination Committee (IADC) published a set of space debris mitigation guidelines (IADC, 2020). According to these guidelines, the following mitigation measures ensure a sustainable space mission (item two, three, and four have already been discussed previously, but the IADC adds more specific information):

1. Limit the release of debris during operations: this should be considered during the conceptual design phase. For the given mission objective, the release of debris during operations should be zero.
2. Reduce the likelihood of a satellite break-up or explosion: IADC gives the following advice (IADC, 2020):
    a) Remove all propellants, fluids, or chemicals before the EoL, to prevent burns, over-pressurisation, or chemical reactions.
    b) Batteries should be designed to be strong enough to withstand pressure build-up, and interfaces with other electrical subsystems should be de-activated, especially the power generation system.
    c) Energy stored in momentum wheels should be discharged before the EoL.
3. EoL strategies: IADC proposes a number of direct requirements and provides advice:
    a) The satellite shall be removed from orbit within 25 years since the Begin-of-Life (BoL).
    b) The success probability of the EoL disposal shall be at least 90%.
    c) In case of re-entry EoL (which is recommended), debris that does not burn up in the atmosphere shall not pose a threat to people or property. Specifically, the casualty rate for a single re-entry event shall be lower than one casualty per 10,000 re-entry events (Klinkrad, 2006; Muelhaupt et al., 2019; Ailor, 2019). It is advised that either as little debris as possible survives re-entry, or the re-entry is aimed at uninhabited locations. Additionally, no toxic materials from the spacecraft should pollute the Earth at the location of impact, or while burning up in the atmosphere.

Spectral Utilisation: Spectral utilisation is the bandwidth that is used for communication between the spacecraft and ground station. A licence is required from the government and International Telecommunication Union.(Secure World Foundation, 2018)

14.3.2 Production Sustainability

This subsection explains the spacecraft's sustainable production. The Brundtland definition of sustainability gives: *"Sustainable development is development that meets the needs of the present without compromising the ability of future generations to meet their own needs."* (Brundtland, 1987, p.292). Hence, (Rosen, 2012) proposed a method that specifically

applies to engineering projects. This method outlines five assessment criteria for sustainability, which will be tailored to the Space Sweeper project. The totality of the production sustainability analysis shall be summarised in a Life Cycle Assessment (LCA) report, which shall comply with the ISO 14040 standard (*ISO 14040: Environmental management - Life cycle assessment - Principles and framework* 2006), as seen in Subsection 14.3.3 .

Material Use: The following three types of materials shall be avoided:

1. Materials resulting in large environmental impacts, either during mining, processing, use, or disposal. To assess this, the environmental impact categories, as explained below, shall be used.
2. Critical raw materials (CRM): Assessing material criticality can be done by looking at its supply risk, as well as economic importance. If both factors are higher than a limit as defined in (Blengini et al., 2020), the material is a CRM. According to (Blengini et al., 2020, p.6), Heavy Rare-Earth Elements (HREEs) and Light Rare-Earth Elements (LREEs) have the highest supply risk, so these shall be avoided at all costs.
3. Toxic materials: It is not feasible to completely eliminate the use of toxic materials, since materials such as brominated flame retardants, lead-based solders or hexavalent chromium are frequently used in electronics (Lincoln et al., 2005, p.139). Furthermore, there is no threshold between non-toxic and toxic. NASA defines a Toxicity Hazard Level (THL) (NASA, 2014), ranging from zero to four. Level zero results in slight irritation on human skin. Level four may result in long-term health issues, such as cancer or internal tissue damage. Obviously, even level zero is undesirable, but it is not critical to human health. Therefore, it is proposed that the maximum NASA THL allowed for the system shall be zero.

Manufacturing Processes: May use a lot of energy (e.g., at high temperatures), or have an environmental impact (greenhouse potential, acidification potential, eutrification potential). Moreover, during prototyping and testing, unnecessary manufacturing may be carried out. The following points are used to increase manufacturing sustainability:

- For prototyping, it is not always necessary to produce the component with the original material. For example, if it is tested whether the components fit together, additive manufacturing with polymers shall be used, since the model is not tested for its material properties.
- Material removed during machining or separating processes shall be sent to a recycling company.
- Non-destructive testing shall be preferred over destructive testing, as it reduces waste.
- Electricity shall be preferred as an energy carrier over fossil fuels.
- The factory shall be equipped with solar panels on the roof.

Energetic and Exergetic Efficiency: A distinction is made between energetic, and exergetic efficiency. Energetic efficiency is the amount of energy that is contained in the desired end product (Stougie et al., 2018). Exergetic efficiency is the amount of exergy (work potential), that is maintained (Stougie et al., 2018). Based on these definitions, both an energy and exergy analysis should be provided. (Stougie et al., 2018) proposes the Total Cumulative Exergy Loss (TCExL) method, which shall be adapted in the production efficiency analysis.

Environmental Impact: Environmental impact shall be measured by means of a set of impact categories, as defined by the ReCiPe 2016 guideline (Huijbregts et al., 2017). Each category shall be assigned a characterisation factor, indicating the impact with respect to a reference (functional unit). The final result is a set of impacts for the endpoint indicators "human health", "ecosystem quality", and "resource scarcity" (Huijbregts et al., 2017, p.13). This analysis shall be applied to the entire mission, starting at the design and ending at the EoL.

Development and Testing: Similar to the manufacturing processes, development and testing may require a lot of resources or result in polluting emissions. When Commercial Off-The Shelf (COTS) components are used, it may not be required to test the component as extensively as an in-house developed component, as the reliability may have already been proven. Testing the component's integration with the system as a whole is still be required. Thus, if possible, COTS components shall be preferred over in-house developed components.

14.3.3 Environmental Life Cycle Assessment

Environmental Life Cycle Assessments (E-LCA) are standardised procedures (ISO14040 and ISO14044) aimed at assessing the environmental footprint of any system, product, or service. Due to its general nature, and the rise in interest in space sustainability in recent years, the many specificities in the sector called for a more meticulous methodology to follow. The ESA then created the first space-specific E-LCA handbook (*Space system Life Cycle Assessment (LCA) Guidelines* 2016), adapting current ISO standards, which are typically used for mass production assets, to the typically low production rates of space systems, as well as the world's first database capable of calculating the environmental impacts of space missions. The framework developed by the ESA, from which the E-LCA of the Space Sweeper will be derived, shown in Figure 14.4 consists in four main steps; defining the goal and scope of the assessment, analysing the inventory, assessing the impact, and interpreting the results. It is also suggested that at least two full iterations shall be made to have a thorough and reliable E-LCA as the outcome. Two levels of E-LCA are presented in (*Space system Life Cycle Assessment (LCA) Guidelines* 2016), however the team focused on the level 1 E-LCA, a system level assessment. As clearly stated in the handbook, "the environmental impact of a space mission is the sum of the impacts of the space segment, the launch segment and the ground segment".

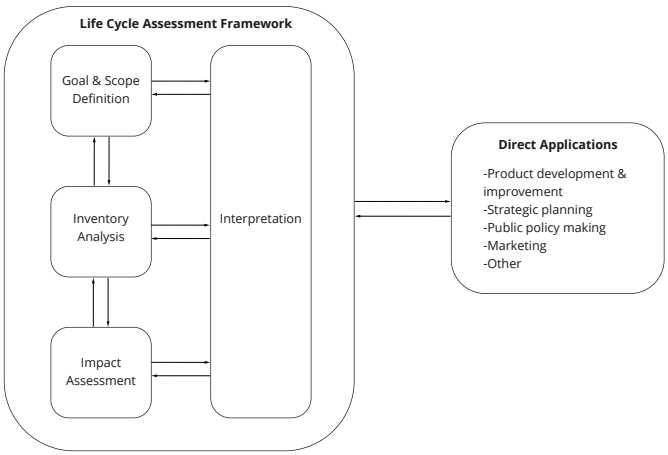

Figure 14.4: Framework for the E-LCA.

Goal and Scope Definition

The main goal of an E-LCA for a space mission is to quantitatively define the environmental impacts caused by it, from the moment it is first proposed until the final seconds of its lifetime. The two most important actions in this stage are to quantify a functional unit (FU), and to specify the system boundaries.

An FU's main purpose is to provide a reference unit such that inputs and outputs can be compared, and it should be consistent with the scope and goal of the assessment, as it can deeply affect the presentation of results. Since our goal is not to compare our system to other missions, but to evaluate its own environmental impact, ESA's suggested FU will be used, defined as "One space mission in fulfilment of its requirements" (*Space system Life Cycle Assessment (LCA) Guidelines* 2016).

System boundaries define which processes are assumed to be included in the system the assessment is being done for. In our case, the launch, space, and ground segments are all included, as well as all phases of the entire mission. Note the infrastructure is investigated separately, due to the availability of data. The boundary chosen is depicted in Figure 14.5, where all the phases of the mission (A to F) are introduced.

Life Cycle Inventory (LCI) Analysis

According to (*ISO 14040: Environmental management - Life cycle assessment - Principles and framework* 2006), this stage is defined as "data collection and calculation procedures to quantify relevant inputs and outputs of a product system". It includes three steps; data collection, data calculation, and allocation.

We can identify two types of data to collect; primary data is collected directly from the system, whereas secondary data comes from LCA databases. As a minimum, the following data is to be collected for each phase (*Space system Life Cycle Assessment (LCA) Guidelines* 2016):

- **Phases A+B:** this step covers the office work and the business travelling of relevant project activities. Both the man-hours and the travel distance (excluding commuting to and back from work) of the in-house staff, suppliers, and costumers are included. When man-hour data is missing from suppliers, the values can be estimated by doubling the man-hours allocated to the in-house staff. For transportation, every transport is included in theory, but practically only aeroplane values are used as they contribute the most. The proxy to be used this time, when no data is found for suppliers, is to assume the distance equals the one travelled by in-house staff. In case no distance data is available, a conservative value of 3000 km can be assumed.
- **Phases C+D:** office work and travelling are modelled as above, however the spacecraft production is now also taken into account, split into model philosophy, and material, equipment and instrument production. Model philosophy includes all models produced in the design state of the mission. Production is a cradle-to-gate LCA (from raw material to factory gate) of each material, equipment and instrument used. For this data to be used in the model, the mass of each material, equipment and instrument is used to scale the LCIs using specific space sector LCA databases, some of which can be found in the handbook.
- **Phase E1 - Spacecraft related activities:** includes S/C transport and preparation, ground station, and control centre operation. It is likely that Space Sweeper will require its own dedicated transport vehicle due to its size. The LCI is then representative of one kilometre of the whole vehicle (v.km). The raw materials and manufacturing processes of the container itself are also included, as well as the end-of-life treatment (unless it is recyclable). Production and EoL LCIs can be divided between the number of uses of the container. S/C preparation covers all activities at the launch site, ranging from electricity and natural gas used, to direct emissions to water and air. LCIs for ground station operation are integrated in the E-LCA by covering electricity and natural gas consumption, as well as energy consumption from other sources as a result of operating the ground station. The LCI for the control centre is divided

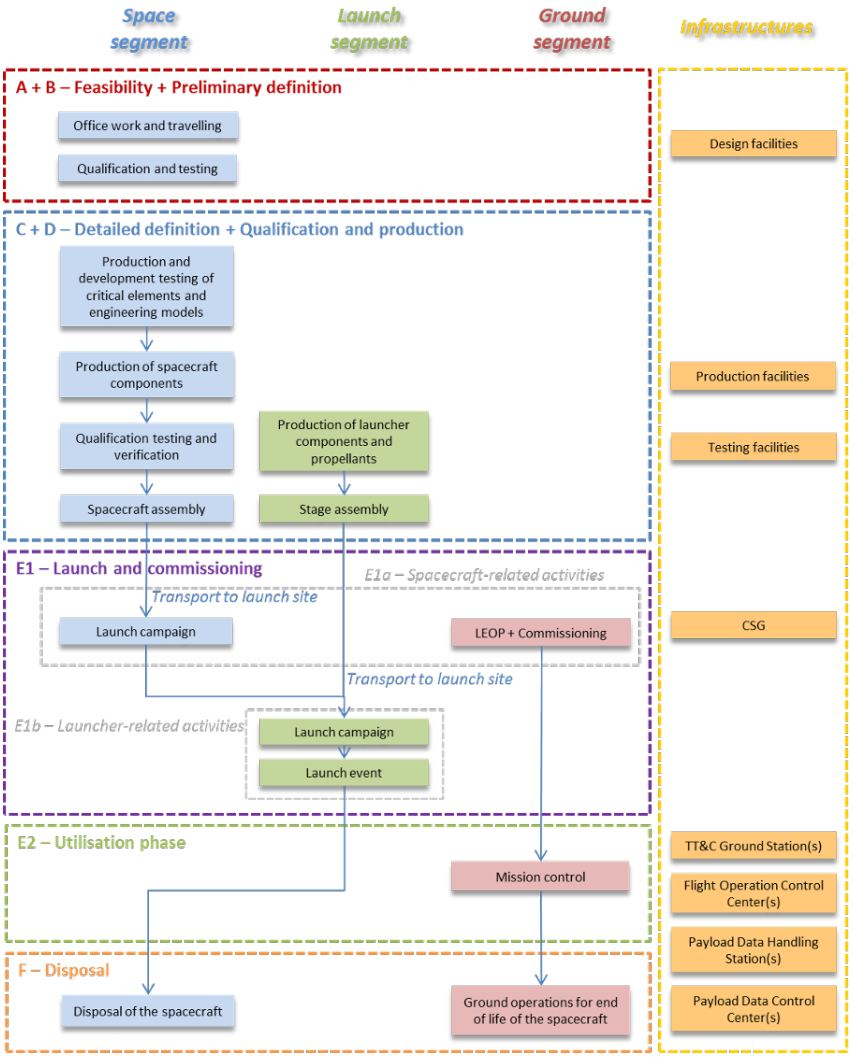

Figure 14.5: System boundaries for the Space Mission being assessed (*Space system Life Cycle Assessment (LCA) Guidelines* 2016).

by the amount of staff that work in the facility. It is included in the E-LCA by analysing the amount of manpower dedicated to the mission alone at control centres during LEOP and commissioning stages.

- **Phase E1 - Launcher related activities:** covers the complete life cycle, from production to the launch event.
- **Phase E2:** covers the ground and control station operations during the operational phase of the mission. Ground station LCIs are scaled based on the time of operation for flight and payload data control at each ground station. Same is used for the control station, using manpower instead of time.
- **Phase F:** covers the EoL activities of the S/C. For the ground segment, operations are assumed to be negligible for this stage of the mission, compared to the space segment. Regarding the space segment, not much can be assessed due to the lack of models that take into account the impact of the EoL procedure on the environment, however the mass that re-enters or is left in space can still be assessed.

To summarise the many phases, the minimum mission specific data required is the following:

- Man-hours of staff in phases A through D
- Staff travels in phases A through D
- System mass budgets
- Mode and distance of transport of components
- Amount, type, and duration of all tests done
- Duration and area of clean room required for assembly
- Mode and distance of transport of S/C to launch site
- S/C preparation activities at launch site
- Chosen launcher
- Man years of mission dedicated manpower for flight operations and payload control centers, commissioning, routine, and launch and early operations phase (LEOP)
- Duration of mission dedicated operations at ground stations for flight control and payload data
- Dry-mass at re-entry into the atmosphere

To limit the amount of data required, and for the timely completion of this assessment, several cut-off criteria must be applied. If materials are to be recycled after use, they can be cut-off. Furthermore, cut-off rules based on mass/volume criteria shall also be considered. As suggested in the handbook, materials than constitute less than 5% of the total component mass can be excluded from the assessment.

The gathered data is used to calculate the results for the previously defined FU. The main calculation procedures as set forth by (*ISO 14040: Environmental management - Life cycle assessment - Principles and framework* 2006) include validation of data, and relating the data to unit processes and the FU.

For allocation, (*Space system Life Cycle Assessment (LCA) Guidelines* 2016) suggests allocating the inputs and outputs of a specific process to other co-products by using a mass criterion, and requires justification and documentation for any planned deviation from this. Monetary allocation is to be avoided at all costs.

Life Cycle Impact Assessment (LCIA)

In this stage, the potential environmental impacts of everything within the chosen system boundary is evaluated using the results achieved in the LCI. As stated by (*ISO 14040: Environmental management - Life cycle assessment - Principles and framework* 2006), the process involves "associating inventory data with specific environmental impact categories and category indicators, thereby attempting to understand these impacts", for which examples are seen in the handbook. The final results are typically represented using a breakdown structure, showing the contribution of the LCI results for the different phases to the impact indicators chosen. (*Space system Life Cycle Assessment (LCA) Guidelines* 2016) also suggests calculating the uncertainty of the outcome by means of a Monte Carlo simulation (at least 5000 iterations), to ensure the transparency of the results. (*ISO 14040: Environmental management - Life cycle assessment - Principles and framework* 2006) introduces the following limitations for this assessment:

- LCIAs only address the issues that are specific to the defined goal and scope, not to the complete system
- Unavoidable uncertainties in the results arise due to the lack of spatial and temporal dimensions.

Interpretation of results

This is the phase where the results of both the LCI and the LCIA are considered and evaluated together, aiming to provide a set of conclusions and recommendations. At this stage, the goal and scope of the LCA are also revised, and iterations are performed as required. (*Space system Life Cycle Assessment (LCA) Guidelines* 2016) also requires a quality assessment of the date and an identification of environmental hot spots in this phase. The interpretation shall be summarised in a report, incorporated with the other mission design reports.

14.4 Project Gantt Chart

The Gantt Chart of the project for the post-DSE period is given in Figure 14.6.

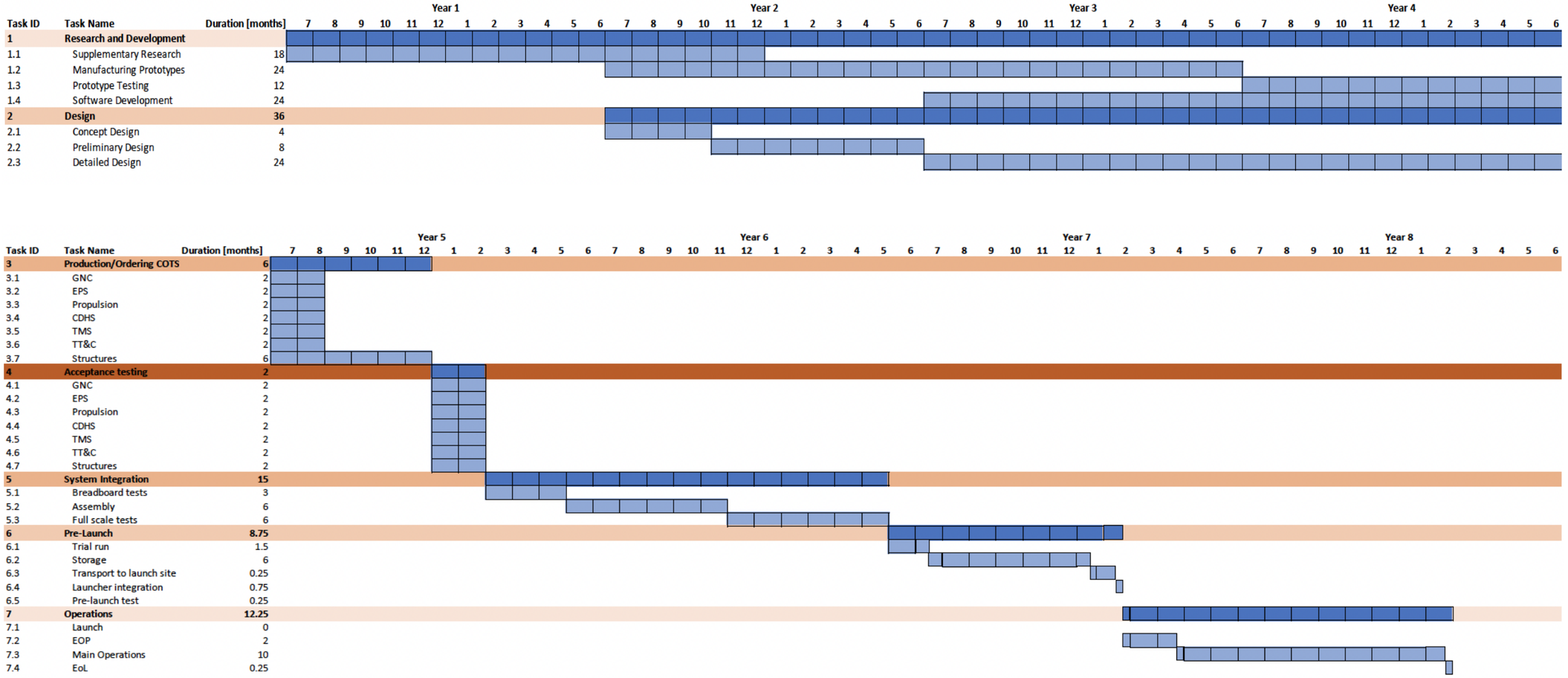

Task ID	Task Name	Duration [months]
1	**Research and Development**	
1.1	Supplementary Research	18
1.2	Manufacturing Prototypes	24
1.3	Prototype Testing	12
1.4	Software Development	24
2	**Design**	**36**
2.1	Concept Design	4
2.2	Preliminary Design	8
2.3	Detailed Design	24
3	**Production/Ordering COTS**	**6**
3.1	GNC	2
3.2	EPS	2
3.3	Propulsion	2
3.4	CDHS	2
3.5	TMS	2
3.6	TT&C	2
3.7	Structures	6
4	**Acceptance testing**	**2**
4.1	GNC	2
4.2	EPS	2
4.3	Propulsion	2
4.4	CDHS	2
4.5	TMS	2
4.6	TT&C	2
4.7	Structures	2
5	**System Integration**	**15**
5.1	Breadboard tests	3
5.2	Assembly	6
5.3	Full scale tests	6
6	**Pre-Launch**	**8.75**
6.1	Trial run	1.5
6.2	Storage	6
6.3	Transport to launch site	0.25
6.4	Launcher integration	0.75
6.5	Pre-launch test	0.25
7	**Operations**	**12.25**
7.1	Launch	0
7.2	EOP	2
7.3	Main Operations	10
7.4	EoL	0.25

Figure 14.6: Gantt chart of the next stages of the project. Note that it starts in July 2022.

Mission Economic Valuation 15

Now that the technical details of the design are explained, an economic valuation of the mission is presented in this chapter. This is done by first delving into the associated costs in Section 15.1. Then, the market analysis is performed in Section 15.2. Following, the return on investment is estimated in Section 15.3 and the profitability of the mission is discussed in **??**.

15.1 Cost Breakdown

For the mission at hand, cost is of particular importance due to the question of accountability of space pollution. An over-estimation of the cost of the programme could result in the denial of funding, meaning the project is cancelled. On the other hand, under-estimation has severe consequences as well, as the allocated budget would run out before the program is completed, risking failure of the program. A realistic and well-documented cost estimation, however, will allow other organisations to do a fair cost assessment, which makes it more attractive for them to join the endeavour of cleaning space debris. This is done by means of a Cost Breakdown Structure (CBS), which is shown in Figure A.1. In the CBS, several high-level assumptions are made to do a consistent cost estimation. These assumptions are discussed first.

15.1.1 Overall Cost Assumptions

As can be seen in the CBS, the costs for each phase are split up into labour cost, cost of components, and the required facilities cost. This should provide more insight into where the different costs originate from for all the different phases, and can be used to identify particularly costly parts of the mission.

Labour Allocation and Costs

Allocation of man-hours to given project phases is a notoriously difficult aspect of cost estimation for large-scale projects. Given the total mission budget, it is not uncommon that the allocated man-hours are underestimated to fit the cost budget of the mission, making this estimate prone to bias. For this reason, an ESA project manager was contacted to get an impression of the personnel necessary in the different aspects of the project.

In terms of engineering labour, ESA commonly allocates for 10-15 engineers per subsystem development for a project of this magnitude. Such a team will typically, among others, include a project manager, an integration and testing engineer, a verification engineer, mechanism engineer, electrical engineer, and architectural engineer. The spacecraft is equipped with 9 critical subsystems, including the ablation payload, detection payload, GNC, EPS, Propulsion, CDHS, TMS, TTC, structures and a separate systems engineering team of approximately 10 members is advised. Thus, a management team of 10 members is expected to account for all subsystems during development. A yearly salary for senior engineers and managers of €200,000 and €300,000 respectively is taken as an estimate [1]. Finally, for large missions, logistics personnel is expected to amount to 200 people from ESA's advice, assuming an average salary of €36,500 for the Netherlands [2]. All salaries account for any associated overhead costs, including office space, company insurance, and parking costs.

Component Cost

In the estimation of the cost of the components per subsystem, it has been identified that there is a large uncertainty. Although specific COTS components were selected, their respective prices are typically not provided in the corresponding data sheets. Therefore, it can be difficult to provide accurate estimations for this part of the cost estimation. To tackle this, both statistical relationships are used, and where possible, actual costs of COTS components are used to calculate the total component cost per subsystem.

For the TTC subsystem, the cost of bought in COTS components is expected to be very low, given the required components are small and basic. From similarly sized components from EnduroSat [3], the cost of the antenna and transceiver required for the mission is estimated to be in the order €10,000 each. With the cost of other COTS being marginal or included in the antenna/transceiver costs, the total component cost of the TTC subsystem is estimated at €30,000.

In terms of the TMS, quotation requests have been sent to potential manufacturers of OSR radiators, ammonia heat pipes, as well as MLI. While heat pipe and OSR manufacturers have not responded to a request for quote, RUAG Space has provided a quote for single-layer COOLCAT 2 NW MLI foil of €3605/roll for rolls of 1.9 m x 50 m. Thereby, covering

[1] Personal communication Barry Zandbergen (lecturer, TU Delft), email dd. 14-06-2022

[2] URL: https://www.statista.com/statistics/1082370/average-annual-salary-in-the-netherlands-by-province/: :text=On%20average%2C%20employees%20in%20the,j [Accessed on 14-06-2022]

[3] URL: https://www.endurosat.com/. Accessed on 21-06-2022.

18.27 m^2 with 10 layers of MLI is expected to cost approximately €6900, assuming no foil is wasted in the manufacturing process. The cost of OSR radiators must be estimated due to a lack of RFQ responses. However, the cost is expected to be on the order of several thousand \$/m^2 according researchers of the "Next generation meta-material based Optical Solar Reflectors" EU-funded OSR development project [4]. Assuming \$5000 /m^2 and using the radiator surface area previously determined, it is expected that the radiators will cost approximately €85000. For heat pipes, no public information on the cost of ammonia-aluminium heat pipes is available. As a first estimation, water-based constant-conductance heat pipes of the same diameter, of 0.5 m length, costing €12.40 per unit, are used as a baseline. This results in an estimated per-meter cost of €24.8 /m. Using a total heat pipe length required of 71.2 m (Table 9.4), this results in an approximate cost of €1800. However, this is likely to be an underestimate, as VCHP's have additional complexity, in addition to the use of a less common and more expensive working fluid. Furthermore, the heat pipes selected for use in the TMS are built specifically for space use and therefore will be produced in far lower numbers than the water-based heat pipes for use in cooling electronics. Considering these three core components of the TMS, the estimated cost of the TMS hardware is approximately €94000.

The structure of the spacecraft shall be designed and produced in-house. For this, a cost estimate is used which relates the production cost of the structure to the weight of the spacecraft, found in (Wertz, Everett, et al., 2011, p.97). Because these relations make use of FY2010, the result of this is then multiplied by 1.34, to account for inflation. Due to the lack of available data, these relationships were also used for the propulsion and CDHS subsystems. For the EPS, the main source of cost are the large solar arrays. Therefore, the cost (in \$ K/W) provided in Table 41 from (Zandbergen, 2021, p.123) for the chosen solar arrays are used. Furthermore, the cost of the batteries and capacitors are taken from (NASA, 2021). Finally, for the EPS, the bus cost was found in (Wertz, Everett, et al., 2011). It is recognised that this introduces a lot of uncertainty, and more accurate estimations should be made in the next design phase, by requesting components costs from the selected supplier.

Facilities Cost

The cost of facilities is highly impacted by the resource and contract provisions from ESA, as the mission client. As an initial conservative estimate, the standard cost of facilities for research, development and production is estimated at €30,000 a day as an average value. The testing facilities are distinguished between subsystem acceptance testing facilities, also rated at €30,000 per day, and €100,000 per day for the combined, specialised testing facility for the payload laser, mirror and lidar systems, considering their more advanced and novel technology. It is assumed that these facilities are to be paid for, for every day of the month while contracted, and man-hours are to be distributed over all seven days of the week, while assuming a 40-hour week per employee.

From industry expertise, it is estimated that a storage facility equipped for maintaining large spacecraft in a clean, temperature-controlled environment is expected to cost €2 million to build, with a storage maintenance/testing cost and a spacecraft maintenance cost of €500,000 per year and €200,000 per year respectively.

To estimate the ground operations facility costs, amazon's ground station service charge of \$10 per minute [5] was used as a rough estimate, amounting to a total facility cost of about €5 million for roughly a year of operation. This is likely an overestimate, considering that using ESOC as the operations centre is expected to be considerably less expensive. In terms of labour costs, a larger ground unit of 20 people is required during the EOP phase with 10 people continuing main operations and EoL operations. Note that given ground operations requires 24/7 operation, 3 teams are implemented in shifts, logically multiplying labour costs by 3.

[4] URL https://www.southampton.ac.uk/news/2018/04/new-thermal-coatings-spacecraft.page [accessed 21-06-2022]

[5] URL: https://aws.amazon.com/ground-station/pricing/. [Accessed on 15-06-2022]

	Phase	Start	End	Labour No. of employees	Labour Number of months	Labour cost [k€]	Components Component cost [k€]	Facilities Facility cost [k€]	Total [k€]	σ/μ
1	R&D	Jul/22	Jul/26							
1.1	Supplementary Research			10	18	3,000	0	16,200	19,200	0.40
1.2	Manufacturing Prototypes			30	24	12,000	66,400	21,600	100,000	0.30
1.3	Prototype Testing			30	12	6,000	1,000	36,000	43,000	0.20
1.4	Software Development			10	24	4,000	43,435	0	47,435	0.35
2	Design	Jul/23	Jul/26							
2.1	Concept Design			36	4	2,400	0	0	2,400	0.20
2.2	Preliminary Design			72	8	9,600	0	0	9,600	0.20
2.3	Detailed Design			135	24	54,000	0	0	54,000	0.20
3	Production/Ordering COTS	Jul/26	Jan/27							
3.1	GNC			5	2	167	8,000	0	8,167	0.35
3.2	EPS			5	2	167	12,000	0	12,167	0.20
3.3	Propulsion			5	2	167	5,112	0	5,278	0.40
3.4	CDHS			5	2	167	5,242	0	5,409	0.45
3.5	TMS			5	2	167	94	0	261	0.25
3.6	TT&C			5	2	167	30	0	197	0.10
3.7	Structures			10	6	1,000	15,276	5,400	21,676	0.30
4	Acceptance testing	Jan/27	Mar/27							
4.1	GNC			5	2	167	0	1,800	1,967	0.25
4.2	EPS			5	2	167	0	1,800	1,967	0.25
4.3	Propulsion			5	2	167	0	1,800	1,967	0.25
4.4	CDHS			5	2	167	0	1,800	1,967	0.25
4.5	TMS			5	2	167	0	1,800	1,967	0.25
4.6	TT&C			5	2	167	0	1,800	1,967	0.25
4.7	Structures			5	2	167	0	1,800	1,967	0.25
5	Integration	Mar/27	Sep/28							
5.1	Breadboard test			10	3	500	0	2,700	3,200	0.20
5.2	Assembly			15	6	1,500	0	5,400	6,900	0.30
5.3	Full-scale test			15	6	1,500	0	5,400	6,900	0.30
6	Pre-launch	Sep/28	Mar/29							
6.1	Trial run			-	1.5	-	-	-	1,408	0.25
6.2	Storage			5	6	500	0	2,350	2,850	0.20
6.3	Transport to launch site			5	0.25	21	0	600	621	0.25
6.4	Launcher integration			10	0.75	125	0	0	125	0.20
6.5	Pre-launch test			10	0.25	42	0	0	42	0.20
7	Operations	Mar/29	Mar/30							
7.1	Launch			0	0	0	98,477	0	98,477	0.25
7.2	EOP			20	2	2,000	0	821	2,821	0.30
7.3	Main Operations			10	10	5,000	0	4,104	9,104	0.30
7.4	EoL			10	0.25	125	0	103	228	0.30
	Other									
-	Development Management			10	72	18,000	0	0	18,000	0.20
-	Operations Management			1	12	300	0	0	300	0.20
-	Systems Engineers			10	48	8,000	0	0	8,000	0.20
-	Logistics			200	72	42,000	0	0	42,000	0.25
	Total					173,779	255,065	113,277	**543,530**	0.27

Cost assumptions	
Acceptance testing facility costs	30 [k€] / day
Prototype testing facility costs	100 [k€] / day
Senior engineer salary	200 [k€] / year
Manager salary	300 [k€] / year
Logistics employee salary	35 [k€] / year

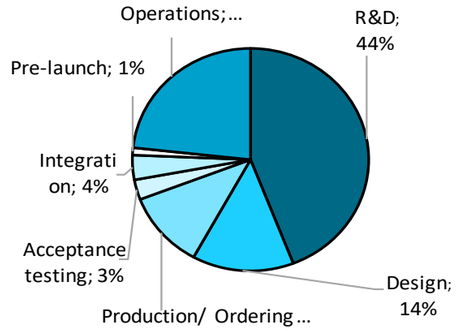

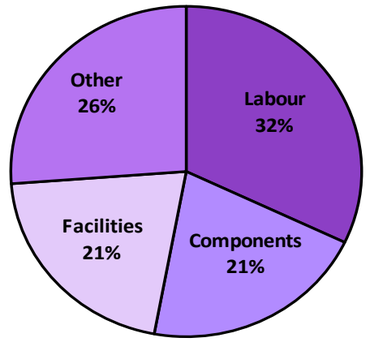

Figure 15.1: Cost Breakdown Structure including cost assumptions and pie charts.

15.1.2 Phase Cost Estimations

To evaluate the cost breakdown of the large-scale project, it is crucial to lay out a preliminary project timeline. The project may be split up into the phases as outlined in the CBS in Figure A.1. A scaled timeline of project phases is illustrated in the Gantt chart Figure 14.6, where the phase IDs are indicated for referral to the CBS. A more extensive explanation of the phase operations and cost estimation processes for each project phase is provided in the following sections.

Research and Technology Development

The attributes that will be focused on in the research phase were discussed in Chapter 14 and include the effects of rotation, shape, and material of debris fragments on ablation efficiency, the morphing mirror development, and the tracking capabilities of the lidar system. In the final half year of the research phase, early prototyping of the developed technologies will commence. ESA has a standard 4-phase prototyping procedure for custom technologies, which is expected to take 3 years. This involves:

- Phase A: feasibility evaluation,
- Phase B: breadboard test with a preliminary design review,
- Phase C: first subsystem model including verification and validation with a critical design review,
- Phase D: final model development with a flight acceptance review.

This is a relatively expensive procedure, although it is highly important as it is the foundation of the entire mission design. In terms of manpower, HiLASE states [6] that there are seven team members and two control engineers involved in the BIVOJ program. Though the program requires nine team members now, construction itself may take more members, though this would likely be outsourced to a secondary company as HiLASE also did (BIVOJ was initially built at the Central Laser Facility in the UK). Given the large scope of this development program (quantifying debris characteristics and developing the laser - including building it), it is estimated that approximately 20 engineers will be hired for prototyping and testing to avoid underestimating the program cost.

In terms of facilities costs, given the specialised research and prototype manufacturing facilities, an average daily cost of €30,000 was assumed from communication with industry experts. Specifically for the acceptance testing facility for the final year of testing, a conservative estimate of the daily rate was taken as €100,000. This assumes that the same facilities are used for the development of the laser, mirror and lidar technologies.

Component costs are difficult to estimate, and include both material that will be used as test debris, and the materials that are used in the laser's construction. In terms of laser cost, the BIVOJ laser cost is taken as reference[7], which cost M€44 (FY 2017), around M€50 in FY2022, assumed to cover the entire cost of development. Given the different specifications desired from the spacecraft, this cost is rounded up to M€60 to account for extra hardware. Given that lidar has a significantly higher TRL, and only needs adjustment to fit the specific application of rapid debris removal, and that the mirror development program is significantly smaller than that for the ablative laser, a rough estimate for the total cost of prototype development and final payload manufacturing is €100 million.

Regarding material cost for testing, only small amounts of material are necessary to test on, given that the depth of debris removed is in the order of nanometres per pulse (Phipps, Boustie, et al., 2017). Some of the materials that are desired to test include fibreglass, steel, copper, and various plastics, as they are the most prevailing in results from the Satellite Orbital Debris Characterization Impact Test (SOCIT), as well as data from the STS missions (Opiela, 2009). These are very cheap materials; an extra material cost of €1 million is approximated for testing.

Finally, the software development and verification cost is often underestimated and must be accounted for in the CBS effectively. For unmanned flight software, the cost of software verification roughly amounts to €700 per line of code with currency conversion and accounting for inflation (Wertz, Everett, et al., 2011, p. 307). Taking the 62050 lines of code computed for all subsystems in Chapter 8, this amounts to €43.4 million. Furthermore, the tracking algorithm for the detection payload is assumed to be bought from an external party and account for an additional 25% of the total software verification cost. The labour cost associated with software development assumes a two-year program with 10 dedicated software engineers.

Design and Production/Ordering COTS

The design phase is a two-year program that runs in conjunction with the final two years of the technology development phase. The concept, preliminary and final sub-phases of this project phase allocate incrementally larger sub-system teams of 4, 8 and 15 senior engineers respectively. There are no associated component and facility costs and design office costs are included in the labour costs.

Smaller teams of engineers are assigned to oversee the ordering of COTS over two months. An additional 6 months is allocated for the production of the custom-built structures subsystems. This longer production time window leaves a considerable margin for any delays with COTS delivery and approval. Again, a daily facility cost of €30,000 is assumed for the production facility. The associated component costs are discussed in subsubsection 15.1.1.

[6] URL: https://www.hilase.cz/en/research-programmes/advanced-laser-development-ald/ [Accessed on 11/06/2022]
[7] URL: https://phys.org/news/2017-01-brits-czechs-world-powerful-super.html [Accessed on 11/06/2022]

Acceptance Testing and Integration

Acceptance testing is planned over two months, with five dedicated testing engineers and a daily testing facility cost of €30,000 per subsystem. It should be noted that such facilities must be booked many months in advance to mitigate delays, as this is a relatively short project phase.

Moreover, the integration phase starts with the breadboard test, which is a relatively short test which inspects how the different subsystems and interfaces fit together before assembly, and optimising configurations. The assembly of the spacecraft assumes a six-month period with standard "testing" facility fees, considering the spacecraft must be built in a clean workspace and full-scale testing should operate in the same facility in the following half year to avoid transport expenses and logistics.

Pre-launch and Operations

As the first operation of the pre-launch phase, a "trial run" of all pre-launch procedures is planned, including transport from the storage facility to the launch site, launcher integration and a pre-launch test without launching, followed by transport back to the storage facility. This would be an effective procedure to rehearse time-pressured pre-launch operations, given that a timely launch proceeding a collision is vital to the success of the mission. This amounts to the cost of all pre-launch operations mentioned, with transport factored in twice.

Furthermore, the launch date of the mission depends on the occurrence of a LEO collision or explosion to be removed. Considering 560 fragmentations have been recorded since 1961 [8], this leads to a conservative estimate of roughly one collision occurring per month. Considering the mission specifically targets large spacecraft fragmentations in LEO, a storage time of 6 months before launch is anticipated.

The transport operation logistics are estimated to amount to €300,000 with the cost of the specialised shipping container costing roughly the same amount. A launch preparation team of 5-10 engineers is expected to oversee transport operations, launcher integration and testing.

It should be noted that the integration phase is planned for completion before September 2028, making the spacecraft "operational" by 2028 according to SS-TL-STK-US-REQ-MI-001. However, the launch is planned for March 2019 given the estimated time for a collision occurrence.

Using the Ariane 62, the estimated launch cost of €73 million was estimated in Section 13.2. An additional launch insurance was estimated at 17.5% of the spacecraft cost (Zandbergen, 2021, p. 59) (where the spacecraft cost comprises the cost of the payload. other subsystems and and integration, including testing costs).

15.1.3 Cost Estimation Analysis

Referring back to the top pie chart in Figure A.1, RD makes up a large proportion of the project cost, which was found to be a responsible decision given that the payload is entirely novel, consisting of the ablation laser, morphing mirror and rapid-tracking lidar system. The extensive testing and supplementary research that goes with prototype development is vital to the success of the mission, and should not be underestimated.

Furthermore, not unexpectedly, the labour cost of the mission makes up a substantial portion of the total cost. From the lower pie chart in Figure A.1, the 26% of “other” costs represents the cost of the launch and software verification alone, indicating the sizable expenses of these project aspects.

Aside from the individual cost sources, and the resulting total cost per phase, also an uncertainty indication is provided in the CBS. While the estimates were discussed with various industry experts from ESA and other aerospace companies to mitigate uncertainty, it is still important to acknowledge this uncertainty. Uncertainty is the estimated standard deviation, divided by the mean value, and is listed in the rightmost column. This means that, for example for an indicated value of 0.3, it is estimated that in 68% of the cases, the estimated cost will lie between $C - 0.3 \cdot C$ and $C + 0.3 \cdot C$, where C is the mean-estimated cost, as provided in the "Total" column in the CBS. This will subsequently be used in a Monte Carlo simulation to simulate different cost scenarios, aiming to provide a more realistic cost estimation. In general, as can be observed from CBS, labour costs have relatively low uncertainty, while component costs have a higher uncertainty. The final results will be discussed in the next section.

The cost estimation of the mission is a critical element in proving feasibility of the mission. The total cost is estimated to be approximately 544 M€. Initially, the customer set the budget lower, namely 400 M€, but after discussion and negotiation, the available budget for this mission is increased to meet this cost estimation. Also, an uncertainty on the total costs is provided, and the fact that a cost estimate, at this phase, brings many uncertainties with it, is not hidden in the corresponding normal distribution. To show this, 1,000,000 samples were taken from this distribution, and the results are showcased in Figure 15.2. This plot is accompanied by Table 15.1, which shows important numerical values from the distribution. Based on this, there is a 75% certainty that the costs remain below M€643. This amounts to a total spacecraft cost of M€298, including launch costs and insurance and excluding development costs. However, series production of the Space Sweeper is expected to reduce its production and assembly time, and associated cost, substantially.

[8] URL: https://www.esa.int/Safety_Security/Space_Debris/About_space_debris. [Accessed on 15-06-2022]

Table 15.1: Uncertainty parameters.

Variable	Cost [M€]
Mean - SD	398
25h percentile	445
Median	544
75th percentile	643
Mean + SD	690

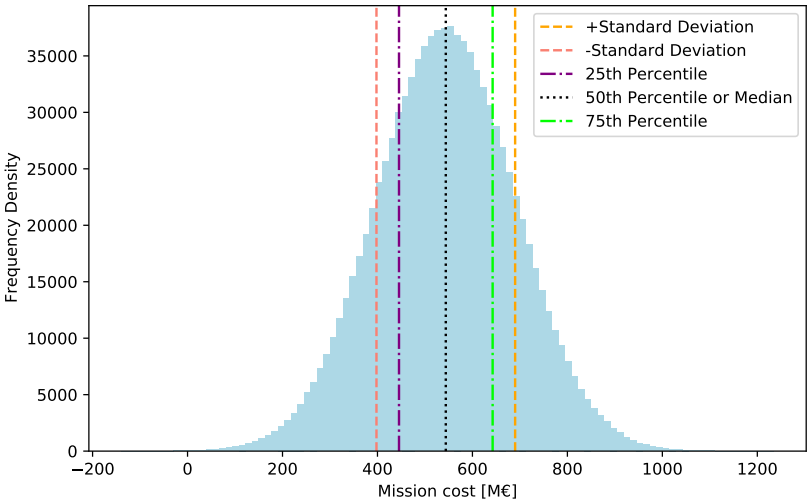

Figure 15.2: Normal distribution of cost estimation.

15.2 Potential Market Analysis

This section serves as an update to the preliminary market analysis done in (Teixeira et al., 2022a). It expands on the potential market opportunities, lays out a method to chose a tertiary mission capable of generating extra revenue, and concludes with the actual choice of mission.

15.2.1 Potential Market Opportunities

In the previous phases of the project, both a primary and a secondary mission were identified, as seen in Section 2.1. Since the spacecraft is being designed in a worst case scenario basis, there will be missions in which our system will be over-designed when thinking of the primary and secondary missions alone, where the opportunity arises to secure extra funding by undertaking other secondary missions. To take advantage of this opportunity, two different approaches can be followed; using the primary payload to perform secondary missions, or investigating the use of secondary payloads, as well as their market potential to secure future funding for the project. The application of these approaches, however, shall not affect the primary mission's requirements, and budgets in any way. Both approaches are analysed below, where a trade-off is present and a final concept for each approach is chosen. The choice of final approach will follow from a second trade-off between the two final concepts.

Approach one - Using the Space Sweeper in an as-is condition

As mentioned before, the idea of the first approach is to use the primary payload to perform an extra secondary mission. The main advantage of this approach is that additional revenue can be obtained without adding any major additional costs. Due to the novel and highly specific nature of Space Sweeper's payload, great difficulty arose when trying to find potential uses for it that are currently scientifically or economically feasible, therefore it was immediately decided to follow approach two. Approach one was kept in the report to provide a few recommendations that should be evaluated in the future, that would most likely require at least some design change. Proposed options to be studied include; using the laser to propel a solar sail on a spacecraft, destroying inter-continental ballistic missiles (ICBMs), providing EoL services to other spacecraft, and renting the payload for all types of testing.

Approach two - Adding an extra payload to the Space Sweeper

The possibility to add a new payload to the spacecraft made choosing possible concepts a simpler task. The team concluded that the market that will be targeted is the Earth Observation Missions (EOM) market, one that is projected to double in revenue within the next decade (*EUSPA EO and GNSS Market Report* 2022). This decision stems from many reasons, with an example being that the system will be deployed in LEO, making any attempt to act as a communications relay, or a space telescope, futile. Of course, not all EOMs can be taken into account. As this would be a secondary mission for our spacecraft, odds are that there are many other spacecraft that have this type of mission as their primary focus, and are be able to provide a better service than the Space Sweeper. Our focus therefore shifted to niche markets within the broader EOM market, where less data supply is available, keeping in mind that demand may also be scarce. Also, there is a higher likelihood that clients in these markets do not have enough money to buy data from primary sellers, and will turn to secondary sources of data. Note that markets that have a steep increase in revenue within the next decade, no matter their market share, will not be completely neglected, as demand may grow bigger than supply, making the more financially strong clients look for other sources of data. According to the market analysis seen in Figure 15.3, the EOM

Table 15.2: Possible applications of EOMs for the markets highlighted in the paragraph above (*EUSPA EO and GNSS Market Report* 2022)

Market	**Application**
Fisheries and Aquaculture	Catch optimisation, fish stock detection, aquaculture site selection.
Maritime and Inland Waterways	Marine pollution monitoring, port security, offshore weather monitoring.
Environmental Monitoring	Coastal monitoring, green house gas (GHG) monitoring, soil monitoring.
Insurance and Finance	Crops and livestock insurance, calculation of indicators for commodities trading.
Urban development and Cultural heritage	Air quality monitoring, light pollution, illegal dwellings.

Table 15.3: Possible applications of secondary payload instruments identified from Table 15.2.

Instrument	**Application**
GHGSAT-Spectrometer	Monitors amounts of GHG gases, targeting CO2 and methane (CH4).
Poseidon-4	Significant wave height, sea surface wind, ocean ice topography.
Microwave radiometer (MWR) - Sentinel 3	soil moisture monitoring, thermal radiation emission.
Compact Infrared Camera (CIRC)	wildfire detection, cloud cover, sea surface temperature.

markets with the smallest market shares, that have possible applications, are the fisheries and aquaculture, and the maritime and inland waterways, and the environmental monitoring markets. The ones who, regardless of their market share, are projected to grow the quickest include the insurance and finance, and the urban development and cultural heritage markets. Examples of applications for EOMs for the highlighted markets are shown in Table 15.2. After researching into the applications described there, the possible secondary payload instruments shown in Table 15.3 were identified.

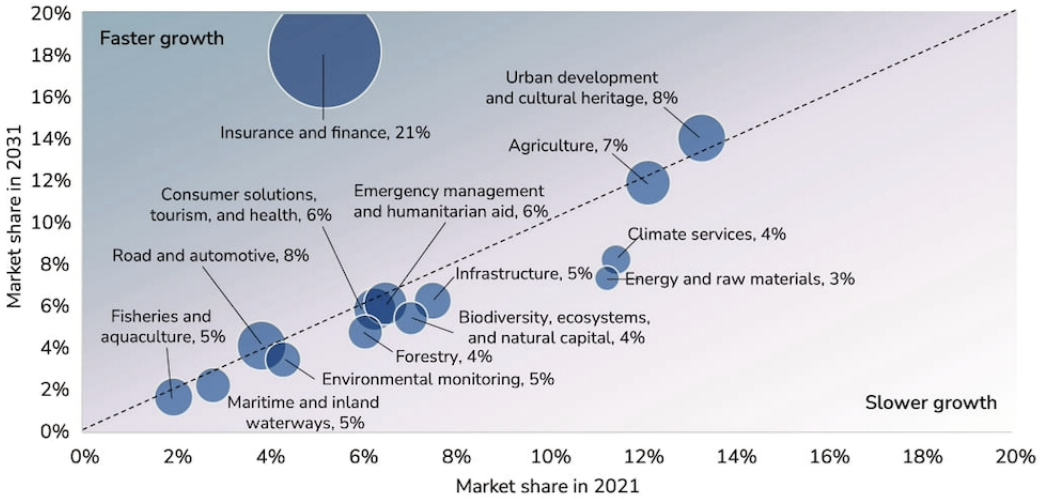

Figure 15.3: Earth observation market share in 2021 and 2031(*EUSPA EO and GNSS Market Report* 2022). Note that the size of the bubbles represents the projected compound annual growth rate (CAGR), also written as a percentage next to each market name.

A qualitative trade-off was then made between the selected instruments. The chosen trade-off criteria were based on the criticality of the system's budgets, as the secondary payload should aim not to affect them, and on the future funding

Table 15.4: Trade-off results between the potential secondary payloads derived in Table 15.3

	Criteria		
Concept	**Mass (High)**	**Data Rate (High)**	**Market Potential (Moderate)**
GHGSAT-Spectrometer	H	L	H
Poseidon-4	L	M	M
MWR-Sentinel 3	M	H	M
CIRC	H	L	H

Table 15.5: Specification table for the CIRC [12] instrument.

Specification	Value
Size	11x18x23 cm
Mass	2.6 kg
Wavelength	8-12 µm
Pixel array	640x480
Spatial resolution	<200 @ 600 km, <130 @ 400 km
FoV	12°x9°
Power	<20 W

that these instruments might bring. Mass was chosen as the first criteria as the mass budget was the most limiting one, as per Subsection 3.4.1, and was therefore given a high weight. Secondly, the interference between the secondary and primary payload was also chosen, as the secondary mission shall not affect the performance of the primary mission in any way, also earning a high weight. This criterion was later discarded as none of the concepts work in the wavelength used by the primary payload, therefore none of them should interfere with its performance. The data rate required was chosen as a criteria as it shows a large difference between concepts, however it was given a moderate weight as it is not very limiting given the TT&C design seen in Chapter 10. Lastly, the market potential had to be included as it is the one and only reason why a secondary mission is being investigated, and was therefore assigned a high weight.

Both the GHGSAT-Spectrometer and the CIRC instruments have quite a low mass, weighing 5.4 kg, and 2.6 kg, respectively[7,8]. An order of magnitude increase is seen for the masses of the other two instruments, with the MWR - Sentinel 3 weighing 24.2 kg, and the Poseidon 4 weighing 60 kg [9,10]. Low values are preferable when it comes to mass, therefore the GHGSAT-Spectrometer and the CIRC were given high scores here, a medium score was given for the MWR-Sentinel 3, whereas a low score was given for the GHGSAT-Spectrometer.

Lower data rates are preferred so that the secondary payload does not affect the data budget of the primary payload to a large extent. Since both the GHGSAT-Spectrometer and the CIRC are image based, they will certainly require a higher data rate. Poseidon-4 and MWR-Sentinel 3 are based on measuring the time difference between a reflected wave, therefore will require smaller data rates. Due to its increased mass, the Poseidon-4 instrument is assumed to have a larger data rate compared to the MWR-Sentinel 3, therefore it received a medium score here, compared to the high score given to the MWR-Sentinel. The two image based instruments were both given low scores.

Finally, for the market potential, due to the increasing awareness of global warming and climate change, which lead to an increasing amount of wildfires globally[11], demand for GHG data and wildfire detection should increase, therefore a high score here, which is desired, was given to the GHGSAT-Spectrometer and the CIRC. The Poseidon-4 altimeter also relates to this, however due to the large amount of already existing altimetry satellites it was given a medium score. Even though there may be a lower demand for soil moisture data, there is also less supply, and due to its market share as seen in Figure 15.3, this market may not be able to afford top level data. For this reason, the MWR-Sentinel 3 was given the same score as the Poseidon-4.

As seen in Table 15.4, there is a clear tie between two instruments, the GHGSAT-Spectrometer and the CIRC. Due to the typically large amounts of data rates required by imaging payloads, a choice still had to be made between the two. This choice ultimately fell in favour of the CIRC, since it weighs less than half of what the GHGSAT-Spectrometer weighs. As seen in Table 15.5, all parameters fit in the systems budgets seen in Subsection 3.4.1. As well as providing valuable Earth observation data to be sold to various costumers, the idea of using this instrument to aid the primary mission also came up, in the sense of using the IR spectrum captured by the camera to detect whether the ablation was successful or not. However, due to the location of the instrument, facing perpendicularly to the laser, this was deemed unfeasible.

[7] URL: https://space.oscar.wmo.int/instruments/view/ghgsat_spectrometer [Accessed on 09-06-2022].
[8] URL: https://space.oscar.wmo.int/instruments/view/circ [Accessed on 09-06-2022].
[9] URL: https://space.oscar.wmo.int/instruments/view/mwr_sentinel_3 [Accessed on 09-06-2022].
[10] URL: https://space.oscar.wmo.int/instruments/view/poseidon_4 [Accessed on 09-06-2022].
[11] URL: shorturl.at/oALNV [Accessed on 09-06-2022].
[12] URL: https://circgs.tksc.jaxa.jp/about_circ_e.html [Accessed on 10-06-2022].

15.3 Return on Investment

This section focuses on updating the profitability analysis done in (Teixeira et al., 2022b), aiming to prove to the client that this is a project worth investing into in the future.

Current Space Debris Removal Market

The market size of commercial space debris removal systems in LEO is insignificant at the current date, given that there are no laws in place to prevent debris creation and pave the way for this market to emerge. However, the market share is expected to rise exponentially as the risk of the Kessler syndrome increases. As mentioned in (Teixeira et al., 2022a), the main stakeholders of this mission are the inhabitants of Earth; therefore, market growth is expected to rise with the early onset of the Kessler syndrome. The rise in awareness, in turn, is proposed to lead the world's governments to start actively applying debris mitigation and cleaning laws. Space debris removal at this scale is likely to require intervention from the UN or other intergovernmental bodies to mandate action to sustain access to LEO. In the same way that fire departments are public services in the interest of the public, space debris removal is a question of public need. Thus, ethically speaking, the removal of space debris should not be a privatised market, but rather a publicly funded service at minimal cost, implying this to be a non-profit mission. With regard to accountability, organisations or states that are responsible for debris generating fragmentations in LEO should be fined to cover these costs, but this is a political concern.

LEO Market Value

As of now, this space system development project is contracted by ESA, assuming a preliminary cost budget of over M€643 million, as explained in Section 15.1. Currently, due to the lack of legal incentive for parties to pay for the debris removal operations that they are responsible for, public funding is required to finance these types of missions.

One possibility of marketing the spacecraft to international stakeholders, including governments and invested organisations, involves demonstrating the value of having an accessible LEO. The value of LEO in 2021 was around B$ 2.34 [13] to B$ 3.50 [14] (FY2021 USD), which is expected to grow to either B$ 4.36 by 2025 (FY2021 USD) [13], or B$ 9.0 by 2026 (FY2021 USD) [14] (depending on a CAGR or 16.9% or 21.5% respectively). Clearly, these values are only educated predictions; however, they give a general sense of an order of magnitude of the cost of spacecraft and launchers in LEO. This estimate does not delve into the cost of losing any associated services, observation or research from LEO spacecraft, or the cost of additional risk in launching missions through LEO if debris builds up. The costs of spacecraft collisions are astronomical, so relatively speaking, the estimated €300 million cost of one Space Sweeper could save billions in future losses.

Political Concerns

A high-powered laser in LEO, if not designed and operated under close international cooperation, will clearly raise concerns with fellow countries, organisations and the public, even though the risk of public harm is very low. As discussed previously, NASA considers any proposal of a powerful laser in space "dead on arrival" [15] for this exact reason. Thus, careful development, manufacturing, operation, and marketing processes are to be implemented, for which public transparency is essential for a laser-based debris removal system to be considered a safe solution in the public eye.

Tertiary mission

As derived in Section 15.2, a secondary payload has been chosen to be included in the Space Sweeper. It aims to provide valuable Earth observation data that can be sold to the highest bidder hoping to generate more funding for the future potential missions.

[13] URL: https://www.researchandmarkets.com/reports/5411783/low-earth-orbit-leo-satellites-global-market [Accessed on 20-05-2022]

[14] URL: https://www.globenewswire.com/en/news-release/2022/03/01/2393893/0/en/Low-Earth-Orbit-LEO-Satellites-Global-Market-Report-2022.html [Accessed on 20-05-2022]

[15] URL: https://web.archive.org/web/20160621185353/http://www.wired.com/2011/10/space-junk-laser/ [Accessed on 12-05-2022]

Conclusions and Recommendations 16

The Kessler syndrome was presented in the introduction of this report, as well as the path to follow to prevent its onset. With this in mind, DSE Team 13 has been working for ten weeks to tackle this problem, with the main goal being designing a space-based system that can clean an entire orbit after any break-up event, provided that it occurs at an orbital altitude between 350 and 1000 km. Upon this final report's completion, the team can safely say that this goal has been achieved to the highest of expectations. All subsystems have been designed to the component level, using COTS components following the sustainability strategy set in the previous stages of the report, when available, and planning technology development programs when required.

The team can say with great confidence that SpaceSweeper can clean over 50% of the debris population generated by any collision or explosion event within the orbital altitudes described above. A 27 kW peak power Nd:YAG laser, operating at 532 nm, will be used for this, along with a state-of-the-art lidar system, bringing the total payload mass to 1423 kg and allowing removal operations up to 250 km away, 30 km above the debris orbit. Due to the low shooting time and number of particles ablated per day, the average S/C power is not at all limiting, leading to a maximum solar array area of 35 m^2. The low efficiency of the payload does lead however to a criticality in the TMS, needing 35 heat pipes to radiate the extra heat away.

With sustainability as the main goal of the mission, a detailed strategy was derived, including a complete environmental life cycle assessment to quantify the entire mission's impact. Furthermore, IADC guidelines are strictly followed in every stage of the mission. A RAMS analysis estimated that the reliability and availability of the mission are 0.915 and 0.993 respectively. Space sustainability is a matter that concerns all of humanity, and for this reason, the Space Sweeper should be utilised as a public service, mandated by an intergovernmental party to ensure that accountable stakeholders are held liable for generated space debris. In this sense, the estimated €300 million cost of the Space Sweeper is marginal relative to the astronomical cost of losing access to LEO.

Furthermore, several recommendations can be made. First of all, on a system level, it would be very beneficial to investigate orbital refuelling such that the system can be reused, considering the fact that the system contains rather advanced technology, including a dedicated laser and lidar system, which would be wasteful to de-orbit after a single orbit is cleaned. Instead, it could be used again for another break-up event, cleaning even more space debris. Besides, multiple technology development plans were developed, which are crucial for the viability of the mission. These development plans included creating an optimal ablation laser design, performing experiments on debris characteristics (size, shape, material, rotational velocities), and developing the laser technologies required for design feasibility. It is recommended that these are developed in more detail, by contacting (more) companies and discussing the possibilities and associated estimated costs. It is expected that current manufacturers can provide a much more accurate estimation of the cost needed to bring these technologies to an adequate TRL. In general, many tests are required to achieve this, which are reflected in the costs of the mission. Additional research, together with manufacturers, is required to perform better research into the EPS subsystem (specifically Li-Ion capacitors), as well as developing a suitable PCDU. The CDHS system also requires the development of military-grade firewall and protection system.

Also, the design proposed was based on many assumptions that had to be made during the design process. By performing a number of additional iterations, it is expected to obtain a more solid design, as currently only a few iterations could be done within the allocated timeframe. During the design optimisation process, only a limited range for the used parameters were used. It is recommended that a Monte Carlo simulation is performed instead, covering a larger part of the design parameter space. Not only are extended Monte Carlo simulations necessary to iterate the design further, but the system itself should be simulated for multiple collision or explosion case studies. Currently, the reference case used is the Kosmos-Iridium collision, whereas using multiple other cases, like the STEP 2 Rocket Body explosion, may provide further insight to develop the design. Factors that may change include a more optimal relative altitude for different collision types or altitudes. More accurate models are recommended to be used, such as more advanced models for determining disturbance torques, and for sizing the magnetic torquers.

Regarding operational risks, the crossing of the polluted orbital region when being inserted into a higher orbit needs to be considered, as there is a danger of colliding with debris yourself. The effect of the laser pointing at Earth also should to be quantified, as no literature was found to indicate the possible effects of a certain wavelength with a certain energy targeting an object on ground, although the systems capabilities of targeting ground objects are limited. That said, public safety is a major priority for this mission.

References

Adly, I, HF Ragai, AE Elhennawy, and KA Shehata (2010). "Adaptive packet sizing for OTAP of PSoC based interface board in WSN". In: *2010 International Conference on Microelectronics*. IEEE, pp. 148–151.

Ailor, W. H. (2019). "Hazards of re-entry disposal of satellites from large constellations". In: *Journal of Space Safety Engineering* 6.2, pp. 113–121.

Andrews, Kenneth S, Dariush Divsalar, Sam Dolinar, Jon Hamkins, Christopher R Jones, and Fabrizio Pollara (2007). "The development of turbo and LDPC codes for deep-space applications". In: *Proceedings of the IEEE* 95.11, pp. 2142–2156.

Ariane 6 User's Manual (Feb. 2021). 2nd ed. Arianespace.

Bilen, Sven, Jesse McTernan, Brian Gilchrist, Iverson Bell, Nestor Voronka, and Robert Hoyt (2010). "Electrodynamic tethers for energy harvesting and propulsion on space platforms". In: *AIAA SPACE 2010 Conference & Exposition*, p. 8844.

Blackburn, E. P. et al. (1969). "Spacecraft Magnetic Torquers". In: *NASA Space Vehicle Design Criteria*. NASA.

Blengini, G et al. (2020). *Study on the EU's list of critical raw materials: Final Report*. Publications Office. DOI: doi/10.2873/11619.

Brundtland, G. H. (1987). "Our common future - Call for action". In: *Environmental Conservation* 14.4, pp. 291–294.

C.Phipps et al. (2012). "Removing Orbital Debris With Lasers". In: *Advances in Space Research* 49.9, pp. 1283–1300.

Camañes, C., B. Champel, M. Mariotto, R. Callegari, A. te Nijenhuis, H. J. van Gerner, J. van Es, and Ramon van den Berg (2019). *D2.1 - Study of the state of the art of Space Thermal Control Systems*. AVS-IMPACTA-D-2.1.

Chiaradia, Ana, Hélio Kuga, and Antonio Bertachini de Almeida Prado (2013). "Onboard and Real-Time Artificial Satellite Orbit Determination Using GPS". In: *Mathematical Problems in Engineering*.

Christian, John A and Scott Cryan (2013). "A survey of LIDAR technology and its use in spacecraft relative navigation". In: *AIAA Guidance, Navigation, and Control (GNC) Conference*, p. 4641.

Cooray, Asantha (2016). "Extragalactic background light measurements and applications". In: *Royal Society Open Science* 3.3, p. 150555.

Crassidis, John, Landis Markley, and Yang Cheng (2007). "Survey of Nonlinear Attitude Estimation Methods". In: *Journal of Guidance, Control, and Dynamics* 30.1, pp. 12–28.

Dissly, Rich, Carl Weimer, Jim Masciarelli, Jonathan Weinberg, Kevin Miller, and Reuben Rohrschneider (2012). "Flash lidars for planetary missions". In: *Workshop on Instrumentation for Planetary Missions*.

Eichler, Hans J. and Oliver Mehl (2001). "Phase Conjugate Mirrors". In: *Journal of Nonlinear Optical Physics Materials* 10.

ESA (2002). *Space product assurance: Cleanliness and contamination control*. Tech. rep. ECSS-Q-70-01A. ESA-ESTEC.

— (2021). *Fahrenheit CFD study report*. Tech. rep. ESA.

EUSPA EO and GNSS Market Report (2022). 1. EUSPA.

Falcon User's Guide (Sept. 2021). SpaceX.

Fang, Bertrand T. and Edward Seifert (2012). "An evaluation of Global Positioning System data for Landsat-4 orbit determination". In: *AIAA*.

Flohrer, T., J. Peltonen, A. Kramer, T. Eronen, J. Kuusela, E. Riihonen, T. Schildknecht, E. Stöveken, E. Valtonen, F. Wokke, et al. (2005). "Space-based Optical Observations of Space Debris". In: *4th European Conference on Space Debris*. Vol. 587, p. 165.

Fox, Bernard, Kevin Brancato, and Brien Alkire (2008). *Guidelines and Metrics for Assessing Space System Cost Estimates*. Tech. rep. United States Air Force.

Giovanni Vulpetti Les Johnson, Gregory L. Matloff (2015). *Solar sails: A Novel Approach to Interplanetary Travel*. second. Praxis Publishing.

Gong, Xuewen, Lei Guo, Fuhong Wang, Wanwei Zhang, Jizhang Sang, Maorong Ge, and Harald Schuh (2019). "Precise Onboard Real-Time Orbit Determination with a Low Cost Single-Frequency GPS Receiver". In: *remote sensing*.

H-IIA User's Manual (Feb. 2015). 4th ed. Mitsubishi Heavy Industries.

Hajiyat, Zahraa Raad Mayoof, Aduwati Sali, Makhfudzah Mokhtar, and Fazirulhisyam Hashim (2019). "Channel coding scheme for 5G mobile communication system for short length message transmission". In: *Wireless Personal Communications* 106.2, pp. 377–400.

Hodgson, Norman, Sebastian Heming, Albrecht Steinkopff, Hatim Haloui, and Tony S. Lee (2019). "Lasers in Manufacturing Conference 2019 Ultrafast Laser Ablation at 1035 nm , 517 nm and 345 nm as a Function of Pulse Duration and Fluence". In.

Huijbregts, M. A. J., Z. J. N. Steinmann, P. M. F. Elshout, G. Stam, F. Verones, M. D. M. Vieira, A. Hollander, M. Zijp, and R. van Zelm (2017). *ReCiPe 2016 v1.1*. RIVM Report 2016-0104a. RIVM.

IADC (2013). *Space Debris: IADC assessment report for 2011*. Tech. rep. IADC-12-06. Inter-Agency Space Debris Coordination Committee.

— (2020). *IADC Space Debris Mitigation Guidelines*. Tech. rep. IADC-02-01. Inter-Agency Space Debris Coordination Committee.

ISO 14040: Environmental management - Life cycle assessment - Principles and framework (2006). 2nd ed. ISO.

Jacklin, S. (2018). *Small-Satellite Mission Failure Rates*. Tech. rep. 220034. NASA.

Jaffe, Paul et al. (Oct. 2019). "Opportunities and Challenges for Space Solar for Remote Installations". In.

Ju, D. (2017). "Attitude control subsystem design of the stable and highly accurate pointing earth-imager". Master's Thesis. Delft, The Netherlands: Delft University of Technology.

Kelso, TS et al. (2009). "Analysis of the Iridium 33-Cosmos 2251 collision". In: *Advances in the Astronautical Sciences* 135.2, pp. 1099–1112.

Kessler, D. J., N. L. Johnson, J.C. Liou, and M. Matney (2010). "The kessler syndrome: implications to future space operations". In: *Advances in the Astronautical Sciences* 137.8, p. 2010.

Kheirabadi, Ali C and Dominic Groulx (2016). "Cooling of server electronics: A design review of existing technology". In: *Applied Thermal Engineering* 105, pp. 622–638.

Kirchner, Georg, Franz Koidl, Fabian Friederich, Ivo Buske, Uwe Völker, and Wolfgang Riede (2013). "Laser measurements to space debris from Graz SLR station". In: *Advances in Space Research* 51.1, pp. 21–24.

Klinkrad, H. (2006). *Space Debris: Models and Risk Analysis*. 1st ed. Chichester, UK: Springer-Praxis.

Koebel, Franck and Jean-François Coldefy (2010). "SCOC3: a space computer on a chip". In: *2010 Design, Automation Test in Europe Conference Exhibition (DATE 2010)*, pp. 1345–1348. DOI: 10.1109/DATE.2010.5457018.

LaViola, J.J. (2003). "A comparison of unscented and extended Kalman filtering for estimating quaternion motion". In: IEE.

Leon-Quiroga, Jorge, Brittany Newell, Mahesh Krishnamurthy, Andres Gonzalez-Mancera, and Jose Garcia-Bravo (2020). "Energy Efficiency Comparison of Hydraulic Accumulators and Ultracapacitors". In: *Energies* 13.7.

Letizia, F., S. Lemmens, D. Wood, M. Rathnasabapathy, M. Lifson, R. Steindl, K. Acuff, M. Jah, S. Potter, and N. Khlystov (2021). "Framework for the Space Sustainability Rating". In: *8th European Conference on Space Debris*.

Levchenko, Igor, Kateryna Bazaka, Stephane Mazouffre, and Shuyan Xu (Nov. 2018). "Prospects and physical mechanisms for photonic space propulsion". In: *Nature Photonics* 12, pp. 649–657.

Ley, W., K. Wittmann, and W. Hallmann (2009). *Handbook of Space Technology*. 1st ed. New York: John Wiley & Sons.

Li, Qingyan, Yafei Yang, Shiyu Yan, Bin Zhang, and Chunhui Wang (2021). "Real-time variable field-of-view scanning of LiDAR by controlling the drive voltage of MEMS micromirror". In: *Optik* 246, p. 167760.

Liedahl, D. A., A. Rubenchik, S.B Libby, S. Nikolaev, and C. R. Phipps (2013). "Pulsed laser interactions with space debris: Target shape effects". In: *Advances in Space Research* 52, pp. 895–915.

Lincoln, J. D., O. A. Ogunseitan, J. D. M. Saphores, J. M. Schoenung, H. Nixon, and A. A. Shapiro (2005). “Environmentally Benign Materials for Electronics: a Review of Current Developments and Emerging Technologies”. In: *International Symposium on Advanced Packaging Materials: Processes, Properties and Interfaces*, pp. 139–143.

Lu, Yafei, Yuan Zhou, Mo Hei, and Dapeng Fan (2014). “Frame frequency prediction for Risley-prism-based imaging laser radar”. In: *Applied Optics* 53.16, pp. 3556–3564.

Mani, K. V., F. Topputo, and A. Cervone (2018). “Dual Chemical-Electric Propulsion Systems Design for Interplanetary CubeSats”. In: *ESA Space Propulsion Conference, Seville, Spain*.

Markley, F. Landis and John L. Crassidis (2014). *Fundamentals of Spacecraft Attitude Determination and Control*. Springer. DOI: DOI10.1007/978-1-4939-0802-8.

Mason, J., J. Stupl, and W. Marshall (2011). “Orbital Debris - Debris Collision Avoidance”. In: *Advances in Space Research* 48.

Meyer, Mike, L Johnson, B Palaszewski, D Goebel, H White, and D Coote (2012). “In-space propulsion systems roadmap”. In: *National Aeronautics and Space Administration, Office of the Chief Technologist*.

Montenbruck, O., E. Gill, and F. Lutze (2000). *Satellite orbits: models, methods and applications*. 1st. Berlin, Germany: Springer.

Mourra, Olivier, Thierry Blancquaert, Carla Signorini, and Ferdinando Tonicello (2008). “European Cooperation for Space Standardization - The New Standard for Electric and Electronic ECSS-E-ST-20-C”. In: *8th European Space Power Conference*. Vol. 661, p. 112.

Muelhaupt, T. J., M. E. Sorge, J. Morin, and R. S. Wilson (2019). “Space Traffic Management in the New Space Era”. In: *Journal of Space Safety Engineering* 6.2, pp. 80–87.

Müller, P (2008). “ESA tracking stations (ESTRACK) facilities manual (EFM)”. In: *Reference: DOPS-ESTR-OPS-MAN-1001-OPS-ONN*.

Musci, R., T. Schildknecht, T. Flohrer, and G. Beutler (2005). “Concept for a Catalogue of Space Debris in Geo”. In.

n.a. (2020). *Executive Summary Report*. Tech. rep. 1.0. CS-ESA-SOR-TD-005. Clearspace Today.

NASA (1975). *Astronautics Structures Manual Volume II*. Tech. rep. NASA TM X-73306. NASA.

— (2014). *Guidelines for Assessing the Toxic Hazard of Spacecraft Chemicals and Test Materials*.

— (2021). *Power State of the Art NASA report*. Tech. rep. NASA.

Opiela, J. N. (2009). “A study of the material density distribution of space debris”. In: *Advances in Space Research* 43.7, pp. 1058–1064.

Parkinson, Bradford W. and Jame J. Spiker (1996). *The Global Positioning System: Theory and Applications*. 8th ed. American Institute of Aeronautics and Astronautics. DOI: https://doi.org/10.2514/4.866388.

Phipps, C. R. (2014). “L’ADROIT – A Spaceborne Ultraviolet Laser System for Space Debris Clearing”. In: *Acta Astronautica* 104.1, pp. 243–255.

Phipps, C. R., M. Boustie, J.-M. Chevalier, S. Baton, E. Brambrink, L. Berthe, M. Schneider, L. Videau, S. A. E. Boyer, and S. Scharring (2017). “Laser impulse coupling measurements at 400 fs and 80 ps using the LULI facility at 1057 nm wavelength”. In: *Journal of Applied Physics* 122.19, p. 193103.

Phipps, Claude, Mitat Birkan, et al. (2010). “Review: Laser-Ablation Propulsion”. In: *Journal of Propulsion and Power* 26.4.

Pieters, Liam (Nov. 2020). “Active Small-scale Space Debris Removal by a Space-based Laser”. TU Delft.

Recommendation ITU-R P. 676-10 (2013). *Attenuation by atmospheric gases P Series Radiowave propagation*.

Rems, F, J. A. Moreno Gonźalez, T. Boge, S. Tuttas, and U. Stilla (2015). “Fast initial pose estimation of spacecraft from lidar point cloud data”. In: *13th Symposium on Advanced Space Technologies in Robotics and Automation*. ASTRA. DLR.

Rivera, Alejandro (2021). “Study of Spacecraft Deployables Failures”. In: *Space Systems Anomalies and Failures (SCAF) Workshop 2022*.

Rongzhi, Zhang and Yang Kaizhong (2020). *Spacecraft Collision Avoidance Technology*. Elsevier. DOI: https://doi.org/10.1016/C2018-0-02148-9.

Rosen, M. A. (2012). “Engineering sustainability: A technical approach to sustainability”. In: *Sustainability* 4.9, pp. 2270–2292.

RUAG Space GmbH (2020). *Thermal Insulation Products*. https://www.ruag.com/system/files/media_document/2020-02/Thermal%20insulations%20products_low_1.pdf.

Schuhmacher, Jonas (Sept. 2021). “Efficient Implementation and Evaluation of the NASA Breakup Model in modern C++”. Bachelorarbeit. Technical University of Munich.

Secure World Foundation (2018). *Space Sustainability: a Practical Guide*.

Shanks, Katie, Sundaram Senthilarasu, and Tapas K Mallick (2016). “Optics for concentrating photovoltaics: Trends, limits and opportunities for materials and design”. In: *Renewable and Sustainable Energy Reviews* 60, pp. 394–407.

Shukla, KN et al. (2015). “Heat pipe for aerospace applications—an overview”. In: *Journal of Electronics Cooling and Thermal Control* 5.01, p. 1.

Slotten, J. D. (2017). “Examination of Debris Cloud Density Resulting From Precession of Argument of Perigee Due to J2 Effect”. In: *7th European Conference on Space Debris* 7.

Smith, D. Todd (2014). “Calculating the system steady-state availability as a function of subsystem steady-state availability”. In: *IEEE SOUTHEASTCON 2014*, pp. 1–3. DOI: 10.1109/SECON.2014.6950731.

SolidWorks (2019). *SOLIDWORKS Simulation 2019 Validation*. Tech. rep. Dassault Systemes.

Soulard, Rémi, Mark N.Quinn, Toshiki Tajima, and Gérard Mourou (2014). “ICAN: A Novel Laser Architecture for Space Debris Removal”. In: *Acta Astronautica* 105.1, pp. 192–200.

Space system Life Cycle Assessment (LCA) Guidelines (Oct. 2016). ESA LCA Working Group.

Speretta, S. (2020). “Spacecraft Attitude Determination and Control Systems and Telecommunications”. Lecture slides from Aerospace Design and Systems Engineering Elements II at TU Delft.

Starin, Scott R. and John S. Eterno (2010). “Attitude Determination and Control Systems”. In.

Steindorfer, Michael A, Georg Kirchner, Franz Koidl, Peiyuan Wang, Beatriz Jilete, and Tim Flohrer (2020). “Daylight space debris laser ranging”. In: *Nature communications* 11.1, pp. 1–6.

Stougie, Lydia, Georgios A Tsalidis, Hedzer J van der Kooi, and Gijsbert Korevaar (2018). “Environmental and Exergetic Sustainability Assessment of Power Generation from biomass”. In: *Renewable Energy* 128, pp. 520–528.

Sumanth, M. (Jan. 2019). “Computation of Eclipse Time for Low-Earth Orbiting Small Satellites”. In: *International Journal of Aviation, Aeronautics, and Aerospace*.

Tafazoli, Mak (2009). “A Study of On-orbit Spacecraft Failures”. In: *Acta Astronautica* 64.2-3, pp. 195–205.

Tajmar, Martin, Oliver Neunzig, and Marcel Weikert (Mar. 2021). “High-Accuracy Thrust Measurements of the EMDrive and Elimination of False-Positive Effects”. In.

Teixeira, G. A., E. Bögel, F. Meijering, J. Struzinski, L. Veithen, J. B. Fernandez, H. Buurmeijer, D. Rehling, P. van Wolfswinkel, and N. Zandvliet (2022a). *Space Sweeper Baseline Report*. 1. TU Delft.

— (2022b). *Space Sweeper Midterm Report*. 1. TU Delft.

Thiagarajah, Siva Priya, Shamini Pillay, Shalini Darmaraju, Rajamani Subramanian, and Michelle Foo May Fung (2013). “The effect of rain attenuation on S-band terrestrial links”. In: *2013 IEEE Symposium on Wireless Technology & Applications (ISWTA)*, pp. 192–197. DOI: 10.1109/ISWTA.2013.6688768.

Vaz, Brendon (2011). “Online Calibration for Star Trackers”. Master Thesis. Ryerson University.

Wang, T. (2010). “Analysis of Debris from the Collision of the Cosmos 2251 and the Iridium 33 Satellites”. In: *Science & Global Security* 18.2, pp. 87–118.

Wang, Yifei, Dennis Y.C. Leung, Jin Xuan, and Huizhi Wang (2016). "A review on unitized regenerative fuel cell technologies, part-A: Unitized regenerative proton exchange membrane fuel cells". In: *Renewable and Sustainable Energy Reviews* 65, pp. 961–977.

Wertz, J.R., H.F. Meissinger, L.K. Newman, and G.N. Smit (2009). *Orbit & Constellation Design & Management*. 2nd. New York: Microcosm Press and Springer.

Wertz, James R, David F Everett, and Jeffery J Puschell (2011). *Space Mission Engineering: The New SMAD*. Microcosm Press.

Winker, David M, William H Hunt, and Chris A Hostetler (2004). "Status and performance of the CALIOP lidar". In: *Laser Radar Techniques for Atmospheric Sensing*. Vol. 5575. SPIE, pp. 8–15.

Wright, D. (2009). "Colliding Satellites: Consequences and Implications". In: *Union of Concerned Scientists* 26.

Xie, Yong-chun, Huang Huang, Yong Hu, and Guo-qi Zhang (2016). "Applications of advanced control methods in spacecrafts: progress, challenges, and future prospects". In: *Frontiers of Information Technology & Electronic Engineering* 17.

Zandbergen, B.T.C. (2021). *AE1222-II: Aerospace Design & Systems Engineering Elements I*. TU Delft.

Zhang, Zhongping, Haifeng Zhang, MingLiang Long, Huarong Deng, Zhibo Wu, and Wendong Meng (2019). "High precision space debris laser ranging with 4.2 W double-pulse picosecond laser at 1 kHz in 532nm". In: *Optik* 179, pp. 691–699.

Zimmermann, Claus, A. Bals, A. Übner, F. Schlerka, and A. Schindler (Jan. 2017). "Development of a New, High-Power Solar Array for Telecommunication Satellites". In: *E3S Web of Conferences* 16.

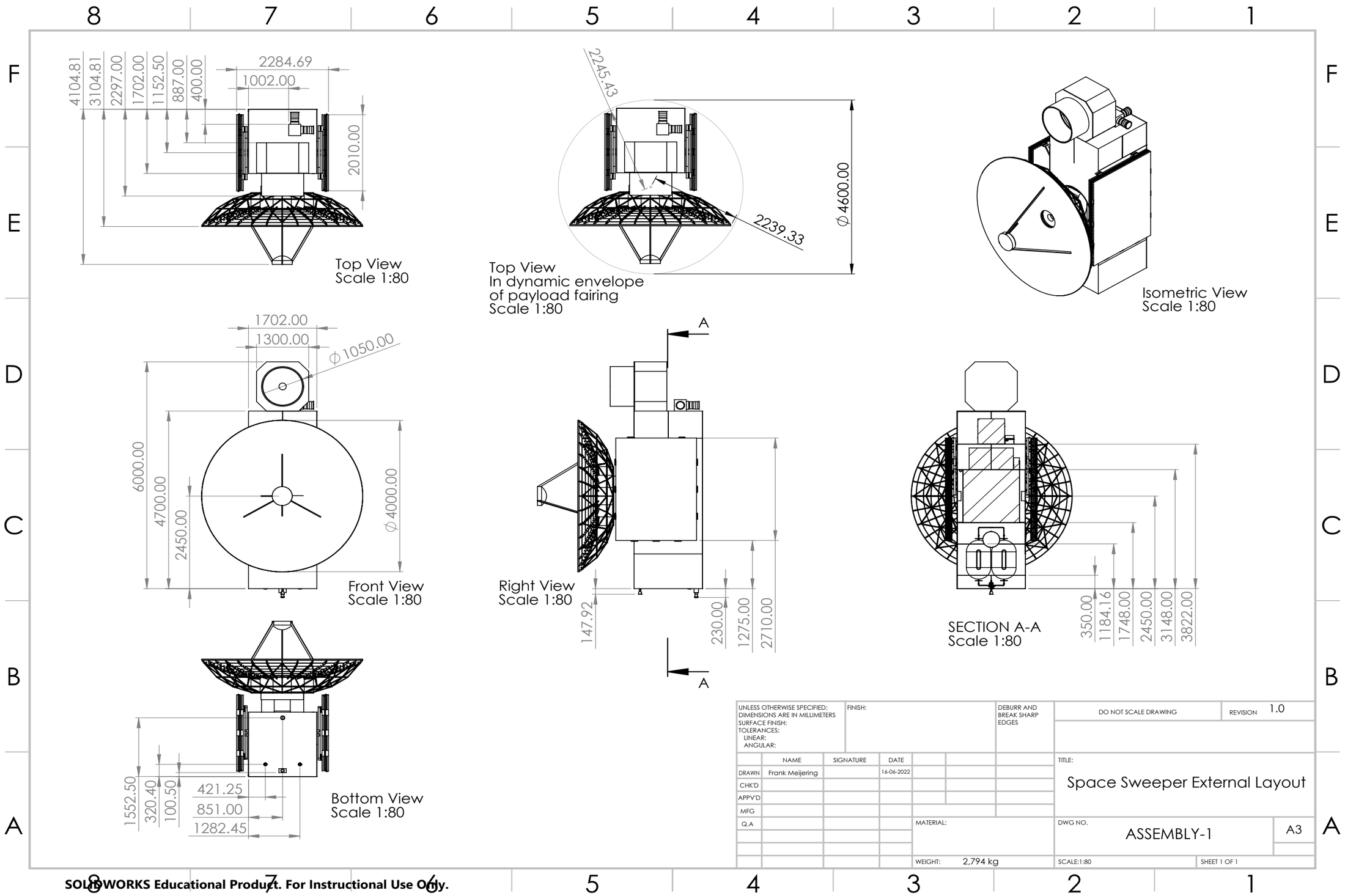

Figure A.1: Technical drawing of the Space Sweeper.